Synthesis and Magnetic Properties of Polyimidosulfur- and Bis(benzoxazolyl)methanide-ligated Complexes

Dissertation

zur Erlangung des mathematisch-naturwissenschaftlichen Doktorgrades

“Doctor rerum naturalium“

der Georg-August-Universität Göttingen

im Promotionsprogramm Chemie

der Georg-August University School of Science (GAUSS)

vorgelegt von

Daniel Lüert

aus Göttingen

Göttingen, 2022

Thesis Committee

Prof. Dr. Dietmar Stalke, Institut für Anorganische Chemie, Georg-August-Universität Göttingen.

Prof. Dr. Franc Meyer, Institut für Anorganische Chemie, Georg-August-Universität Göttingen.

Prof. Dr. Thomas Waitz, Institut für Anorganische Chemie, Georg-August-Universität Göttingen.

Members of the Examination Board

Reviewer: Prof. Dr. Dietmar Stalke, Institut für Anorganische Chemie, Georg-August-Universität Göttingen.

Second Reviewer: Prof. Dr. Franc Meyer, Institut für Anorganische Chemie, Georg-August-Universität Göttingen.

Additional Reviewer: Prof. Dr. Thomas Waitz, Institut für Anorganische Chemie, Georg-August-Universität Göttingen.

Further members of the Examination Board

Jun.-Prof. Dr. Anna Krawczuk, Institut für Anorganische Chemie, Georg-August-Universität Göttingen.

Dr. Matthias Otte, Institut für Anorganische Chemie, Georg-August-Universität Göttingen.

PD Dr. Michael John, Institut für Organische Chemie, Georg-August-Universität Göttingen.

Date of the oral examination: 01.09.2022

Für meine Familie

“Success is stumbling from failure to failure with no loss of enthusiasm.“

– Winston S. Churchill

Publications

Major parts of this thesis have been published in:

[1] C. M. Legendre,‡ D. Lüert,‡ R. Herbst-Irmer, D. Stalke. Benchmarking magnetic and spectroscopic properties on highly stable 3d metal complexes with tuneable bis(benzoxazol-2-yl)methanide ligands. *Dalton Trans.* **2021**, 50, 16810-16818.[1]

[2] D. Lüert, R. Herbst-Irmer, D. Stalke. Structural and Magnetic studies on Lanthanide Bis(benzoxazole-2-yl)methanides. *Eur. J. Inorg. Chem.* **2021**, 5085-5090.[2]

[3] D. Lüert, A.-K. Kreyenschmidt, C. M. Legendre, R. Herbst-Irmer, D. Stalke. A Sodium Sodate as Precursor for Lanthanide Bis(4-*R*-benzoxazol-2-yl)methanide Single-Molecule Magnets. *Inorg. Chem.* **2022**, *61*, 5234-5244.[3]

[4] D. Lüert, R. Herbst-Irmer, D. Stalke. Sodium and sodium sodate precursors for polynuclear terbium(III) complexes. **2022**, *manuscript in preparation*.[4]

[5] D. Lüert, C. M. Legendre, R. Herbst-Irmer, D. Stalke. Alkali Metal Based Triimidosulfite Cages as Versatile Precursors for Single-Molecule Magnets. *Chem Eur. J.* **2022**, *28*, e202104470.[5]

[6] Y. Ding, S. K. Sarkar, M. Nazish, S. Muhammed, D. Lüert, P. N. Ruth, C. M. Legendre, R. Herbst-Irmer, P. Parameswaran, D. Stalke, Z. Yang, H. W. Roesky. Stabilization of Reactive Nitrene by Silylenes without Using a Reducing Metal. *Angew. Chem. Int. Ed.* **2021**, *60*, 27206-27211.[6]

[7] M. Nazish, A. Harinath, D. Lüert, C. Köhler, R. Herbst-Irmer, D. Stalke, H. W. Roesky. Reactivity of silylene with gallium- and boron tribromide under reducing conditions resulted in a completely unforeseen product. **2022**, *manuscript in preparation*.[7]

‡ These authors contributed equally.

Table of Contents

Abbreviations

Å	Ångstrom
ac	alternating current
ACS	American Chemical Society
AILFT	*ab initio* Ligand Field Theory
a.u.	arbitrary units
BCE	Before the Common Era
BOC	*tert*-Butyloxycarbonyl
Box, L$_1$	Bis(benzoxazol-2-yl)methanide
btaH	1*H*-1,2,3-Benzotriazole
BZHbox, L$_2$	Bis(4-benzhydryl-benzoxazol-2-yl)methanide
calc.	calculated
CASSCF	Complete Active Space multiconfiguration Self Consistent Field
CCDC	Cambridge Crystallographic Database Centre
CShMs	Continuous Shape Measures
CIF	Crystallographic Information
COT^{2-}	1,3,5,7-Cyclooctatetraene
Cy$_3$PO	Tricyclohexylphosphine oxide
Cp^{ttt}	C_2H_5*t*Bu$_3$-1,2,4
δ	chemical shift (ppm)
D	zero-field splitting (ZFS) parameter
dc	direct current
DCM	Dichloromethane
Dmp	2,6-dimestylphenyl
E	rhombic zero-field splitting parameter
EPR	Electron Paramagnetic Resonance
equiv.	Equivalent(s)
ESI	Electrospray Ionization
Et$_2$O	Diethylether
et al.	lat.: *et alii,*
h	hours
H	magnetic field strength
Hhfac	Hexafluoro acetylacetone
HMDS	1,1,1,3,3,3-Hexamethyldisilazane / Bis(trimethylsilyl)amine

J	magnetic exchange coupling constant
J	magnetic quantum number (lanthanide ions), total angular momentum
L	orbital angular momentum
L^a	1-(2-Hydoxybenzamido)-2-(2-hydroxy-3-methoxy-benzylideneamino)-ethane
LIFDI	Liquid Injection Field Desorption Ionization
Ln	Lanthanides (Ce-Lu)
μ_B	Bohr magneton
mbar	Millibars
Me	methyl
Mebox, L_4	Bis(4-methyl-benzoxazol-2-yl)methanide
MHz	megahertz
MPMS	Magnetic Properties Measurement System
MS	Mass Spectrometry
M_s/M_J	magnetic quantum number
m/z	mass/charge
ν (Hz, cm^{-1})	frequency
NEVIP2	second order n-electron valence state perturbation theory
NMR	Nuclear Magnetic Resonance
Oe	Oersted
PB	Phonon Bottleneck Relaxation
Pc	Phthalocyanine
ppm	parts per million
QTM	Quantum Tunneling of Magnetization
r.t.	room temperature (298 K)
S	spin angular momentum
Sbox	Bis(benzothiazole-2-yl)methanide
SC-XRD	Single Crystal X-ray Diffraction
SIM/SMM	single-ion magnet/ single-molecule magnet
SOC	Spin-Orbit Coupling
SQUID	Superconducting Quantum Interference Device
T (K)	temperature
τ	relaxation time

*t*Bu	*tertiary* Butyl
*t*Bubox, L_3	Bis(4,6-*tert*-butyl-benzoxazol-2-yl)methanide
*t*BuLi	*tert*-Butyllithium
thf	tetrahydrofuran
tmeda	*N*,*N*,*N*',*N*'-tetramethylethane-1,2-diamine
tms	trimethylsilyl
U_{eff}	effective thermal energy barrier to spin reversal
VTVH	variable temperature variable field
χ'	molar in-phase susceptibility
χ''	molar out-of-phase susceptibility
$\chi_{\mathrm{M}}T$	product of the molar susceptibility and the temperature
X-ray	X-ray radiation

List of Box Compounds

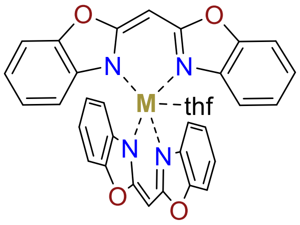

M = Mn^{II} (**1**), Fe^{II} (**2**)

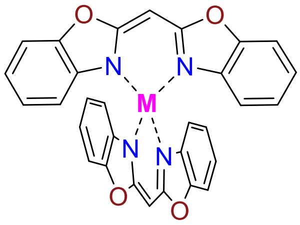

M = Co^{II} (**3**), Ni^{II} (**4**)

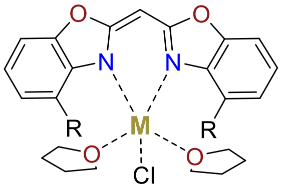

R= benzyhydryl

M = Mn^{II} (**5**), Fe^{II} (**6**)

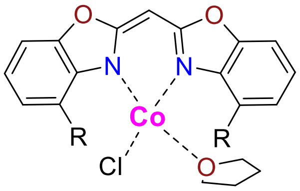

R= benzhydryl

7

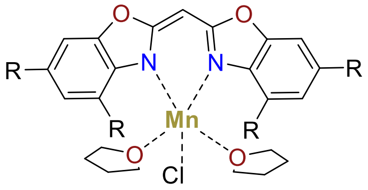

R= *t*Bu

8

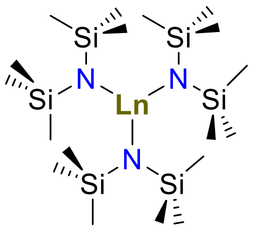

Ln = Gd^{III} (**9**), Ho^{III} (**10**)

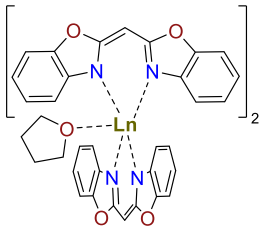

Ln = Eu^{III} (**11**), Tb^{III} (**12**),

Dy^{III} (**13**), Ho^{III} (**14**),

Er^{III} (**15**)

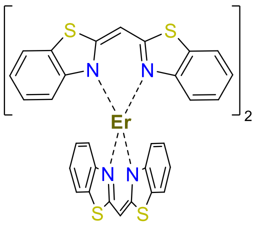

16

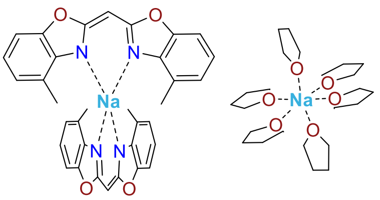

17

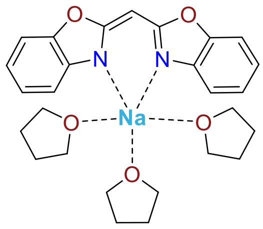

18

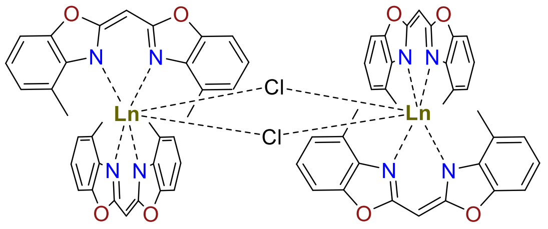

Ln = Gd^{III} (**19**), Dy^{III} (**20**), Er^{III} (**21**)

List of SN Compounds

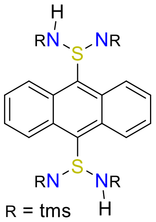

22

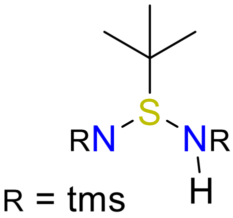

23

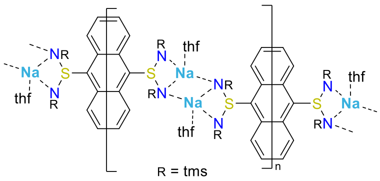

24

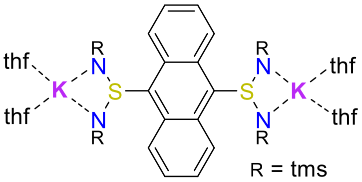

25

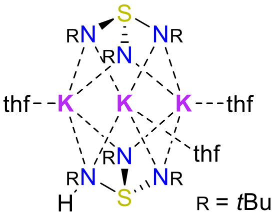

26

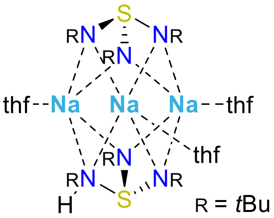

27

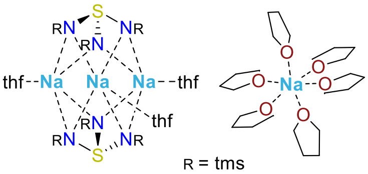

28

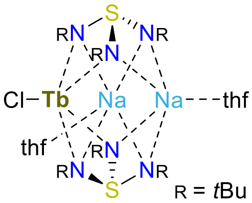

29

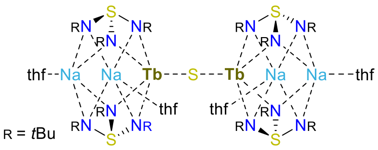

30

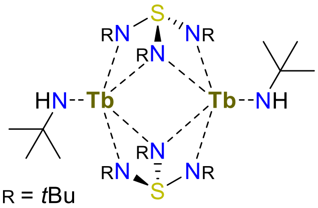

31

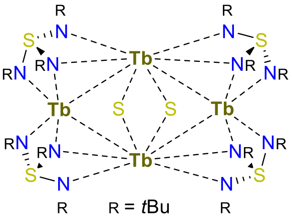

32

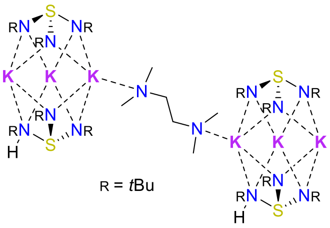

33

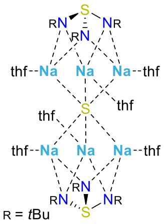

34

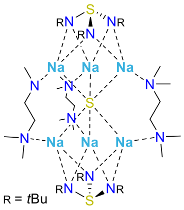

35

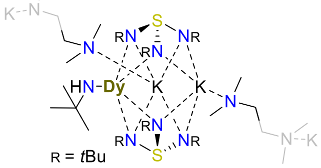

36

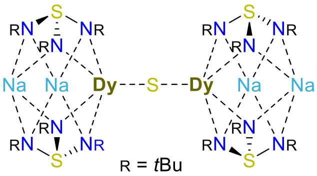

37

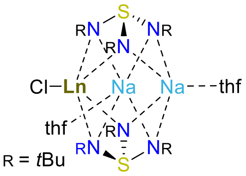

Ln = Dy^{III} (**38**), Er^{III} (**39**)

1. General Introduction

1.1. Transformation of data storage

How to preserve information for the next generation was and remains the key endeavor for humankind. Homo sapiens started employing cave paintings to conserve valuable cultural knowledge back in 30,000 BCE. A major role portrays the origin of writing about 3,200 BCE. Books were from now on the medium to maintain findings and wisdom for centuries.[8] Before the nineteenth century, the compass was the first and only application for magnetism.[9] The discovery of the dynamoelectric principle by Siemens stimulated the development of new applications of magnetism.[10] Only 70 years ago, for the first time in history,[11] data was digitalized on magnetic tapes. Further improvements and minimization allowed us to create high-density data storage, present in various devices in our daily life (**Figure 1.1.a**). However, this fast-proceeding top-down approach will soon hit the borders of classical physics, and further progress is hampered by the uncertainty principle in quantum physics and the lithographic manufacturing cycle.[12] The data we generate every year increases exponentially (**Figure 1.1.b**) and requires our storage capacities to exceed at the same pace. Therefore, one approach starts from the molecular entity to realize superior data storage systems, the corresponding physical and chemical background is rolled out in the following chapters. This thesis will shine light on promising but neglected materials and correlate structural and magnetic properties to provide more basic knowledge to this young scientific field.

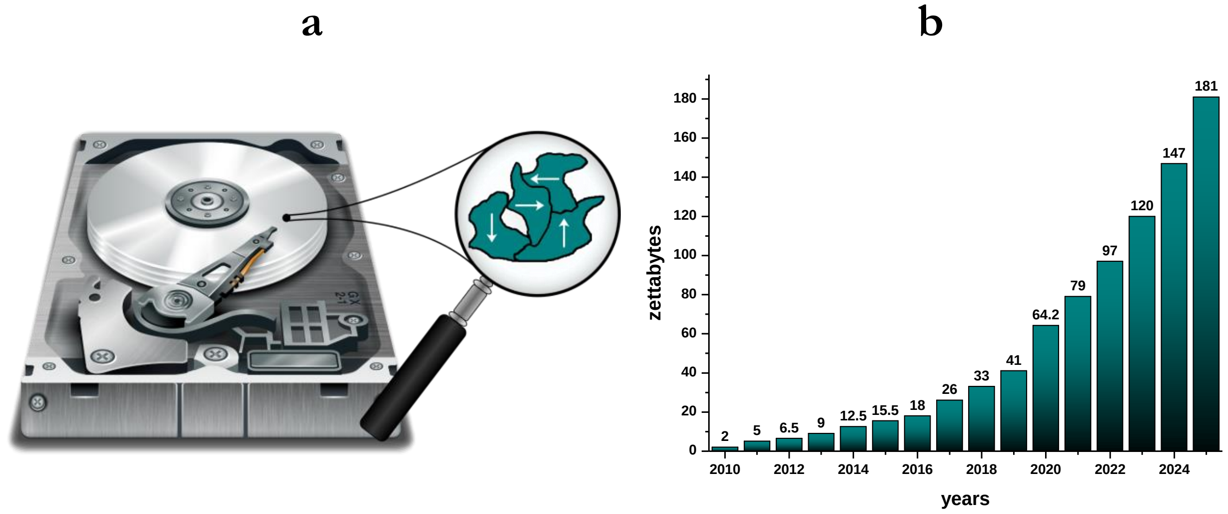

Figure 1.1. (**a**) Magnetic domains in a hard disk drive (HDD). (**b**) Estimated volume of data created, captured, copied, and consumed worldwide from 2010 to 2025. Created in accordance with Ref.[13]

1.2. Fundamentals of single-molecule magnets

The origin of magnetism is fundamentally different in a ferromagnet and a single-molecule magnet (SMM). For a traditional magnet, the magnetic moment stems from the formation of three-dimensional domains, consisting at least of 10^6 molecules with an aligned spin (**Figure 1.1.a**).[14] Magnetic hysteresis roots in the domain stability and vanishes only when thermal motion breaks them apart. For this phenomenon to happen, each ferromagnetic material has a critical temperature under which the magnetization is blocked, called the Curie temperature.[15] However, an SMM is related but comprises only a single molecule, which is magnetically isolated and is not interacting with neighboring molecules. In the literature, there is a differentiation between single-ion (SIMs) and single-molecule magnets (SMMs), while the former consists of only one metal center and the latter is applied for clusters with numerous metal ions.[14] The general building block of an SMM is a paramagnetic core where transition metal or lanthanide ions are employed and a diamagnetic shell with organic or inorganic ligands.[16] The first example of an SMM was recorded back in 1993, when the manganese acetate cluster $Mn_{12}O_{12}(OAc)_{16}(H_2O)_4$ further devoted as Mn_{12}, remained magnetized at 2 K for several months, after switching off the external field.[17]

When an SMM is exposed to a magnetic field, its unpaired spins align with the orientation of the external field to the most energetically preferred direction. The most favorable orientation is further referred to an anisotropy or easy axis, while the least favorable axis is a plane perpendicular to this axis. The anisotropy of magnetization is described by the axial (*D*) and rhombic (*E*) zero-field splitting (ZFS) parameters with the combination of the spin (*S*) in the following Hamiltonian:[18]

$$\hat{H} = \left[D\hat{S}_z^2 - S(S+1)/3 + E\left(\hat{S}_x^2 - \hat{S}_y^2\right)\right] \qquad (\mathbf{1\text{-}1})$$

$\hat{S}$ devotes to a spin operator, which defines the spin projection along a specific direction. One criterium for a good SMM is that the rhombic contribution E should be minimized to zero, while the axial contribution D is required to be tuned with an axial ligand symmetry around the metal center.

Two phenomena provoke zero-field splitting: first- and second-order spin-orbit coupling. The former applies for ions with unquenched orbital angular momenta, where spin-orbit coupling (SOC) induced splitting in the electronic ground state of a system. The latter, mixing of the electronic ground states with the excited states, which display second-order spin-orbit coupling, results in a significantly smaller effect since it is divided by the energy difference between the states (~10^4 cm^{-1}).[19] To illustrate the second-order SOC phenomenon, a d^8 metal ion (Ni(II)) in an octahedral ligand field is considered (**Figure 1.2.b**). We expect a ^3F ground term from Russell-

Saunders schemata that splits in a $^3A_{2g}$ ligand field term. Broadly speaking, an A term does not display first-order SOC, but the derived excited states, $^3T_{1g}$ and $^3T_{2g}$, can mix with the ground state. Noteworthily, assuming a strict octahedral environment, an elevation of degeneracy is not observed, and the mixing of these states decreases the energy of the ground state term. However, there is usually a distortion from an ideal symmetry, lifting the degeneracy of the spin-triplet ground state and causing anisotropy.[18] A true first-order SOC is observed for a Co^{II} ion in a weak octahedral ligand field with a ^4F free ion ground state term, which splits into a $^4T_{1g}$ ground state term (**Figure 1.2.a**). Applying a tetragonal distortion (D_{4h}) results in two states, labeled as $^4A_{2g}$ and ^4E_g, that further split via SOC into six Kramers doublets.[19b]

Two criteria evaluate the performance of an SMM, the blocking temperature of magnetization (T_B) and the effective energy barrier for spin reversal (U_{eff}). The former can be illustrated in a simplified way as the highest temperature to which magnetic hysteresis is present. To determine U_{eff}, the axial contribution D is of significant importance for a high energy barrier, while the contribution of S is elucidated in more detail in chapter 1.4, depending on the spin system as exemplified in equations (**1-2**) and (**1-3**).

$$U_{\text{eff, integer spins}} = |D|S^2 \tag{1-2}$$

$$U_{\text{eff, half-integer spins}} = |D|(S^2 - 1/4) \tag{1-3}$$

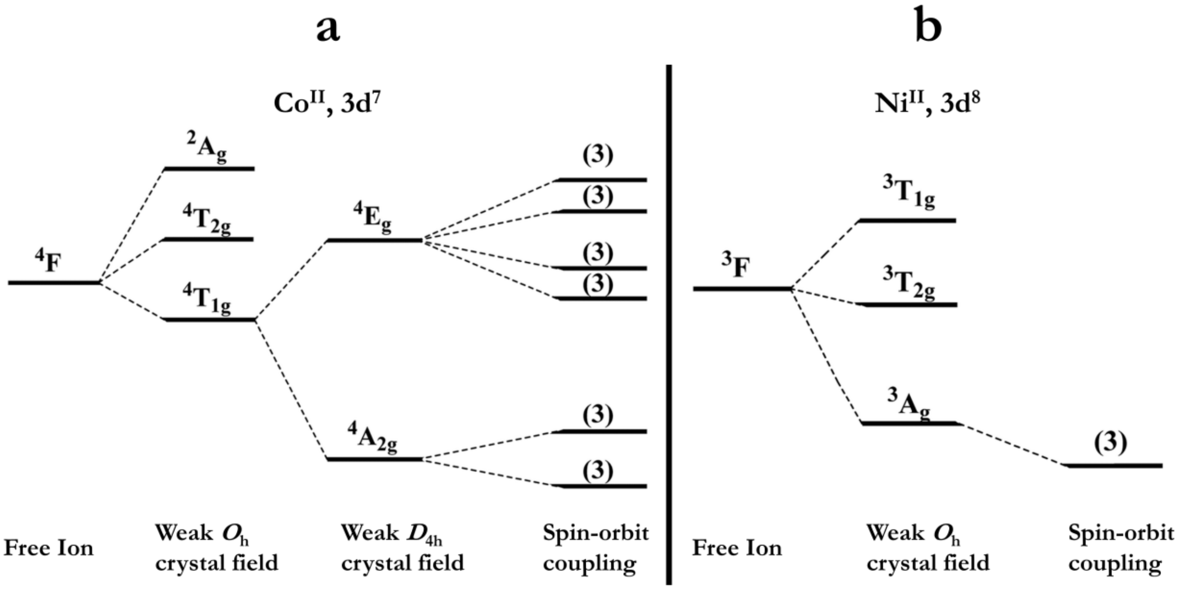

Figure 1.2. (**a**) Energy level diagram of high-spin Co^{II} in an axial distorted octahedral crystal field displaying first-order SOC, with the multiplicity of energy levels provoked by SOC shown in brackets. (**b**) Ni^{II} in a weak octahedral crystal field, displaying second-order SOC, with the multiplicity of energy levels provoked by SOC illustrated in brackets. Reproduced from Ref.[18] with permission from the Royal Society of Chemistry.

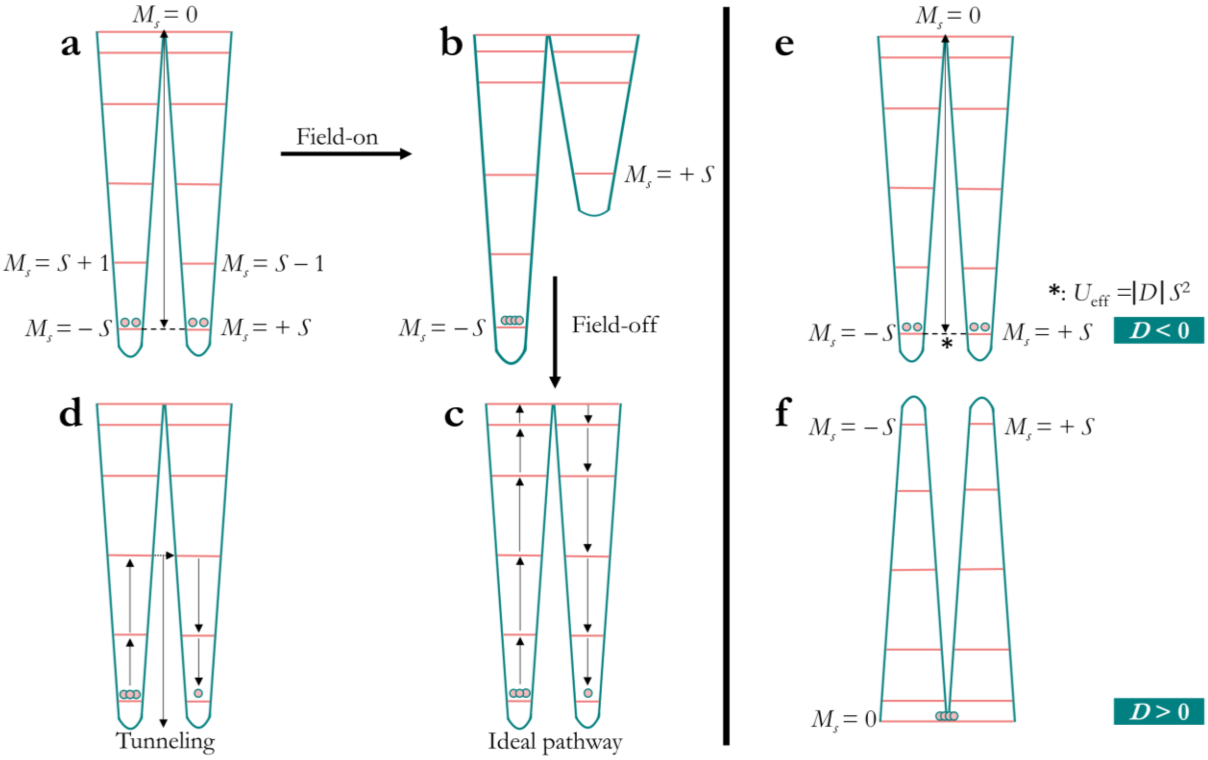

Figure 1.3. The double-well energy diagram representing the magnetization and relaxation in SMMs: (**a**) Zero-field splitting (ZFS) effect on the spin state S causes a separation of both wells. (**b**) Switching on an external magnetic field results in the $M_s = +S$ destabilization, which depopulation is preferred. (**c**, **d**) Turning off the external field facilitates various relaxation processes. (**e**, **f**) Double-well potential for negative (**e**) and positive (**f**) D value. (**f**) Here the double-well energy diagram is flipped and no SMM behavior is observed. Created in accordance with Ref.[16,18].

The zero-field splitting effects are well studied for transition metal complexes but rather rudimentarily investigated for lanthanide complexes. For a 3d complex, its total spin S consists of $2S+1$ spin states with a spin quantum number M_s for each sublevel. To illustrate the behavior of an SMM, the double-well potential with the $\pm M_s$ levels on different potential wells, split by an energy barrier U_{eff}, is utilized. For a system under zero-field conditions, all M_s levels are arranged in degenerated pairs in the $M_s = -S$ and $M_s = +S$ states, which always require a bistable ground state for all SMMs (**Figure 1.3.a**). When applying an external field, the $M_s = -S$ well is stabilized while the $M_s = +S$ well is destabilized. Once the system reaches magnetic saturation, a population of only the $M_s = -S$ level occurs (**Figure 1.3.b**). Next, the field is turned off, and the return to equilibrium is facilitated over various relaxation processes, which are covered in the next chapter in more detail.[15,16,20] Last, the above-presented model for an SMM requires a negative D value (**Figure 1.3.e**), only then the largest $\pm M_s$ states are the ground states. However, many transition metal complexes display a positive D value, resulting in a vertical flipped double-well potential with no energy barrier between both spin representations, and no SMM behavior is observed (**Figure 1.3.f**).

1.3. Relaxation mechanisms

1.3.1. Spin-lattice relaxation T_1

The relaxation induced by the energy transfer of a molecule with its surrounded lattice devotes to the term spin-lattice relaxation (T_1). Basically, this process can be characterized with a spin relaxing from the destabilized "spin up" to the stabilized "spin down" orientation. Energy is discretely transferred via phonons, which are cumulative, long-distance vibrations in solids.[21] There are two types of phonons: acoustic phonons, which refer to the cooperative motion of atoms in the crystalline material, and optical phonons, caused by intramolecular vibrations. The exact influence of these vibrations on the magnetic behavior of SMMs is still investigated.[22] To describe the relaxation, the specific relaxation rate τ^{-1} is used and given as:

$$\tau^{-1} = AH^{n_1}T + CT^{n_2} + \tau_0^{-1}\exp\left(-\frac{U_{\mathrm{eff}}}{k_{\mathrm{B}}T}\right) + Q \tag{1-4}$$

where T devotes to the specific temperature dependency and A, C, τ_0^{-1}, and Q are treated as free-to-fit parameters since their determination is highly challenging. The four contributing terms of the relaxation processes are outlined below in detail. The first method to measure the spin-lattice relaxation is to employ a magnetic properties measurement system (MPMS). The second method is to measure via pulsed electron paramagnetic resonance (EPR) spectrometer. The MPMS device performs alternating current (ac) susceptibility measurements from the bulk material with a 0.01 to 1500 Hz frequency range. Fast relaxing systems with T_1 < 0.1 ms are off the detection limit. EPR machines possess a high-resolution range up to T_1 ~ 1 μs since a specific transition is probed. However, EPR devices are far less common than MPMSs.[23] The measurement principle of an MPMS device is further elucidated in chapter 1.6.

1.3.1.1. Orbach process

This process refers to a concerted two-phonon or a two sequential one-phonon mechanism. A spin system is excited to a high-energy M_s state when the energy absorbed from a phonon matches the energy gap. Subsequent relaxation proceeds from this transition state with the release of energy via a phonon to the lattice (**Figure 1.4.a**). There is no limit to only one M_s state being involved. Various transition states increasing in energy may pass through before an energy emission via a phonon occurs. This is the ideal scenario for a good SMM since the more excited states pass through, the higher the energy barrier to spin reversal. The requirements for a spin system to show

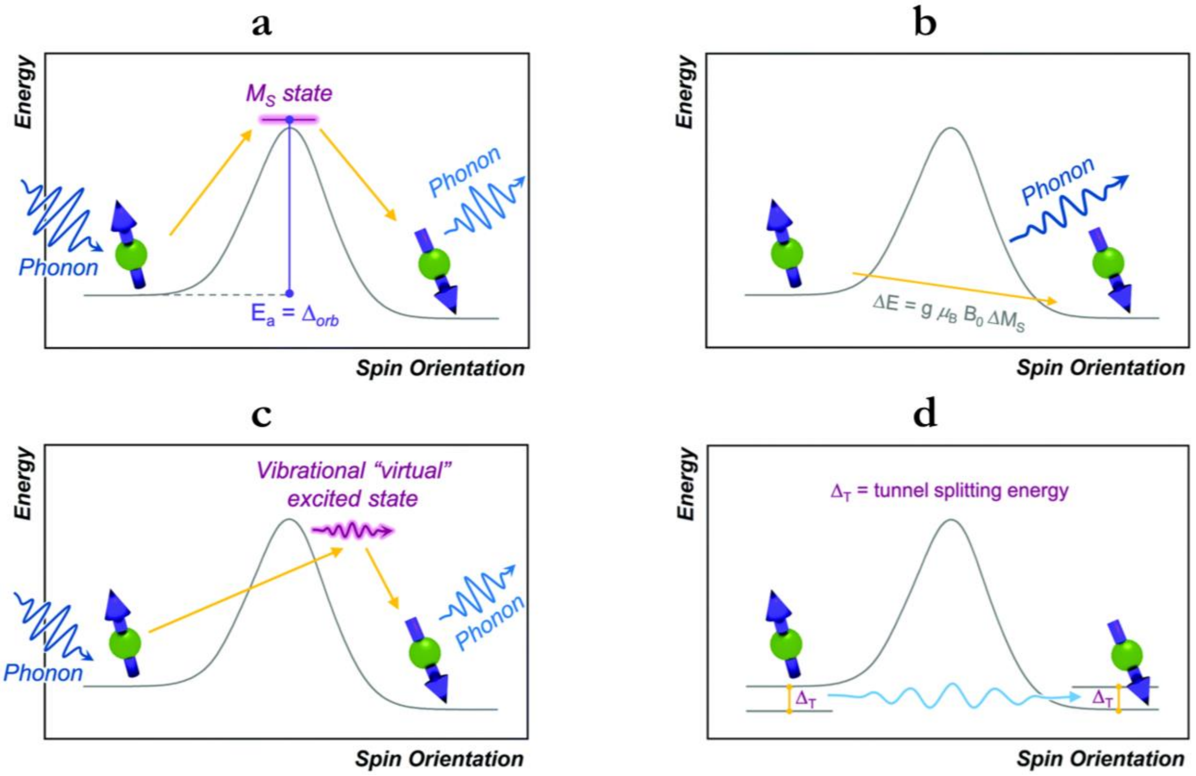

Figure 1.4. Depiction of the Orbach process (**a**), the direct process (**b**), the Raman process (**c**), and the quantum tunneling process (**d**) in a reaction-coordinate diagram fashion. (**a**): The M_s state relates to the excited transition state for the relaxing spin system, while Δ_{orb} denotes as U_{eff} in the SMM literature. (**b**): The Zeeman energy correlates to the spin-flip energy and releases a phonon after relaxation. (**c**): The superposition of vibrational states is displayed as the "virtual" state with no specified energy level. (**d**): Ground-state associated tunneling acts upon any input energy. Reproduced from Ref.[21] with permission from the Royal Society of Chemistry.

the Orbach process is a spin $S > \frac{1}{2}$, since there must be more than two ($M_s = \pm\frac{1}{2}$) M_s levels for transition states. According to the Arrhenius law, the relaxation rate for the Orbach process is defined by:

$$\tau^{-1} = \tau_0^{-1}\exp\left(-\frac{U_{\text{eff}}}{k_{\text{B}}T}\right) \tag{1-5}$$

Here τ^{-1} represents the constant rate and τ_0^{-1} is defined as the attempt frequency, which indicates the probability of this mechanism participating as a relaxation process. Typical values of τ_0^{-1} range from 10^{-2} to 10^{-10} s^{-1}, while U_{eff} refers to the energy barrier and k_{B} is the Boltzmann constant (chapter 1.2.) The accessibility of phonons and the energy gap of the excited M_s states can both affect τ_0^{-1}. A priori calculations of τ_0^{-1} are challenging since the methods are developed for the solid-state and not for molecular systems. For that reason, experimental data is used.

1.3.1.2. Direct process

A molecule undergoes a direct transition from one crystal field microstate to another with no activation energy involved in this process. The direct process is facilitated by an phonon that matches the energy gap between both spin representations and is either absorbed or emitted, as depicted in **Figure 1.4.b**.[21,24]

$$\tau^{-1} = AH^{n_1}T \qquad (\textbf{1-6})$$

Equation (**1-6**) combines the free-to-fit parameter A, the magnetic field H and $n_1 = 2$ for a non-Kramers ion and $n_1 = 4$ for a Kramers ion. One can perform field-dependent measurements to identify the direct process, which usually leads to a decay of the relaxation times $\tau^{-1}$for high fields (H).[22]

1.3.1.3. Raman process

Raman relaxation usually occurs at higher temperatures and absorbs and emits phonons different in energy compared to the direct process. The discrepancy in energy among the two lattice waves has to match precisely the released energy and is facilitated via a superposition of lattice vibrations (**Figure 1.4.c**). The Raman process can be considered a two-phonon process that includes a short-lived virtual excited state of the lattice.[21,24] The corresponding relaxation rate is derived from:

$$\tau^{-1} = CT^{n_2} \qquad (\textbf{1-7})$$

C is like A and τ_0^{-1}, an experimentally measured factor, while n_2 has various values according to the conditions. Typical values are 9 for Kramers ions, 7 for non-Kramers ions, 5 for the occurrence of low-lying states, and 2 when the temperature is much higher than the Debye temperature.[19a]

1.3.1.4. Quantum tunneling process

All previously elucidated relaxation processes are facilitated upon an energy input or through phonon absorption and emission. The quantum tunneling of magnetization (QTM) short-cuts the energy barrier for spin reversal between both spin representations by tunneling straight through (**Figure 1.4.d**). This phenomenon can occur in a system's ground (QTM) or excited state (thermally assisted QTM). The last contribution to the total relaxation rate is the free-to-fit parameter Q covering the QTM process, ascribed in eq. **1-8.**

$$\tau^{-1} = Q \tag{1-8}$$

QTM is a free-to-fit parameter, it is often excluded from determining the energy barrier, especially for field-induced SMMs, where its impact is usually low.[21] Previous attempts to minimize the QTM contribution to the relaxation of SMMs are presented in chapter 1.5.

1.3.2. Spin-spin relaxation T_2

The fundamental difference between spin-lattice and spin-spin relaxations is that no thermal activation energy is required for spin-spin relaxation. Both spin representations exist simultaneously in the form of a superposition, which can be illustrated as a "spinning coin" being neither head nor tails. From this virtual transition state, any interaction with the surroundings changes the energy of the superposition and courses relaxation. These features are of major importance for quantum computing technologies, further elucidated in chapter 1.7. Also, the relaxation times are much faster than for a T_1 relaxation, ranging from milliseconds to a few nanoseconds.[21]

1.4. Selected milestones in SMMs development

This chapter shines light on the progressive development of SMMs in the last 30 years, which is illustrated in **Figure 1.5.**[25] The first example of an SMM was the aforementioned dodecanuclear manganese-oxo cluster Mn_{12}.[17] Within this complex, four Mn^{4+} ($S = 3/2$) and eight Mn^{3+} ($S = 2$) are coupled by oxo-bridge ions giving rise to a spin ground state of $S = 10$. In 1996, macroscopic QTM was detected in an SMM, manifesting in steps in the hysteresis loop. At this early state of SMM development, the focus was on maximizing the spin ground state S since equations (**1-2** and **1-3**) indicated a higher energy barrier for large values of S. Consequently, high-nuclearities based on Mn^{3+} ions with Mn_6,[26] Mn_{19},[27] Mn_{25},[28] Mn_{31},[29] and Mn_{84} clusters were reported.[30] However, many of these systems had lower U_{eff} and T_{B} values than the Mn_{12} archetype.[25] Therefore, a high-spin ground state and a high number of metal ions were determined to be not the critical criteria for better performing SMMs since D exhibits an inversely proportional dependency to S^2 according to $U = |D| S^2$ (chapter 1.2).[31] Novel and high-performing SMMs were synthesized in a serendipitous process featuring cyano-bridged SMMs,[32] lanthanide-based SMMs, 3d-4f SMMs,[33] actinide-based SMMs,[34] radical-bridged SMMs,[35] MOF-based SMMs,[36] and organo-metallic SMMs (**Figure 1.5.**).[37] The highlights of these findings are outlined in more detail in the following paragraphs.

Searching for better bridging ligands to enhance the magnetic exchange coupling, the cyano group seemed desirable because both atoms can coordinate as a strong σ-donor and a weak π-acceptor.[25] A prominent example is the $MnMo_6$ from the LONG group in 2002 (**Figure 1.5.**).[38] Despite enriching a new family of SMMs, the overall magnetic performance remained still low.

In 2003, the group of ISHIKAWA employed lanthanides for the first time in SMMs, which led to the highest observed energy barrier for this time.[39] Here, the phthalocyanine ligand (Pc) was implemented in a Terbium complex $[TbPc_2]^-$ with $U_{\mathrm{eff}} = 230\ \mathrm{cm}^{-1}$ (**Figure 1.5**). Further, due to its stability and planarity, this system is an ideal candidate for surface deposition.[40] Among all described Ln-SIMs, this family was the most studied one and provided much inspiration for novel SMMs. The synergy of a high-spin ground state and large magnetic anisotropy was considered to reduce QTM in polynuclear 3d-4f-metal clusters.[33,34,41] The first recorded example to name here is the $[CuL^{a}Tb(hfac)_2]_2$, with the hexafluoro acetylacetonate ligand (**Figure 1.5.**).[42] Other developments focused on polynuclear lanthanide SMMs, which show high energy barriers but only narrow hysteresis loops. Therefore, a highlight in this development branch was the finding of radical-bridged SMMs, where the diffuse orbital distribution of the radical can penetrate the outer shell of the Ln^{3+} ion and establish effective magnetic exchange coupling.[25,35]

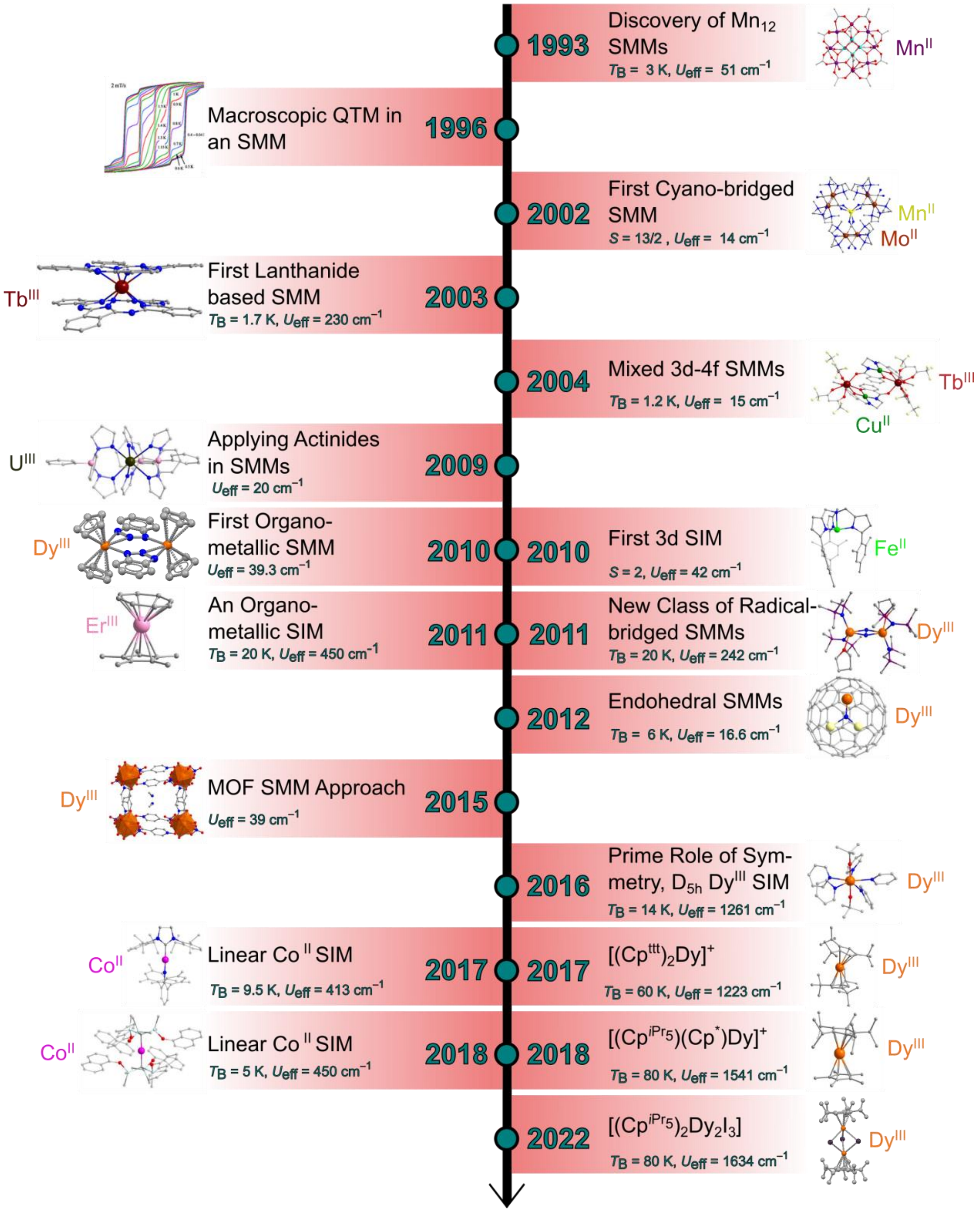

Figure 1.5. Developmental steps in the field of SMMs from 1993 to 2022. Despite 2 images all others are republished with the permission of Ref.[25]; permission conveyed through Copyright Clearance Center, Inc. The timeline is created in accordance with Ref.[25] Moreover, $[(Cp^{iPr5})_2Dy_2I_3]$[43] and $[\{Cp_2Dy(\mu\text{-bta})\}_2]$[44] are created from the CIF file retrieved from the CCDC database.

In 2009, also actinide systems were probed to enhance SMM behavior by introducing the $U(Ph_2BPz_2)_3$ based on a diphenylbis(pyrazolborate) ligand (**Figure 1.5.**).[45] Better magnetic performances were expected from actinides since the 5f-systems have a greater radial extension, which is accompanied by stronger spin-orbit coupling, and it bears a higher potential for magnetic exchange coupling than observed for lanthanides.[46] These hopes were promising; however, the radioactivity and synthetic challenges of 5f-based complexes did not attract many scientists to explore this field systematically.[46e]

An unconventional approach included SMMs in fullerenes or metal-organic frameworks (MOFs).[36,47] In 2012, an endohedral $DySc_2N@C_{80}$ fullerene from GREBER started this new family of SMMs (**Figure 1.5.**).[48] This work illustrated that the magnetic properties of SMMs can be tuned upon being introduced to a MOF. However, SMMs encapsulating in a MOF structure provided no significant improvement in SMM performance.[25]

Most important breakthroughs were achieved when the focus shifted toward d- and f-metal SIMs featuring axial point symmetries. The rise of the cyclopentadienide (Cp) based organo-metallic SIMs finally enabled an almost linear coordination environment for lanthanide systems.[49] This development was initiated by LAYFIELD, MCDOUALL, WINPENNY, and co-workers in 2010, with an organometallic Dy^{III} SMM $[\{Cp_2Dy(\mu\text{-bta})\}_2]$ with two 1,2,3-benzotriazole ligand bridging between both metal center (**Figure 1.5.**).[50] From 2016 to 2018, the most significant steps were taken to apply both concepts. The groups of MILLS and LAYFIELD reported a cyclopentadienyl (Cp^{ttt} = $C_2H_5\textit{t}Bu_3$-1,2,4) based Dy^{III} SIM, $[(Cp^{ttt})_2Dy]^+$ with magnetic hysteresis up to 60 K and an energy barrier of 1223 cm^{-1}.[51] Only one year later, the promising Cp functionalization was found with the $[(Cp^{\textit{i}Pr5})(Cp^*)Dy]^+$ SIM, with a T_B of 80 K and an U_{eff} of 1541 cm^{-1} ($Cp^* = C_5Me_5$.), which was the record holder until this year.[52] The recently published state-of-the-art SMM $[(Cp^{\textit{i}Pr5})_2Dy_2I_3]$ comprises two coupled Dy^{III} centers and exhibits an energy barrier of 1634 cm^{-1}.[43] For transition metal SIMs, linear Co^{II} complexes are the best-known SIMs today. Prominent examples are the [(sIPr)CoNDmp][53] (Dmp = 2,6-dimestylphenyl) with an U_{eff} of 413 cm^{-1}, and $[Co(C(SiMe_2ONaph)_3)_2]$[54] with the highest recorded energy barrier of 450 cm^{-1}. Despite the promising development of transition metal SIMs, they are far behind lanthanide-based SIMs. The next chapter will focus more intensely on design strategies for lanthanide-based SMMs.

1.5. Design strategies for lanthanide-based SMMs

This chapter aims to transfer the landmarks on the route to state-of-the-art SMMs to new avenues of design strategies for f-metal SIMs. Unlike transition metals, the 4f orbitals of lanthanides are effectively shielded by the outer 5s and 5p electrons.[55] Hence, the coordination mode is similar to the free ions as the degeneracy of the 4f orbitals is not quenched upon ligand coordination.[56] A detailed picture of the electronic interactions in tripositive lanthanide ions is depicted in **Figure 1.6.** There are three perturbations to the central field Hamiltonian, the electron repulsion (Coulomb repulsion), the spin-orbit coupling, and the crystal field splitting. A typical order of 10^2 cm^{-1} accounts for the crystal field splitting described as the term symbol of $^{2S+1}L_J$, which is the least perturbation to the central field. The quantum numbers S, L, and J refer to the spin angular momentum, the orbital angular momentum, and the total angular momentum. Each Stark sublevel corresponds to a state split by $^{2S+1}L_J$ into the superimposed magnetic states M_J, which defer from the M_s states employed for d-metal SMMs. Further, the M_J states are split into $+M_J$ and $-M_J$ when exposed to a magnetic field.[22]

Modeling a lanthanide complex with the corresponding crystal field Hamiltonian is highly challenging as it consists of many terms. Therefore, applying the concepts of electrostatics to design novel SMMs were introduced by LONG and RINEHART in 2011.[57] Considering that spin and orbital momenta are coupled, all f-electrons act cohesively, resulting in the well-defined M_J states. SIEVERS proposed the corresponding theory of aspherical electron density 40 years ago.[58] A Dy^{3+} ion with a term symbol of $^6H_{15/2}$ has the lowest representation of the M_J state with a prolate shape ($M_J = 1/2$) (**Figure 1.7.a**), while the largest ($M_J = 15/2$) has an oblate shape (**Figure 1.7.b**).

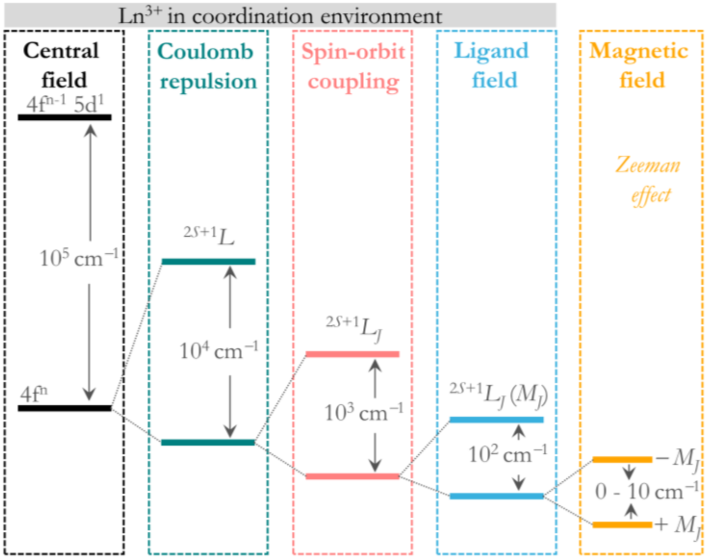

Figure 1.6. Electronic interactions for a triply oxidized lanthanide ion (Ln^{3+}) and their typical magnitudes. Created in accordance with Ref.[22]; permission conveyed through Copyright Clearance Center, Inc.

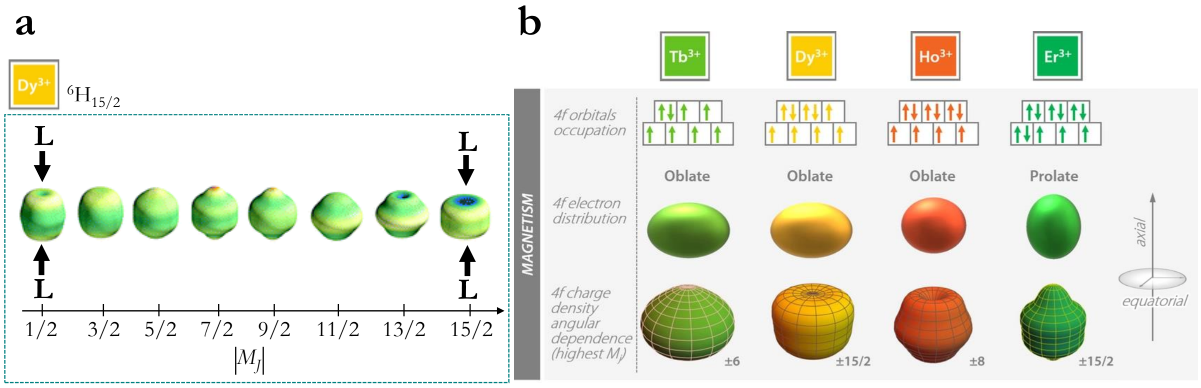

Figure 1.7. (**a**) Representation of the angular M_J-dependence of the total 4f shells density, comprising the lowest spin-orbit coupled state for Dy^{3+}. All M_J states degenerate in the absence of the crystal field. Republished with permission of the Royal Society of Chemistry, from Ref.[56]; permission conveyed through Copyright Clearance Center, Inc. (**b**) Summary of tripositive lanthanides and their characteristics most relevant for SMMs. Republished with permission of John Wiley & Sons, from Ref.[22]; permission conveyed through Copyright Clearance Center, Inc.

There is a smooth transition between both states from a prolate to an oblate spheroid. Therefore, employing an axial ligand field makes the highest M_J state (oblate) lowest in energy, which stabilizes the most magnetic projection and increases the energy successively to the lowest state ($M_J = 1/2$) (prolate) (**Figure 1.7.**).[55,57,59] Hence, the energy levels are nicely separated and overlap with an ideal double-well potential (**Figure 1.8.a**). The closest case for an almost linear ligand field is achieved for Cp ligands in the record holder $[(Cp^{iPr5})(Cp^{*})Dy]^{+}$ exhibiting an L–Dy–L angle of 162.5 °.

There are practical concerns about having the largest representation of the M_J states as the ground state. Apart from the $[(Cp^{ttt})_2Dy]^{+}$ system (**Figure 1.8.a**), other lanthanide metallocenes exhibit the smallest or highly mixed states as the ground state (**Figure 1.8.b-e**). Some groups have focused on symmetry strategies to optimize the M_J energy levels and minimize the QTM process via ideal symmetry elements. However, none of the 32 crystallographic point groups show the ideal symmetry, while C_n ($n \geq 7$), S_8/D_{4d}, C_{5h}/D_{5h}, and S_{12}/D_{6d} minimize transversal CFs and should be preferred for high-performing SMMs.[56] Mainly, a pentagonal-bipyramidal (D_{5h}) symmetry was studied intensively and resulted in many benchmark systems, such as the $[Dy(Cy_3PO)_2(H_2O)_5]Cl_3$ with the tricyclohexylphosphine oxide ligand.[60] Each SIM requires a bistable ground state as illustrated with the double-well potential (**Figure 1.3.a**). For Kramers ions with an odd number of fermions, the magnetic states are split into various Kramers doublets, comprising one eigenstate and the time-reversed state.[56]

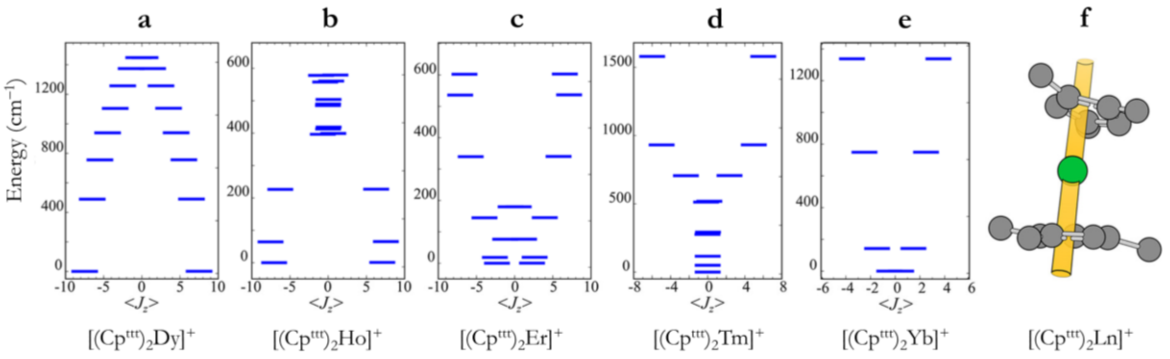

Figure 1.8. Electronic structure $[(Cp^{ttt})_2Ln]^+$ with Dy^{3+}(**a**), Ho^{3+}(**b**), Er^{3+}(**c**), Tm^{3+}(**d**), and Yb^{3+}(**e**), calculated with CASSCF-SO, with a 1000 Oe field along the quantization axis. Crystal field axes for $[(Cp^{ttt})_2Ln]^+$ (**f**), *t*Bu groups are truncated, and hydrogen atoms are omitted for clarity. Reproduced with permission from Ref.[61], https://pubs.acs.org/doi/10.1021/jacs.5b12124, under the terms of a CC BY 4.0 license, https://creativecommons.org/licenses/by/4.0/. Further permissions related to the material excerpted should be directed to the ACS.

According to the Kramers theorem, both eigenvalues of the doublet must be equal and therefore are degenerated.[62] This fact guarantees a bistable ground state for all Kramers ions, which is one reason why Dy^{III}- and Co^{II}-ions are ideal candidates for SMMs.

Another crucial point was identified when the dysprosocenium family was studied. Constrained vibrational modes are of tremendous importance to limit phonons that interfere with the crystal field potential to initiate relaxation processes.[51b,59,61,63] Appling rigid ligands such as the Cp ligand results in high blocking temperatures and fewer QTM phenomena. Additionally, the paramagnetic center of SIMs should be isolated magnetically from neighboring molecules (> 8 Å). Interactions such as hydrogen bonds or π-π-stacking should be minimized, as they give rise to high energy phonons that initiate relaxation and hamper the blocking of magnetization.[20a,64]

In summary, one should focus on these crucial points when designing new SIMs with dysprosium(III):

1. A strong axial crystal field potential is required to establish a large crystal field splitting between the states with the largest as the ground state and minimize rhombic interactions.
2. A rigid coordination environment close to the metal center is desirable to block high-energy vibrations that manipulate the crystal field potential via phonons.
3. The avoidance of intermolecular interactions is desirable and achieved by shielding the metal center from all sorts of interaction (e.g., hydrogen bonds, π-π-stacking).

1.6. SQUID – Super Quantum Interference Device

1.6.1. History and physical background

There are various systems to investigate the magnetic properties of matter. The sensing techniques root in induction, fluxgate, magnetoresistors, Hall effect, magneto-optical, resonance, and SQUID principles for most devices.[9] The highest sensitivity to detect magnetic flux has the SQUID (Super Quantum Interference Device), which accuracy is at a resolution level of 10^{-17} T at cryogenic temperatures.[65] The Quantum Design company offers the most used SQUIDs,[66] the MPMS-XL (approximately 1000 sold machines) and the latest model, the MPMS3 (about 200 sold machines).[67] Both models are operated at the University of Göttingen and were used to conduct the magnetic measurements in this thesis. The following paragraphs are solely devoted to SQUIDs' physical principles and measurement techniques.

KAMERLINGH-ONNES discovered the phenomenon of superconductivity when he cooled mercury below 4.2 K, and the magnitude of its electrical resistance instantly dropped to an immeasurable level in 1911.[65,68] Subsequent studies revealed that numerous materials show a similar superconducting transition below a specific temperature.[69] Usually, resistivity is caused by the scattering of electrons moving through an object. The Bardeen-Cooper-Schrieffer (BCS) theory explains the lack of scattering in the superconducting state with a phonon interaction between electrons, which results in weakly bonded electron pairs (Cooper pairs) with an integer spin.[70] The work of MEISSNER showed another unique property of superconductivity:[71] A material in its superconducting state placed in a magnetic field expels the magnetic flux from its interior (**Figure 1.9.b**). Above the transition temperature, the magnetic field lines pass through the material (**Figure 1.9.a**). After switching off the magnetic field and maintaining the superconducting state, a current remains around the material, and the magnetic flux is trapped within the ring at a constant level. (**Figure 1.9.c**) Additionally, only discrete values of the magnetic flux are allowed, which are given by multiples of the magnetic flux quantum:[65]

$$\Phi_0 = h/(2e) \approx 2.068 \cdot 10^{-15}\ \mathrm{Wb} \tag{1-9}$$

With the Planck constant *h* and the electron charge *e*, the unit Weber (Wb) per square meter equals one tesla (T). For the case of a superconducting loop separated by a barrier material with regular resistivity, one would assume a fast decay of superconductivity due to the wave function of the Cooper pairs. Nevertheless, the electrons tunnel across the barrier, which is called Josephson junction since JOSEPHSON first predicted this phenomenon in 1964.[72] A current exhibits no voltage decay when penetrating a resistive barrier when its width is less than the coherence length and currents are below the critical current of the barrier (**Figure 1.9.d**).[65]

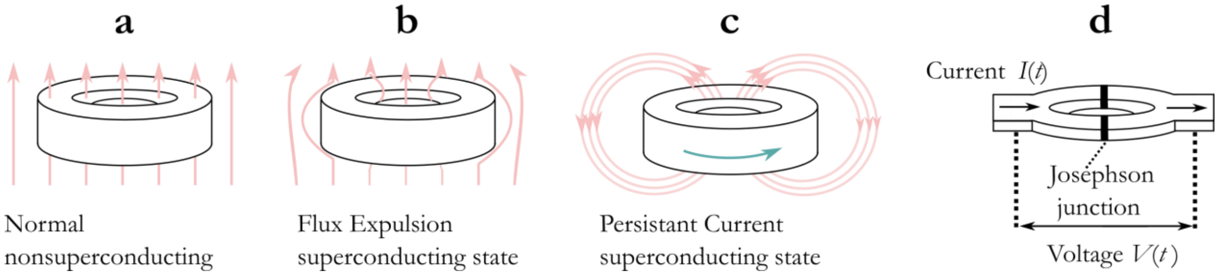

Figure 1.9. (**a**-**c**) Meissner effect illustrated for a superconducting ring cooled while exposed to an applied magnetic field. (**d**) SQUID loop separated by two Josephson junctions. Created in accordance with Ref.[65]

1.6.2. The measurement principle of SQUID magnetometers

The phenomenon of the Josephson effect is used in SQUID magnetometers, which act as a flux to voltage amplifier to measure small infinitesimal changes in the magnetic flux. The actual SQUID consists of a superconducting loop separated by one or more Josephson junctions and is not larger than a 2-euro coin (**Figure 1.9.d**).[67,69] When charging a new specimen into the magnetometer, a clear drinking straw functions as the sample holder, while the crystalline sample is first charged into small caps and coated with oil before being transferred into the straw. The oil to preserve the anisotropy of the material since it freezes the sample during the measurement and blocks magnetic torquing. Inside the magnetometer, the specimen is moved parallel to the magnetic field along the superconducting pick-up coils to detect the changes in the magnetic flux and convert these to a so-called voltage VSQUID plot (**Figure 1.10.**). To center the specimen, the direction x is plotted versus VSQUID, which is demonstrated for a paramagnetic compound with a maximum of the VSQUID signal at an x-position of 2 cm (**Figure 1.10.**).

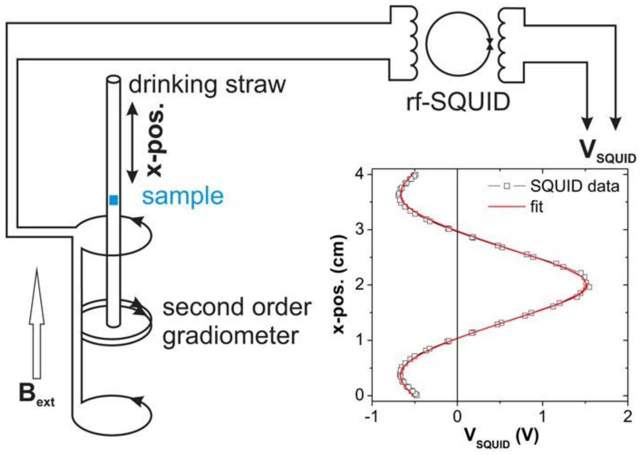

Figure 1.10. Illustration of a SQUID magnetometer architecture equipped with a 2^{nd} order gradiometer. The centering procedure is performed by plotting VSQUID vs. the sample position (x-pos. (cm). Reproduced from Ref.[67] with the permission of AIP Publishing.

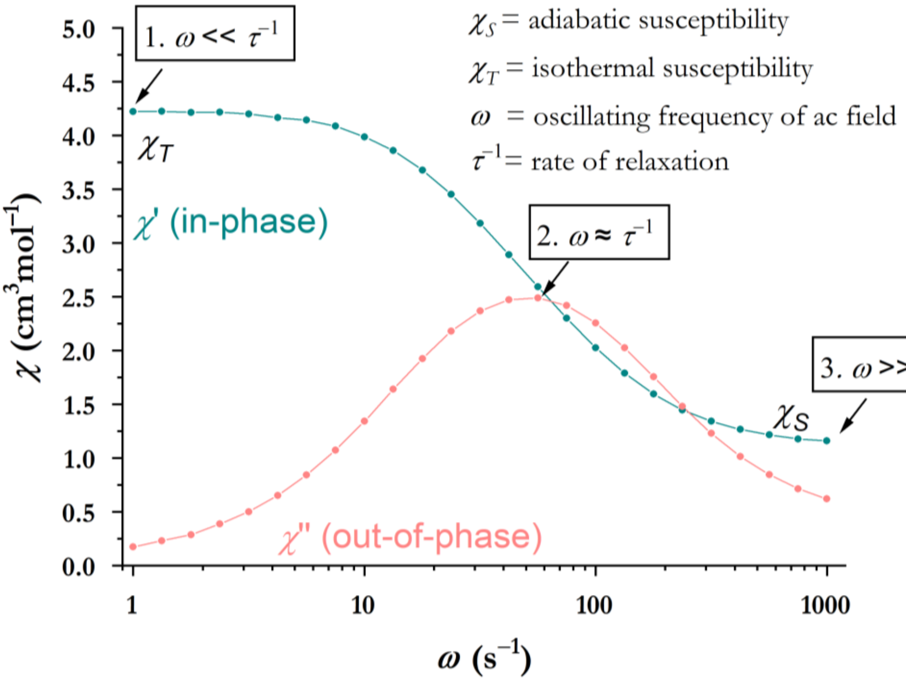

Figure 1.11. Depiction of χ' and χ'' susceptibilities versus the frequency of the ac field ω. For a specific temperature, SMM behavior is detected as the χ'' signal exhibits a maximum at $\omega \approx \tau^{-1}$, while χ' decreases. Created in accordance with Ref.[73]

Further, the usage of a pick-up coil, applied as a second-order gradiometer, accurately suppresses any effect of external magnetic fields.[67] The corresponding position in the magnetometer is in-between the double pick-up coil. For a diamagnetic sample, the maximum would occur at a negative VSQUID value. Magnetic relaxation is then recorded via alternating current (ac) susceptibility measurements. Therefore, an oscillating ac field is applied, while its frequency ($\omega = 2\pi\upsilon$) and the temperature is modulated, which leads to three possible scenarios:

1. $\omega << \tau^{-1}$: The relaxation rate τ^{-1} of the system is much faster than the ac frequency ω for a given temperature, which can be envisioned as the fast return to equilibrium for both representations of the double-well potential. Here, the measurement of the isothermal susceptibility χ_T is possible (**Figure 1.11.**).
2. $\omega \approx \tau^{-1}$: Next, the timescale of the relaxation rate τ^{-1} of the system is equivalent to the oscillating ac frequency for a given temperature. Here, the response of the system consists of two parts: the in-phase (χ') and the out-of-phase (χ'') susceptibility (**Figure 1.11.**).
3. $\omega >> \tau^{-1}$: In this case, the magnetic moments of the system cannot keep up with the perturbing ac field as it oscillates too fast. A return to equilibrium and energy exchange with the lattice is not possible, allowing to detect the adiabatic susceptibility χ_S (**Figure 1.11.**).[73]

To distinguish between a regular paramagnet and an SMM, one must search for maxima in the out-of-phase susceptibility χ''. A paramagnet should not display slow relaxation as $\chi_T = \chi_S$, which results in a zero value for χ'' according to equation (**1-11**). Further, its χ' value is constant and refers directly to χ_S as the second part of the equation (**1-10**) is zero. For an SMM, the relaxation rate and energy barrier can be extracted from the maxima in a χ' vs. χ'' plot, known as the Argand diagram and referred to as the Cole-Cole plot in this thesis.[73] Detailed procedures are stated in the experimental part (5.2.4).

$$\chi'(\omega) = \chi_S + \frac{(\chi_T - \chi_S)}{1 + \omega^2\tau^2} \tag{1-10}$$

$$\chi''(\omega) = \frac{(\chi_T - \chi_S)}{1 + \omega^2\tau^2}\,\omega\tau \tag{1-11}$$

1.7. Application and future technologies

The properties of magnetic molecules are promising centerpieces in various fields of research directed toward novel technologies, ranging from quantum computing,[74] high-density data storage systems,[22,25] medical imaging applications,[75] to other electron spin techniques (**Figure 1.12.**).[76]

Quantum computing is envisioned to revolutionize our current digital landscape into a second information age. In conventional computation, all operations are based on two states (0 or 1), whereas multiple states can be accessed in quantum computing via a superposition of two states, illustrated as a spinning coin being neither head nor tails.[74b] Already, 60 quantum qubits will outperform our current processor power.[77] An essential goal is to design qubits with long spin-spin (T_1) and spin-lattice (T_2) relaxation times. T_2 refers to the lifetime of information, while T_1 represents the maximum memory storage time and determines the time between each computational cycle.[74c]

A recent milestone was the implementation of Grover's quantum algorithm in the $[\mathrm{TbPc_2}]^-$ SIM.[77] The authors were able to embed a single molecule between two gold electrodes via the electromigration technique, which uses a high current to turn a single gold wire into two electrodes separated by 1 nm.[78] Such a molecular spin transistor allowed coherent control of a single nuclear spin and its readout in a non-destructive method. The following steps would focus on other SMMs with higher nuclear spin values to manipulate larger databases.

Previous chapters have shed light on the physical and magnetic properties of SMMs. Here, the focus is directed toward their application challenges. The deposition of molecular entities is still at

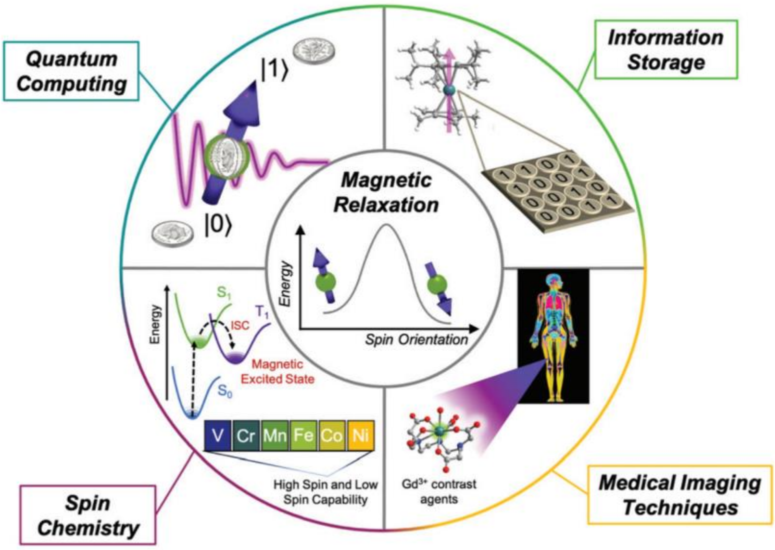

Figure 1.12. Schematic depiction of fields were magnetic properties of molecules, and its relaxation dynamic is relevant for novel technological developments. Reproduced from Ref.[21] with permission from the Royal Society of Chemistry.

its beginning and has only been shown in a few cases on surfaces. However, neither multilayer nor 3-dimensional single crystals have been successfully employed yet.[40,79] Here, the endeavor is to maintain the magnetic properties during and after the deposition process. Second, addressing the employed molecules and localize magnetic fields on a scale of a few nanometers is highly challenging, as no technology is hitherto developed. Most work in this direction were on the $[TbPc_2]^-$ SIM embedded between two gold electrodes.[77,80] Last, one must predict and monitor heat dissipation for such small entities, which have progressed in recent years but have barely scratched the surface of this field.[81] More theoretical tools are in high demand to better understand phonon-electron interaction. With an optimistic view on further enhancement of current SMMs, the first SMM-based model storage systems in the lab are imagined 20-30 years from today.[82]

Medical imaging techniques require specific contrast agents to provide essential diagnostic information, such as detecting blood-brain barrier disruption, which cannot be retrieved using other noninvasive techniques. Common contrast agents are mainly based on Gd^{III}-compounds, while Mn^{II}- or Fe^{II}-compounds are rarer in use. Also, metal-free prototypes exist but have not been put into practice yet. A better understanding of magnetic relaxation is crucial in enhancing the resolution of tissues and the target specificity of these paramagnetic complexes.[75]

1.8. Bis(benzoxazol-2-yl)methanes – a versatile ligand platform

1.8.1. From *β*-diketones to *β*-diketimines

There are two synthetic approaches for altering a *β*-diketone into a *β*-diketimine. Both procedures utilize the co-condensation reaction between a ketone and a primary amine.[83] In 1966, DORMAN employed ethylene glycol to turn one ketone moiety of the 1,3-diketone into a ketoketal, which was then reacted with 2 equiv. of an arylamine (**Scheme 1.1.a**).[84]

The second procedure starts with a single condensation reaction of one ketone function, resulting in the *β*-enaminoketonato ligand (**Scheme 1.1.b**). Here, two additional steps are necessary to receive the *β*-diketimine system. First, the use of a powerful alkylation agent is required, where the triethyloxonium tetrafluoroborate, also known as a Meerwein reagent, alkylates the second ketone function (**Scheme 1.1.b**).[85] Then the condensation reaction paired with deprotonation yields the *β*-diketimine.[86]

In most metal complexes, the *β*-diketimine features a $\varkappa^2$-(*N*,*N'*) bidentate coordination mode through both nitrogen donor atoms, giving rise to a six-membered metallacyclic ring. Upon deprotonation, the negative charge is delocalized on the C_3N_2 ring, while significant parts of the electron density of HOMO and HOMO−1 are distributed at the nitrogen and γ-C positions, which demonstrate nucleophilic properties (**Scheme 1.2.**). Hence, tailoring the γ-C position with electron-withdrawing groups compensates for ligand donation and limits the reactivity of the γ-C position. Consequently, the β-C positions exhibit an electrophilic character that can be tuned with electron-withdrawing substituents to assemble electron-poor compounds more resistant to oxidation.[87]

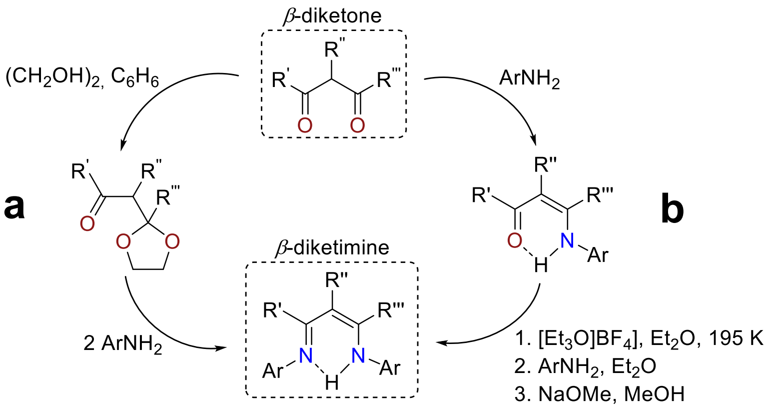

Scheme 1.1. The generalized genesis of *β*-diketimines from their related *β*-diketones. (**a**) Synthesis introduced by DORMAN via a ketoketal.[84] (**b**) Synthesis proposed by MCGEACHIN featuring a four-step reaction.[86]

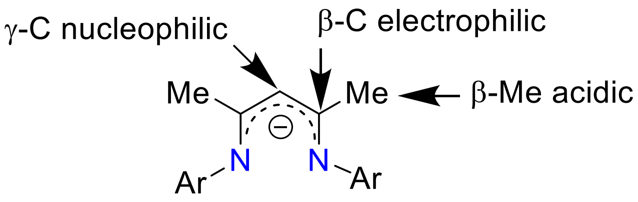

Scheme 1.2. General reactivity profile of the *β*-diketimines from their related *β*-diketones. Created in accordance with Ref.[87]

1.8.2. From *β*-diketimines to bis(benzoxazol-2-yl)methane's

For more than 50 years, the *β*-diketimine ligand scaffold has shaped crucial fields in chemistry and stabilized metal ions in low oxidation states across the entire Periodic Table.[83,86,88] The desirable properties of nacnac were mimicked by introducing the bis(benzoxazol-2-yl)methane's that root on procedures from FLORANLI,[89] DIXNEUF,[90] and STALKE.[91] This new system mirrors the coordination design of a six-membered metallacycle and enriches the coordination mode by two additional donor atoms from the backbone. The most common ligands feature oxygen, nitrogen, or sulfur donor atoms, and asymmetrically substituted derivatives comprise two different donor atoms for even more diverse coordination modes (**Scheme 1.3.**). Furthermore, the extension of the aromatic ring provides an electron-rich system, which establishes more rigidity and leads to an almost planar coordination sphere. Adjustments along the C_6 perimeter with various groups are feasible and fine-tune the coordination pocket. Within our group, seven ligand modifications have been introduced and deeply studied in main group chemistry (**Scheme 1.3.**).[2,92]

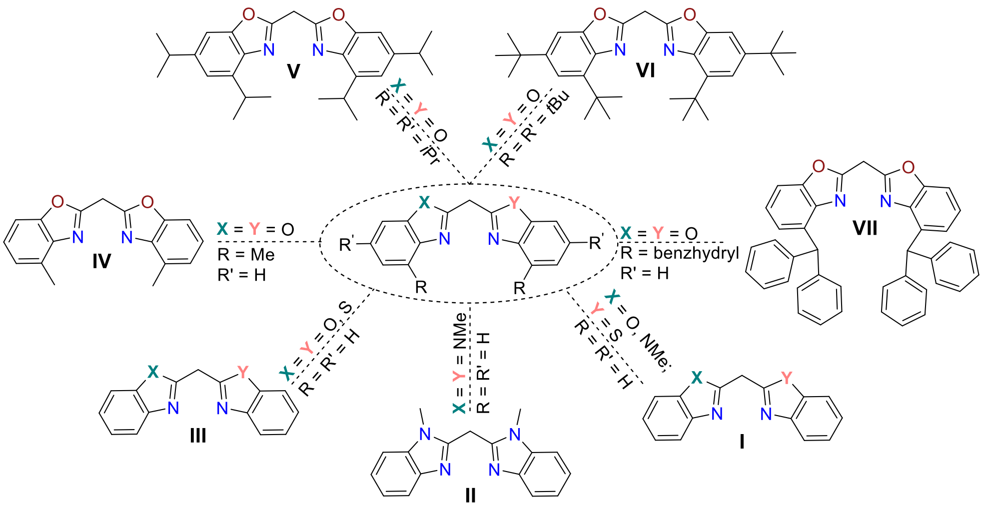

Scheme 1.3. Overview of symmetrically and asymmetrically substituted bis(*R*,*R'*-benzoxazol-2-yl)methane ligands proposed within the group of STALKE. Corresponding references are **I**,[93] **II**,[93] **III**,[91] **IV**,[94] **V**,[95] **VI**,[96] **VII**.[97] Created in accordance with Ref.[92]

1.9. The sulfur-nitrogen ligand platform

1.9.1. Discovery of sulfur-nitrogen chemistry – a historical view

GREGORY and SOUBEIRAN initiated a new discipline in chemistry with their discovery of the first sulfur-nitrogen compound back in 1835 and 1838,[98] while Schenck determined its exact constitution to be S_4N_4 (tetrasulfur tetranitride).[99] From there on, many scientists contributed to elucidate their properties. Further milestones were the work of GOEHRING, [100] suggesting an eight-membered ring for S_4N_4 that could finally be verified by X-ray diffraction experiments in 1947, and her work on the subsequent polymer polythiazyl $(SN)_n$.[101] The latter exhibited electrical conductivity and superconductive properties at around 0.3 K.[102]

Around the same time, sulfur diimide was prepared and accessed by GOEHRING and WEIS, based on the reaction of *n*-butylamine and sulfur tetrachloride (**Scheme 1.4.a**).[103] However, this initial approach was hampered by synthetic difficulties handling the SCl_4.[104]

An improved procedure was announced by CLEMENS, BELL, and O'BRIEN, who prepared sulfur diimide from SCl_2 and *tert*-butylamine.[105] Here, the crude product has a polymeric structure, and the monomer $(S^{IV}(NtBu)_2)$ is accessible via pyrolysis (**Scheme 1.4.**). This root enabled new avenues for the rise of sulfur-nitrogen chemistry in the last century and is still used to access sulfur diimide.

More challenging was the journey from sulfur diimides to sulfur triimides. In 1970, GLEMSER and WEGENER were finally able to isolate tris(*N*-trimethylsilylimido)sulfur $(S^{VI}(NSiMe_3)_3)$ from the reaction of NSF_3 and $[Li\{N(SiMe_3)_2\}]$, which marks the first observation of a monomeric sulfur compound in the oxidation state +VI with the coordination number three (**Scheme 1.5.**).[106] The same group prepared the *tert*-butyl substituted analogue ($S^{VI}(NtBu)_3$, **L$_{10}$**) seven years later. Here, NSF_3 and 2 equiv. of $[Li\{N(SiMe_3)(tBu)\}]$ form the $(Me_3SiN)S(NtBu)_2$, which reacts with an additional equiv. of $[Li\{N(SiMe_3)(tBu)\}]$ to $S^{VI}(NtBu)_3$).[107] Also, tetrafluoride (OSF_4) was applied by SUNDERMEYER and LIDY to acquire higher yields of $S^{VI}(Ntms)_3$ in an improved procedure.[108] precursors (NSF_3 and OSF_4) and limited progress of sulfur triimide chemistry.

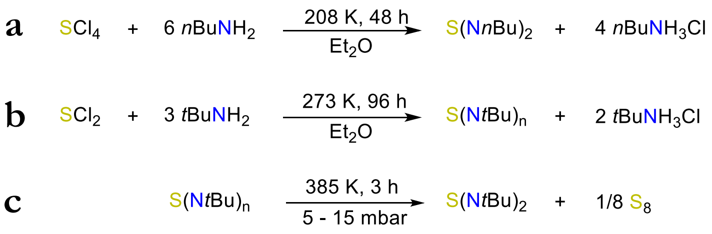

Scheme 1.4. (**a**) Preparation of $S(NnBu)_2$ from SCl_4 in Et_2O.[103] (**b**-**c**) This procedure starts from SCl_2 and yields the Polymer $S(NtBu)_n$, which is further cracked to give the monomer $S(NtBu)_2$.[105]

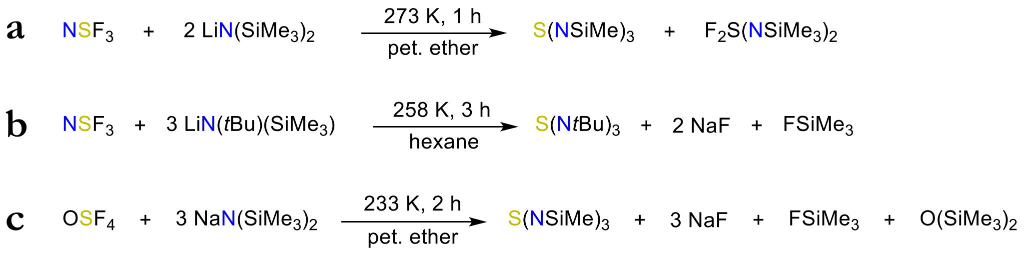

a $NSF_3 + 2\ LiN(SiMe_3)_2 \xrightarrow[\text{pet. ether}]{\text{273 K, 1 h}} S(NSiMe)_3 + F_2S(NSiMe_3)_2$

b $NSF_3 + 3\ LiN(tBu)(SiMe_3) \xrightarrow[\text{hexane}]{\text{258 K, 3 h}} S(NtBu)_3 + 2\ NaF + FSiMe_3$

c $OSF_4 + 3\ NaN(SiMe_3)_2 \xrightarrow[\text{pet. ether}]{\text{233 K, 2 h}} S(NSiMe)_3 + 3\ NaF + FSiMe_3 + O(SiMe_3)_2$

Scheme 1.5. (**a**) Preparation of $S(NSiMe_3)_3$ from NSF_3 and $LiN(SiMe_3)_2$ in petroleum ether.[106] (**b**) Procedure to access $S(N\mathit{t}Bu)_3$ from NSF_3 and $LiN(\mathit{t}Bu)(SiMe_3)$ in hexane.[107] (**c**) Improved route to $S(NSiMe_3)_3$ via OSF_4 and $NaN(SiMe_3)_2$.[108]

The next milestone was achieved when STALKE and FLEISCHER proposed their modified strategy for sulfur triimides in 1998.[109] In this context, the $[Li_4\{NtBu)_3S_2]$ ($\mathbf{L}_9$) was oxidized via bromine and allowed the access of $S^{VI}(N\mathit{t}Bu)_3$ in a more straightforward approach with good scalability. Synthetic details are referred to in chapter 3.8.1.

1.9.2. Polyimido sulfur anions and the nature of the S–N bond

Polyimido sulfur anions are a versatile class of ligands ascribed to the wide range of oxidation states of the central sulfur (+I to +VI) atom that can hold up to four NR (R=H, alkyl) substituents. The NR group represents an isoelectric replacement of the oxo (O) ligand, and the considerations from LANGMUIR suggest similar chemical and physical properties for isovalent species.[110] However, all polyimido analogues are sensitive to moisture and oxygen and require Schlenk or dry Box techniques for handling. The broad diversity of the sulfur oxide and imide scaffold is portrayed in **Table 1.1.**

For many centuries, the concept of hypervalency was employed to describe the nature of the S–N bond. This assumption would imply the participation of vacant d-orbitals resulting in a d^2sp^3 hybridization of the central sulfur atom. The well-known SO_2 was believed to comprise two S=O bonds and one lone pair at the sulfur atom. Despite the findings of computational scientists that exclude any d-orbital contribution to the bonding,[111] hypervalent sulfur remained a long-lasting misconception in many textbooks.[112]

Table 1.1. Comparison of sulfur imides with their isoelectric sulfur oxides. Created in accordance with Ref.[113]

Sulfur(IV) oxides		Sulfur(IV) imides		Sulfur(VI) oxides		Sulfur(VI) imides	
Sulfur dioxide	$\mathbf{SO}_2$	Sulfur diimide	$S(\mathbf{N}R)_2$	Sulfur trioxide	$\mathbf{SO}_3$	Sulfur triimide	$S(\mathbf{N}R)_3$
Sulfite	$\mathbf{SO}_3^{2-}$	Triimidosulfite	$S(\mathbf{N}R)_3^{2-}$	Sulfate	$\mathbf{SO}_4^{2-}$	Tetraimidosulfate	$S(\mathbf{N}R)_4^{2-}$
Sulfinate	$R\mathbf{SO}_2^{-}$	Diimidosulfinate	$RS(\mathbf{N}R)_2^{-}$	Sulfonate	$R\mathbf{SO}_3^{-}$	Triimidosulfonate	$RS(\mathbf{N}R)_3^{-}$

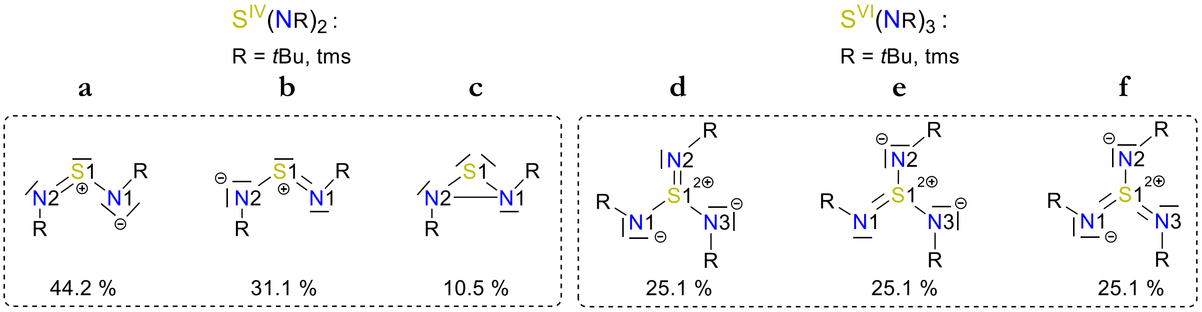

Scheme 1.6. (**a**) Illustration of NBO/NRT analysis of $S(NR)_2$ and $S(NR)_3$. (**a-c**) Formal atomic charges S1 +1.11 e, N1 −0.71 e, N2 −0.77 e. Bond orders: (S1–N1) 1.49 (covalent 1.04, ionic 0.45), (S1–N2) 1.33 (covalent 0.98, ionic 0.35). (**d-f**) Formal atomic charges: (S1) +1.90 e, (N) −0.63 e. Bond orders: (S–N) 1.33 (covalent 0.97, ionic 0.35). In all other schemes, formal charges are omitted for clarity. Created in accordance with Ref.[114]

In recent years, the sulfur di- and triimide were re-studied via high-resolution X-ray diffraction experiments and DFT calculation for the solid and gas phase.[115] One lone pair is located at each nitrogen atom for experimental and theoretical data, and the central sulfur atom is sp^2-hybridized. Therefore a π-system is positioned below and above the SNx plane being in tune with the corresponding π-orbitals, allowing an efficient redistribution of charges.[113] Employing the NBO/NRT (natural bond orbital/natural resonance theory) analysis, STALKE and ENGELS determined a raised covalent contribution for the S–N bond orders with a 4-center-6-electron bonding (**Scheme 1.6.**).[114] Furthermore, this also decreases the charge distribution at the nitrogen donors, referring to a sp^3-hybridized sulfur center. Moreover, all π-orbitals are polarized, suggesting a significant ionic contribution, and three resonance structures are found and exemplified below (**Scheme 1.6.**).[113,114,116]

1.9.3. Recent developments of SMMs featuring the SN scaffold

Until 2015, polyimido ligands were well established in the field of stabilizing lithium aggregates and other main group metals. The finding of a cobalt(II)-based SMM $[Co\{N\textit{t}Bu)_3SMe\}_2]$ opened a new avenue of application for this ligand platform.[117] At this time, $[Co\{N\textit{t}Bu)_3SMe\}_2]$ was the best performing cobalt-based SIM for more than half a year, which inspired our group to expand this research to other systems.[117] The first lanthanide-based SMM was presented one year later (**Figure 1.13.**).[118] However, lithium-halide co-complexation limited their magnetic performance. In the same year, a trigonal planar cobalt SIM with acute N–Co–N bite angles was proposed but ranging below the magnetic performance of the archetype.[119] Avoiding lithium precursors and utilizing the potassium species facilitated the finding of $[ClDy\{Ph_2PCH_2S(N\textit{t}Bu)_3\}_2]$ with a butterfly-shaped hysteresis up to 3.5 K.[120] The latest developments in the field of tetrahedral cobalt SIMs identified the ideal N–Co–N bite angle to be 76-78° despite the previous assumptions that smaller angles lead to larger ZFS as approaching the linear coordination. The ability of the S–N bond to adjust to the required bite angle promoted the finding of $[\mathrm{Co}\{(\mathrm{N}t\mathrm{Bu})_2\mathrm{SPh}\}]$ with an N–Co–N bite angle of 72.7°, displaying an energy barrier of $U_{\mathrm{eff}} = 283\ \mathrm{cm}^{-1}$ that ranges among the best recorded tetrahedral cobalt(II) SIMs today.[121] In the field of lanthanide-based SMMs, imidosulfonate and imidosulfinate ligands were compared. Here, the imidosulfonates tend to provide better geometries for high-performing SMMs. Nevertheless, lithium-halide co-complexation is still hampering the magnetic properties and should be addressed to improve the overall performance.

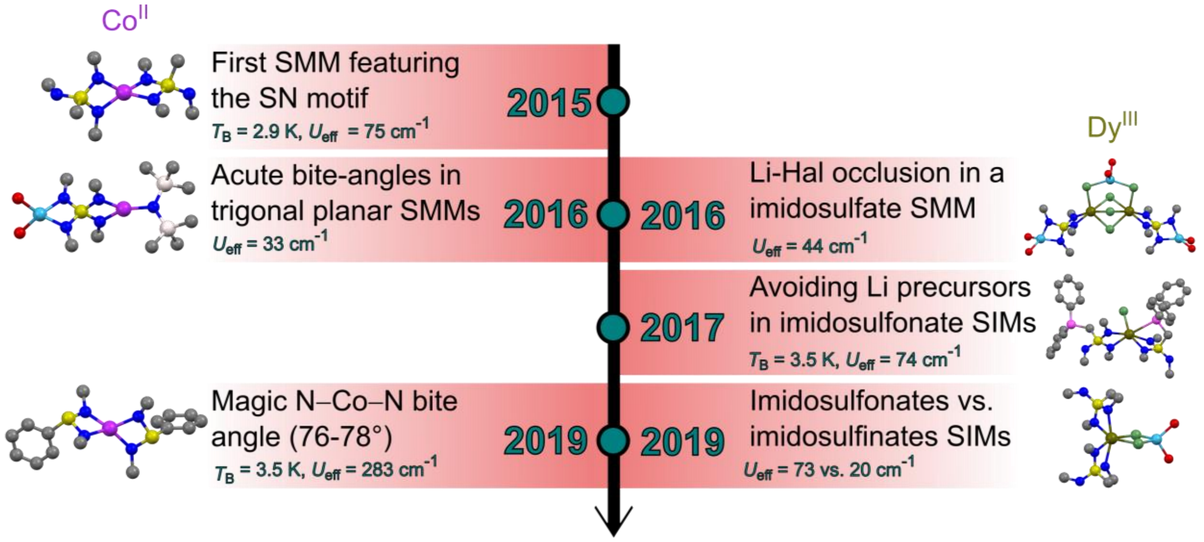

Figure 1.13. Selected milestones in SMM development featuring polyimido ligands. *tert*-Butyl groups are truncated, hydrogen atoms are omitted, and for thf moieties, only the oxygen donor is depicted for clarity. All images are created from the CIF files from the CCDC database with the program Mercury. Findings for the Co^{II} compounds were published in Ref.[117,119,121] and for Dy^{III} compounds in Ref.[118,120,122] Publications on Color code: C (grey), N (blue), O (red), S (yellow), Si (white), Co^{II} (pink), Cl(green), Dy^{III} (brown), Li (light blue), P (rose).

2. Scope and Motivation

This work aims to generate two new approaches toward novel magnetic materials. The first focus will shine a light on the air-stable and easily tunable bis(benzoxazole-2-yl)methanide (**Box**) ligand family that was never employed in d- and f-metal chemistry before (**Scheme 2.1.**). Here, the goal is to establish air-stable benchmark systems of single-molecule magnets (SMMs), which allow profound studies of magneto-structural correlations and qualify for high-resolution charge density experiments.

Various coordination modes are feasible with these ligands, such as *N,N'*- or *N,O* fashion. The d-metal complexes may encounter the ideal tetrahedral geometry for SMMs, which our group has recently promoted. Complexes comprising f-metal centers are expected to form mono- or dinuclear species and help to elucidate coupling phenomena between lanthanides.

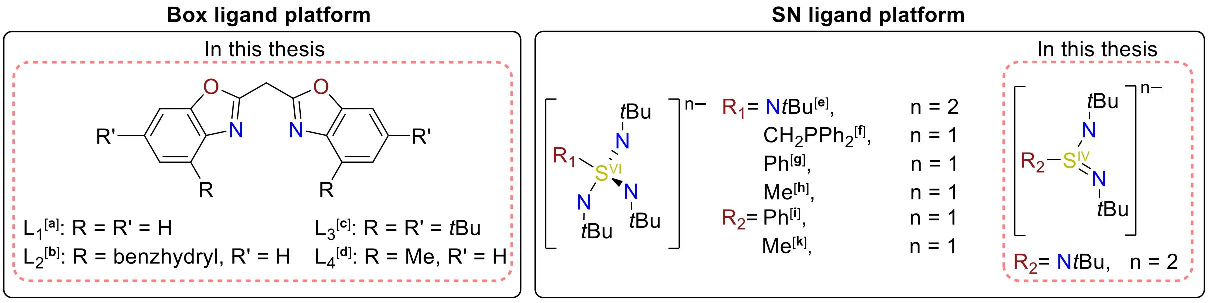

Scheme 2.1. Overview of the Box ligand scaffold (**left**) and the SN ligand platform (**right**) covered in this thesis. [a]: [89–91]; [b]: [97]; [c]: [96]; [d]: [94]; [e]: [118,123]; [f]: [119–121]; [g]: [121,122]; [h]: [117,121,122]; [i]: [121,122]; [k]: [121].

Second, finding a Co^{II} SIM featuring the SN ligand scaffold initiated a new approach toward high-performing SIMs. In the following years, f- and d-metal compounds with imidosulfate, -sulfonate, and -sulfinate ligands were investigated (**Scheme 2.1.**). However, these reported f-metal compounds do not exhibit an axial ligand geometry that is crucial for high-performing SMMs. Such a linear coordination mode is hard to accomplish for traditional polyimido ligands. Therefore, this thesis evaluates various alkali-metal-based triimidosulfites as versatile precursors for SMMs, demonstrating a linear coordination mode that is beneficial for fine-tuning the local anisotropy in such systems. A coordination mode with two ligands sandwiching one lanthanide ion is envisioned. Starting with the well-known lithium precursor [Li$_4${N*t*Bu)$_3$S$_2$] (**L**$_9$), the higher homologues with sodium and potassium are feasible and should provide fruitful chemistry.

3. Results and Discussion

Major parts of this thesis have been published in or submitted to peer-reviewed journals.[1-7]

3.1. Essential structural features for the Box scaffold

Additional structural features are essential to consider when the solid-state structures are discussed in the following chapters. For any protonated Box ligand, both oxazole moieties are positioned in a plane. These planar ligands exhibit a folding angle between the C2 spacer and both oxazole moieties upon deprotonation of the C2 position. To illustrate this feature, one plane is fitted through the nine atomic positions of each moiety, while the resulting angle is devoted as folding or butterfly angle (**Figure 3.1.**). Moreover, the subsequent metal complexes exhibit a dislocation of the metal ion from the C_3N_2 plane, exemplified as M···C_3N_2, as depicted in **Figure 3.1.** For complexes with more than one Box ligand, the twist angles between the ligands were determined via the corresponding planes through the C_3N_2 units. All calculations for the folding angles, twist angles, and the deviations from the C_3N_2 plane were performed with SHELXL employing the MPLA command.[124]

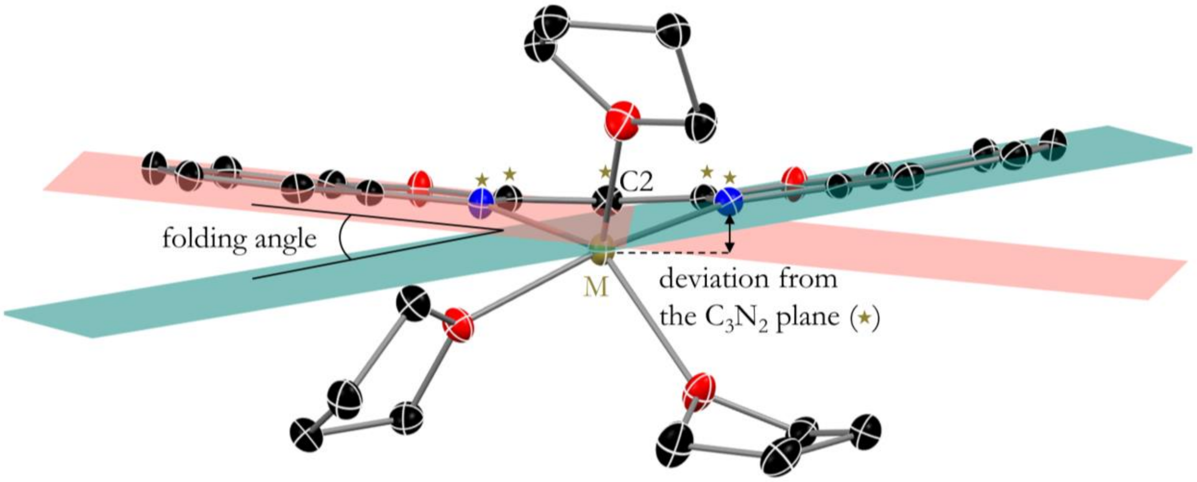

Figure 3.1. Essential structural features of the solid-state structure of metallated Box complexes. This illustration is based on the xyz values deduced from the CIF file of $[(thf)_3Na(NCOC_6H_4)_2CH]$ (**18**) and was created with the program Mercury in accordance with Ref.[3]

3.2. Bis(benzoxazol-2-yl)methanide based d-metal complexes

Major sections of this chapter have been published in:

[1] C. M. Legendre, D. Lüert, R. Herbst-Irmer, D. Stalke, *Dalton Trans.* **2021**, *50*, 16810-16818.

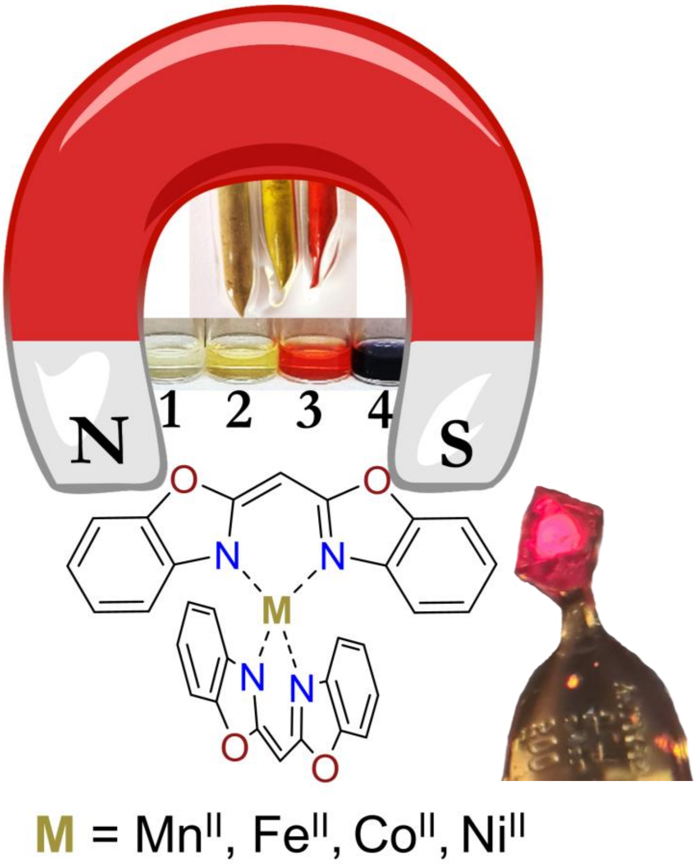

Parts of this illustration are reproduced from Ref.[1] with permission from the Royal Society of Chemistry.

3.2.1. Ligand and precursor synthesis

The bis(benzoxazol-2-yl)methane (**L₁**) ligand, further devoted as Box, was synthesized via established procedures from FLORANLI,[89] DIXNEUF,[90] and STALKE.[91] Prior, an ethylbisimidate dihydrochloride linker was prepared from the reaction of malonic dinitrile with ethanol and hydrogen chloride (**Scheme 3.1.**). The ethanol attacks the nitrile carbon position, forming a nucleophilic imine, followed by a protonation via hydrogen chloride. With the increased electrophilic character, a nucleophilic attack from the 2-aminophenol is enabled, resulting in bis(benzoxazole-2-yl)methane (**L₁**) (**Scheme 3.2.**) The corresponding potassium precursor (**L₁K**) was prepared to access the transition metal complexes according to a route from KRETSCH and STALKE (**Scheme 3.3.**).[125]

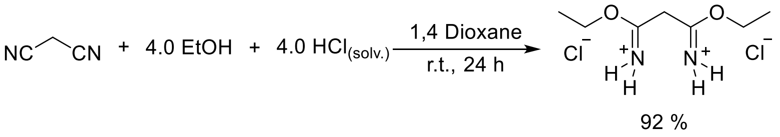

Scheme 3.1. The ethylbisimidate dihydrochloride linker is available upon the reaction of malonic dinitrile with ethanol and hydrogen chloride in 1,4 dioxane.

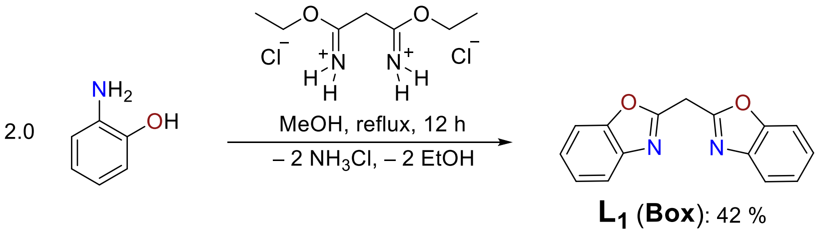

Scheme 3.2. Preparation of bis(benzoxazole-2-yl)methane (**L₁**) from 2-aminophenol and the ethylbisimidate dihydrochloride linker in methanol.

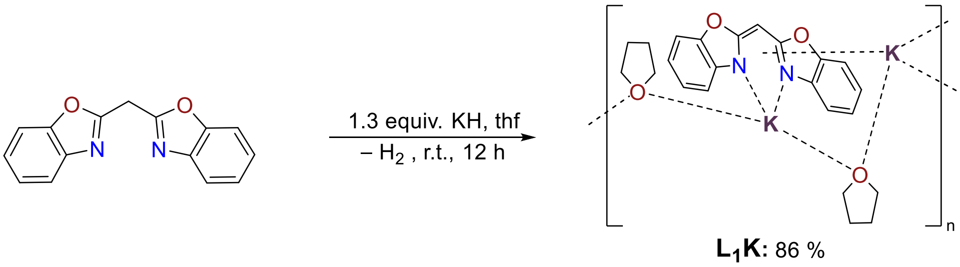

Scheme 3.3. Deprotonation of **L₁** with KH in thf forming a polymeric zig-zag structure motif in the solid-state structure.[125]

3.2.2. Synthesis and solid-state structures of $[(thf)_nM^{II}(Box)_2]$

A suitable precursor for introducing d-metals to the Box ligand system is an alkali metal precursor. In particular, the potassium complex **L_1K** was chosen for this purpose. Consequently, **L_1K** was combined with the corresponding transition metal halides in a standard metathesis reaction with potassium chloride precipitating (**Scheme 3.4.**). Upon stirring the reaction mixtures, a color change is observed for all cases, and after 24 h all mixtures were filtrated to remove the precipitated potassium chloride or unreacted solids. The crude products were crystallized for purification and the yield of the crystalline solids are 46 % for $[(thf)Mn(Box)_2]$ (**1**), 29 % for $[(thf)Fe(Box)_2]$ (**2**), 70 % for $[Co(Box)_2]$ (**3**), and 50 % for $[Ni(Box)_2]$ (**4**), respectively. For **2**, a better yield (51 %) was achieved with direct deprotonation of the Box ligand with the iron(II)-HMDS salt. Detailed procedures are reported in the experimental part. Moreover, the $[M(Mebox)_2]$ (**1***-**4***) series with M = Mn (**1***), Fe (**2***), Co (**3***), and Ni (**4***) displayed a similar yield trend. The synthesis must be carried out under inert conditions since the deprotonated ligand **L_1K** is sensitive to moisture. However, after transmetalation, the formed d-metal complexes $[Co(Box)_2]$ (**3**) and $[Ni(Box)_2]$ (**4**) are extremely stable in solution for some weeks and the solids for several months. LEGENDRE and STALKE reported analogue complexes (**1***-**4***) (**Scheme 3.4.**), which were published together with the **1**-**4** series and discussed herein for better comparability.[1]

Huge colorful, needle-shaped crystals were obtained for **1**-**4** from slow evaporation of *n*-pentane into a saturated thf solution at 238 K. The single crystals suitable for X-ray diffraction (SC-XRD) experiments are light green, yellow, red, and dark green (**1**-**4**).

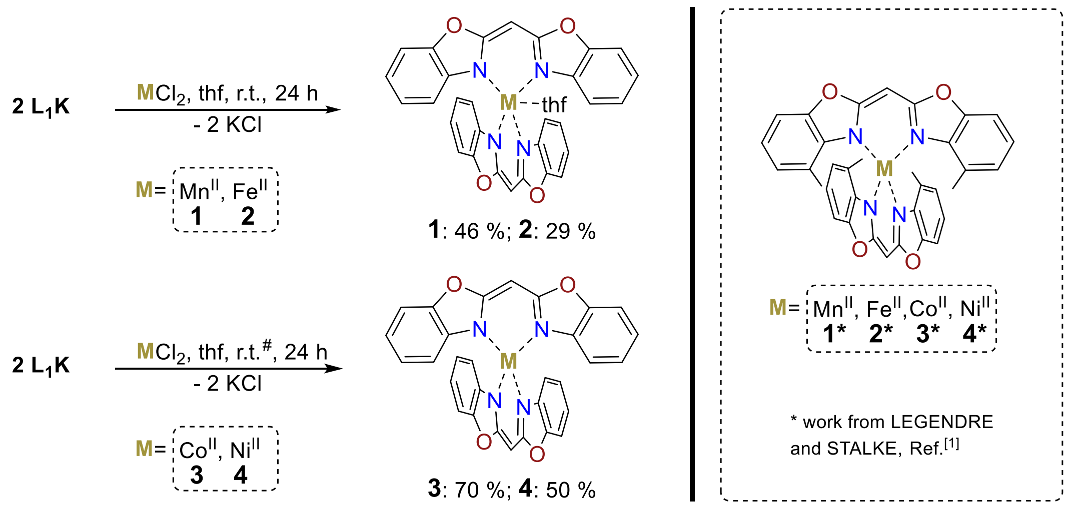

Scheme 3.4. (**left**) Synthesis of **1**-**4** from **L_1K** and the corresponding metal-halides in thf in moderate yields. # The $[Ni(Box)_2]$ complex (**4**) did not form under standard r.t. conditions. Therefore, the mixture was refluxed for 2 h. (**right**) Analogue complexes (**1***-**4***) with the bis(4-Me-benzoxazol-2-yl)methanide ligand, reported by LEGENDRE and STALKE, displayed for comparability. Reproduced from Ref.[1] with permission from the Royal Society of Chemistry.

The subsequent structure analysis revealed complexes consisting of a single divalent M^{2+} cation with M = Mn(**1**), Fe(**2**), Co(**3**), and Ni(**4**), coordinated in an *N*,*N*'-chelating fashion by two ligands (**Figure 3.2.**). Complex **1** and **2** are isomorphous with one complex molecule in the asymmetric unit, displaying the monoclinic space group *C*2/*c* and featuring an additional thf coordination to the metal ion, which results in a trigonal-bipyramidal geometry (**Figure 3.2.a**). Further, we identified two uncoordinated thf molecules placed on symmetry elements within the crystal lattice, which are omitted for clarity in this chapter. Next, the $[Co(Box)_2]$ (**3**) and $[Ni(Box)_2]$ (**4**)compounds are also isomorphous, each with two complex molecules in the asymmetric unit, showing the monoclinic space group $P2_1/n$, with a tetrahedral coordination mode. A rational explanation for the different coordination geometries might root in steric properties as the larger Mn^{2+}- Fe^{2+}-ions allow an additional thf coordination, and second in the preference of Co^{2+}- and Ni^{2+}-ions for a tetrahedral ligand field. The two nitrogen atoms coordinate the metal ion almost equidistantly. The individual M–N bond lengths (**Table 3.1.**) are in alignment with the decreasing ionic radii from Fe(II) to Ni(II). A range of 2.1368(15)-2.1588(13) Å for **1** to 1.949(5)-1.975(5) Å for **4** is typical for such compounds (**Table 3.1.**).[126]

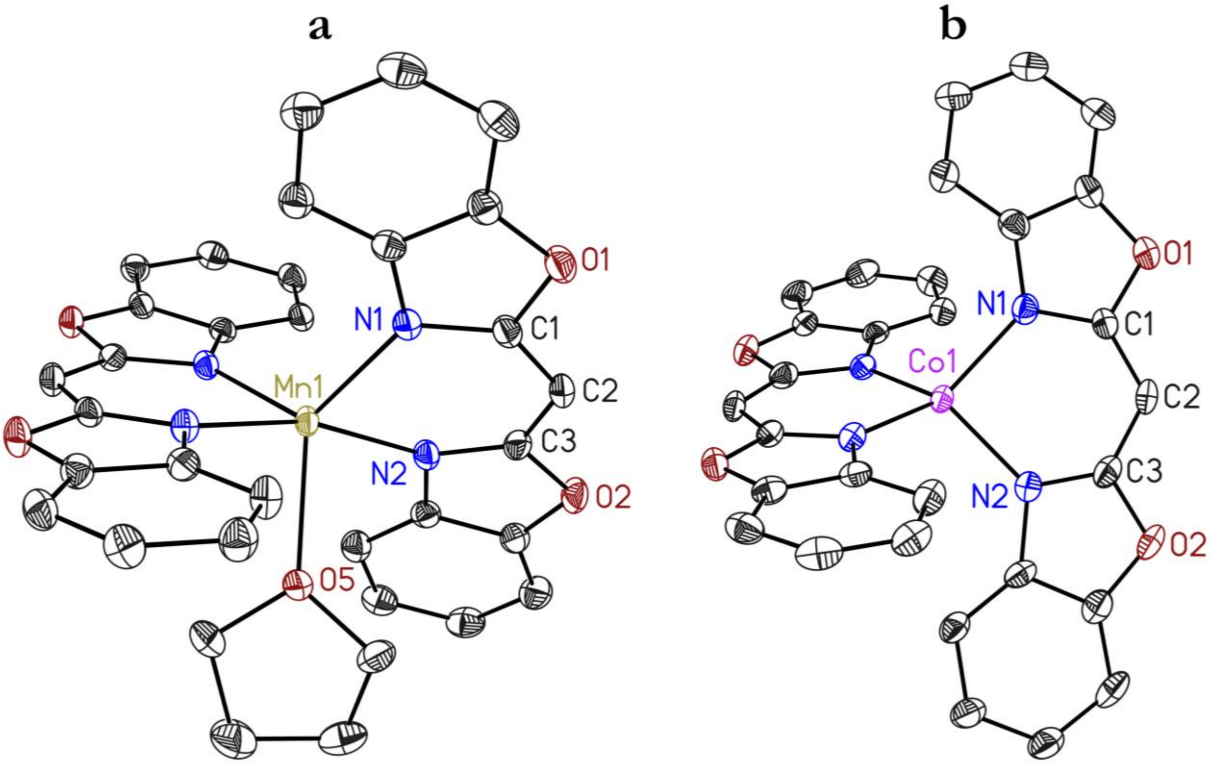

Figure 3.2. (**a**) Solid-state structure of **1**-**2**, illustrated is the $[(thf)Mn(Box)_2]$ (**1**), while $[(thf)Fe(Box)_2]$ (**2**) is isostructural and shown in the crystallographic section. (**b**) Solid-state structures of **3**-**4**, illustrated is the $[Co(Box)_2]$ (**3**), while $[Ni(Box)_2]$ (**4**) is isostructural and shown in the crystallographic section. Thermal ellipsoids are displayed at a probability level of 50%. The hydrogen atoms and lattice solvent molecules are omitted for clarity. Reproduced from Ref.[1] with permission from the Royal Society of Chemistry.

Table 3.1. Selected bond lengths [Å] and angles [°] for complexes **1**-**4**. (*) Complex **4** displays week SC-XRD data. Reproduced from Ref.[1] with permission from the Royal Society of Chemistry.

	1	**2**	**3**	**4***
N–M$_{range}$	2.1368(15)-2.1588(13)	2.0837(15)-2.1026(15)	1.977(3)-1.991(3)	1.949(5)-1.975(5)
N–M–N$_{range}$	85.82(5)-86.20(6)	87.14(6)-87.22(5)	92.80(12)-92.89(12)	91.7(2)-91.3(2)
N1–C1/N2–C3	1.343(2)-1.334(2)	1.343(16)-1.333(16)	1.341(4)-1.333(4)	1.353(8)-1.339(9)
C1–C2/N2–C3	1.385(2)-1.388(2)	1.385(2)-1.389(2)	1.389(5)-1.384(5)	1.356(10)-1.394(10)
Twist angles	54.25(6)	56.07(6)	63.63(15)-64.32(14)	62.3(3)-61.3(4)
Folding angles[a]	5.57(6)-7.53(7)	5.57(6)-7.90(7)	2.02(17)-12.50(9)	2.7(3)-11.30(19)
M···C_3N_2 plane	0.219(2)-0.491(2)	0.230(2)-0.516(2)	0.031(4)-0.216(5)	0.029(8)-0.156(11)

[a] Folding angle range for two ligands (**1**,**2**) and four ligands (**3**,**4**).

Bite angles of N1–M–N2 and N3–M–N4 for [(thf)Mn(Box)$_2$] (85.82(5)-86.20(5)°), [(thf)Fe(Box)$_2$] (87.14(6)-87.22(5)°), [Co(Box)$_2$] (92.80(12)-92.89(12)°), and [Ni(Box)$_2$] (91.7(2)-91.3(2)°) are more acute than the ideal tetrahedral angle. The ideal N–M–N angle for a distorted Co(N$_2$R)$_2$ complex is 78°, from which 1-4 deviate by 10-15°.[121]

Next, to elucidate the structural variations of the complexes from an ideal tetrahedron, a simple metric from ADDISON and REEDIJK was utilized:[127]

$$\tau_4 = \frac{360° - (\alpha + \beta)}{141°} \tag{3-1}$$

For a τ_4 value of 1, the ideal tetrahedral symmetry is reached. As the deviation from 1 grows, the distortion from a T$_d$ symmetry increases. The parameters *a* and *β* represent the largest angles in the four-coordinated species.[128] According to equation (**3-1**) we determined the degree of deviation from an ideal tetrahedron, which was most vital in **1** (τ_4 = 0.53) and the least in **3** (τ_4 = 0.63) (**Table 3.2.**).

Comparing the C1–C2/N2–C3 and N1–C1/N2–C3 bond lengths of the C_3N_2 *nacnac*-like chelating unit, one can conclude that the π-system is fully conjugated and extends throughout the entire virtually planar ligands. In previous studies, this feature was discovered for the alkali metal species of the bis(benzoxazol-2-yl)methane ligand.[125] Both ligands (N1C2N2-, N3C5N4-units) are twisted by around 60°, in particular, 54.25(6)° for **1**, 56.07(6)° for **2**, 63.63(15)-64.32(14)° for **3**, and 61.3(4)-61.3(4)° for **4**, respectively. Interestingly, the **1***-**4*** series displays twist angles close to 90 °, which is most likely attributed to the additional methyl substitution.

Table 3.2. Structural τ_4 parameters for **1**-**4**. Reproduced from Ref.[1] with permission from the Royal Society of Chemistry.

	1	**2**	**3**	**4**
α angle	120.90	117.18	133.20	134.20
β angle	164.14	164.49	137.33	140.40
τ_4	0.53	0.56	0.63	0.61

For the folding angles in **3** (2.02(17)-12.5(9)°) and **4** (2.7(3)-11.30(19)°), we recorded the most substantial span compared with the angles for **1** (5.57(6)-7.53(7)°) and **2** (5.57(6)-7.90(7)°). The metal is further elevated from the C_3N_2 plane for **1** (0.219(2)-0.491(2)°) and **2** (0.230(2)-0.516(2)°) than for **3** (0.031(4)-0.216(5)°) and **4** (0.029(8)-0.156(11)°), ascribed to the additional thf coordination. Such trends are not detected for the **1***-**4*** series, which is isomorphous.

The metal ions are well-separated (> 10 Å) in complex **1**-**4**, which is crucial for the magnetic properties, and the lattice solvents of **1** and **2** effectively prevent any potential intermolecular π-π interaction among the Box ligands.[20a,64] For **3** and **4**, no lattice solvent is present, and long-range π interaction is caused by the proximity of neighboring ligands with the shortest distance of 3.51 Å. One remarkable feature of **3** is a high X-ray diffraction resolution up to 0.50 Å, which qualifies for in-depth electron density studies. Elemental analysis data from the dried solids are in high agreement with the SC-XRD data. For further details, the reader is referred to the experimental section.

3.2.1. Spectroscopic characterization of $[(thf)_nM^{II}(Box)_2]$

Standard ^{1}H- and ^{13}C-NMR experiments with a wider range were executed for **1**-**4**. Typical issues with paramagnetic complexes did limit further elucidation of CH coupling and exact signal assignment. However, we were able to resolve all expected signals, and the spectra for $[Co(Box)_2]$ (**3**), which is displayed for reference, while data for $[(thf)Mn(Box)_2]$ (**1**), $[(thf)Fe(Box)_2]$ (**2**), and $[Ni(Box)_2]$ (**4**) can be retrieved from the experimental section (chapters 5.3.1-5.3.4). Under the premise that the signal at −74.98 ppm (^{1}H-NMR) can be assigned to the hydrogen atom at aromatic position in close proximity to the paramagnetic center (8), the other aromatic positions can be identified as portrayed in **Figure 3.3.** COSY-NMR data provided insights to assign the signal at −24.64 ppm (^{1}H-NMR) (6). For the 5 and 7 positions, we assume the assignment as depicted below. The two quaternary carbons positions at 2 and 3 are hard to distinguish, while position 4 is assumed to be the signal at 369.01 ppm.

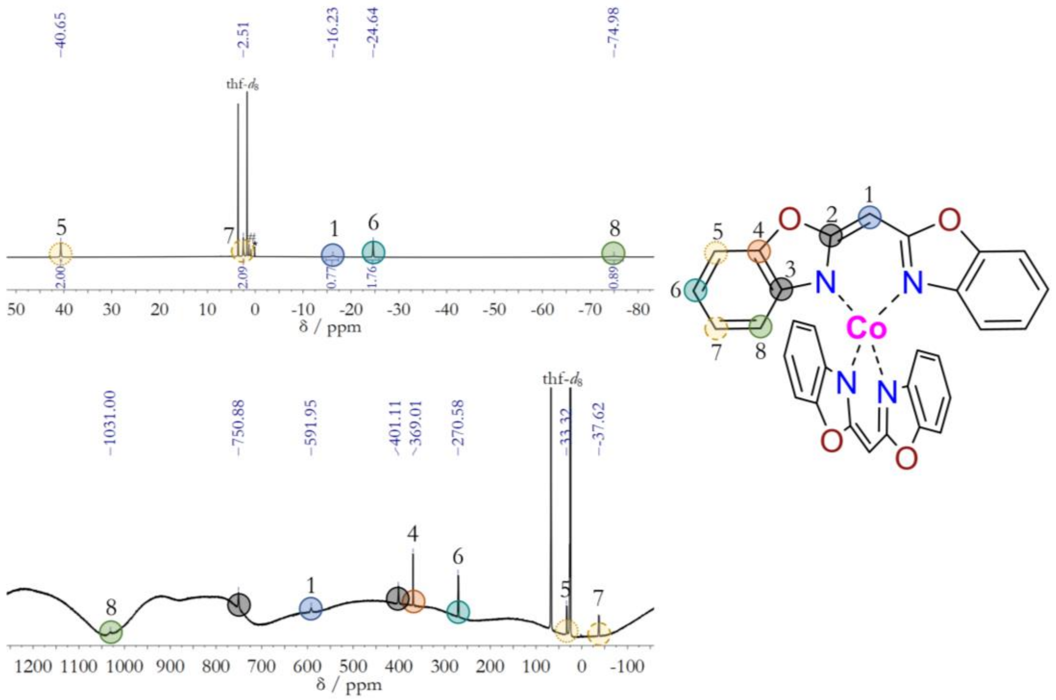

Figure 3.3. (**a**) ^{1}H-NMR data for [Co(Box)$_2$] (**3**) in thf-d_8. (**b**) ^{13}C-NMR data for **3** in thf-d_8. An exact signal assignment is challenging with paramagnetic complexes. Beside the two quaternary carbon positions 2 and 3, all signals could be assigned correctly, applying different measuring techniques. Reproduced from Ref.[1] with permission from the Royal Society of Chemistry.

Next, the [(thf)$_n$M(Box)$_2$] (**1**-**4**) and [(M(Mebox)$_2$] (**1***-**4***) series were characterized by UV-vis spectroscopy in solution and the solid-state. The high extinction coefficient values (**Table 3.3.**) suggest that the intense absorption bands are ascribed to a charge transfer from the metal to the ligand. Below 380 nm, the aromatic backbone's expected π → π* excitation was observed. There are substantial differences in absorption between **1**-**4** and **1***-**4***. Notably, the substituent variation drastically affects the absorption patterns of the manganese and iron complexes (**1** and **2**). Complex **1** illustrates no absorption in the visible range, whereas **1*** exhibits various highly energetic absorption bands that lead to its bright yellow color (**Figure 3.4.**). In contrast, [(thf)Fe(Box)$_2$] absorbs only weakly in the visible range, while **2*** shows its maxima at 399, 422, and 516 nm. Instead, minor deviations are noticed for cobalt (**3**, **3***) and nickel (**4**, **4***) that are almost identical. Related Ni(II) complexes featuring the *β*-diketimide scaffold demonstrate comparable UV-vis data, while Co(II) complexes have a broader range.[83,86,129] These distinctions between both series can probably be assigned to the additional thf coordination on the metal center that might be favored in the solution. Further, the bathochromic shift from **1***-**4*** to **1**-**4** is vital for **4** and **4*** (Δλ ~30 nm) due to the potential hyperconjugation in **1***-**4***.[130] These experimental trends are reproduced with theoretical calculations, exhibiting absorption wavelength values that are in good agreement with each other and only frequently off the range. Here, possible reasons are the different spatial arrangements of the molecules in solution and the solid-state since the coordinates for calculations were derived from the solid-state structures. Therefore, solid-state UV-vis measurements were performed, revealing different results for **1** and **2** than in solution. The absorption maxima for **1** and **1*** show a significant bathochromic shift in relation to the solution data. Moreover, the solid-state UV-vis measurements for **2** and **2*** demonstrate a similar absorption pattern as found for **2*** in solution. Also, **3** and **3*** are in good alignment with the data in the solution. These findings conclude that the spectroscopic deviations between **1**, **1*** and **2**, **2*** are most likely attributed to the methyl substituent rather than to the additional thf coordination for **1** and **2**.

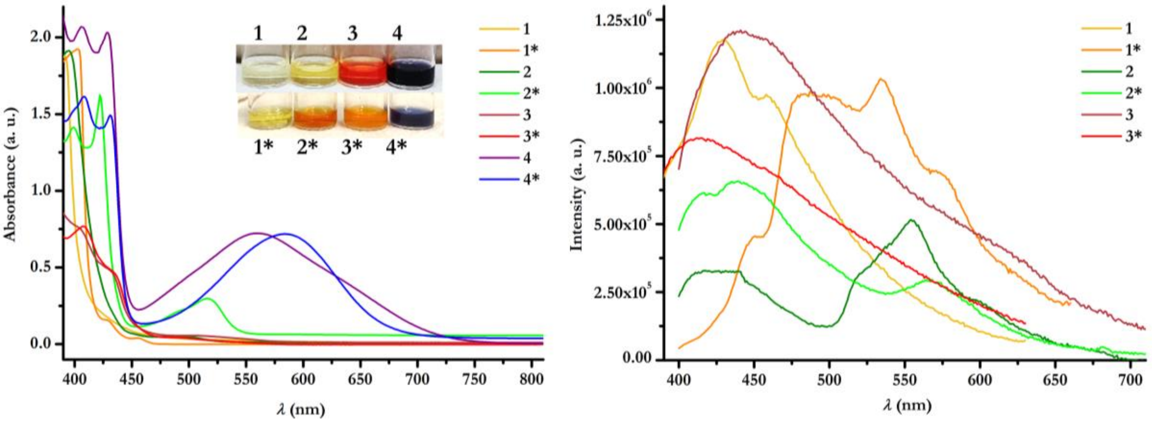

Figure 3.4. UV-vis spectra of the $[(\mathrm{thf})_n\mathrm{M(Box)_2}]$ (**1**-**4**) series with M = Mn (**1**), Fe (**2**), Co (**3**), and Ni (**4**) and the $[\mathrm{M(Mebox)_2}]$ (**1***-**4***) series with M = Mn (**1***), Fe (**2***), Co (**3***), and Ni (**4***) in (thf) solution (**left**) and the solid-state (**right**). Reproduced from Ref.[1] with permission from the Royal Society of Chemistry.

Table 3.3. Absorption wavelengths and extinction coefficients in solution compared with CAM-B3LYP calculations for the **1**-**4** and **1***-**4*** series. Reproduced from Ref.[1] with permission from the Royal Society of Chemistry.

		$\lambda_{\mathrm{experimental}}$ (nm)	$\lambda_{\mathrm{simulated}}$ (nm)	λ_{max}, ε ($\mathrm{cm^{-1}\,mol^{-1}\,L}$)
1	$[(\mathrm{thf})\mathrm{Mn(Box)_2}]$	391	416	391 (ε = 18 762)
1*	$[\mathrm{Mn(Mebox)_2}]$	402, 429, 455	418	402 (ε = 19 241)
2	$[(\mathrm{thf})\mathrm{Fe(Box)_2}]$	395, 492	410	395 (ε = 19 136)
2*	$[\mathrm{Fe(Mebox)_2}]$	399, 422, 516	443	422 (ε = 16 251)
3	$[\mathrm{Co(Box)_2}]$	404, 430, 513	403, 468, 721	404 (ε = 7579)
3*	$[\mathrm{Co(Mebox)_2}]$	408, 434, 490	414, 619, 749	408 (ε = 7680)
4	$[\mathrm{Ni(Box)_2}]$	406, 429, 560	429, 558	406 (ε = 2069)
4*	$[\mathrm{Ni(Mebox)_2}]$	408, 431, 584	445, 564, 581	408 (ε = 1615)

3.2.2. Magnetic properties of $[(thf)_nM^{II}(Box)_2]$

State-of-the-art transition metal-based SIMs and their crucial design features were introduced in chapter 1.4. The aim of **1-4** was not to compete among high-performing SIMs. Instead, our intention was directed toward air-stable complexes with an easy tunable and robust ligands platform, which could serve as magnetic and spectroscopic benchmarks systems.

First, direct current (dc) measurements in a magnetometer allowed us to determine the molar susceptibility χ_M. The temperature dependency of $\chi_M T$ is plotted below, and all complexes were found to be paramagnetic (**Figure 3.5.**). The high-temperature values of $\chi_M T$ for the manganese and nickel complexes are close to the expected spin-only values of 4.38 and 1.99 $cm^3\ mol^{-1}\ K$. Noteworthily, for **1** and **1***, the $\chi_M T$ values deviate from each other, which might stem from the difficulties in weighing as several solvent molecules are present. Higher $\chi_M T$ values than the spin-only systems were identified for cobalt (2.50 vs. 1.87 $cm^3\ mol^{-1}\ K$) and iron (3.50 vs. 3.00 $cm^3\ mol^{-1}\ K$), indicating a substantial orbital contribution. The $\chi_M T$ values are stable while decreasing the temperature and start decreasing below 50 K. This phenomenon is characteristic of magnetic saturation for the cases of manganese and iron, whereas for the nickel complexes, an earlier and smoother decrease is present. Weak intermolecular interactions between the magnetic centers should be considered for **4** and **4***, as their intermolecular distance is shorter than observed in **1** and **2**. A more fluent decay is also examined for the cobalt complexes and can be ascribed to its high anisotropy values.

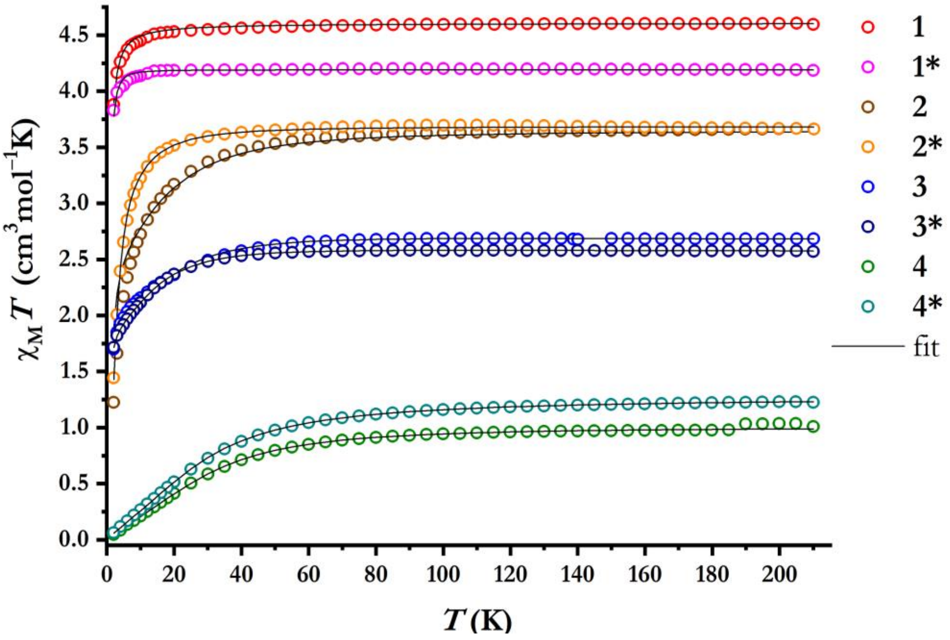

Figure 3.5. Temperature dependency of $\chi_M T$ for **1**-**4** and **1***-**4*** from 210 to 2 K. The corresponding fits are performed with the JulX-2s program.[131] Reproduced from Ref.[1] with permission from the Royal Society of Chemistry.

Acquiring variable field variable temperature data (VTVH) enabled a simultaneous fit employing the JulX-2s program to receive accurate values for the static magnetic parameters.[131] The corresponding spin Hamiltonian was used:[132]

$$\hat{H} = \mu_{\mathrm{B}}\left(S_{\mathrm{x}}g_{\mathrm{x}}B_{\mathrm{x}} + S_{\mathrm{y}}g_{\mathrm{y}}B_{\mathrm{y}} + S_{\mathrm{z}}g_{\mathrm{z}}B_{z}\right) + D\left[\hat{S}_{\mathrm{z}}g^{2} - \frac{1}{3}S(S+1) + \frac{E}{D}\left(\hat{S}_{\mathrm{x}}^{2} - \hat{S}_{\mathrm{y}}^{2}\right)\right] \qquad (\mathbf{3\text{-}2})$$

where, *g* refers to the electronic *g* matrix with its diagonal elements g_x, g_y, and g_z, whereas *D* and *E* are the axial and rhombic ZFS parameters. We found small and positive ZFS parameters for the manganese and iron complexes (**Table 3.4.**), most accurately described as isotropic ($g_x = g_y = g_z$). Larger values are displayed for the nickel complexes, however positive, leading to a flipped double-well potential with no effective energy barrier (**Figure 1.3.f**).[133] Only both cobalt complexes (**3**, **3***) exhibited a negative *D* value and were recognized as potential single-molecule magnets (SMM). The difference in the ZFS splitting in these two complexes could stem from their deviation from an ideal tetrahedral geometry around the cobalt center. Comparing the calculated τ_4 values (eq. **3-1**) for **3** ($\tau_4 = 0.63$) and **3*** ($\tau_4 = 0.88$), **3** is further away from an ideal tetrahedron ($\tau_4 = 1$) and should therefore result in higher magnetic anisotropy.[121,132,134] Furthermore, the best fit was achieved with anisotropic *g* values ($g_x \approx g_y < g_z$), usually anticipated for a distorted tetrahedral environment. For the manganese complexes, slow relaxation processes other than Orbach relaxation might still occur, as previously reported in Mn^{2+} complexes with a non-zero or even positive *D* value.[135]

Further, we recorded alternating current (ac) susceptibility data for all complexes, while **1***, **3**, and **3*** exhibited field-induced SMM behavior. In this thesis, only the data for **3** is discussed and the interested reader is directed to the corresponding publication for **1*** and **3***.[1]

Table 3.4. Selected experimental magnetic data for **1**-**4** and **1***-**4***. Reproduced from Ref.[1] with permission from the Royal Society of Chemistry.

		D (cm^{-1})	*E*/*D*	$g_{x,\,y,\,z}$	U_{eff} (cm^{-1})[	τ_0 (s)
1	[Mn(thf)(Box)$_2$]	−0.03	0	2.05	–	–
1*	[Mn(Mebox)$_2$]	0.5	0	1.96	6.0	$4.14 \cdot 10^{-5}$
2	[Fe(thf)(Box)$_2$]	11.7	0.3	2.21	–	–
2*	[Fe(Mebox)$_2$]	6.9	0	2.22	–	–
3	[Co(Box)$_2$]	−25.0	0	2.27, 2.27, 2.58	18	$1.85 \cdot 10^{-6}$
3*	[Co(Mebox)$_2$]	−18.4	0.02	2.28, 2.21, 2.51	45	$2.47 \cdot 10^{-11}$
4	[Ni(Box)$_2$]	67.5	0	2.00	–	–
4*	[Ni(Mebox)$_2$]	55.0	0	2.00, 2.00, 2.71	–	–

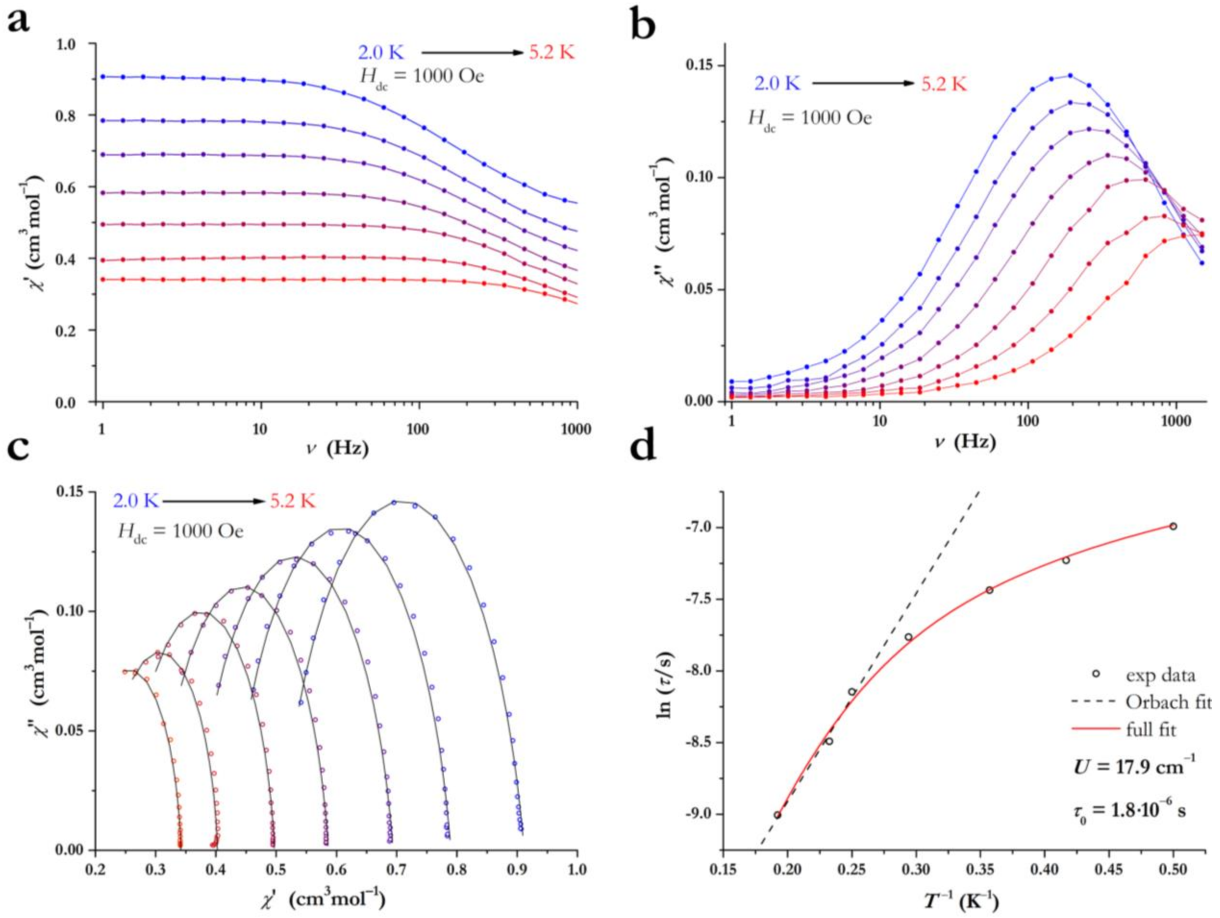

Figure 3.6. Magnetic data for **3** under a dc field of 1000 Oe. Dynamic in-phase (**a**) and out-of-phase (**b**) susceptibility versus variable frequencies from 2.0 to 5.2 K (lines: a guide for the eyes). Cole-Cole plot (**c**) with corresponding CC-fit data; Arrhenius plot (**d**) with red curve exemplifying the full fit of all relaxation processes, and the dashed line demonstrates a sole Orbach regression. Reproduced from Ref.[1] with permission from the Royal Society of Chemistry.

The general procedures of the ac data measurement process are thoroughly described in the magnetic part (chapter 5.2.4). For [Co(Box)$_2$] (**3**), no maxima in the out-of-phase susceptibility under zero-field conditions were found in the temperature range from 2.0 to 20.0 K. Probing the sample under various dc fields, maxima typical for induced SMMs were observed, and the optimal dc field was determined to be 1000 Oe. The in-phase susceptibility χ' starts dropping at an oscillating ac field frequency of 200 Hz (**Figure 3.6.a**). Here, the out-of-phase susceptibility χ'' illustrates a maximum at 2.0 K, and their maxima are further shifted toward higher frequencies with the increase of temperature up to 5.2 K (**Figure 3.6.b**). This phenomenon is characteristic of a temperature-depending process. To extract the relaxation rate τ^{-1} and the effective energy barrier U_{eff}, χ'' was plotted versus χ' in the so-termed Cole-Cole plot (**Figure 3.6.c**). However, the Cole-Cole plot portrays more narrow-shaped semi-circles, indicating that slow magnetization only partially occurs through an SMM-related Orbach process. An accurate fit of the Cole-Cole plot was performed employing the CC-fit program with one relaxation process, and the corresponding τ values were used to construct the Arrhenius plot (**Figure 3.6.d**).[136] For modulating the Arrhenius data, direct processes were excluded, as their impact was neglectable, and only Orbach, Raman, and QTM processes were taken into account:

$$\tau^{-1} = CT^{n} + \tau_0^{-1} \exp\left(-\frac{U_{\mathrm{eff}}}{k_{\mathrm{B}}T}\right) + \mathrm{QTM} \tag{3-3}$$

The full fit gives rise to an effective energy barrier of 17.9 cm^{-1}, with a significant Raman (C = 150 $\mathrm{s}^{-1}\mathrm{K}^{-n}$) contribution and moderate QTM ($\tau_{\mathrm{QTM}}{}^{-1}$ = 484.7 s^{-1}) influence (**Table 3.5.**). Further, an *n* value close to two and the narrow-shaped semi-circles indicate the presence of a phonon bottleneck (PB) relaxation, which is different from a true SMM behavior. The spins resonate with only a few phonon modes for a PB effect, allowing no complete relaxation of spins as they are being excited by phonons again.[137] PB can be identified via various sweep rates in hysteresis measurements, as the coercivity decreases upon faster rates. However, no hysteresis is detected for **3**, and we attribute the slow relaxation in **3** to both a PB and SMM effect, as there are previously reported systems where both phenomena coexist.[138]

Computational studies facilitate a backup of the experimental data and assess deeper insights into the energy levels of the d-orbitals. Therefore, CASSCF-NEVPT2 calculations using the ORCA software were performed for [Co(Box)$_2$] (**3**), based on the geometry retrieved from the single-crystal X-ray diffraction data and correlated to **3***.[139] The strength of the spin-orbit coupling was determined with *ab initio* ligand field theory (AILFT) which produced the d-orbital splitting and permitted us to quantify the energy gap between the d-orbitals d_{xy} and $d_{x^2-y^2}$ (**Table 3.6.**).[121] Good agreement was found for the calculated parameters with the experimental data, suggesting a substantial lack of axial magnetic anisotropy in complexes **3** and **3***. For **3** the calculated d-orbital contribution is more favorable than the experimentally found one. However, besides the more significant D value, the rhombic parameter E/D is considerably larger than in **3***. This fact may illuminate the better magnetic performance of **3*** and the deviation in their preferred relaxation process.

Table 3.5. Best fitting parameters for **3** and **3***. Reproduced from Ref.[1] with permission from the Royal Society of Chemistry.

	τ_0 (s^{-1})	U_{eff}	n	C ($\mathrm{s}^{-1}\mathrm{K}^{-n}$)	$\tau_{\mathrm{QTM}}{}^{-1}$ (s^{-1})
3	$1.8\cdot10^{-6}$ ($\pm2.3\cdot10^{-7}$)	17.9 (±1.2)	2.0 (±0.5)	150.0 (±34.8)	484.7 (±42.2)
3*	$2.5\cdot10^{-11}$ ($\pm8.1\cdot10^{-12}$)	45.0 (±3.1)	9.0 (±3.4)	$3.6\cdot10^{-3}$ ($\pm1.4\cdot10^{-2}$)	0

Table 3.6. Selected computational details for **3** and **3***. Reproduced from Ref.[1] with permission from the Royal Society of Chemistry.

	D (cm^{-1})	E/D	$g_{x,y,z}$	ΔE (d_{xy}, $d_{x^2-y^2}$) (cm^{-1})
3	−43	0.12	2.07, 2.21, 2.64	1348
3*	−27	0.02	2.13, 2.14, 2.45	2358

3.2.3. Summary and concluding remarks for [(thf)$_n$M^{II}(Box)$_2$] complexes

The presented systems are successfully synthesized and characterized by NMR, MS, UV-VIS, SC-XRD, and SQUID techniques. [Co(Box)$_2$] (**3**) is identified to be a field-induced SMM, as various spin-lattice processes are detected. In particular, a coexisting phonon bottleneck contribution is present. The cobalt and nickel complexes (**3**, **4**) are air-stable and accessible in a straightforward approach, offering a versatile and tunable platform for benchmarking analytical and computational methods. Moreover, high-resolution X-ray diffraction experiments are feasible for **3** and **3*** and open more pathways to evaluate other magneto-structural correlations.

3.3. Bis(4-benzhydryl-benzoxazol-2-yl)methanide based d-metal complexes

3.3.1. Ligand and precursor synthesis

This chapter juxtaposes the coordination chemistry and the magnetic properties of the bis(4-benzhydryl-benzoxazol-2-yl)methanide based d-metal complexes with the **1**-**4** series from the previous chapter.

KRETSCH and STALKE proposed a detailed procedure to access the bis(4-benzhydryl-benzoxazol-2-yl)methane ligand, which was followed in this thesis and starts from the 2-methoxyaniline (**Scheme 3.5.**).[97] First, the amine function of the 2-methoxyaniline is protected via a *tert*-butyloxycarbonyl group (BOC). Next, a reaction with *t*BuLi and benzophenone fosters the formation of a carbamateol and an oxazin-2-one. Both species result in the 2-benzhydryl-6-methoxyaniline upon reduction with hydrogen. Last, the methoxy group is turned into a hydroxy function employing BBr_3. The general cyclocondensation reaction of the ethylbisimidate dihydrochloride linker with 2 equiv. of 3-benzhydryl-2-aminophenol gave the bis(4-benzhydryl-benzoxazol-2-yl)methane ligand (**L_2**).

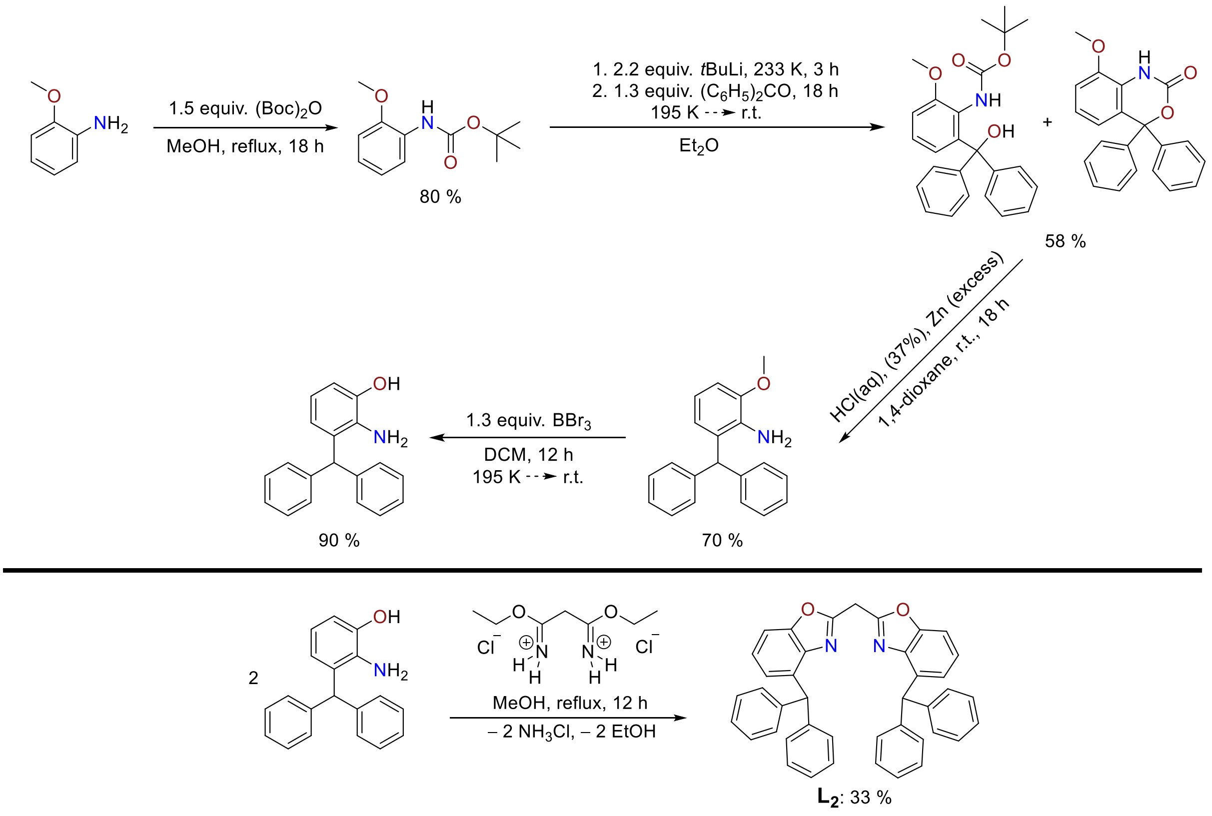

Scheme 3.5. Synthesis of bis(4-benzhydryl-benzoxazol-2-yl)methanide (**L_2**) in a five-step root starting from 2-methoxyaniline. Created in accordance with Ref.[97]

3.3.2. Synthesis and solid-state structures of $[(thf)M^{II}Cl\{(4\text{-benzhydryl-}NCOC_6H_3)_2CH\}]$

The pK_a value of $\mathbf{L_2}$ (Bzhbox) is higher than for $\mathbf{L_1}$ (Box), which hampers the use of HMDS salts to deprotonate this ligand. Potassium hydride is a stronger base and sufficient to deprotonate the ligand. Subsequent metathesis reactions with the transition metal halides yielded the desired complexes (**Scheme 3.6.**).

Yellow (**5**), orange (**6**), and brown (**7**) block-shaped crystals suitable for X-ray diffraction experiments were acquired from a concentrated solution of thf/toluene applying the slow evaporation technique (chapter 6.1). All three complexes crystallize in monoclinic space groups, *C*2/*c* for $[(thf)_2MnCl(4\text{-benzhydryl-}NCOC_6H_3)_2CH]$ (**5**), and $[(thf)_2FeCl(4\text{-benzhydryl-}NCOC_6H_3)_2CH]$ (**6**) and $P2_1/c$ for $[(thf)CoCl(4\text{-benzhydryl-}NCOC_6H_3)_2CH]$ (**7**). The isostructural compounds **5** and **6** show half a molecule, whereas **7** displays an entire molecule in the asymmetric unit (**Figure 3.7.**). The solid-state structures of **5**-**7** comprise a central divalent M^{2+} cation (M = Mn (**5**), Fe (**6**), and Co (**7**), and two negative charged ligands ($\mathbf{L_2}^-$ and Cl^-). Additionally, **5** and **6** contain two neutral thf ligands, while **7** illustrates only one thf donor side (**Figure 3.7.**). The initial goal was to attain the dimeric analogues to the $[(thf)_nM(\mathbf{L_1})_2]$ series (**1**-**4**). Despite a molar ratio of 2:1 or 1:1, we always isolated the monomeric complexes $[(thf)_nMCl(\mathbf{L_2})]$. This examination is most likely attributed to the steric of the benzhydryl groups that shield the metal center and prevent the substitution of the second halide with another $\mathbf{L_2}$ ligand.

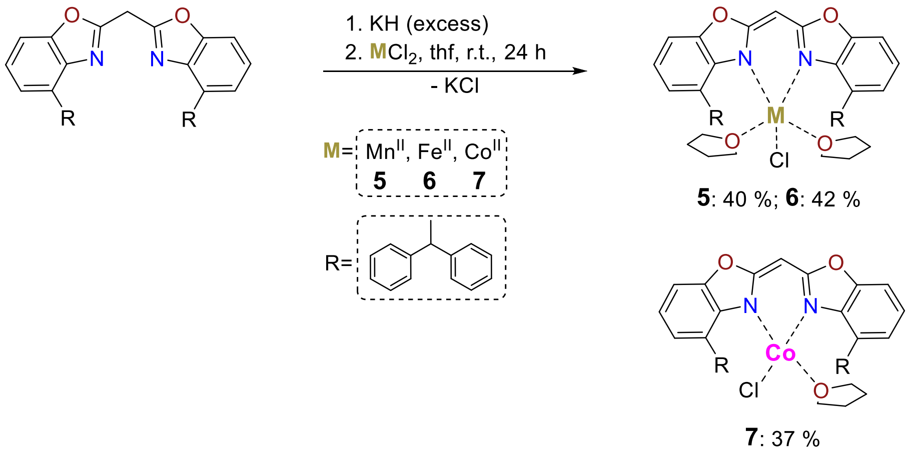

Scheme 3.6. Procedure to $[(thf)_nM^{II}Cl\{(4\text{-benzhydryl-}NCOC_6H_3)_2CH\}]$ with M = Mn^{II} (**5**), Fe^{II} (**6**) (n = 2), and Co^{II} (**7**) (n = 1).

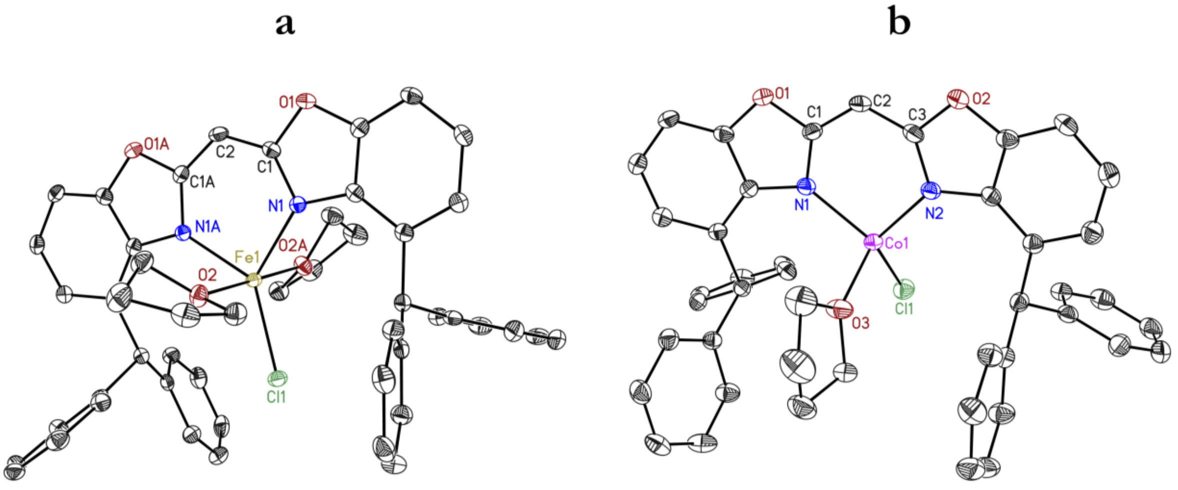

Figure 3.7. (**a**) The solid-state structure of [(thf)$_2$FeCl{(4-benzhydryl-NCOC$_6$H$_3$)$_2$CH}] (**6**), while **5** is isostructural and only displayed in the crystallographic section (chapter 5.3.5). (**b**) The solid-state structure of [(thf)CoCl{(4-benzhydryl-NCOC$_6$H$_3$)$_2$CH}] (**7**). Thermal ellipsoids are displayed at a probability level of 50 %. The hydrogen atoms and lattice solvent molecules are omitted for clarity.

Table 3.7. Continuous Shape Measures (CShMs) of the coordination geometry for the M^{2+} ion environments in **5**-**6**, retrieved from the SHAPE program, exhibiting the lowest residue for a trigonal bipyramid polyhedron.[140]

	JTBPY-5[a]	SPY-5[b]	TBPY-5[c]	vOC-5[d]	PP-5[e]
5	4.101	4.984	1.850	5.720	27.749
6	3.844	4.922	1.664	5.689	28.640

[a] D$_{3h}$, Johnson trigonal bipyramid; [b] D$_{4v}$, Square pyramid; [c] D$_{3h}$, Trigonal dipyramid; [d] C$_{4v}$, Vacant octahedron (Johnson square pyramid, J1); [e] D$_{5h}$, Pentagon.

Table 3.8. Continuous Shape Measures (CShMs) of the coordination geometry for the M^{2+} ion environment in **7**, retrieved from the SHAPE program, displaying the lowest residue for a seesaw polyhedron.[140]

	SP-4[a]	T-4[b]	SS-4[c]	vTBPY-4[d]
7	3.112	6.424	1.604	27.220

[a] D$_{4h}$, Square; [b] T$_d$, Tetrahedron; [c] C$_{2v}$, Seesaw; [d] C$_{3v}$, Axially vacant trigonal bipyramid.

Next, the coordination geometry for **5**-**7** was elucidated with the SHAPE software.[140] A numerical evaluation is performed with the experimentally measured geometries of **5**-**7** to their ideal symmetries. The obtained residues range from 0 to 100, while 0 refers to a structure entirely coincident in shape with the reference polyhedron. For **5** and **6**, a trigonal bipyramidal (D$_{3h}$)

Table 3.9. Selected bond lengths [Å] and angles [°] for complexes **5**-**7**.

	5	**6**	**7**
M–N$_{range}$	2.1421(12)	2.067(2)	2.0028(18)-2.0031(19)
N–M–N$_{range}$	95.37(7)	95.62(12)	98.69(8)
M–Cl	2.3382(7)	2.254(2)	2.2327(8)
M–O	2.2579(10)	2.192(2)	2.0110(17)
Folding angles	0	0	9.67(9)
M···C_3N_2 plane	0.014(2)	0.013(3)	0.080(3)

geometry and for **7**, a seesaw (C_{2v}) geometry are the most accurate descriptions of the symmetry, as the continuous shape measures (CShMs) demonstrate the lowest residue values of 1.664-1.850 for **5**-**6** (**Table 3.7.**) and 1.604 for **7** (**Table 3.8.**). Reviewing the M–N bond length range, the decrease from **5** (2.1421(12) Å) to **7** (2.0028(18)-2.0031(19) Å) is in alignment with the trend of the ionic radii from Mn^{II} to Co^{II} and related compounds (**Table 3.9.**).[1,126] Similar behavior is determined for the M–O and M–Cl distances, while the former ranges from 2.3382(7)-2.2327(8) Å and the latter from 2.2579(10)-2.0110(17) Å for **5**-**7**. The reported angles for N–M–N motif in **5**-**7**, ranging from 95.37(7)° for **5** to 98.69(8)° for **7**, are more expansive than detected for the **1**-**4** series and about 20° wider than the ideal N–M–N angle of 76-78° in $Co(N_2R_2)_2$ complexes.[121] For **5** and **6**, the metal center and the ligand backbone are located in a plane. However, for **7**, a folding angle between the oxazole moieties (9.67(9)°) is present.

3.3.3. Magnetic properties of [(thf)$_n$M^{II}Cl{(4-benzhydryl-NCOC$_6$H$_3$)$_2$CH}]

First, acquiring direct current (dc) measurements in a magnetometer allowed us to determine the molar susceptibility χ_M. The temperature dependency of $\chi_M T$ is presented below, and all complexes were found to be paramagnetic (**Figure 3.8.**). The high-temperature values of $\chi_M T$ for the manganese and iron complexes are in good alignment with the expected spin-only values (4.41 and 2.99 cm^3 mol^{-1} K), while the calculated values are 4.30 and 3.00 cm^3 mol^{-1} K. **7** shows a higher $\chi_M T$ value (2.82 cm^3 mol^{-1} K) than the spin-only system of $S = 3/2$ (1.875 cm^3 mol^{-1} K), indicating a substantial orbital contribution, which is typical for such cobalt(II) complexes.[121,141] The $\chi_M T$ values of **5** and **6** are stable while decreasing the temperature and quickly decay below 10 K, while **7** decreases below 50 K.

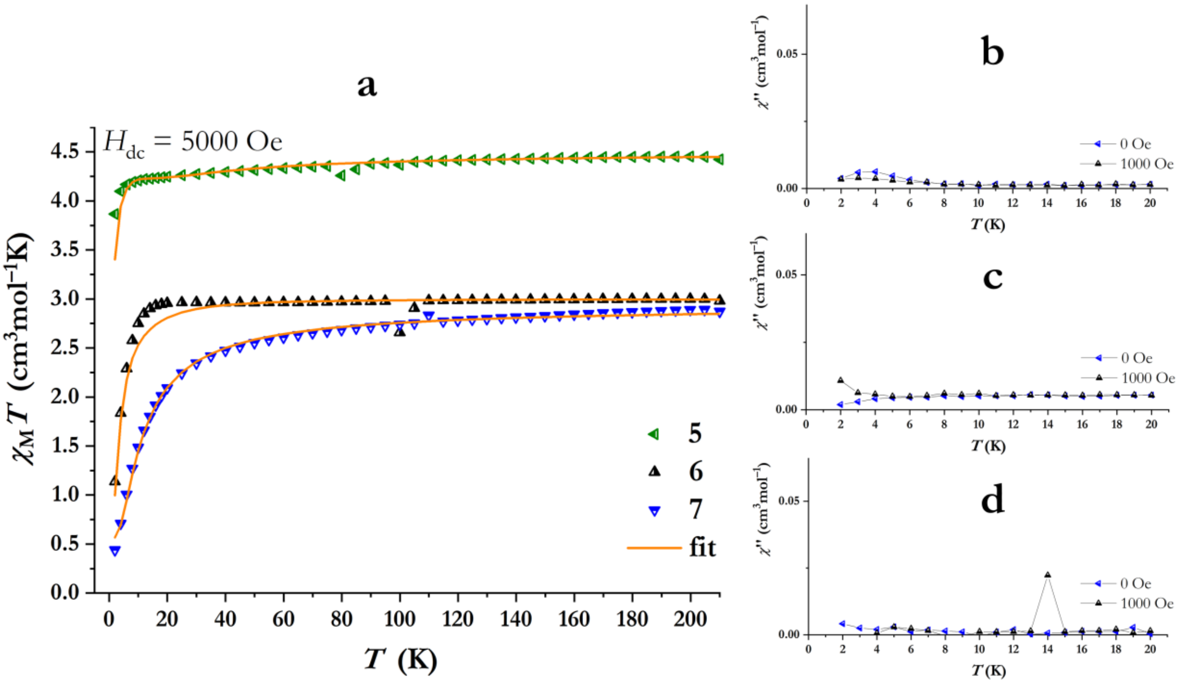

Figure 3.8. (**a**) Temperature-dependency of $\chi_M T$ for [(thf)$_n$M^{II}Cl{(4-benzhydryl-NCOC$_6$H$_3$)$_2$CH}] with M = Mn^{II} (**5**), Fe^{II} (**6**) (n = 2), and Co^{II} (**7**) (n = 1) from 210 to 2 K.. The corresponding fits were performed with the JulX-2s program.[131] (**b**-**d**) Temperature-dependency of the χ'' response with and without a dc field at a frequency of 1000 Hz for **5** (**b**), **6** (**c**), and **7** (**d**).

Next, conducting variable field variable temperature data (VTVH) enabled a simultaneous fit employing the JulX-2s program.[131] In order to receive accurate values for the static magnetic parameters, the corresponding spin Hamiltonian was applied (see chapter 3.2.2).[132]

All ZFS parameters for **5**-**7** had positive values, leading to a flipped double-well potential and no effective energy barrier (**Figure 1.3.f**).[133] Complex **6** is most accurately described with isotropic *g* values ($g_x = g_y = g_z$) (**Table 3.10.**). The best fit for the manganese and cobalt compounds **5** and **7** was achieved with anisotropic *g* values ($g_x \approx g_y < g_z$) (**Table 3.10.**). Subsequent measurements of the ac susceptibility at zero dc field and under an applied dc field were performed to probe for SMM behavior. None of these complexes (**5**-**7**) exhibited maxima for the out-of-phase susceptibility χ'' neither with nor without a dc field in the temperature range from 2 to 20 K.

Table 3.10. Selected experimental magnetic data for **5**-**7**.

		D (cm^{-1})	E/D	$g_{x,y,z}$	U_{eff} (cm^{-1})	τ_0 (s)
5	[(thf)$_2$MnCl(4-benzhydryl-NCOC$_6$H$_3$)$_2$CH]	1	0.3	1.92, 1.92, 2.40	–	–
6	[(thf)$_2$FeCl(4-benzhydryl-NCOC$_6$H$_3$)$_2$CH]	8.7	0.09	2.12	–	–
7	[(thf)CoCl(4-benzhydryl-NCOC$_6$H$_3$)$_2$CH]	26.9	0.08	2.30, 2.30, 2.81	–	–

3.3.4. Summary and concluding remarks for $[(thf)_nM^{II}Cl(L_2)]$ (5-7)

Within this chapter, three d-metal complexes featuring the bis(4-benzhydryl-benzoxazol-2-yl)methanide ligand are fully characterized via NMR, MS, SC-XRD, and SQUID techniques. Initially, isostructural complexes to the $[(thf)_nM(\mathbf{L_1})_2]$ series (**1**-**4**) were envisioned. Nevertheless, the monomeric complexes $[(thf)_nMCl(\mathbf{L_2})]$ were always isolated. This observation is most likely attributed to the steric of the benzhydryl groups that shield the metal center and prevent the substitution of the second halide with another $\mathbf{L_2}$ ligand. Subsequent magnetic measurements illustrated the absence of SMM behavior in all three complexes. Therefore, future experiments should evaluate other Box systems with less sterically demanding substituents. The next chapter investigates the *tert*-butyl substituted Box ligand.

3.4. Excursus: Bis(4,6-*tert*-butyl-benzoxazol-2-yl)methanide based d-metal complexes

Major parts of this chapter have been published in the bachelor thesis of Oliver Mönner in ***2021****.*

3.4.1. Ligand and precursor synthesis

In cooperation with O. Mönner,[142] the bis(4,6-*tert*-butyl-benzoxazol-2-yl)methane ligand was prepared according to established procedures from KÖHNE and STALKE.[80] Starting from the 3,5-di-*tert*-butylphenol, an electrophilic aromatic substitution is facilitated via a standard nitration agent (**Scheme 3.7.**). Subsequent reduction of the nitro group with pure hydrogen resulted in the 3,5-di-*tert*-butyl-2-aminophenol in high yield. The general cyclocondensation reaction of an ethylbisimidate dihydrochloride linker with 2 equiv. of the 3,5-di-*tert*-buytlphenol gave $\mathbf{L_3}$ (***t*****Bubox**)(**Scheme 3.7.**).

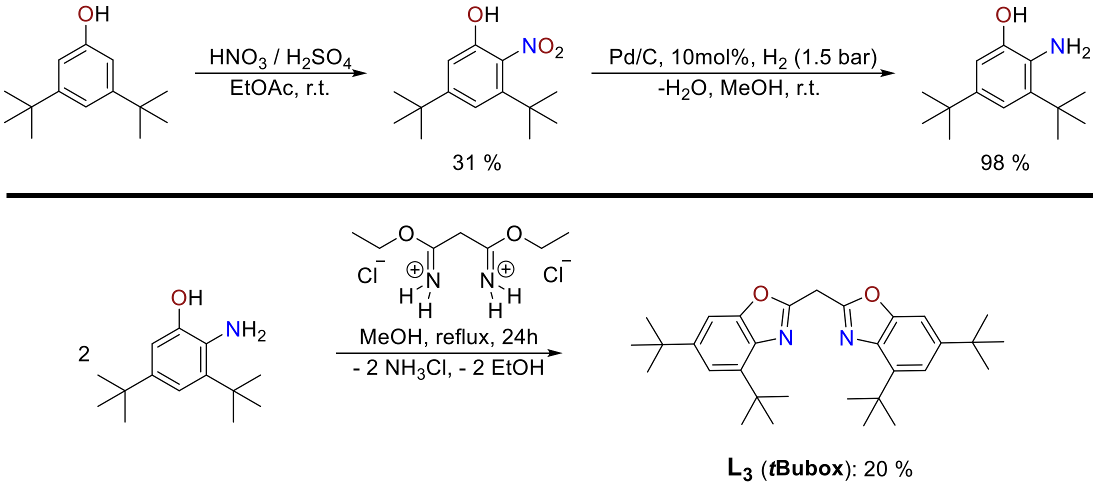

Scheme 3.7. (**top**) Synthesis of 3,5-di-*tert*-butyl-2-aminophenol from 3,5-di-*tert*-buytlphenol. (**bottom**) Preparation of bis(4,6-*tert*-butyl-benzoxazole-2-yl)methane ($\mathbf{L_3}$) from 2-aminophenol and the bisimidate linker in methanol.[96]

3.4.2. Synthesis and solid-state structures of $[(\mathrm{thf})_2\mathrm{Mn^{II}Cl}\{(4,6\text{-}t\mathrm{Bu\text{-}NCOC_6H_2})_2\mathrm{CH}\}]$

In order to prepare transition metal complexes, the ligand was first deprotonated via potassium hydride, as described in the work of KÖHNE and STALKE.[96] Then, 1 equiv. of the deprotonated ligand $\mathbf{L_3}$ was treated with 1 equiv. of manganese chloride in thf, forming complex **8** in high yield. Precipitated potassium chloride and unreacted solids were removed via filtration (**Scheme 3.8.**).

Yellow, plate-shaped crystals suitable for SC-XRD experiments were obtained for **8** from a saturated toluene solution at 238 K. Despite the employed stoichiometry, the structural analysis unveiled a complex consisting of a single divalent Mn^{2+} cation coordinated ion an *N*,*N*'-chelating fashion by one *t*Bubox ligand, two thf moieties and one chloride (**Figure 3.9.**). Again, the correct molar ratio (1:2) for forming a dimeric complex did not result in $[M(\mathbf{L_3})_2]$ complexes. Only the monomeric complex $[(thf)_2MCl(\mathbf{L_3})]$ was isolated, which is in agreement with the observations for the benzhydryl substituted Box ligand (chapter 3.3.) The coordination pattern of **8** is different than for the related transition metal Box complexes $[(thf)_nM^{II}(\mathbf{L_1})_2]$ (**1**-**4**) that coordinate two Box ligands. The asymmetric unit of **8** illustrates one complex molecule and one lattice toluene moiety with the monoclinic space group $P2_1/n$. The Mn–N distance (2.1873-2.1926(16) Å) is slightly longer as recorded for the $[(thf)Mn(\mathbf{L_1})_2]$ (**1**), and the N–Mn–N angle (98.61°) is less acute than for **1**, but within the range of related complexes.[143] Both oxazole moieties are twisted by an angle of 6.30(11)°, while the manganese ion is almost in-plane with the C_3N_2 moiety (**Table 3.11.**).

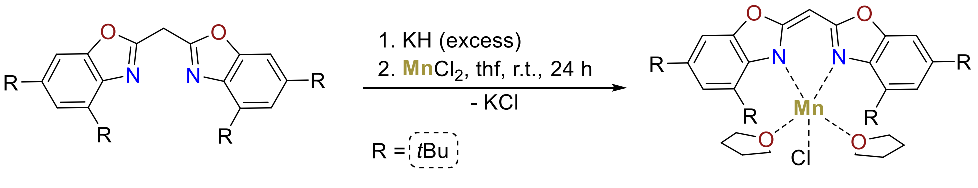

8: 42 %

Scheme 3.8. Synthesis of $[(thf)_2ClMn(\mathbf{L_3})]$ (**8**) in thf. First, Ligand $\mathbf{L_3}$ is deprotonated via potassium hydride, and second, a metathesis reaction with $MnCl_2$ gives complex **8**. Despite the stoichiometry, in **8** only one *t*Bubox ligand coordinates to the manganese ion.

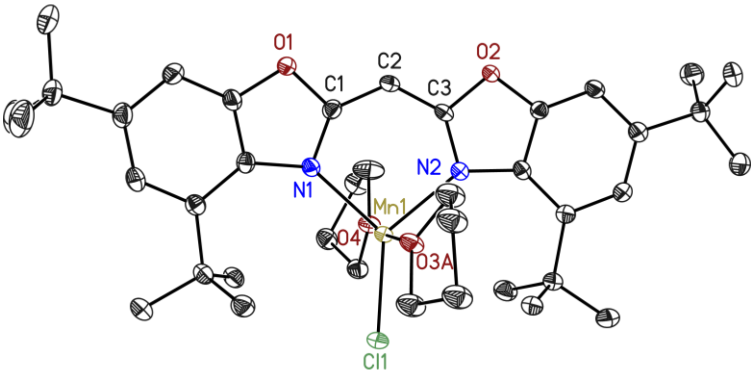

Figure 3.9. Solid-state structure of $[(thf)_2MnCl\{(4,6\text{-}t\text{Bu-NCOC}_6H_2)_2CH\}]$ (**8**). Thermal ellipsoids are displayed at a probability level of 50%. The hydrogen atoms and lattice solvent molecules are omitted for clarity.

Table 3.11. Selected bond lengths [Å] and angles [°] for complex **8**.

	$N–Mn_{range}$	$N–Mn–N_{range}$	Folding angles	$M\cdots C_3N_2$ plane
1	2.1873(16)- 2.1926(16)	98.61	6.30(11)	0.04(2)

3.4.3. Magnetic properties of $[(thf)_2Mn^{II}Cl\{(4,6\text{-}t\text{Bu-NCOC}_6H_4)_2CH\}]$

The molar susceptibility χ_M was recorded from 2 to 210 K and plotted as $\chi_M T$ vs. T (**Figure 3.10.**). The high-temperature value of $\chi_M T$ for **8** (2.88 $cm^3\ mol^{-1}$ K) differs from the expected spin-only values of 4.38 $cm^3\ mol^{-1}$ K. Various lattice solvents are present that influence the accurate molar mass and henceforth, the $\chi_M T$ values. Although, the unfavorable ligand geometry might explain these deviations. Applying eq. **3-2** in the JulX-2s software afforded the corresponding fit.[131] Further, the best fit was achieved with anisotropic g values ($g_x \approx g_y < g_z$) and a positive axial zero-field splitting parameter D, indicating the absence of SMM behavior (**Table 3.12.**). More insight into whether SMM behavior is present or not was accomplished via an oscillating ac field, scanning low-temperature regions at various frequencies. As expected from the dc data, no maxima in the out-of-phase susceptibility were detectable without or with a dc field (**Figure 3.10.b**).

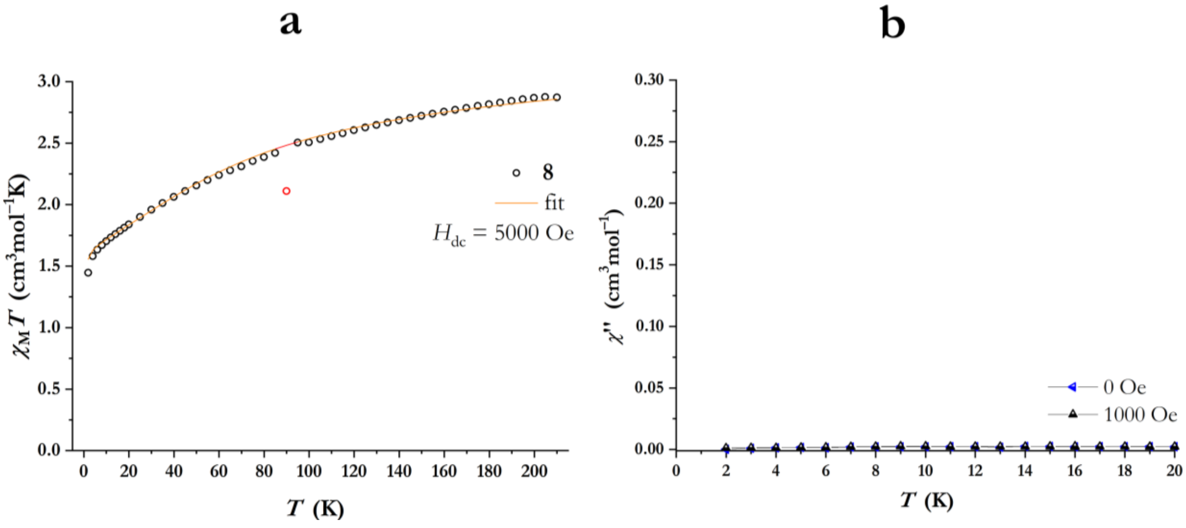

Figure 3.10. (**a**) Temperature-dependency of $\chi_M T$ for **8** from 210 to 2 K. The corresponding fit was performed with the JulX-2s program.[131] (**b**) Temperature-dependency of the χ'' response with and without a dc field at a frequency of 1000 Hz for **8**.

Table 3.12. Selected experimental magnetic data for **8**.

		D (cm^{-1})	E/D	$g_{x,\,y,\,z}$	U_{eff}	τ_0 (s)
8	$[(thf)_2MnCl(t\text{Bubox})_2]$	77.80	0.01	1.63, 1.63, 2.0	–	–

3.4.4. Summary and concluding remarks for $[(thf)_2Mn^{II}Cl\{(4,6\text{-}t\text{Bu-NCOC}_6H_2)_2CH]$

The manganese complex **8** was fully characterized by NMR, MS, SC-XRD, and SQUID techniques. Synthetic attempts to introduce two *t*Bubox ligands to an Mn^{II} metal center failed, despite the correct stoichiometries (1:2), and resulted in the reported complex. Assuming similar reasons as discussed in chapter 3.3.4. However, to retrieve magneto-structural correlations, isostructural transition metal complexes to the d-Box and d-Mebox series are required. The remaining chlorido ligand also hampers the magnetic performance. Henceforth, no further efforts were made to characterize the missing transition metal complexes containing $\mathbf{L_3}$. The following chapters will shed light on lanthanide Box ($\mathbf{L_1}$) and Mebox ($\mathbf{L_4}$) complexes.

3.5. Bis(benzoxazol-2-yl)methanide (L_1) based f-metal complexes

Major sections of this paragraph have been published in:

[2] D. Lüert, R. Herbst-Irmer, D. Stalke, *Eur. J. Inorg. Chem.* **2021**, 5085-5090.

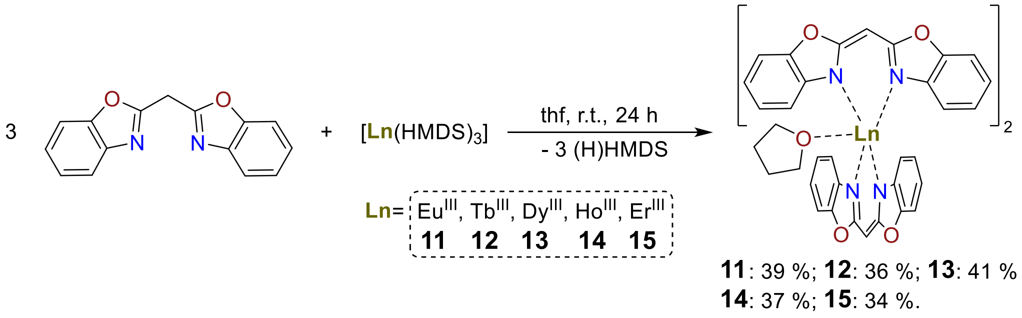

Parts of this illustration are reproduced from Ref.[2]

3.5.1. Precursor synthesis and characterization

The bis(benzoxazole-2-yl)methanide (**L$_1$**) ligand was synthesized as stated in chapter 3.2.1. Next, the trivalent lanthanide hexamethyldisilazanide salts Ln(HMDS)$_3$ were prepared using a modified procedure of HART and BRADLEY (**Scheme 3.9.**).[144] Therefore, the KHMDS salt was treated with the corresponding Ln(III)-chloride in thf (**Scheme 3.9.**). Next, the formed [Ln(HMDS)$_3$] complexes were extracted in *n*-pentane and sublimated twice at 443 K and 5·10^{-2} mbar, while their yield is in the expectancy range of prior procedures.[144] Since this complex family was first reported and characterized in the early 1970s, one might assume that all solid-state structures are well-known nowadays.

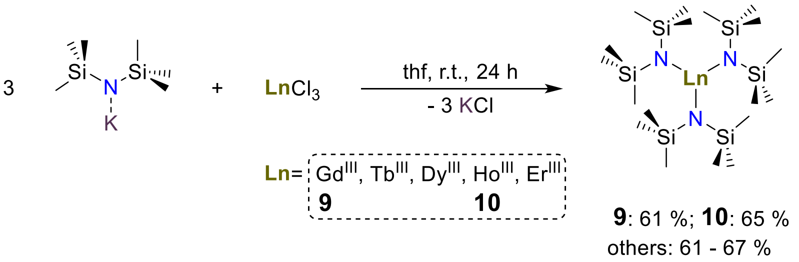

Scheme 3.9. Synthesis of [Ln(HMDS)$_3$] with [K(HMDS)] and Ln(III)-chloride in thf. Only complexes **9** and **10** have not been described in the solid-state. Reprinted with permission from Ref.[2]

Table 3.13. Crystallographic details for all published and newly determined [Ln(HMDS)$_3$] structures.

	Space group	*a* (Å)	*b* (Å)	*c* (Å)	*T* (K)	Ln–N (Å)	Ln···N$_3$ plane
Ce[145]	$P\bar{3}1c$	16.3243(4)	16.3243(4)	8.2873(2)	173	2.320	0.310
Nd[146]	$P\bar{3}1c$	16.476(13)	16.476(13)	8.485(7)	295	2.29	0.34
Sm[147]	$P\bar{3}1c$	16.4735(7)	16.4735(7)	8.3995(5)	203	2.258	0.49
Eu[148]	$P\bar{3}1c$	16.48	16.48	8.41	295	2.259	0.04
Gd[2]	$P\bar{3}$	16.301(3)	16.301(3)	8.313(2)	100	2.252	0.598
Tb[149]	$P\bar{3}1c$	16.3765(15)	16.3765(15)	8.3493(8)	173	2.232	0.604
Tb[2]	$P\bar{3}$	16.368(3)	16.368(3)	8.320(2)	100	2.245	0607
Dy[150]	$P\bar{3}1c$	16.403(7)	16.403(7)	8.464(4)	295	2.215	0.522
Dy[2]	$P\bar{3}$	16.256(3)	16.256(3)	8.328(2)	100	2.226	0.594
Ho[2]	$P2_1/n$	8.302(2)	27.999(8)	16.275(4)	100	2.230	0.597
Er[150]	$P\bar{3}1c$	16.373(2)	16.373(2)	8.491(1)	295	2.211	0.578
Tm[151]	$P2_1/n$	8.310(1)	28.077(1)	16.271(1)	123	2.199	0.649
Yb[152]	$P\bar{3}1c$	16.364(4)	16.364(4)	8.536(6)	293	2.183	0.522
Lu[153]	$P\bar{3}1c$	16.166(1)	16.166(1)	8.231(1)	100	2.191	0.648

However, the [Gd(HMDS)$_3$] (**9**) and the [Ho(HMDS)$_3$] (**10**) are the ones that have not been described in the solid-state yet. Hence, we conducted SC-XRD experiments to file the missing data. Interestingly, all lanthanide(III) [Ln(HMDS)$_3$] complexes are isostructural but not isomorphous. Both **9** and **10** form colorless needles, and the former crystallizes in the trigonal space group $P\overline{3}1c$, while the latter displays the monoclinic space group $P2_1/n$. The asymmetric unit for **9** shows 1/3 of the complex molecule, while **10** displays an entire molecule in their asymmetric unit (**Figure 3.11.**). Both feature a severe disorder of the lanthanide center. Among all previously reported structures, the trigonal space group dominates, and only for the thulium compound, a monoclinic system was found.[151] Moreover, most data sets were recorded at room temperature. Therefore, we recorded low-temperature data for [Tb(HMDS)$_3$] and [Dy(HMDS)$_3$]. Both remain in their trigonal crystal system but illustrate a slightly different space group ($P\overline{3}$ vs. $P\overline{3}1c$). Global trends are present from the Ce(III) to the Lu(III) complex (**Table 3.13.**). First, the Ln–N distance decreases from 2.320 to 2.191 Å, and second, the dislocation of the lanthanide from the N$_3$ plane increases from 0.310 to 0.648 Å. In summary, these results identified a second example for a monoclinic space group ([Ho(HMDS)$_3$], **10**) among all [Ln(HMDS)$_3$] and suggest a space group transition upon a temperature gradient.

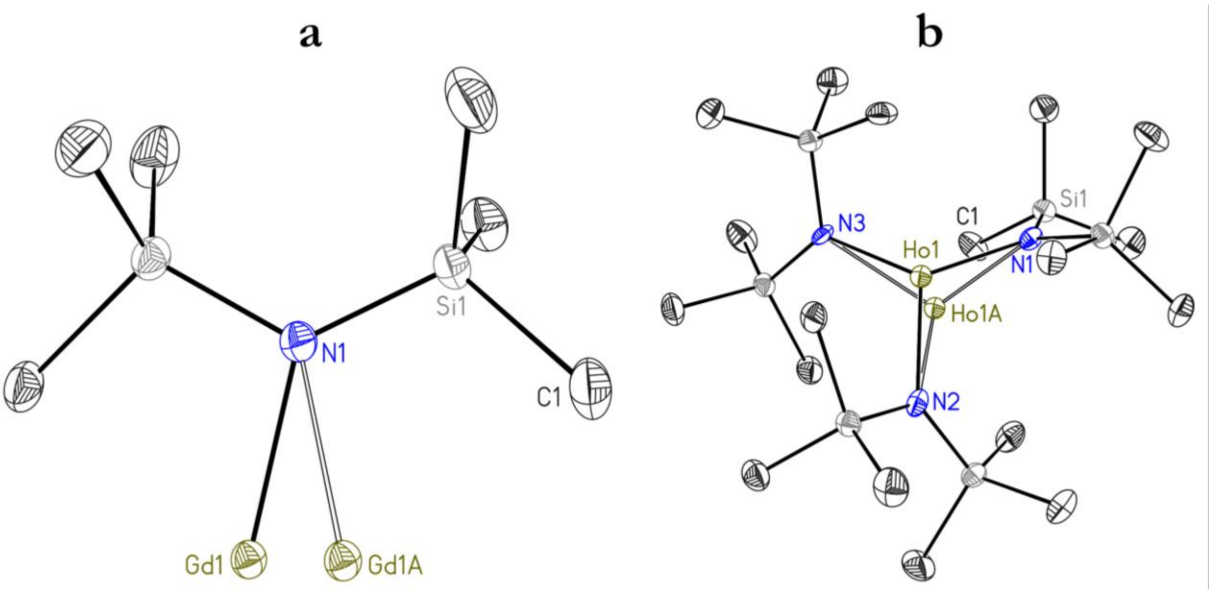

Figure 3.11. (**a**) The asymmetric unit of [Gd(HMDS)$_3$] (**9**), with 1/3 of the complex molecule. (**b**) The asymmetric unit of [Ho(HMDS)$_3$] (**10**) contains one entire molecule. Thermal ellipsoids are displayed at a probability level of 50%. The hydrogen atoms and lattice solvent molecules are omitted for clarity. Reprinted with permission from Ref.[2]

3.5.2. Synthesis and solid-state structures of [(thf)Ln^{III}{(NCOC$_6$H$_4$)$_2$CH}$_3$] (11-15)

The bis(benzoxazole-2-yl)methanide ligand devoted as Box (**L$_1$**) was prepared in accordance with established procedures (chapter 3.2.1). The lanthanide complexes [(thf)Ln^{III}{(NCOC$_6$H$_4$)$_2$CH}$_3$] (**11**-**15**) were available upon direct deprotonation of the Box ligand with the corresponding [Ln(HMDS)$_3$] salts (**Scheme 3.10.**). Formed H(HMDS) was removed under reduced pressure, and the resulting complexes were obtained in moderate yields ranging from 34 to 41 %.

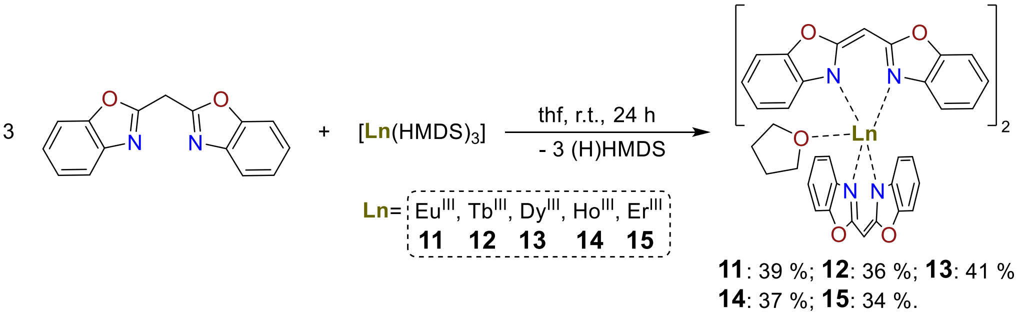

Scheme 3.10. Synthesis of [(thf)Ln^{III}{NCOC$_6$H$_4$)$_2$CH}] (**11**-**15**) in moderate yields from [Ln(HMDS)$_3$] and **L$_1$** in thf.

Blue (**11**) and yellow green (**12**-**15**) block-shaped crystals suitable for SC-XRD experiments were attained from slow evaporation of *n*-pentane into a saturated thf solution at 243 K after 24h. All complexes crystallize isomorphously in the monoclinic space group $P2_1/c$. One complex molecule and two lattice thf molecules are found in the asymmetric unit. The structure motif of **11**-**15** comprises a central trivalent Ln^{3+} cation (Ln = Eu (**11**), Tb (**12**), Dy (**13**), Ho (**14**), Er (**15**)) and three negatively charged ligands that coordinate in an *N,N'*-chelating fashion. Additionally, one thf moiety is bonded to the lanthanide center (**Figure 3.12.a**). Solvent-free complexes are accessible by avoiding thf and following the procedure above with toluene. The corresponding dysprosium analogue **13'** is depicted in the crystallographic section (chapter 6.5.14.). Lastly, the sulfur analogue (NCSC$_6$H$_4$)$_2$CH to (NCOC$_6$H$_4$)$_2$CH (**L$_1$**) was also treated with the [Ln(HMDS)$_3$] salts. These complexes did not crystallize, and only the [Er^{III}{(NCSC$_6$H$_4$)$_2$CH}$_3$] (**16**) complex was successfully isolated. Therefore, all analysis data are only reported in the experimental section (chapter 5.3.16).

The Ln–N distance trend for [(thf)Ln^{III}{NCOC$_6$H$_4$)$_2$CH}$_3$] (**11**-**15**) is in alignment with the decreasing ionic radii from Eu^{III} to Er^{III} (**Table 3.14.**). Interestingly, the lanthanides coordinated almost equidistantly for the N3/N4 ligand, while the other two ligands illustrated deviations in their Ln–N bond lengths. For the N(1)C(2)N(2) unit, the longest Ln–N bond lengths are recorded, increasing from 2.440(2) Å for **15** to 2.503(2) Å for **11**, respectively. Further, the lanthanide centers are elevated from the C$_3$N$_2$ plane, which is most substantial for the N(1)C(2)N(2) unit, ranging from 1.308(4) to 1.265(3) Å for **11**-**15**. All Ln–N(3) bonds exhibit the smallest bond lengths, decreasing from 2.450(9) to 2.390(2) Å. The least dislocation of the metal ion from the C$_3$N$_2$ plane is examined for the N(5)C(8)N(6) unit, ranging from 0.481(4) to 0.434(4) Å from Eu(1) to Er(1). Characteristic for Box ligands is the folding angle between both benzoxazole moieties that differs from ideal planarity. Again, the most prominent angles are determined for the N(1)C(2)N(2) unit, ranging from 17.30(9) (**11**) to 20.48° (**15**). The smallest folding angles of 7.48 to 7.69° for **11**-**15** correlate with the shortest Ln–N distances at the N(3)C(5)N(4) unit.

Juxtaposing the C(1)-C(2) bond lengths of ligand $\mathbf{L_1}$ with the deprotonated ligand $\mathbf{L_1}^-$ in **11**-**15**, a decrease from 1.489(2) ($\mathbf{L_1}$) to 1.393(3)-1.386(4) Å ($\mathbf{L_1}^-$ in **11**-**15**) is detected. A contrary phenomenon occurred for the N(1)–C(1) (1.334(4)-1.337(3) Å) bonds that are elongated compared with $\mathbf{L_1}$ (1.286(2) Å). This feature has been previously described for Box systems.[91,92] Comparing the twist angles between the different ligands, the angle between the N(1)C(2)N(2) moiety and the N(3)C(5)N(4) is, on average, 29.41° for **11**-**15**. Larger angles are reported for the N(3)C(4)N(4) and the N(5)C(5)N(6) unit, ranging from 76.25(8) to 77.04(9)° and from 79.11(6) to 79.76(7)° between N(1)C(2)N(2) and N(5)C(5)N(6). NMR and mass spectrometry data are in great alignment with the solid-state data (chapters 5.3.11. to 5.3.15.)

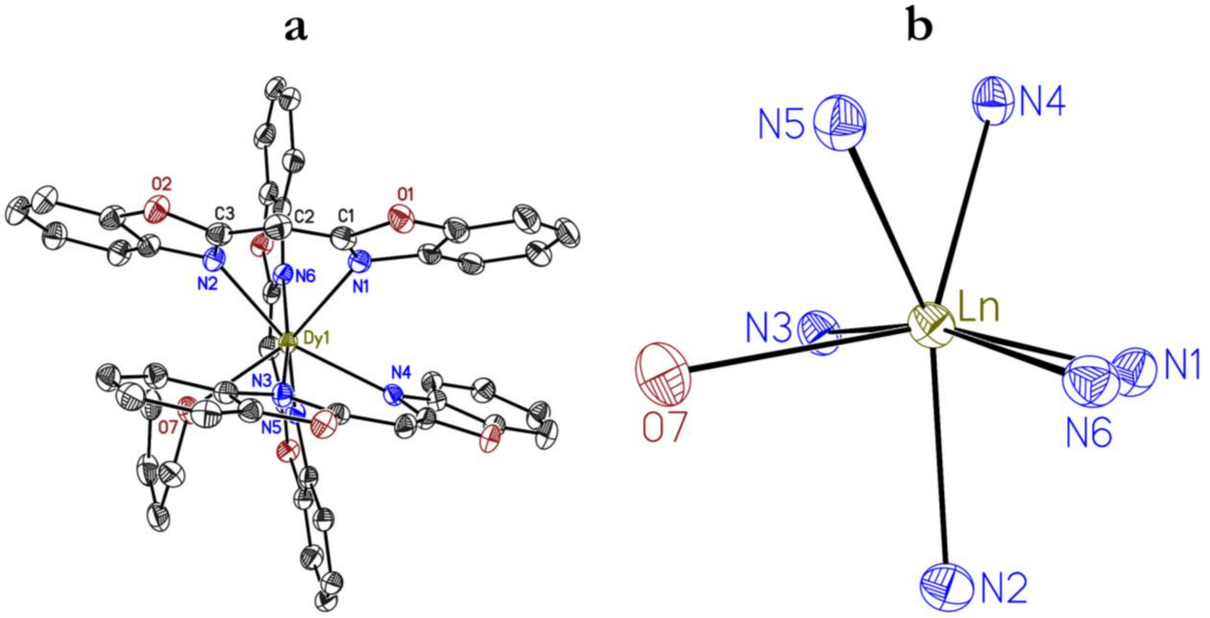

Figure 3.12. (**a**) The solid-state structure of [(thf)Dy^{III}{(NCOC$_6$H$_4$)$_2$CH}$_3$] (**13**), complexes **11**-**15** are isostructural and displayed in the crystallographic section (chapters 5.3.11 to 5.3.15). Thermal ellipsoids are displayed at a probability level of 50%. The hydrogen atoms and lattice solvent molecules are omitted for clarity. (**b**) Coordination polyhedron of the lanthanide centers with Ln (Ln = Eu^{III} (**11**), Tb^{III} (**12**), Dy^{III} (**13**), Ho^{III} (**14**), and Er^{III} (**15**)), while all non-coordinating atoms are omitted for clarity. Reprinted with permission from Ref.[2]

Table 3.14. Selected bond lengths [Å] and angles [°] for [(thf)Dy^{III}{$(NCOC_6H_4)_2CH$}$_3$] (**11**-**15**).

	Ln = Eu (**11**)	Ln = Tb (**12**)	Ln = Dy (**13**)	Ln = Ho (**14**)	Ln = Er (**15**)
Ln–N(1)	2.503(2)	2.480(2)	2.474(2)	2.460(2)	2.440(2)
Ln–N(2)	2.468(2)	2.448(2)	2.432(2)	2.429(2)	2.411(2)
Ln···C_3N_2 plane[a]	1.308(4)	1.285(3)	1.279(3)	1.276(3)	1.265(3)
Ln–N(3)	2.450(2)	2.430(2)	2.416(2)	2.404(2)	2.390(2)
Ln–N(4)	2.453(2)	2.434(2)	2.417(2)	2.414(2)	2.396(2)
Ln···C_3N_2 plane[b]	0.576(4)	0.545(3)	0.546(3)	0.541(3)	0.541(4)
Ln–N(5)	2.449(2)	2.431(2)	2.413(2)	2.414(2)	2.396(2)
Ln–N(6)	2.464(2)	2.444(2)	2.425(2)	2.420(2)	2.405(2)
Ln···C_3N_2 plane[c]	0.481(4)	0.457(3)	0.441(4)	0.446(3)	0.434(4)
Ln–O(7)	2.501(2)	2.495(2)	2.487(2)	2.477(2)	2.460(2)
N1-C2-N2[d]	17.30(9)	18.89(8)	18.77(8)	19.64(7)	20.48(8)
N3-C5-N4[d]	7.66(11)	7.48(10)	7.64(10)	7.61(9)	7.69(11)
N5-C8-N6[d]	10.47(9)	10.55(8)	10.62(8)	10.38(7)	10.19(9)
Twist angles[e]					
N(1)N(2)C(2)-N(3)N(4)C(5)	28.77(14)	29.67(13)	29.45(13)	29.56(11)	29.58(14)
N(3)N(4)C(4)-N(6)N(5)C(8)	77.04(9)	76.25(8)	76.45(8)	76.37(7)	76.56(9)
N(1)N(2)C(2)-N(6)N(5)C(8)	79.17(7)	79.11(6)	79.36(6)	79.33(5)	79.76(7)

[a] Deviation of Ln^{III} from N(1)C(2)N(2) plane; [b] Deviation of Ln^{III} from N(3)C(5)N(4) plane; [c] Deviation of Ln^{III} from N(3)C(5)N(4) plane; [d] Folding angle for corresponding Box unit; [e] Angles between the three ligand moieties.

3.5.3. Magnetic properties [(thf)Ln^{III}{$NCOC_6H_4)_2CH$}$_3$]

The previous chapters focused on transition metal complexes, which could be operated as air-stable benchmark systems. However, lanthanides usually outperform the magnetic properties of d-metal systems due to higher numbers of unpaired electrons, unquenched orbital angular momenta, and large intrinsic anisotropies. The interested reader is referred to the general introduction section (chapter 1.5.). Therefore, we were fueled to study the lanthanide analogues of this ligand scaffold. Magnetic measurements of direct current (dc) magnetic susceptibility as a product of the temperature ($\chi_M T$) are plotted versus the temperature (**Figure 3.13.**). At high temperature, $\chi_M T$ ($cm^3\ mol^{-1}\ K$) exhibits values of 11.89 for **12**, 13.80 for **13**, 13.70 for **14**, and 11.91 for **15**, where the calculated ones for the free ions are 11.82 for **12**, 14.17 for **13**, 14.07 for **14**, and 11.48 for **15**.[14] Except for the terbium and erbium compounds **12** and **15**, the measured $\chi_M T$ values are lower than the calculated ones but still within the range of related lanthanide(III) complexes. [14,20b,25,39,55,154] Since the crystal field splitting magnitude is comparably small in lanthanides (**Figure 1.6.**) and the M_J states are statistically populated at high temperatures, the free-ion approximation is generally valid. When T slowly decreases, this approximation becomes less and less accurate as higher energy levels

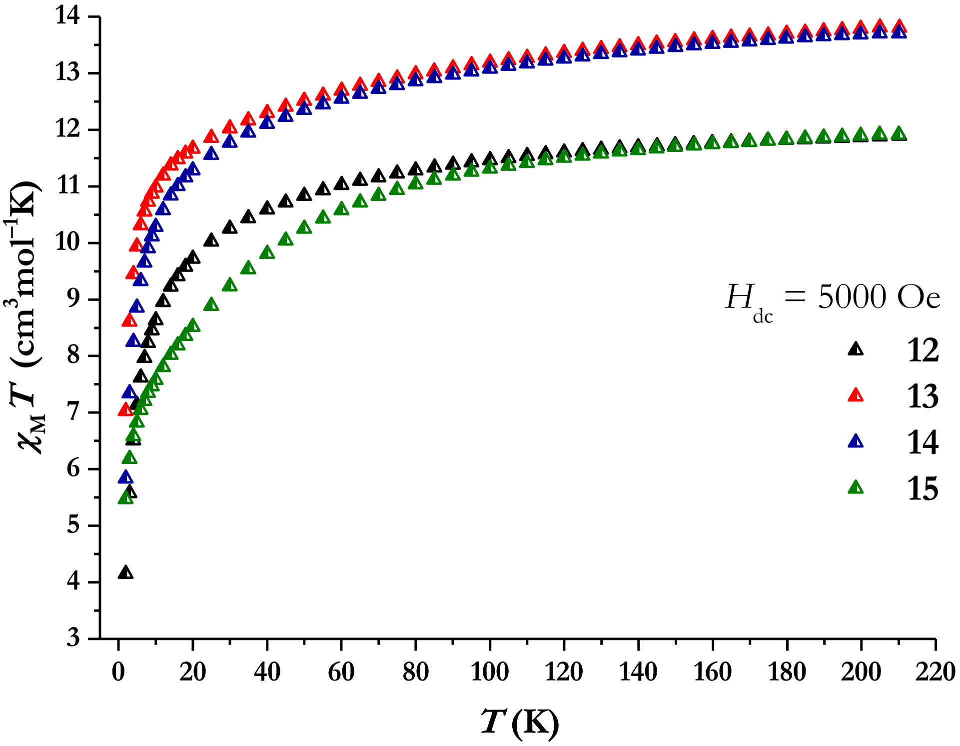

Figure 3.13. Temperature-dependency of $\chi_M T$ for [(thf)Ln^{III}\{(NCOC$_6$H$_4$)$_2$CH\}$_3$] with Ln^{III} = Eu^{III} (**11**), Tb^{III} (**12**), Dy^{III} (**13**), Ho^{III} (**14**), Er^{III} (**15**) under an applied field of H_{dc} = 5000 Oe.

are successively depopulated. Two direct consequences occur from this behavior: First, the anisotropy of the system rises upon cooling, and second, $\chi_M T$ no longer follows the Curie law.[19b] Here, the above-described phenomena are present; the product of $\chi_M T$ is first slightly reduced when the temperature is slightly decreased to 40 K. Below 40 K, the decrease is sharper until it reaches 4.15 (**12**), 7.03 (**13**), 5.84 (**14**), and 5.47 (**15**) cm^3 mol^{-1} K at 2 K, respectively.

Further, to probe for SMM behavior, measurements of the magnetic susceptibility at a dynamic alternating current (ac) field of 3 Oe were performed for **12** to **15**. For none of the four complexes, a drop of χ' and the presents of χ'' signals were detected under a zero dc field. Consequently, these complexes either exhibit no SMM behavior above 2 K or under the barrier processes such as quantum tunneling of magnetization (QTM) are arising. Therefore, to inhibit QTM fully or to some extent, an additional dc field of 1000 Oe was applied during the ac measurements. Unfortunately, also these conditions did not result in the presence of SMM behavior. The magnetic data can be retrieved from the supporting information of Ref.[2]. The europium complex **11** was not probed for SMM behavior as the non-Kramers ion Eu^{III} has a non-magnetic ground state $^7F_0$, and no SMM behavior has previously been reported for this lanthanide.[19b,55] Previously reported SIMs featuring an ideal pentagonal bipyramidal (D_{5h}) geometry demonstrate promising SMM behavior.[56,60] Their general structure motif includes axial ligands located on the main magnetic axes and equatorial ligands assembled in a pseudo-5-fold symmetry.[56]

Table 3.15. Continuous Shape Measures (CShMs) of the coordination geometry for the Ln^{3+} ion environments in **11**-**15**, retrieved from the SHAPE program, displaying the lowest residue for a capped octahedron.[140a,140b,155]

	JETPY-7[a]	JPBPY-7[b]	CTPR-7[c]	COC-7[d]	PBPY-7[e]	HPY-7[f]	HP-7[g]
11	17.907	8.321	1.664	1.264	4.616	19.993	33.021
12	17.777	8.365	1.646	1.174	4.694	20.245	33.278
13	17.841	8.155	1.608	1.223	4.525	20.527	33.277
14	17.849	8.183	1.625	1.171	4.569	20.464	33.407
15	17.962	8.082	1.614	1.173	4.456	20.631	33.474

[a] C_{3v}, Johnson elongated triangular pyramid J7; [b] D_{5h}, Johnson pentagonal bipyramid J13; [c] C_{2v}, Capped trigonal prism; [d] C_{3v}, Capped octahedron; [e] D_{5h}, Pentagonal bipyramid; [f] C_{6v}, Hexagonal pyramid; [g] D_{7h}, Heptagon.

The former results in strong stabilization of the largest M_J 15/2 doublet, while the latter causes a minimization of transversal crystal fields and effective suppressing of QTM. For example, $[Dy(Cy_3PO)_2(H_2O)_5]^{3+}$ with the tricyclohexylphospine oxide (Cy_3PO) combines both elements and is among the best-performing systems, illustrating a pentagonal bipyramidal geometry.[60c]

The SHAPE software elucidated deviations from a pentagonal bipyramidal (D_{5h}) polyhedron for **11**-**15**.[140a,140b,155] Here, a numerical evaluation is performed with the experimentally measured geometries of **11**-**15** to ideal symmetries. The obtained residues range from 0 to 100, while 0 refers to a structure entirely coincident in shape with the reference polyhedron. A capped octahedron (C_{3v}) is the most accurate description of the symmetry of **11**-**15**, as the continuous shape measures (CShMs) exhibit the lowest residues (1.171-1.264) (**Table 3.15.**). Also, neutral ligands in the equatorial sphere do not manipulate the electron density as strongly as negatively charged ligands do, and the axial anisotropy is only slightly decreased for neutral ligands. However, complexes **12**-**15** exhibit a C_{3v} symmetry, which is not beneficial for suppressing QTM as a D_{5h} symmetry and further the charged Box ligands coordinated equatorial complete with the axial anisotropy. These circumstances may explain the absence of SMM behavior.

3.5.4. Summary and concluding remarks for $[(thf)Ln^{III}\{(NCOC_6H_4)_2CH\}_3]$

The missing solid-state structures of the $[Ln(HMDS)_3]$ series for Ln = Gd (**9**) and Ho (**10**) were reported. Their subsequent Box complexes **11**-**15** were successfully synthesized and fully characterized by NMR, EA, MS, SC-XRD, and SQUID techniques. A capped octahedron is most accurate in portraying the coordination geometry of **11**-**15**, confirmed by continuous shape measures with the SHAPE software. Magnetic studies revealed the absence of SMM behavior for **12**-**15**, and conceivable reasons are examined. Enhancement of magnetic performance should be achieved with lower coordination numbers, which could be put into practice with more bulky Box ligands and the avoidance of donating solvents. Therefore, the next chapter focuses on the methyl-substituted Box ligand and derived lanthanide complexes.

3.6. Bis(4-methyl-benzoxazol-2-yl)methanide based f-metal complexes

Major sections of this paragraph have been published in:

[3] D. Lüert, A.-K. Kreyenschmidt, C. M. Legendre, R. Herbst-Irmer, D. Stalke, *Inorg. Chem.* **2022**, *61*, 5234-5244.

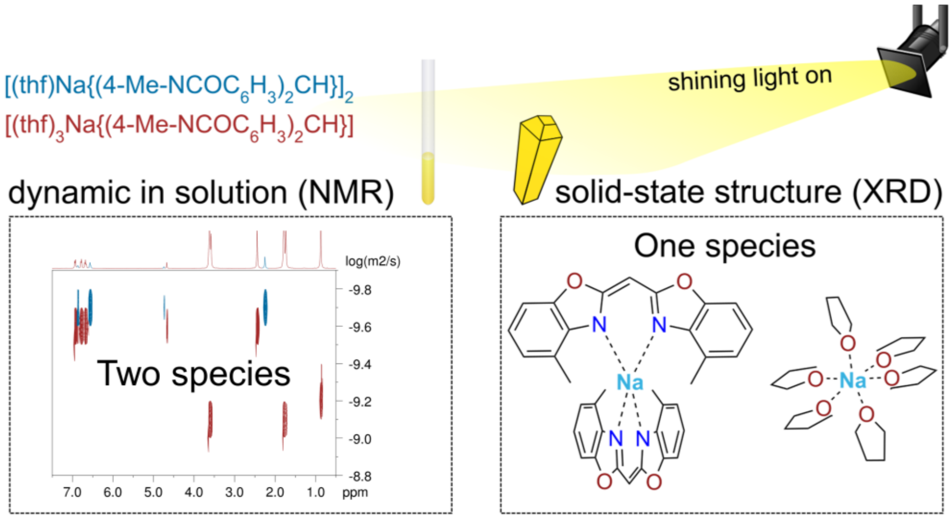

Reprinted with permission from Ref.[3], https://pubs.acs.org/doi/abs/10.1021/acs.inorgchem.1c03714. Copyright 2022 American Chemical Society.

3.6.1. Ligand and precursor synthesis and characterization

The bis(4-methyl-benzoxazole-2-yl)methanide (**L**$_4$) ligand was prepared via well-established procedures from DAUER and STALKE.[94] Again, an ethylbisimidate dihydrochloride agent links both oxazole moieties in a cyclocondensation reaction to give **L**$_4$ as reported for **L**$_1$-**L**$_3$ (**Scheme 3.11.**). Alkali metal precursors have previously been introduced with lithium and potassium for **L**$_4$. Lithium often triggers lithium-halide co-complexation in salt metathesis reactions, and potassium's ion radius is larger than the average ion radius for lanthanide ions.[156] However, sodium matches the size of the late lanthanides, and co-complexation phenomena do not occur. Therefore, the hitherto unknown sodium complex of the Mebox ligand was prepared and characterized. The [Na(thf)$_6$][Na{4-Me-NCOC$_6$H$_3$)$_2$CH}$_2$] (**17**) precursor is accessible via the treatment of ligand **L**$_4$ with Na(HMDS) in thf (**Scheme 3.12.**). Formed (H)HMDS was then removed under reduced pressure, and **17** was obtained in high yields (76 %).

Crystals of [Na(thf)$_6$][Na{4-Me-NCOC$_6$H$_3$)$_2$CH}$_2$] (**17**) suitable for X-ray diffraction experiments were acquired from a saturated thf solution at 243 K after 96 h. Huge colorless block-shaped crystals, displaying the monoclinic space group $P2_1/c$ with six solvent separated ion pairs in the asymmetric unit, were acquired for **17**. The six entities vary slightly in their bond lengths, angles, and degree of disorder. That suggests discussing the crystallographic parameter range (**Table 3.16.**). In the sodium sodate **17**, the coordination environment of each sodium ion is slightly different.

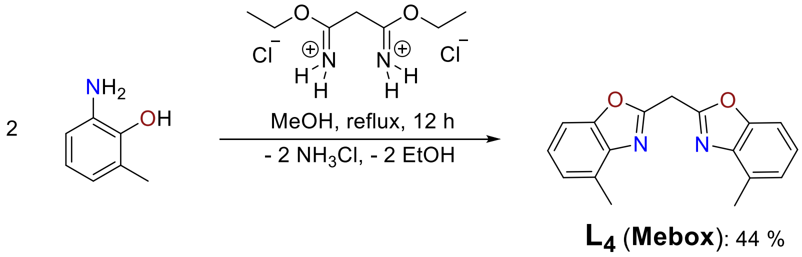

Scheme 3.11. Preparation of bis(4-methyl-benzoxazole-2-yl)methane (**L**$_4$) from 2-amino-3-methylphenol and the ethylbisimidate dihydrochloride linker in methanol.

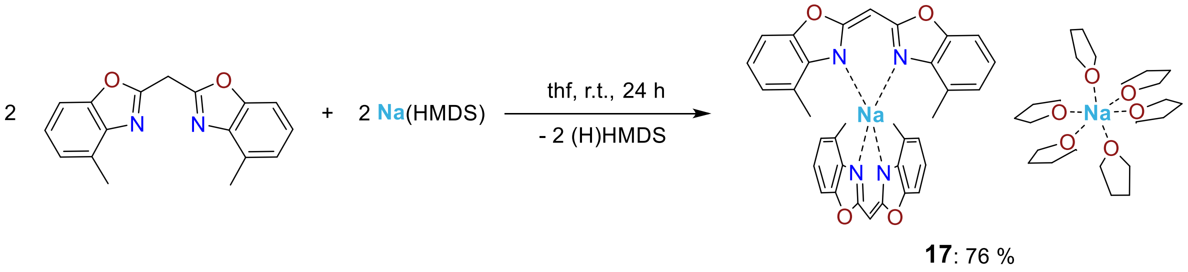

Scheme 3.12. Synthesis of [Na(thf)$_6$][Na{4-Me-NCOC$_6$H$_3$)$_2$CH}$_2$] (**17**) employing **L**$_4$ and Na(HMDS) in thf under r.t. conditions. Reprinted with permission from Ref.[3], https://pubs.acs.org/doi/abs/10.1021/acs.inorgchem.1c03714. Copyright 2022 American Chemical Society.

The first sodium ion is coordinated in a distorted tetrahedral fashion from two negatively charged Mebox ligands to provide the anion, whereas the second is bound to six thf donor molecules in a distorted octahedral fashion (**Figure 3.14.a**). Such a structural motif is unique for all known alkali metal Box derivates and marks a rare example of sodium sodates.[157] The Na–N distances range from 2.356(3) to 2.400(3) Å (ignoring discorded groups), which is in alignment with other sodium derivatives.[158] We reported a range from 82.14(9) to 83.10(9)°, which is more acute than the ideal tetrahedral angle for the N–Na–N bite angle. Next, the sodium center is dislocated from both chelating C_3N_2 planes scaling from 0.021(5) to 0.708(4) Å, respectively. Moreover, the butterfly folding angles of both benzoxazole moieties were determined (5.02(6)-18.62(11)°), and the twist angle between the Mebox ligands spans from 80.65(11) to 85.80(10)°, illustrating a slight deviation from the ideal orthogonal orientation. In the cation, the Na–O bond lengths stretch from 2.303(3) to 2.405(3) Å and is in accordance which other $[Na(thf)_6]^+$ cations.[157a–f] The previously reported $[Na(thf)_6][Li\{(2\text{-}NC_5H_4)_2CH\}_2]$ shows almost identical Na–O bond lengths (av. 2.378(2) Å) with **17**. Based on the elemental analysis data, two of the six thf molecules found in the solid-state structure are removed upon the drying procedure. Mass spectrometry data recorded a fragment of one ligand and one sodium ion at *m/z*: 301.09 (100).

Observations in the solid-state frequently differ from the behavior in the solution.[159] Therefore, the dynamic of **17** in solution was further analyzed to understand to what extent the solvent separated ion pair is maintained. For this study, the sodium analogue $[(thf)_3Na\{(NCOC_6H_4)_2CH\}]$ (**18**) with the Box ligand (**L₁**) was prepared and characterized in the same way to correlate these results.

Complex $[(thf)_3Na\{(NCOC_6H_4)_2CH\}]$ (**18**) was accessed by the equimolar reaction of **L₁** with Na(HMDS) in thf (**Scheme 3.13.**). After removal of (H)HMDS and two cycles of recrystallization, **18** was obtained in good yield (62 %).

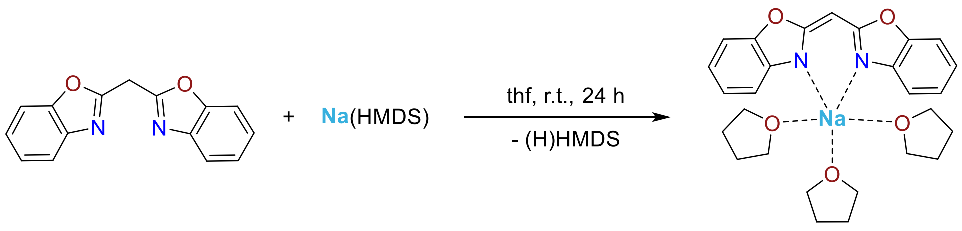

18: 62 %

Scheme 3.13. Synthesis of $[(thf)_3Na\{(NCOC_6H_4)_2CH\}]$ (**18**) from **L₁** and Na(HMDS) in thf at r.t. conditions. Reprinted with permission from Ref.[3], https://pubs.acs.org/doi/abs/10.1021/acs.inorgchem.1c03714. Copyright 2022 American Chemical Society.

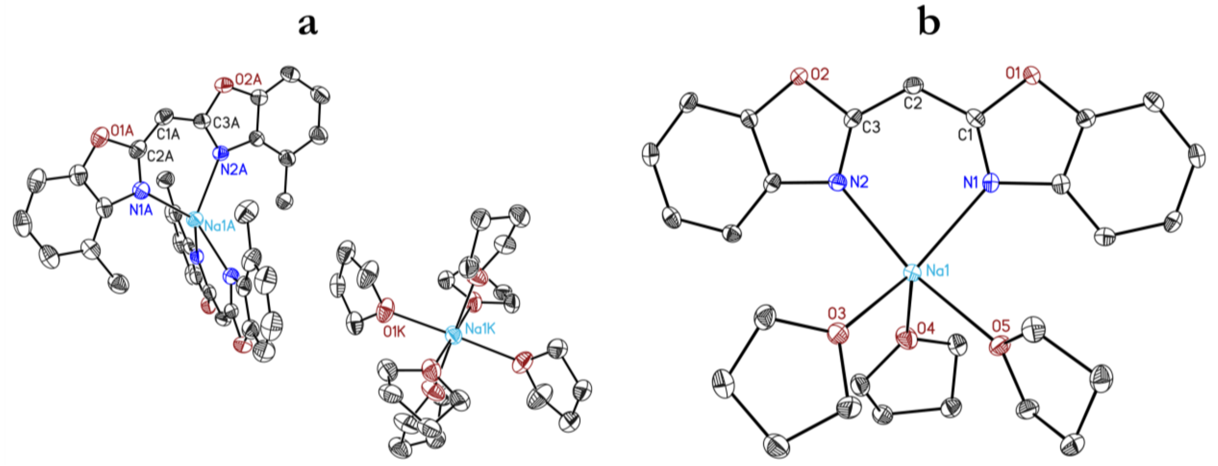

Figure 3.14. (**a**) The solid-state structure of [Na(thf)$_6$][Na{4-Me-NCOC$_6$H$_3$)$_2$CH}$_2$] (**17**), here, only one of the six complex molecules of the asymmetric unit is depicted. (**b**) The solid-state structure of [(thf)$_3$Na{(NCOC$_6$H$_4$)$_2$CH}] (**18**). Thermal ellipsoids are displayed at a probability level of 50 %. The hydrogen atoms and lattice solvent molecules are omitted for clarity. Reprinted with permission from Ref.[3], https://pubs.acs.org/doi/abs/10.1021/acs.inorgchem.1c03714. Copyright 2022 American Chemical Society.

Table 3.16. Selected bond lengths [Å] and angles [°] for [Na(thf)$_6$][Na{4-Me-NCOC$_6$H$_3$)$_2$CH}$_2$] (**17**) (disordered groups ignored) and [(thf)$_3$Na{(NCOC$_6$H$_4$)$_2$CH}] (**18**).

	Na–N$_{range}$	Na–O$_{range}$	N–O–N angle	Folding angle[a]	Na···C$_3$N$_2$[b]	Twist angles[c]
17	2.356(3)-2.400(3)	2.303(3)-2.405(3)	82.14(9)-83.10(9)	5.02(6)-18.62(11)	0.021(5)-0.708(4)	80.65(11)-85.80(10)
18	2.3958(17)-2.4191(17)	2.3121(14)-2.3698(15)	80.15(5)	14.89(6)	0.553(2)	-

[a] The angle between both benzoxazole moieties; [b] The range of dislocations of Na from the N(1)C(2)N(2) plane (**18**); the range of dislocation from the N(1)C(2)N(2) plane and N(3)C(5)N(4) plane (**17**) is listed; [c] The range of the angles between the N(1)C(2)N(2) and N(3)C(5)N(4) planes.

Pale-yellow crystals were obtained for [(thf)$_3$Na(NCOC$_6$H$_4$)$_2$CH] (**18**), and SC-XRD analysis revealed the orthorhombic space group *Pna*2$_1$ with one complex molecule in the asymmetric unit. Here, the mononuclear contact ion pair comprises a sodium *N,N'*-chelated from one negatively charged ligand moiety and three additionally coordinated thf molecules (**Figure 3.14.b**). Both Na–N bond lengths are not equidistantly and illustrate minor deviations (2.3958(17)-2.4191(17) Å) (**Table 3.16.**). These M–N$_{av.}$ values are in accordance with the prior recorded homologs with lithium (2.000 Å) and potassium (2.758 Å). Again, a dislocation of the sodium ion from the C$_3$N$_2$ plane (0.553(2) Å) is present. The ligand's typical folding angle of 14.89(6)° demonstrates the slight bend in the ligand scaffold. Both features are consistent with the lithium and potassium homologs. Subsequent elemental analysis of **18** unveiled the loss of one thf molecule during the drying procedure. Further, the corresponding MS fragment of **18** was detected at m/*z* 273.05 (100). ^{1}H- and ^{13}C-NMR data can be retrieved from the experimental section (chapters 5.3.17. and 5.3.18.) or the supporting information of the corresponding publication.

3.6.2. DOSY-NMR analysis of $[Na(thf)_6][Na\{4\text{-}Me\text{-}NCOC_6H_3)_2CH\}_2]$ (17) and $[(thf)_3Na\{(NCOC_6H_4)_2CH\}]$ (18)

The content of this paragraph is based on the measurements and analysis performed by A.-K. KREYENSCHIDT and have been published together with all other content of this chapter. The interested reader is referred to her Ph.D. thesis. Diffusion ordered NMR spectroscopy (DOSY) has flourished in recent years as a sophisticated tool to shed light on aggregation and determine molecular weights in solution.[160] For $[(thf)_3Na\{(NCOC_6H_4)_2CH\}]$ (**18**), the DOSY-ECC-based[161] analysis suggests a contact ion pair in solution, which aligns with the solid-state observation. The $\log(D_{\text{x, norm}})$ was calculated to be −9.0524 at r.t. conditions, giving a molecular weight of 397 g/mol considering the dissipated spheres and ellipsoid (DSE) geometry. This molecular weight matches the sodium Box complex with two thf molecules $[(thf)_2Na(NCOC_6H_4)_2CH]$ ($MW_{\text{diff, DSE}}$ = 5 %) (**Table 3.17.**). Repeating this measurement at higher temperatures (323 K) implies the presence of the mono-solvated species with one thf molecule $[(thf)Na(NCOC_6H_4)_2CH]$ ($MW_{\text{diff, DSE}}$ = −6 %). Furthermore, the low-temperature data (243 K) corresponds to the di-solvated species $[(thf)_2Na(NCOC_6H_4)_2CH]$ (**Figure 3.15.a**). Next, $[Na(thf)_6][Na\{4\text{-}Me\text{-}NCOC_6H_3)_2CH\}_2]$ (**17**) illustrates a $\log(D_{\text{x, norm}})$ value of −9.0717, which corresponds to the di-solvent-coordinated sodium $[(thf)_2Na(4\text{-}Me\text{-}NCOC_6H_3)_2CH]$ complex that deviates from the solid-state picture. Therefore, a separated ion pair does not exist at room temperature. Also, at high temperatures, the determined molecular weight suggests the presence of an equilibrium between the mono- and di-solvated aggregate, similar to **18**. Interestingly, at low temperatures, we detected two species (**Figure 3.15.b**). Species 2 with a ($\log(D_{\text{x, norm}})$ = −9.2125 provided an MW_{DSE} = 748 g mol^{-1} and correlates perfectly with the dimer $[(thf)Na\{(4\text{-}Me\text{-}NCOC_6H_3)_2CH\}]_2$ containing two thf molecules. Additional DOSY experiments in acetonitrile indicate also a binuclear dimer ($MW_{\text{diff, DSE}}$ = −1 %).

Table 3.17. Molecular mass calculated based on diffusion coefficients in thf for **18**, comparing different solvation aggregates at various temperatures.

	243 K	298 K	323 K
$MW_{\text{det, DSE}}$ [g mol^{-1}]	416	397	368
$[(thf)Na\{(NCOC_6H_4)_2CH\}]$	−17 %	−13 %	−6 %
$[(thf)_2Na\{(NCOC_6H_4)_2CH\}]$	0 %	5 %	13 %
$[(thf)_3Na\{(NCOC_6H_4)_2CH\}]$	17 %	23 %	33 %

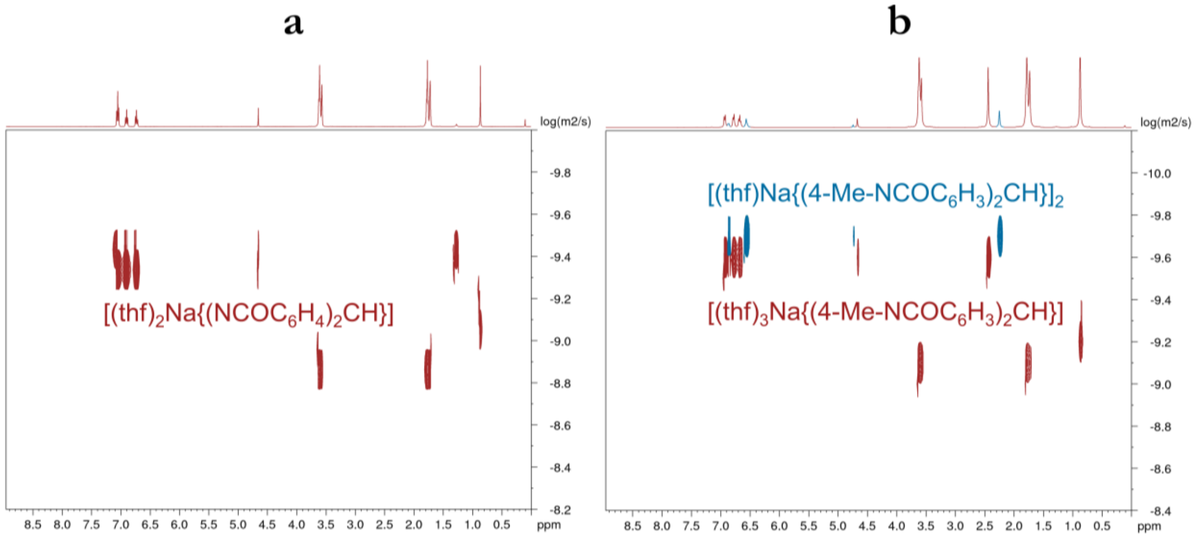

Figure 3.15. (**a**) DOSY-NMR spectrum of [(thf)$_3$Na{(NCOC$_6$H$_4$)$_2$CH}] (**18**) in thf-d_8 at 243 K. The set of signals can be assigned to the di-solvated species [(thf)$_2$Na(NCOC$_6$H$_4$)$_2$CH]. (**b**) DOSY-NMR spectrum of [Na(thf)$_6$][Na{4-Me-NCOC$_6$H$_3$)$_2$CH}$_2$] (**17**) in thf-d_8 at 233 K. Here, two species appear, the dimer [(thf)Na{4-Me-NCOC$_6$H$_3$)$_2$(CH}]$_2$) depicted in blue, and the lower band of signals can be ascribed to the trisolvated monomer ([(thf)$_3$Na{4-Me-NCOC$_6$H$_3$)$_2$CH}]), illustrated in red. Reprinted with permission from Ref.[3], https://pubs.acs.org/doi/abs/10.1021/acs.inorgchem.1c03714. Copyright 2022 American Chemical Society.

Table 3.18. Determined masses for both species of **17** that occurred at 233 K in thf. Calculations root in diffusion coefficients and the deviation [%] of the determined molecular weights for three feasible aggregates are depicted.

	Species 1	**Species 2**
$MW_{\text{det, DSE}}$ [g mol^{-1}]	748	497
[(thf)Na{(4-Me-NCOC$_6$H$_3$)$_2$CH}]$_2$	0 %	50 %
[Na{(4-Me-NCOC$_6$H$_3$)$_2$CH}]$^-$	−23 %	16 %
[(thf)$_3$Na{(4-Me-NCOC$_6$H$_3$)$_2$CH}]	−31 %	4 %

For species 1, an MW_{DSE} = 497 g mol^{-1} was detected and matched a tri-solvated complex [(thf)$_3$Na{(4-Me-NCOC$_6$H$_3$)$_2$CH}] (**Table 3.18.**). Considering the anion [Na{(4-Me-NCOC$_6$H$_3$)$_2$CH}]$^-$ observed in the solid-state structure, this aggregate is not present in solution due to high deviations from the determined MW_{DSE} (−23 %). Further experiments performed in toluene did not illuminate dimeric structures, which are only present in donor solvents at low temperatures. Decreasing the temperature shifted the signal ratio toward the dimeric species 1.

3.6.3. Synthesis and solid-state structures of $[(\mu\text{-Cl})\text{Ln}^{\text{III}}\{4\text{-Me-NCOC}_6\text{H}_3)_2\text{CH}\}_2]_2$

The subsequent lanthanide complexes were attained by the reaction of 2 equiv. of precursor **17** with 1 equiv. of LnCl_3 (Ln =Gd^{III}, Dy^{III}, Er^{III}) in toluene at r.t conditions (**Scheme 3.14.**). Various molar ratios (1:2 or 1:3) resulted in the same disubstituted complex $[(\mu\text{-Cl})\text{Ln}^{\text{III}}\{4\text{-MeNCOC}_6\text{H}_3)_2\text{CH}\}_2]_2$. Upon reaction, the light-yellow solution is turned into a dark yellow suspension after 24 h and yields **19**-**21**, after removing precipitated sodium chloride, in moderate yields as a yellow solid.

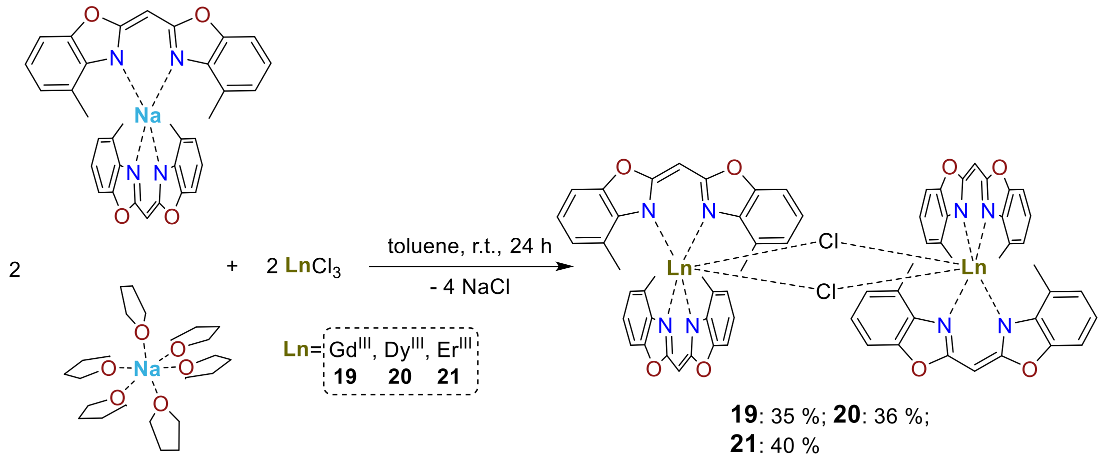

Scheme 3.14. Synthesis of $[(\mu\text{-Cl})\text{Ln}^{\text{III}}\{4\text{-Me-NCOC}_6\text{H}_3)_2\text{CH}\}_2]_2$ with Ln = Gd^{III} (**19**), Dy^{III} (**20**), Er^{III} (**21**), from $[\text{Na(thf)}_6][\text{Na}\{4\text{-Me-NCOC}_6\text{H}_3)_2\text{CH}\}_2]$ (**17**) in toluene at r.t. conditions. Reprinted with permission from Ref.[3], https://pubs.acs.org/doi/abs/10.1021/acs.inorgchem.1c03714. Copyright 2022 American Chemical Society.

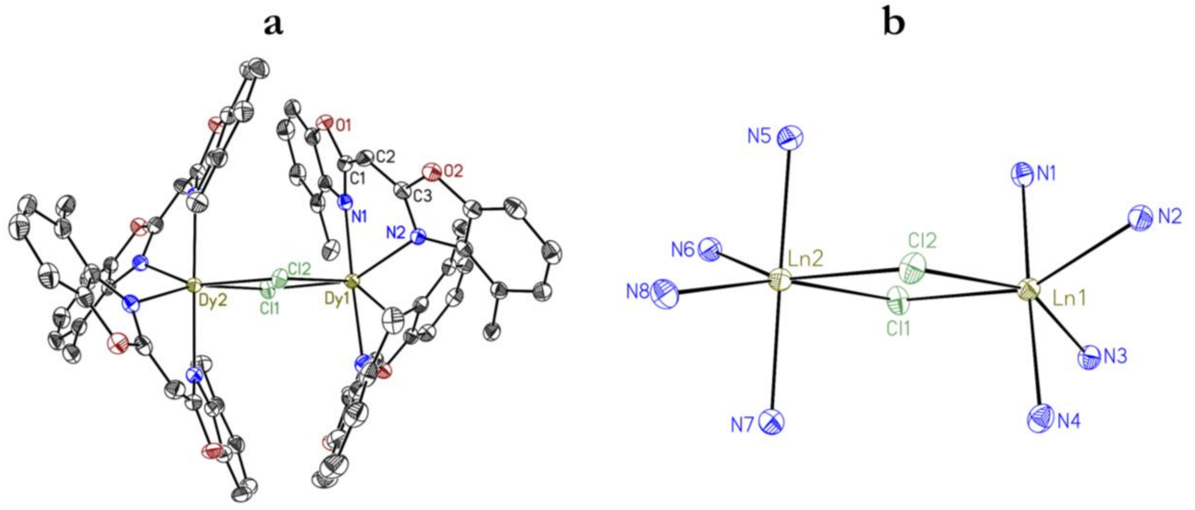

Figure 3.16. (**a**) The solid-state structure of $[(\mu\text{-Cl})\text{Dy}^{\text{III}}\{4\text{-Me-NCOC}_6\text{H}_3)_2\text{CH}\}_2]_2$ (**20**), complexes **19** and **21** are isostructural and displayed in the crystallographic section (chapters 5.3.19 and 5.3.21). Thermal ellipsoids are displayed at a probability level of 50%. The hydrogen atoms and lattice solvent molecules are omitted for clarity. (**b**) Coordination polyhedron of the Ln_2Cl_2 four-membered ring with Ln (Ln = Gd^{III} (**19**), Dy^{III} (**20**), and Er^{III} (**21**)), while all non-coordinating atoms are omitted for clarity. Reprinted with permission from Ref.[3], https://pubs.acs.org/doi/abs/10.1021/acs.inorgchem.1c03714. Copyright 2022 American Chemical Society.

Crystals that qualify for X-ray diffraction experiments of **19**-**21** were grown from a saturated toluene solution at r.t. conditions. All three complexes are isomorphous and share the triclinic space group $P\bar{1}$ with one complex molecule and two additional lattice toluene molecules in the asymmetric unit (**Figure 3.16.a**). Enabling the bridging of two lanthanide atoms by the same ligand via mutual N,O-coordination failed. However, the increase of steric hindrance of the Mebox ligand effectively suppresses a third halide substitution, different from the Box ligand (chapter 3.5),[2] and results in a central Ln_2Cl_2 four-membered ring. Therefore, this ligand system is an appropriate design for bridged systems. The reported complexes comprise two lanthanide ion Ln^{III} each *N*,*N'*-chelated by two negatively charged ligands and two μ-bridging chlorine atoms (**Figure 3.16.a**). Interestingly, the twist angles for the two ligands on either side differentiate, fluctuating from 64.50(15)° to 69.92(17)° (**Table 3.19.**). The Ln–N bond lengths trend aligns with the lanthanide contraction from gadolinium to erbium, decreasing from average values of 2.419 Å in **19** to 2.372 Å in **21**.

Table 3.19. Selected bond lengths [Å] and angles [°] for $[(\mu\text{-Cl})Ln^{III}\{4\text{-MeNCOC}_6H_3)_2CH\}_2]_2$ (**19**-**21**)

	Ln = Gd^{III} (**19**)	Ln = Dy^{III} (**20**)	Ln = Er^{III} (**21**)
$Ln–N_{range}$	2.378(3)-2.460(3)	2.359(2)-2.414(2)	2.335(3)-2.409(3)
Ln(1)···C_3N_2 plane[a]	1.431(5)	1.388(3)	1.348(4)
Ln(2)···C_3N_2 plane[b]	1.438(5)	1.401(3)	1.366(4)
Ln(2)···C_3N_2 plane[c]	1.219(5)	1.208(3)	1.193(4)
Ln(1)···C_3N_2 plane[d]	1.227(5)	1.214(3)	1.195(4)
Ln(1)···Ln(2)	4.3016(9)	4.2543(9)	4.2282(9)
Ln(1)–Cl	2.7277(11)-2.7480(11)	2.7032(8)-2.7235(9)	2.6849(10)-2.7053(10)
Ln(2)–Cl	2.7140(11)-2.7480(11)	2.6844(9)-2.7102(8)	2.6684(11)-2.6965(9)
Ln(1)–Cl(1)–Ln(2)	104.46(4)	104.31(3)	104.34(3)
Ln(1)–Cl(2)–Ln(2)	103.30(4)	103.06(3)	103.02(3)
N–Ln(1)–N	79.07(11)-79.61(12)	79.79(7)-80.39(8)	80.44(10)-80.96(10)
N–Ln(2)–N	80.66(11)-80.68(12)	81.45(8)-81.53(7)	81.96(10)-82.05(9)
Twist angles[e]			
N(1)N(2)C(2)-N(3)N(4)C(5)	69.92(17)	69.58(11)	68.65(14)
N(5)N(6)C(8)-N(7)N(8)C(11)	65.16(17)	65.32(11)	64.50(15)

[a] Dislocation of Ln^{III} from the N(1)N(2)C(2) plane; [b] Dislocation of Ln^{III} from the N(3)N(4)C(5) plane; [c] Dislocation of Ln^{III} from the N(5)N(6)C(8) plane; [d] Dislocation of Ln^{III} from the N(7)N(8)C(11) plane; [e] Angles between both benzoxazole moieties.

Table 3.20. Continuous Shape Measures (CShMs) of the coordination geometry for the Ln^{3+} ion environments in **19**-**21**, retrieved from the SHAPE program, portraying the lowest residue for an octahedron.[140a,140b,162]

		HP-6[a]	PPY-6[b]	OC-6[c]	TPR-6[d]	JPPY-5[e]
2	Gd1	32.124	19.248	3.667	8.521	22.788
	Gd2	32.121	22.370	1.941	11.310	26.134
3	Dy1	32.007	19.659	3.371	8.752	23.252
	Dy2	32.481	22.148	1.902	11.205	25.881
4	Er1	32.030	19.988	3.139	8.926	23.582
	Er2	32.852	21.947	1.895	11.241	25.616

[a] D_{6h}, Hexagon; [b] C_{5v}, Pentagonl pyramid; [c] O_h, Octahedron; [d] D_{3h}, Trigonal prism; [e] C_{5v}, Johnson pentagonal pyramid (J2).

Intramolecular distances of the two lanthanide centers range from 4.3016(9) for **19** to 4.2282(9) Å for **21**, hence in the anticipated range for magnetic coupling. Next, the M–Cl bond lengths are also essential for metal coupling. Here, the regions fluctuate between 2.7140(11) to 2.7480(11) Å in **19**, 2.6844(9) to 2.7235(9) Å in **20**, and 2.6684(11) to 2.7053(10) Å in **21** that follows the trend for the ionic radii. A dislocation of the lanthanide centers from their corresponding C_3N_2 plane is noticed and further elucidated for the three complexes. Each side of the dimer illustrates a displacement of similar values, exemplified for complex **20** (1.388(3)-1.401(3) Å) for the first side and (1.208(3)-1.214(3) Å) for the second side. Data for **19** and **21** are depicted below (**Table 3.19.**). The bite angle (N–Ln–N) ranges from 79.07(11) to 82.05(9)° for **19**-**21** and correlates again with the expected trend of the lanthanide radii. Last, the coordination environment of the six-coordinated complexes **19**-**21** was examined with the SHAPE software.[140a,140b,162] The lowest residues are reported for the octahedron, which is the most accurate description of the coordination environment of the presented complexes (**Table 3.20.**). Also, the trigonal prism is feasible, showing significantly higher residues than detected for the octahedron.

3.6.4. Magnetic properties of $[(\mu\text{-Cl})Ln^{III}\{4\text{-Me-NCOC}_6H_3)_2CH\}_2]_2$

First, the magnetic susceptibility is measured from 210 to 2 K. The consequent data is depicted as the product of the molar susceptibility and the temperature ($\chi_M T$) versus the temperature (T). For $\chi_M T$ (cm^3mol^{-1}), we detected high-temperature values of 15.45 for **19**, 28.73 for **20**, and 23.67 for **21**, whereas the values for two independent lanthanide ions are 15.75 for **19**, 28.34 for **20**, and 22.96 for **21**. Hence the recorded values are in the expectancy range for dinuclear lanthanide complexes.[163] From 210.0 to 20.0 K, the $\chi_M T$ values for **19** stayed

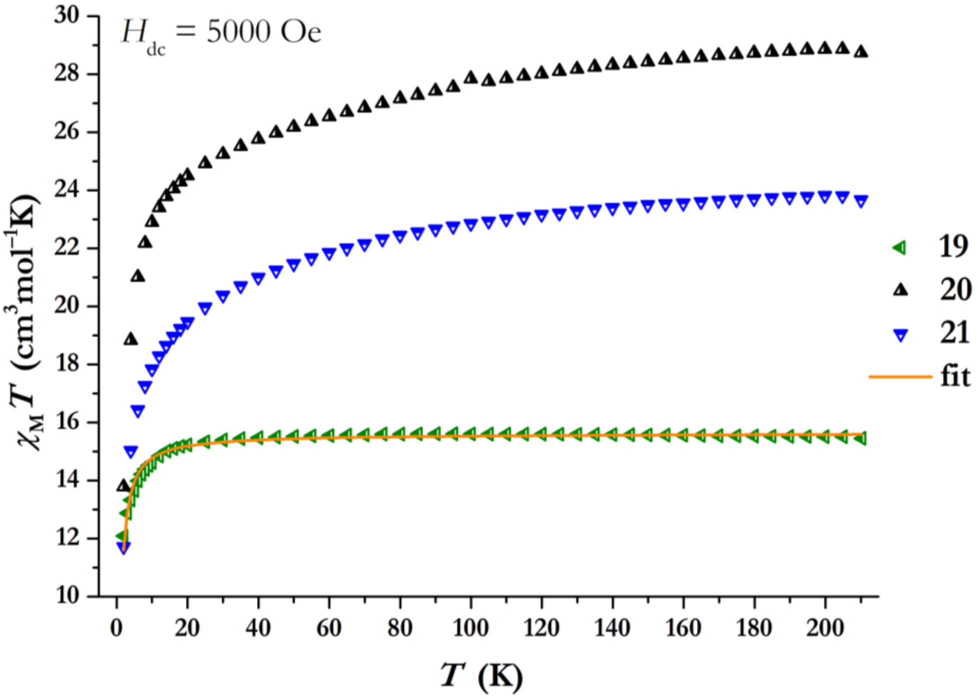

Figure 3.17. Temperature-dependency of $\chi_M T$ for **19**-**21**, under an applied field of H_{dc} = 5000 Oe. The orange line represents the fit to the data, which was performed with the PHI program by N.F. Chilton.[164] Reprinted with permission from Ref.[3], https://pubs.acs.org/doi/abs/10.1021/acs.inorgchem.1c03714. Copyright 2022 American Chemical Society.

constant while continuously decreasing for **20** and **21**, reaching 12.09, 13.78, and 11.78 cm^{3}mol^{-1} at 2.0 K, which are close but different from the single ion values (**Figure 3.17.**). Differences between **19** and **20**-**21** originate in divergences in the magnetic anisotropies of **20** and **21** since the Gd^{III} compound **19** illustrates an isotropic shell.[57,163e,165] The distance mentioned above between the lanthanide centers (4.3016(9) to 4.2282(9) Å) is in the typical range of magnetic coupling (3.6-7.0 Å).[163a–e] For the diffuse chloride orbitals, overlap with the metal orbitals is anticipated,[166] hereafter, we modeled the $\chi_M T$ versus T data for **19**. An excellent tool is the PHI program, which was employed to determine the magnetic exchange coupling.[164] We examined a weak antiferromagnetic coupling as $J = -0.035$ cm^{-1}, consistent with usually small magnetic coupling values between lanthanide ions bridged through diamagnetic halides.[163b,163e] Moreover, the two calculated magnetic vectors of the Ln^{III} centers are assumed to be parallel since the measured angles between the magnetic moments are smaller than 5°. Therefore, one can employ the simplified equation (**3-4**) to determine the exact magnetic dipolar coupling interaction for the scenario of parallel magnetic moments:[167]

$$E_{\mathrm{dip}} = -\left\{\frac{\mu_0}{4\pi}\right\}\frac{\mu_i \mu_j}{r^3}\left[3\cos^2(\theta) - 1\right] \tag{3-4}$$

Here, μ_0 refers to the vacuum permeability ($1 \cdot 10^{-7}$ [kg m s^{-2} A^{-2}]), μ_i and μ_j represent the magnetic moment (10.646 μ_B for Dy^{3+}, 7.937 μ_B for Gd^{3+} [$\mu_B = 9.274 \cdot 10^{-24} J \cdot T^{-1}$]), and the angle θ describes the angle between the orientation of the magnetic vectors and the distance of both metal centers. For $\theta > 54.75°$ antiferromagnetic coupling is anticipated, while for $\theta < 54.75°$ ferromagnetic coupling is expected.[167b]

For the dysprosium complex (**20**), an angle of 89.622° was determined, suggesting an antiferromagnetic interaction. This is in good agreement with our experimental results that suggest a weak antiferromagnetic coupling (**Figure 3.17.**). Derived calculations of the expected dipolar coupling of the two lanthanide centers resulted in 0.623 cm^{-1} for the dysprosium dimer **20** and 0.34 cm^{-1} for the gadolinium analogue **19**. These values are larger than determined experimentally but still small as expected for this compound class. One must consider that this is a simplified approach with a rough estimation of the dipolar interaction since the magnetic vectors are not ideally parallel.

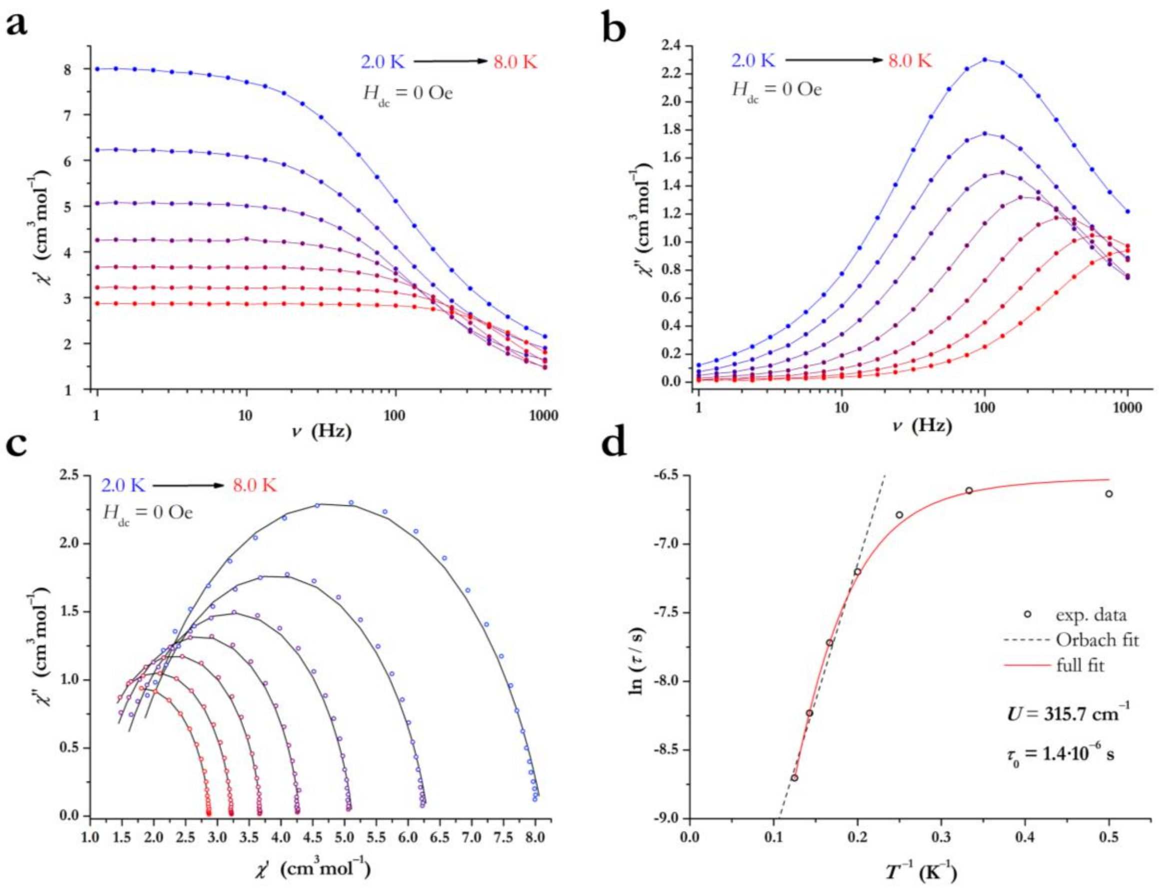

Figure 3.18. Magnetic data for $[(\mu\text{-Cl})\text{Dy}^{\text{III}}\{4\text{-Me-NCOC}_6\text{H}_3)_2\text{CH}\}_2]_2$ (**20**) under zero dc field conditions. Dynamic in-phase (**a**) and out-of-phase (**b**) susceptibilities versus variable frequencies from 2.0 to 8.0 K. Lines are guides for the eyes. (**c**) Cole-Cole plot with corresponding CC-fit data. (**d**) Arrhenius plot with the red curve exemplifying the full fit of all relaxation processes and the dashed line demonstrating a sole Orbach regression. Reprinted with permission from Ref.[3], https://pubs.acs.org/doi/abs/10.1021/acs.inorgchem.1c03714. Copyright 2022 American Chemical Society.

In order to probe for SMM behavior, further measurements of the magnetic susceptibilities under a dynamic, alternating current (ac) field of 3.0 Oe were performed for **20** and **21**. The Er^{III} complex (**21**) did not exhibit any out-of-phase maxima χ'' under a zero dc field. Inhabitation of possibly occurring quantum tunneling processes was unsuccessful since the applied dc field did not reveal any maxima for χ''. Therefore, complex **21** exhibits no SMM behavior. However, dysprosium complexes are more prone to display SMM behavior. Hence we envisioned superior magnetic properties for $[(\mu\text{-Cl})Dy^{III}\{4\text{-Me-NCOC}_6H_3)_2CH\}_2]_2$ (**20**). Remarkably, **20** shows signals of the dynamic out-of-phase susceptibility χ'' under a zero dc field. Up to 8.0 K, maxima of χ'' were observable in the frequency range of our magnetometer. The corresponding Cole-Cole plot was derived from in-phase (χ') and out-of-phase (χ'') data and fitted with the CC-fit program (**Figure 3.18.c**).[136]

This fit is constructed on a generalized Debye model and affords the parameter a ($0 < a < 1$), which relates to the width of the relaxation time distribution. An a parameter equaling zero exemplifies a relaxation with one time constant.[168] Here, the χ' / χ'' ratio displays a value of > 2, and the corresponding a parameter is found in a range of 0.01-0.23 (2.0-8.0 K), indicating a wide range of relaxation times being within the expectancy range for dinuclear Dy^{III}-complexes.[169] The subsequent Arrhenius plot was constructed from the output relaxation times τ. Considering Raman, Orbach, QTM, and direct relaxation processes (eq. **3-3**), the full fit gave rise to an energy barrier of $U = 315.7\ \text{cm}^{-1}$, illustrated as the red curve (**Figure 3.18.d**).

$$\tau^{-1} = CT^n + \tau_0^{-1}\exp\left(-\frac{U_{\text{eff}}}{k_B T}\right) + \text{QTM} \qquad (3\text{-}3)$$

The maxima of χ'' start at higher frequencies, which is a sign of the presence of QTM processes. Therefore, various dc fields were tested to suppress QTM entirely or to some extent, resulting in an optimal field of 1000 Oe for complex **20**. Previous measurements were repeated under these conditions and processed as aforementioned (**Figure 3.19.**). Here, the maximum for χ'' starts at a frequency of 2 Hz and shifts toward higher frequencies as the temperature increases (**Figure 3.19.b**), demonstrating a true temperature-dependency with almost no QTM. The low-temperature data in the Cole-Cole plot illustrates a small shoulder, however, the data is best fitted with only one relaxation process (**Figure 3.19.c**). Moreover, the overall shape of the curve in the Arrhenius plot is almost linear, suggesting the Orbach process to be the dominant relaxation process for high temperatures (**Figure 3.19.d**). For this reason, we excluded QTM and direct processes for the full fit and manipulated the fit with Raman and Orbach processes, which resulted in an energy barrier of $378.9\ \text{cm}^{-1}$, which is 20 % higher than observed at zero field conditions (**Table 3.21.**).

Next, a structural comparison with analogue complexes from the CCDC database is conducted to file and correlate the reported magnetic properties. Nevertheless, no dysprosium halide (Dy_2Cl_2) dimer with only nitrogen ligands has been previously reported. Lowering the criteria and allowing oxo or additional chlorido ligands to this coordination motif, one can find closely related structures.[170] The height of the energy barrier for **19** is above average for such dysprosium complexes.[169,170b,171] The $[Cp_2Dy(\mu\text{-Cl})]_2$ analogue features similar magnetic performances as reported for **19**.[172] However, also better performing SMMs involving both oxo and nitrogen ligating systems, showing U values of up to 640.4 cm^{-1}.[163c,163e,173] Their coordination polyhedron is far from a linear mode. The broad range of energy barriers can partially be assigned to different point groups, referred by TONG and colleagues.[56]

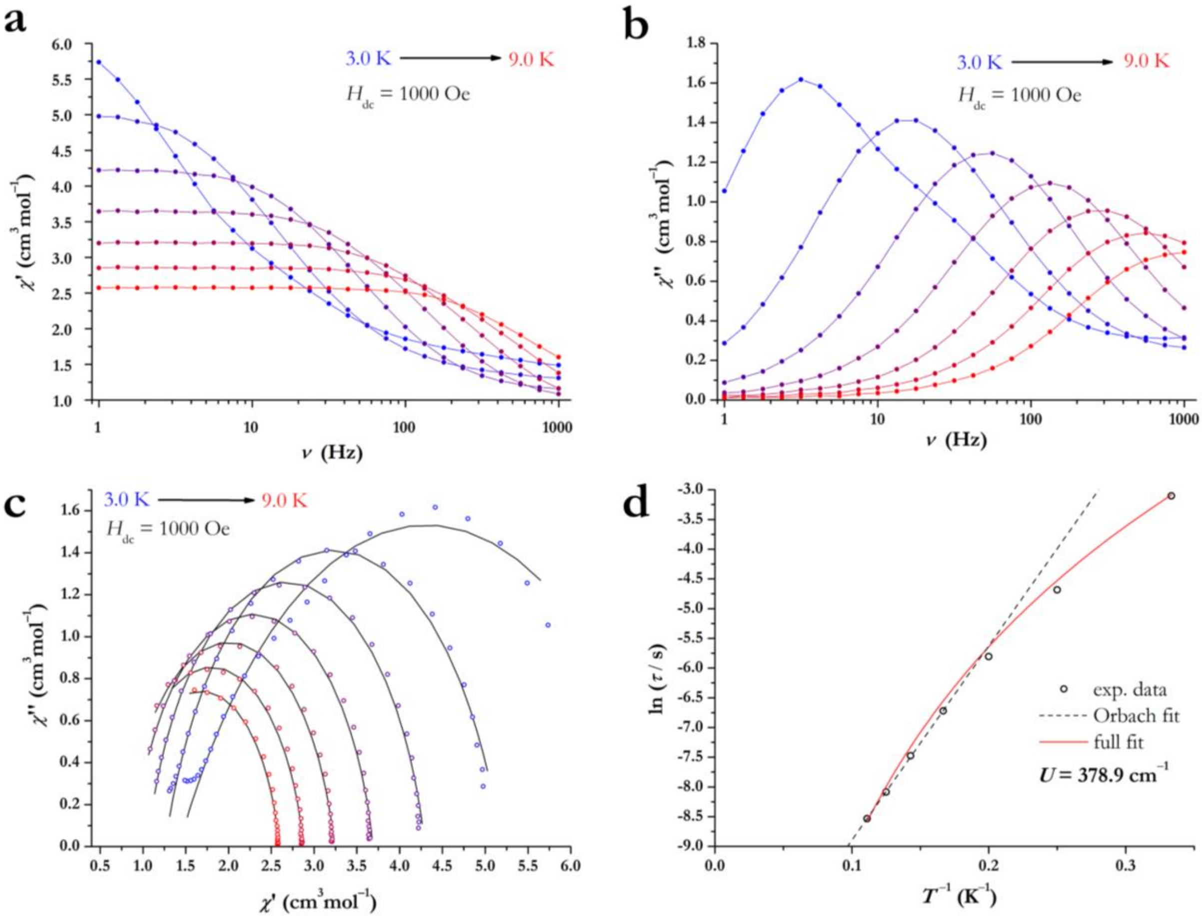

Figure 3.19. Magnetic data for $[(\mu\text{-Cl})Dy^{III}\{4\text{-Me-NCOC}_6H_3)_2CH\}_2]_2$ (**20**) under an applied dc field of 1000 Oe. Dynamic in-phase (**a**) and out-of-phase (**b**) susceptibilities versus variable frequencies from 3.0 to 9.0 K. Lines are guides for the eyes. (**c**) Cole-Cole plot with corresponding CC-fit data. (**d**) Arrhenius plot with the red curve exemplifying the full fit of all relaxation processes and the dashed line demonstrating a sole Orbach regression. Reprinted with permission from Ref.[3], https://pubs.acs.org/doi/abs/10.1021/acs.inorgchem.1c03714. Copyright 2022 American Chemical Society.

Table 3.21. Best fitting parameter for $[(\mu\text{-Cl})\mathrm{Dy^{III}}\{4\text{-Me-NCOC}_6\mathrm{H}_3)_2\mathrm{CH}\}_2]_2$ (**20**). R_2 gives the error of the full fit.

	U (cm^{-1})	τ_0 (s)	C (s^{-1}K^{-n})	n	τ_{QTM} (s)	R_2
20 (0 Oe)	315.7 (±1.0)	$1.4\cdot10^{-6}$ ($\pm1.0\cdot10^{-9}$)	0.73 (±0.3)	4.3 (±0.20)	671.2 (±60)	0.99905
20 (1000 Oe)	378.9(±30)	$4.6\cdot10^{-6}$ ($\pm2.0\cdot10^{-7}$)	0.10 (±0.1)	5.2 (±1.3)	0	0.98445

TONG investigated the influence of certain point groups and their transverse crystal-field terms on their effective suppression of QTM processes. If the symmetry requirements are encountered, considerably large energy barriers are conceivable for no linear systems (see chapter 1.5).

Next, the main magnetic axes of the two Dy$^{\mathrm{III}}$ ions are calculated based on the orientation of the magnetic ground state with an electrostatic model (**Figure 3.20.**). Unfortunately, these calculations are not transferrable to Er$^{\mathrm{III}}$ since both metals possess different electronic shapes. The axes for **20** are almost parallel, slightly leaning toward the chlorine bridges, which is in alignment with the nearly identical Dy$^{\mathrm{III}}$ ions and their weak interaction. Furthermore, the position of the magnetic axes implies that the current ligand polyhedron is neither ideal for prolate (e.g. Er$^{\mathrm{III}}$) nor oblate (e.g. Dy$^{\mathrm{III}}$) formed lanthanide ions.

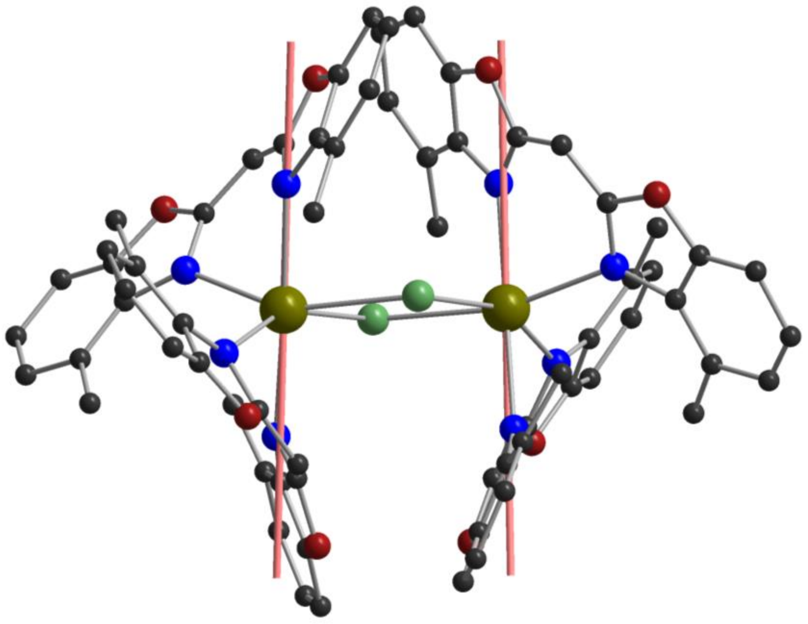

Figure 3.20. Orientation of the two main magnetic axes (light coral) of the ground state for both Dy$^{\mathrm{III}}$ centers of $[(\mu\text{-Cl})\mathrm{Dy^{III}}\{4\text{-Me-NCOC}_6\mathrm{H}_3)_2\mathrm{CH}\}_2]_2$ (**20**), calculated with the program Magellan and illustrated with the program Diamond 3.[174] All hydrogen atoms are omitted for clarity. Color code: C: (black), N: (blue), O: (red), Cl: (green), and Dy: (gold). Reprinted with permission from Ref.[3], https://pubs.acs.org/doi/abs/10.1021/acs.inorgchem.1c03714. Copyright 2022 American Chemical Society.

3.6.5. Summary and concluding remarks for $[(\mu\text{-Cl})Ln^{III}\{4\text{-Me-NCOC}_6H_3)_2CH\}_2]_2$ and their sodium precursors

Within this chapter, two sodium precursors, in particular, the sodium sodate $[Na(thf)_6][Na\{4\text{-Me-NCOC}_6H_3)_2CH\}_2]$ (**17**) and the $[(thf)_3Na\{(NCOC_6H_4)_2CH\}]$ (**18**) are studied. **17** represents the first reported example of an alkali metal Box derivative featuring a solvent separated ion pair, which is generally a rarely observed structure motif. DOSY-NMR studies unequivocally demonstrated that under r.t. conditions, the solvent separated ion pair is not maintained, while the equilibrium is shifted toward the dimer at low temperatures. The subsequent dinuclear lanthanide(III) complexes $[(\mu\text{-Cl})Ln^{III}\{4\text{-Me-NCOC}_6H_3)_2CH\}_2]_2$ (**19**-**21**) with Ln = Gd^{III} (**19**), Dy^{III} (**20**), and Er^{III} (**21**) were analyzed via SC-XRD and SQUID magnetometry. The Dy^{III}-complex **20** demonstrates a true SMM signature with energy barriers of 315.7 cm^{-1} (0 Oe) and 378.9 cm^{-1} (1000 Oe), respectively. Further, the Gd^{III}-complex (**19**) provided insights into the magnetic interaction between both Dy^{III} centers, best described as a weak antiferromagnetic coupling with a value of $-0.035\ cm^{-1}$. However, the main contribution to the studied SMM behavior stems from the single ion properties as the coupling is weak. Perspectives for improvement should focus on optimizing the coordination environment to attain a tetrahedral mode with a bulky weakly-coordinating counter ion. Studies with bulkier Box systems such as *t*Bu- or benzhydryl-groups are envisioned. Removing the remaining halide with KC_8 or Mg, could be perused as well.

3.7. Excursus: Functionalized sulfinates for d-and f-metal chemistry

Major parts of this chapter have been published in the master thesis of M. Ed. M. REDECKER and in the bachelor thesis of M. PÖHLMANN.[175] Here, I provided the synthetic ideas and conducted the structural (via SC-XRD) and magnetic (via SQUID) analysis.

3.7.1. Ligand and precursor synthesis

The feedstock for all subsequent reactions is the bis(trimethylsilyl)sulfurdiimide (**L_5**), which WANNAGAT and KUCKERTZ were initially prepared in 1962.[104] Later, SCHERE and WIES improved the procedure,[176] while the most sophisticated approach came from HAUBOLD and colleagues and is still in use today.[177] The procedure from HAUBOLD was applied to synthesize **L_5**, starting from thionyl chloride that was treated with 2 equiv. Li(HMDS) and yielded the bis(trimethylsilyl)sulfurdiimide (**Scheme 3.15.**).

The double bond in **L_5** is predestinated for nucleophilic addition reactions with lithiated precursors. Compound **L_6** $[\{(thf)_2Li(NSiMe_3)_2S\}_2An]$ (An = $C_{14}H_8$) was previously described by SCHULZ and STALKE and was attained from the reaction of Li_2An and **L_5** (**Scheme 3.16.**).[178] The *t*Bu substituted analogue $[Li\{t\text{BuS}(NSiMe_3)_2\}]_2$ (**L_7**) was prepared from *t*BuLi and **L_5** according to the methods of PAUER and STALKE.[179] Last, $[(thf)Li\{MeS(NSiMe_3)_2\}]_2$ (**L_8**) was accessed via a reaction of **L_5** with MeLi, first reported by SELINKA and STALKE and later published by SCHULZ, STALKE, and coworkers.[180]

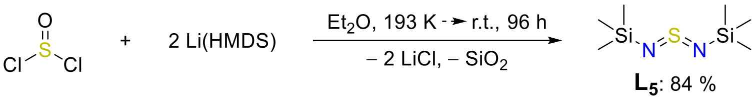

Scheme 3.15. Synthesis of bis(trimethylsilyl)sulfurdiimide (**L_5**) from the reaction of thionyl chloride and Li(HMDS) in Et_2O.[177]

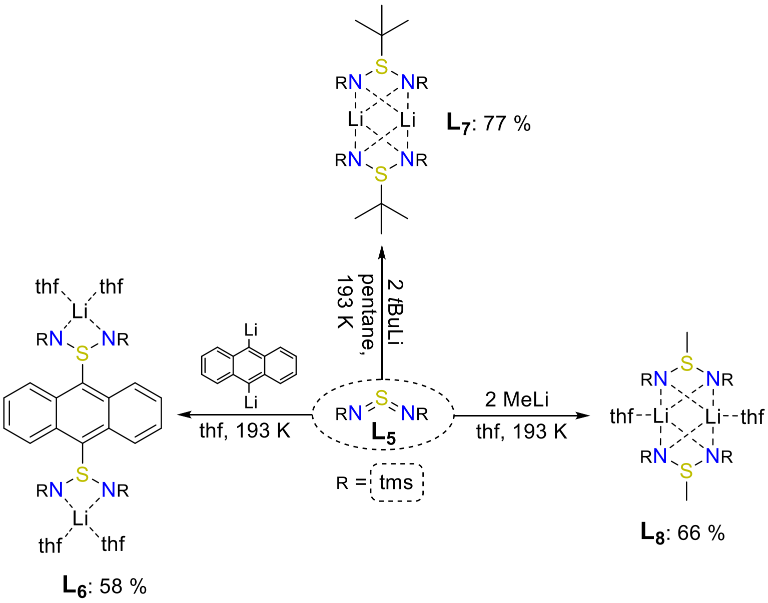

Scheme 3.16. Synthesis of $[\{(thf)_2Li(NSiMe_3)_2S\}_2An]$ (An = $C_{14}H_8$) (**L_6**), $[Li\{t\text{BuS}(NSiMe_3)_2\}]_2$ (**L_7**), and $[(thf)Li\{MeS(NSiMe_3)_2\}]_2$ (**L_8**) from bis(trimethylsilyl)sulfurdiimide.[178,179,180]

3.7.2. Synthesis and magnetic properties of $\mathbf{L_6}$ based d- and f-metal complexes

To access the corresponding d- and f-metal complexes of the anthracenyl sulfinate ligand $\mathbf{L_6}$, we employed a salt metathesis reaction that yielded [{(thf)$_2$LiCl$_2$(thf)$_n$M^{II}(NSiMe$_3$)$_2$S}$_2$An] with M= Co^{II} and Mn^{II} and [{(thf)$_2$LiCl$_2$Ln^{III}Cl(NSiMe$_3$)$_2$S}$_2$An] with Ln^{III}= Dy^{III} and Er^{III} (**Scheme 3.17.**). Crystals suitable for X-ray diffraction experiments were obtained from a saturated thf solution at 238 K after 48 h. The solid-state structures are illuminated in chapters 6.6.1 to 6.6.4, and the interested reader is referred to the master thesis of M. REDECKER for a detailed discussion.[175] Magnetic data for all four complexes were recorded via SQUID magnetometry, illustrated in **Figure 3.21.** First, magnetic measurements of $\chi_M T$ were performed under a static dc field of 5000 Oe, decreasing the temperature from 210 to 2 K. The successive depopulation of the Stark levels causes a linear decrease that drops more rapidly below 30 K, and the values are within the assumed range for dinuclear lanthanide complexes.[163] Probing for SMM behavior was done under an oscillating ac field. However, no response of the out-of-phase susceptibility was found neither with nor without a dc field (**Figure 3.21.b-c**). Next, the corresponding manganese and cobalt complexes were analyzed the same way. Accurate values for the static magnetic parameters were obtained from the fit of the variable temperature variable field data (VTVH) with the dc data applying the JulX-2s program that works on the spin Hamiltonian (eq. **3-2**), chapter 3.2.2) [132]

The manganese complex [{(thf)$_2$LiCl$_2$(thf)Mn(NSiMe$_3$)$_2$S}$_2$An] exhibits a positive ZFS parameter that flips the double-well potential, and no SMM behavior is expected (**Table 3.22.**), while anisotropic g values ($g_x \approx g_y < g_z$) are the best fitting parameters.[133]

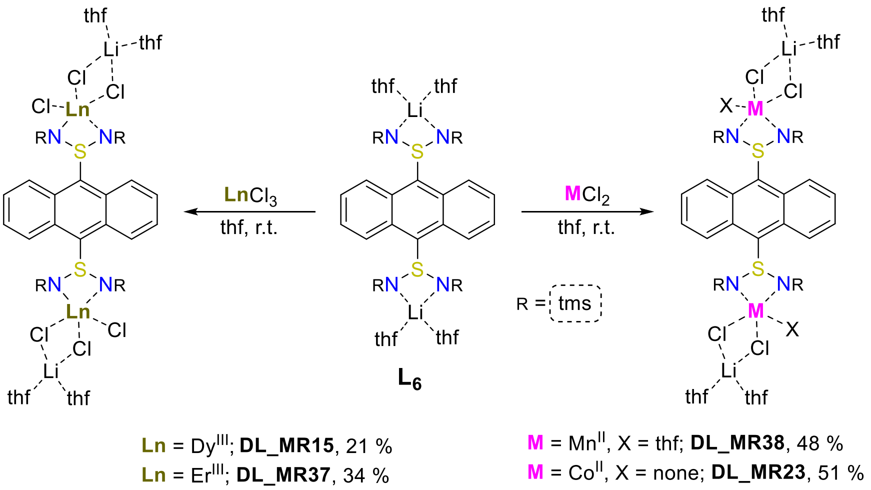

Scheme 3.17. Synthetic route to d- and f-metal complexes based on the anthracenyl sulfinate ligand $\mathbf{L_6}$.

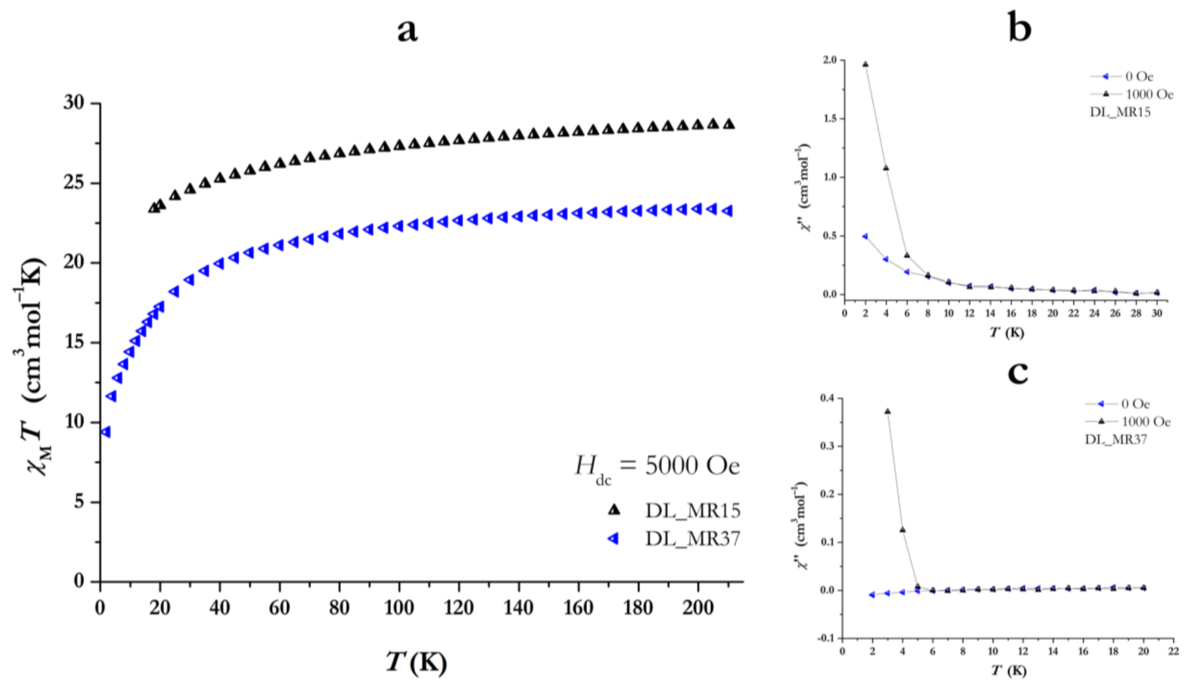

Figure 3.21. (**a**) Temperature-dependency of $\chi_M T$ for **DL_MR15** and **DL_MR37**, under an applied field of H_{dc} = 5000 Oe. Temperature-dependency of the χ'' response with and without a dc field at 1488 Hz for **DL_MR15** (**b**) and **DL_MR37** (**c**).

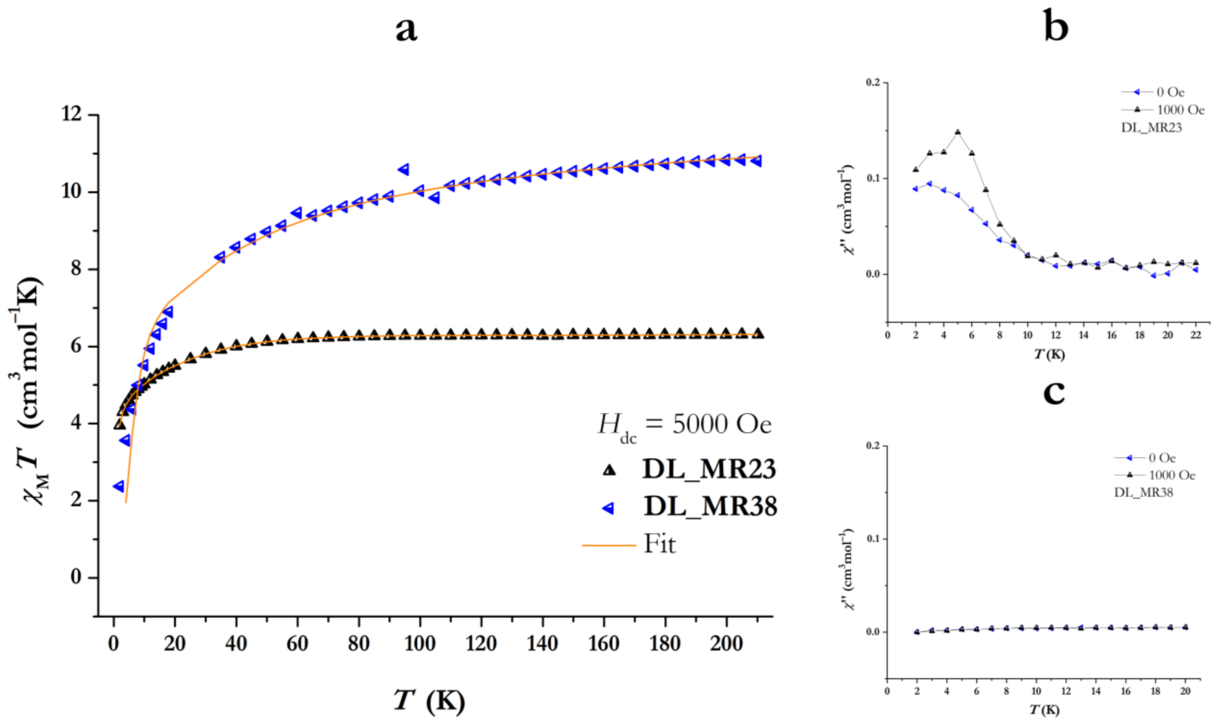

Figure 3.22. (**a**) Temperature-dependency of $\chi_M T$ for **DL_MR23** and **DL_MR38**, under an applied field of H_{dc} = 5000 Oe. Temperature-dependency of the χ'' response with and without a dc field at 1488 Hz for **DL_MR38** (**b**) and **DL_MR23** (**c**).

Table 3.22. Selected experimental magnetic data for **DL_MR23** [$\{(thf)_2LiCl_2Co(NSiMe_3)_2S\}_2An$] and **DL_MR38** [$\{(thf)_2LiCl_2(thf)Mn(NSiMe_3)_2S\}_2An$].

	$D_1 = D_2$ (cm^{-1})	E/D	$g_{x,\,y,\,z}$	U_{eff} (cm^{-1})	τ_0 (s)
DL_MR23	–26.24	0	2.06, 2.06, 2.06	13.32 (±3.14)	$4.62 \cdot 10^{-7}$ ($\pm 1 \cdot 10^{-7}$)
DL_MR38	50.31	0.11	2.23, 2.23, 2.40	–	–

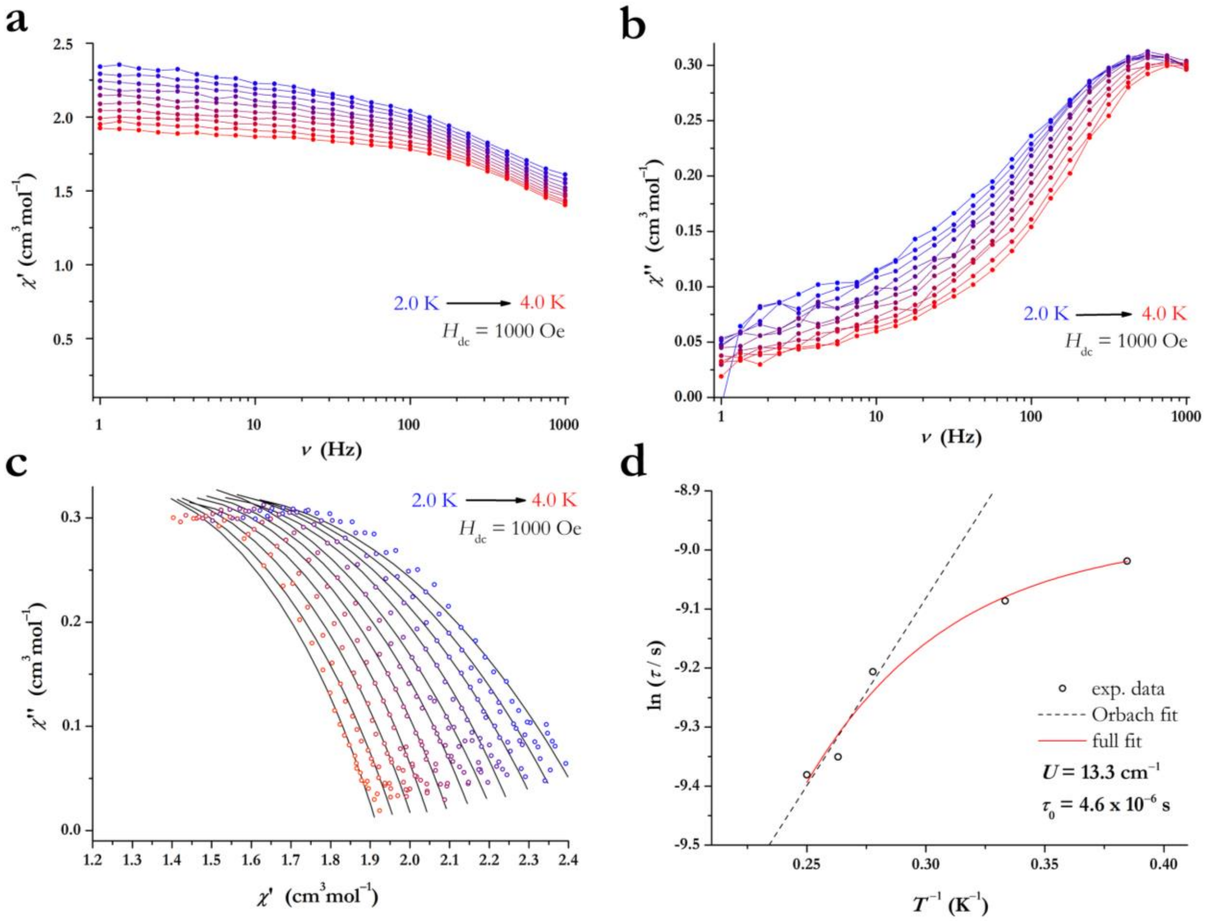

Figure 3.23. Magnetic data for [$\{(thf)_2LiCl_2Co(NSiMe_3)_2S\}_2An$] (**DL_MR23**) under an applied dc field of 1000 Oe. Dynamic in-phase (**a**) and out-of-phase (**b**) susceptibilities versus variable frequencies from 2 to 4 K. Lines are guides for the eyes. (**c**) Cole-Cole plot with corresponding CC-fit data. (**d**) Arrhenius plot with the red curve exemplifying the full fit of all relaxation processes and the dashed line demonstrating a sole Orbach regression.

For the cobalt analogue [$\{(thf)_2LiCl_2Co(NSiMe_3)_2S\}_2An$] (**DL_MR23**), all g values are best described as isotropic ($g_x = g_y = g_z$), and negative D values are found, indicating SMM behavior (**Table 3.22.**). Henceforth, subsequent ac field measurements were performed as stated in previous chapters. The out-of-phase susceptibility χ'' shows a maximum at a frequency of 500 Hz for the temperature data at 2 K (**Figure 3.22.**). For one to extract the relaxation times, maxima at lower frequencies are better since the SQUID device is limited to a maximum frequency of 1000 Hz. Therefore, the typical arc shape of the Cole-Cole plot is not present, as the χ'' data beyond the maxima are out of the detection range for SQUID magnetometers(**Figure 3.23.b-c**). The Arrhenius plot gives an energy barrier $U = 13.3\ \mathrm{cm}^{-1}$ that accounts for all relaxation processes.

3.7.3. Synthesis and magnetic properties of L_7 and L_8 based dysprosium complexes

The subsequent dysprosium complexes featuring ligand **L_7** and **L_8** were accessed via metathesis reactions with the dysprosium halides under ambient temperatures. Precipitating lithium chloride was removed via filtration and resulted in $[(\mathrm{thf})_2\mathrm{LiCl}_2\mathrm{Dy}\{\mathrm{MeS}(\mathrm{NSiMe}_3)_2\}_2]$ (**DL_MR17**) and $[(\mathrm{thf})_2\mathrm{LiCl}_2\mathrm{Dy}\{t\mathrm{BuS}(\mathrm{NSiMe}_3)_2\}_2]$ (**DL_MR16**) in good yields (**Scheme 3.18.**). The solid-state structures are illustrated in chapters 6.6.5 to 6.6.6, and the interested reader is referred to the master thesis of M. REDECKER for a detailed discussion.[175]

SQUID magnetometry was used to elucidate the magnetic properties of both dysprosium complexes. Initially, the $\chi_\mathrm{M}T$ values are plotted versus a temperature range from 2 to 210 K (**Figure 3.24.a**). The curve shape is as expected for mononuclear dysprosium complexes and is discussed in chapter 3.5.3. The high-temperature values of $\chi_\mathrm{M}T$ are 14.06 ($\mathrm{cm}^3\,\mathrm{mol}^{-1}\,\mathrm{K}$) for **DL_MR17** and 14.24 ($\mathrm{cm}^3\,\mathrm{mol}^{-1}\,\mathrm{K}$) for **DL_MR16**, where the theoretical value is 14.17 ($\mathrm{cm}^3\,\mathrm{mol}^{-1}\,\mathrm{K}$) for both,[14] and therefore within the range of related lanthanide(III) complexes.[14,20b,25,39,55,154] The free-ion approximation is generally valid since the crystal field splitting magnitude is comparably small in lanthanides (**Figure 1.6.**) with statistically populated M_J states at high temperatures. Next, probing for signals of the out-of-phase response via an oscillating ac field at a frequency of 1000 Hz resulted in maxima for **DL_MR16** and **DL_MR17**.

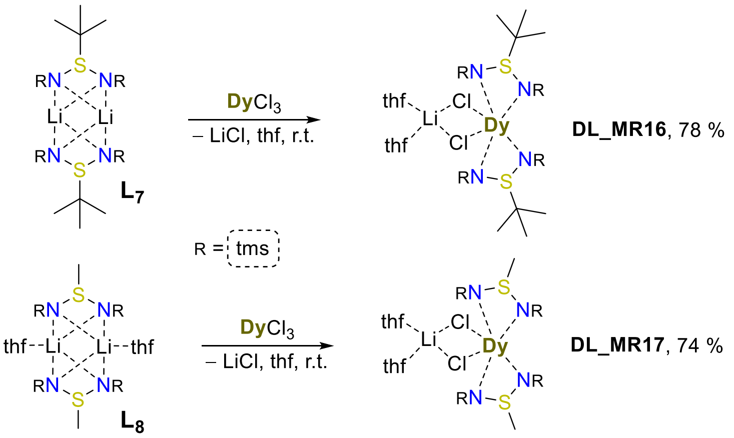

Scheme 3.18. Synthesis of $[(\mathrm{thf})_2\mathrm{LiCl}_2\mathrm{Dy}\{\mathrm{MeS}(\mathrm{NSiMe}_3)_2\}_2]$ (**DL_MR17**) and $[(\mathrm{thf})_2\mathrm{LiCl}_2\mathrm{Dy}\{t\mathrm{BuS}(\mathrm{NSiMe}_3)_2\}_2]$ (**DL_MR16**) from the corresponding lithium precursors in thf.

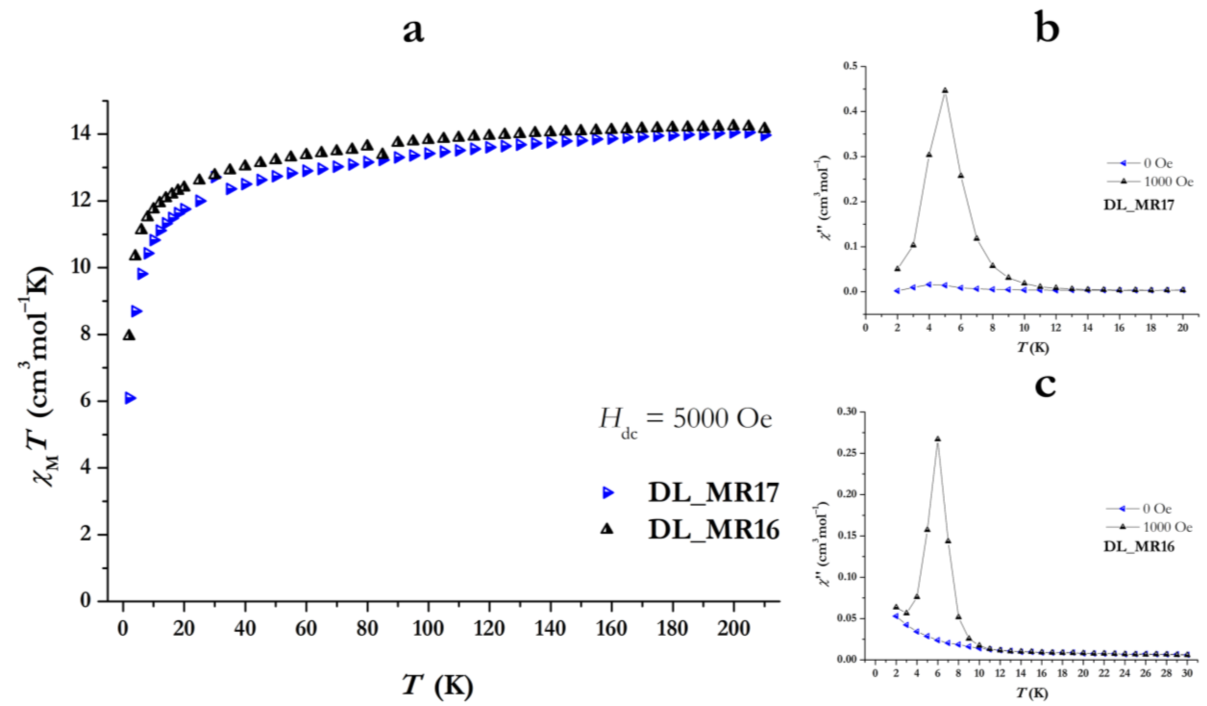

Figure 3.24. (**a**) Temperature-dependency of $\chi_M T$ for **DL_MR17** and **DL_MR16**, under an applied field of H_{dc} = 5000 Oe. Temperature-dependency of the χ'' response with and without a dc field at 1000 Hz for **DL_MR17** (**b**) and **DL_MR16** (**c**).

[(thf)$_2$LiCl$_2$Dy{*t*BuS(NSiMe$_3$)$_2$}$_2$] (**DL_MR16**) exhibits a maximum of χ'' at 6 K, whereas [(thf)$_2$LiCl$_2$Dy{MeS(NSiMe$_3$)$_2$}$_2$] (**DL_MR17**) at 5 K under a field of 1000 Oe. Under zero-field, no maxima were detected. The highest response was achieved at H_{dc} = 1200 Oe for **DL_MR16** and H_{dc} = 1000 Oe for **DL_MR17**. Therefore, succeeding measurements were run under these conditions. For [(thf)$_2$LiCl$_2$Dy{MeS(NSiMe$_3$)$_2$}$_2$] (**DL_MR17**) and [(thf)$_2$LiCl$_2$Dy{*t*BuS (NSiMe$_3$)$_2$}$_2$] (**DL_MR16**), the maxima of χ'' occur at low frequencies and shift toward higher frequencies with increasing the temperature, which display a true temperature dependency (**Figure 3.25.b** and **Figure 3.26.b**). The Cole-Cole plots (**Figure 3.25.c** and **Figure 3.26.c**) were fitted via the CC-fit program, and the extracted relaxation times were used to construct the corresponding Arrhenius plot (**Figure 3.25.d**; **Figure 3.26.d**). Here, a full fit of all data applying (eq. **3-3**) resulted in an energy barrier of 37.7 cm^{-1} for **DL_MR17** and 56.1 cm^{-1} for **DL_MR16**, respectively (**Table 3.23.**).

Table 3.23. Best fitting parameter for **DL_MR16** [(thf)$_2$LiCl$_2$Dy{*t*BuS(NSiMe$_3$)$_2$}$_2$] at H_{dc} = 1200 Oe and **DL_MR17** [(thf)$_2$LiCl$_2$Dy{MeS(NSiMe$_3$)$_2$}$_2$] at H_{dc} = 1000 Oe. R_2 displaces the error of the full fit.

	U (cm^{-1})	τ_0 (s)	C (s^{-1}K^{-n})	n	τ_{QTM} (s)	R_2
DL_MR16	56.1 (±2.1)	$1.66 \cdot 10^{-9}$ ($\pm 1.0 \cdot 10^{-9}$)	0.060 (±0.03)	6.06 (±0.26)	0	0.99998
DL_MR17	37.7 (±3.7)	$9.56 \cdot 10^{-7}$ ($\pm 1.0 \cdot 10^{-8}$)	0.60 (±0.2)	5.96 (±0.14)	0	0.99985

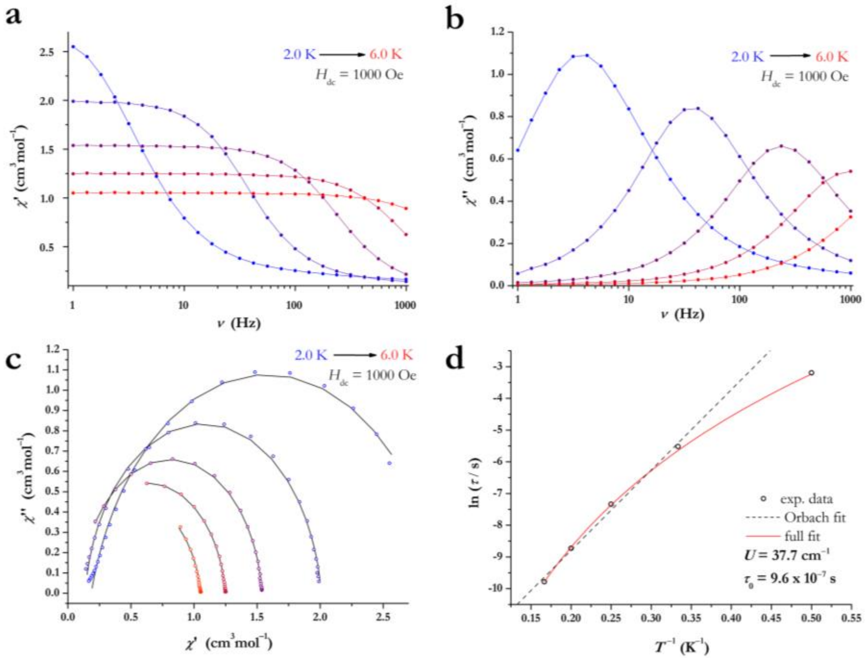

Figure 3.25. Magnetic data for $[(thf)_2LiCl_2Dy\{MeS(NSiMe_3)_2\}_2]$ (**DL_MR17**) under an applied dc field of 1000 Oe. Dynamic in-phase (**a**) and out-of-phase (**b**) susceptibilities versus variable frequencies from 2.0 to 6.0 K. Lines are guides for the eyes. (**c**) Cole-Cole plot with corresponding CC-fit data. (**d**) Arrhenius plot with the red curve exemplifying the full fit of all relaxation processes and the dashed line demonstrating a sole Orbach regression.

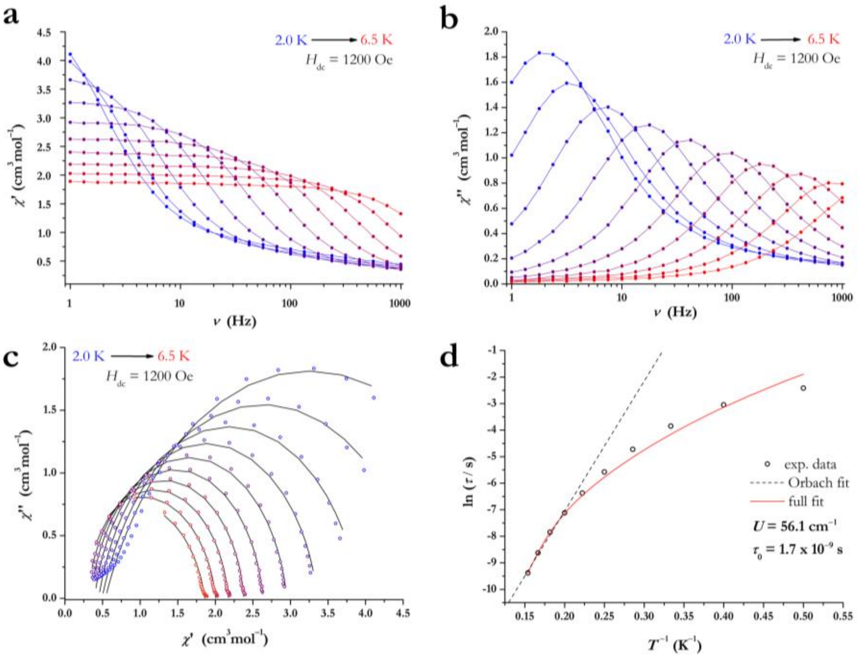

Figure 3.26. Magnetic data for $[(thf)_2LiCl_2Dy\{t\text{BuS}(NSiMe_3)_2\}_2]$ (**DL_MR16**) under an applied dc field of 1200 Oe. Dynamic in-phase (**a**) and out-of-phase (**b**) susceptibilities versus variable frequencies from 2.0 to 6.5 K. Lines are guides for the eyes. (**c**) Cole-Cole plot with corresponding CC-fit data. (**d**) Arrhenius plot with the red curve exemplifying the full fit of all relaxation processes and the dashed line demonstrating a sole Orbach regression.

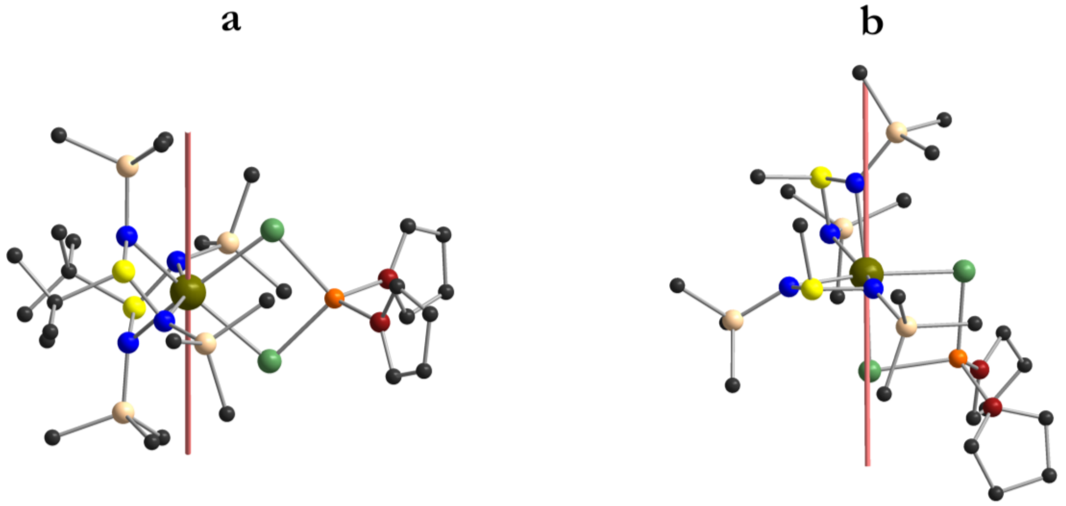

Figure 3.27. Orientation of the main magnetic axes (light coral) of the ground state for both Dy^{III} centers of [(thf)$_2$LiCl$_2$Dy{*t*BuS(NSiMe$_3$)$_2$}$_2$] (**DL_MR16**) and [(thf)$_2$LiCl$_2$Dy{MeS(NSiMe$_3$)$_2$}$_2$] (**DL_MR17**), calculated with the program Magellan and illustrated with the program Diamond 3.[174] All hydrogen atoms are omitted for clarity. Color code: C: (black), N: (blue), O: (red), Si: (light brown), Li: (orange), Cl: (green), and Dy: (gold).

The initial target was building an alternating chain with each lanthanide center chelated by two sulfinate ligands. However, adjusting stoichiometry did not result in the desired complexes. Most likely the lithium-halide co-complexation is hindering the further substitution of the chlorido ligand. Nevertheless, the magnetic axes for both complexes are calculated based on the electrostatic model in the program Magellan to determine the next areas of investigation (**Figure 3.27.**).[174] Here, the main magnetic axes are oriented away from the donor atoms since the remaining halides influence the geometry strongly. Future approaches should focus on fine-tuning the local geometry to align the magnetic axes with the ligand field.

3.7.4. Summary and concluding remarks for functionalized sulfinates for d-and f-metal chemistry

This chapter introduced six new metal complexes and studied their magnetic properties via SQUID magnetometry. First, the anthracenyl substitutes sulfinate **L$_6$** formed dinuclear d- and f-metal complexes were. Where, only the cobalt candidate [{(thf)$_2$LiCl$_2$Co(NSiMe$_3$)$_2$S}$_2$An] illustrated SMM behavior. However, our initial target was building an alternating chain with each metal center chelated by two sulfinate ligands. We assume that the co-complexation of lithium chloride hampered the coordination of a second sulfinate ligand. Therefore, one should avoid the lithium species and instead focus on the protonated ligand **L$_6$** or employ a heavier alkali metal homolog that is less likely to trigger a lithium halide co-complexation. This approach is further elucidated in the next chapter.

Second, two field-induced dysprosium SMMs were reported based on the methyl-[(thf)Li{MeS(NSiMe$_3$)$_2$}]$_2$ (**L$_8$**) and *tert*-butyl- [Li{*t*BuS(NSiMe$_3$)$_2$}]$_2$ (**L$_7$**) substituted diimidosulfinate ligand. The solid-state analysis demonstrated the presents of lithium chloride co-complexation, as reported for the complexes mentioned above in this chapter. Despite the lack of pure axial ligand symmetry, maxima in the out-of-phase susceptibility stemming from SMM behavior were detected up to 5.0 K for[(thf)$_2$LiCl$_2$Dy{MeS(NSiMe$_3$)$_2$}$_2$] (**DL_MR17**) and up to 6.0 K for [(thf)$_2$LiCl$_2$Dy{*t*BuS(NSiMe$_3$)$_2$}$_2$] (**DL_MR16**). Again, further improvements are feasible upon avoiding the lithium precursor and removing the remaining chloride ligands. The next paragraph puts these ideas into practice.

3.7.5. Strategies to avoid lithium halide co-complexation

In order to apply the abovementioned improvement strategies, the lithiated ligands **L$_6$** and **L$_7$** were first protonated via an ammonia salt. For this, the lithium species **L$_6$** and **L$_7$** were suspended in *n*-pentane with 2 equiv. *t*BuNH$_3$Cl (**Scheme 3.19.**). [An{S(NSiMe$_3$)(NHSiMe$_3$)}$_2$] (**22**) was obtained as yellow crystals and [*t*BuS(NSiMe$_3$)(NHSiMe$_3$)] (**23**) as colorless crystals, both in high purity after two cycles of recrystallization. In 1989, HÄNSSGEN and coworkers isolated **23** already via a modified procedure, however they did not report the solid-state structure.[181]

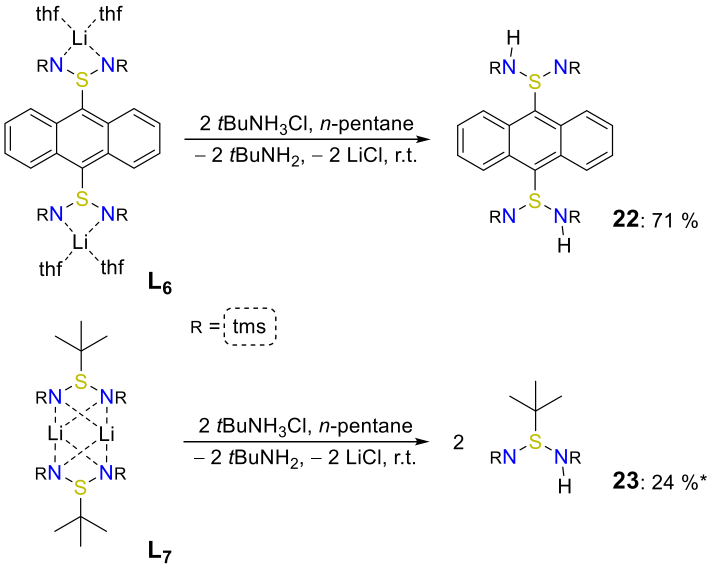

Scheme 3.19. Synthesis of the protonated sulfinate species [An{S(NSiMe$_3$)(NHSiMe$_3$)}$_2$] (**22**) [*t*BuS(NSiMe$_3$)(NHSiMe$_3$)] (**23**) employing 2 equiv. of the *t*BuNH$_3$Cl salt with L$_6$ and L$_7$. * The yield is not optimized.

Yellow needle-shaped crystals suitable for X-ray diffraction experiments were obtained for [An{S($NSiMe_3$)($NHSiMe_3$)}$_2$] (**22**), displaying the monoclinic space group *P*2$_1$/*n*. [*t*BuS($NSiMe_3$)($NHSiMe_3$)] (**23**) formed colorless blocks that also qualify for further charge density studies due to their high resolution (up to 0.45 Å) and crystallizes in the triclinic space group $P\bar{1}$. The asymmetric unit of **22** contains half a complex moiety (**Figure 3.28.a**), while two entire molecules are placed in the asymmetric unit of **23** (**Figure 3.28.b**). The S–N bonds are not equidistant and scale from 1.535(10) to 1.653(7) Å for **22** and from 1.5778(12) to 1.6517(12) for **23** (**Table 3.24.**). These deviations between both S–N bond lengths are attributed to the protonation of one nitrogen donor side, while the N–H distance (0.79(4)-0.92(3) Å) is within the frame for such complexes.[120,182] Next, the S–C bond lengths are slightly shorter for **22** (1.809(7) Å) than for **23** (1.8548(14)-1.8570(15) Å), as the former is associated with the electron-rich backbone of an anthracenyl substituent. Interestingly, the influence of the *tert*-butyl group led to an acuter N–S–N angles in **23** (107.84(7)-108.41(6)°) than reported for **22** (114.5(6)°)with the anthracenyl spacer.

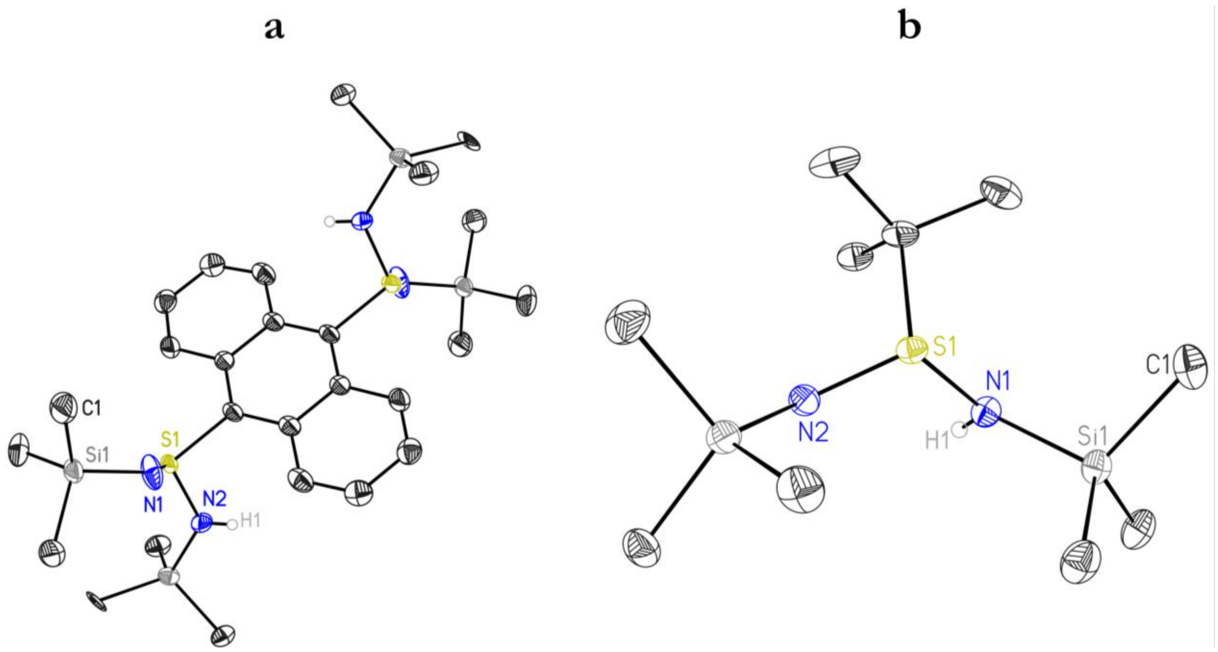

Figure 3.28. (**a**) The solid-state structures of [An{S($NSiMe_3$)($NHSiMe_3$)}$_2$] (**22**) (An = $C_{14}H_8$) and (**b**) [*t*BuS($NSiMe_3$)($NHSiMe_3$)] (**23**). Thermal ellipsoids are displayed at a probability level of 50%. Hydrogen atoms and lattice solvent molecules are omitted for clarity. The hydrogen atoms, apart from H1 that could be taken from the Fourier map and refined freely, are omitted for clarity

Table 3.24. Selected bond lengths [Å] and angles [°] for [An{S($NSiMe_3$)($NHSiMe_3$)}$_2$] (**22**) (An = $C_{14}H_8$) and [*t*BuS($NSiMe_3$)($NHSiMe_3$)] (**23**).

	S–N$_{range}$	S–C$_{range}$	N–H$_{range}$	N–H$_{range}$	N(1)-S(1)-N(2)$_{range}$
22	1.535(10)-1.653(7)	1.809(7)	0.79(4)	0.79(4)	114.5(6)
23	1.5778(12)-1.6517(12)	1.8548(14)-1.8570(15)	0.85(2)-0.92(3)	0.85(2)-0.92(3)	107.84(7)-108.41(6)

The initial approach to proceed with the protonated species **22** was to employ the bis(trimethylsilyl)amine metal salts to introduce d- and f-metals to this ligand. Therefore, the corresponding $[Ln(HMDS)_3]$ (with Ln = Dy^{III} and Er^{III}) and the $[M(HMDS)_2]$ (with M = Co^{II}, Fe^{II}) were combined with 0.5, 1.0, and 2.0 equiv. of **22**. However, neither donating nor non-donating solvents facilitated any reaction under ambient temperatures. Moreover, all attempts to apply reaction conditions at higher temperatures failed. Assumingly, either the steric bulkiness of the precursors is too high or the basicity of the HMDS salts is not strong enough to abstract the proton from the sulfiniminamine. This issue was addressed by preparing the sodium $[An_{0.5}\{S(SiMe_3N)_2(thf)_2Na_2(NSiMe_3)_2S\}An_{0.5}]_n$ (**24**) and potassium $[(thf)_2K(NSiMe_3)_2S\}An\{S(SiMe_3N)_2K(thf)_2\}]$ (**25**) homologs to $\mathbf{L_6}$. Where 2.2 equiv. of the alkali metal hydrides were deployed and treated with **22** in thf resulting in the abovementioned complexes **24** and **25** (**Scheme 3.20.**). Both **24** and **25** were obtained as red block-shaped crystals suitable for X-ray diffraction experiments. **24** is arranged in a chain-like structure, where each sodium center is four-fold coordinated by three nitrogen donors of two sulfinate ligands and one thf moiety, crystallizing in the monoclinic space group $P2_1/n$ (**Figure 3.29.**) The potassium homolog **25** displays one entire complex molecule in the asymmetric unit and crystallizes in the monoclinic space group $P2_1/c$. The coordination environment of the potassium ions is analog to the lithium species $\mathbf{L_6}$. Distances for the M–N bonds follow the ionic radii trend from lithium to potassium and show values of 2.361(3)-2.609(3) Å for **24** and 2.777(4)-3.002(4) Å for **25** (**Table 3.25.**). A similar trend is present for the M–O bond lengths for **24** (2.271(15)-2.289(14) Å) and **25** (2.707(4)-2.767(4) Å), respectively.

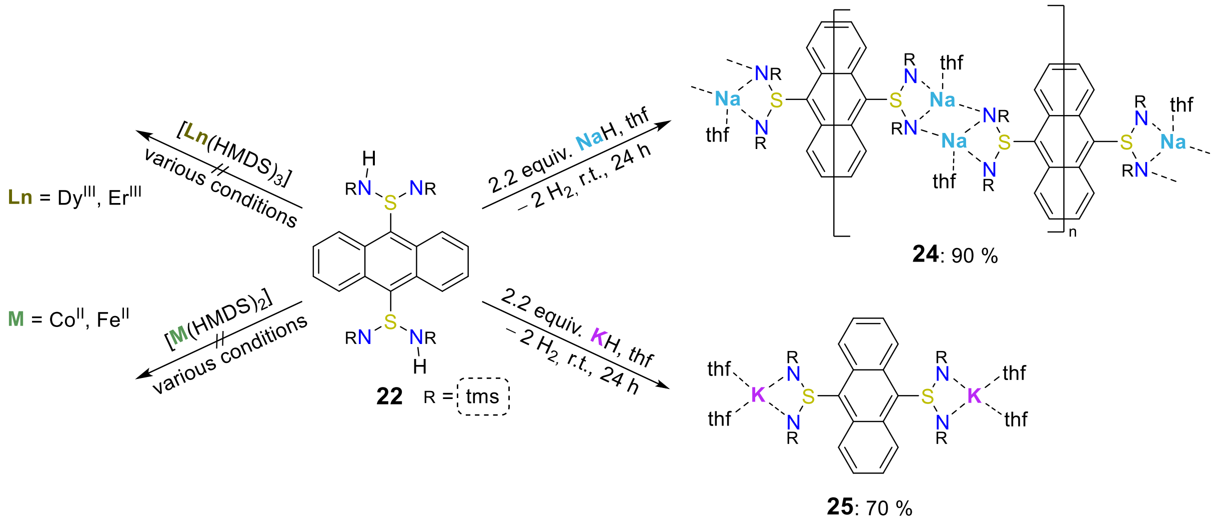

Scheme 3.20. (**left**) Attempts to synthesize d- and f-metal complexes by employing the corresponding HMDS salts $[An\{S(NSiMe_3)(NHSiMe_3)\}_2]$ (**22**). (**right**) Procedure to access the sodium $[An_{0.5}\{S(SiMe_3N)_2(thf)_2Na_2(NSiMe_3)_2S\}An_{0.5}]_n$ (**24**) and potassium $[(thf)_2K(NSiMe_3)_2S\}An\{S(SiMe_3N)_2K(thf)_2\}]$ (**25**).

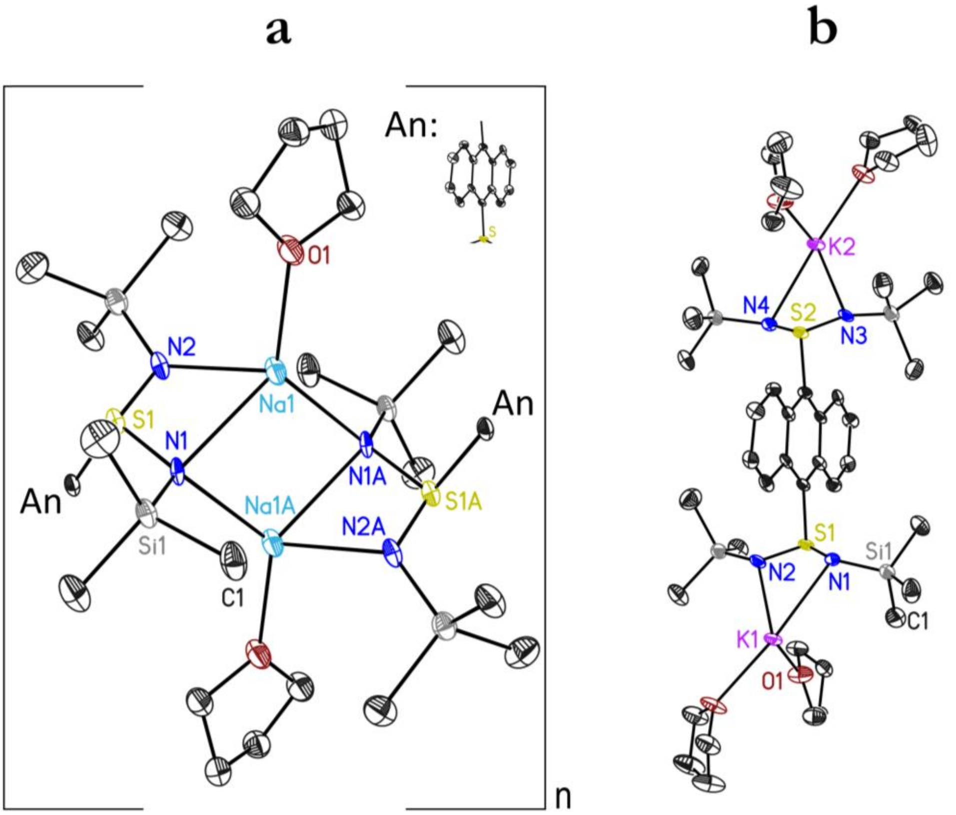

Figure 3.29. (**a**) Solid-state structure of $[An_{0.5}\{S(SiMe_3N)_2(thf)_2Na_2(NSiMe_3)_2S\}An_{0.5}]_n$ (**24**) (An = $C_{14}H_8$) and (**b**) $[(thf)_2K(NSiMe_3)_2S\}An\{S(SiMe_3N)_2K(thf)_2\}]$ (**25**). Thermal ellipsoids are portrayed at a probability level of 50%. The hydrogen atoms, apart from the ones attached to nitrogen atoms and lattice solvent molecules, are omitted for clarity.

Table 3.25. Selected bond lengths [Å] and angles [°] for $[An_{0.5}\{S(SiMe_3N)_2(thf)_2Na_2(NSiMe_3)_2S\}An_{0.5}]_n$ (**24**) and potassium $[(thf)_2K(NSiMe_3)_2S\}An\{S(SiMe_3N)_2K(thf)_2\}]$ (**25**).

	M–N$_{range}$	M–O$_{range}$	S–N$_{range}$	M–M	N–S–N$_{range}$
24	2.361(3)-2.609(3)	2.271(15)-2.289(14)	1.591(3)-1.616(3)	3.186(3)	105.76(16)
25	2.777(4)-3.002(4)	2.707(4)-2.767(4)	1.588(4)-1.618(4)	–	104.9(2)-106.0(2)

Almost equidistant values are found for the range of the S–N bond lengths and the N–S–N angles for **24** and **25**. Last, the Na–Na distance of 3.186(3) Å is in the typical range for such compounds.[5]

Subsequent reactions with **24** and **25** using the d- and f-metal halide salts were carried out in donating and non-donating solvents. None of these reactions succeeded, and additional heating of the reaction mixture did not result in the formation of the desired complexes (**Scheme 3.21.**).

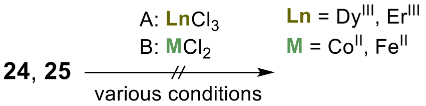

Scheme 3.21. Attempts to synthesize d- and f-metal complexes by employing the d- and f-metal halides with **24** and **25**.

3.7.6. Summary and concluding remarks for strategies to avoid lithium halide co-complexation

Starting from **L_6** and **L_7**, the coordinated lithium ions were successful removed via protonation with *t*$BuNH_3Cl$ giving rise to $[An\{S(NSiMe_3)(NHSiMe_3)\}_2]$ (**22**) (An = $C_{14}H_8$) and [*t*$BuS(NSiMe_3)(NHSiMe_3)]$ (**23**). Attempts to metalate **22** directly via the d- or f-metal bis(trimethylsilyl)amine salts remained unsuccessful. Therefore, the sodium and potassium complexes of **23** were prepared. Despite the reactivity of **L_6**, no reaction with the lanthanide(III) halides were observed for $[An_{0.5}\{S(SiMe_3N)_2(thf)_2Na_2(NSiMe_3)_2S\}An_{0.5}]_n$ (**24**) (An = $C_{14}H_8$) and $[(thf)_2K(NSiMe_3)_2S\}An\{S(SiMe_3N)_2K(thf)_2\}]$ (**25**). Furthermore, similar experiments are feasible for **23** and will be continued by KALLENBACH.

3.8. Alkali metal based triimidosulfites in lanthanide chemistry I

Major sections of this paragraph are in preparation to publish in:

[4] D. Lüert, R. Herbst-Irmer, D. Stalke. **2022**, *in preparation.*[4]

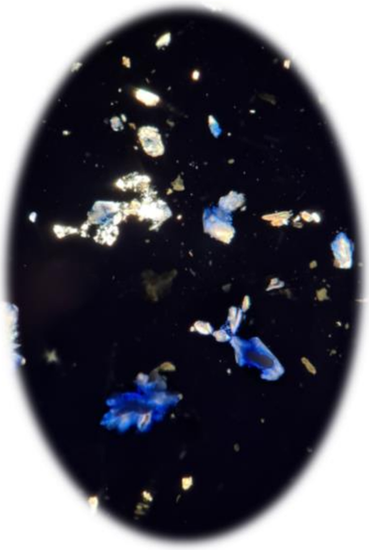

Crystals of **26** and **27** form blue radicals under exposure to oxygen.

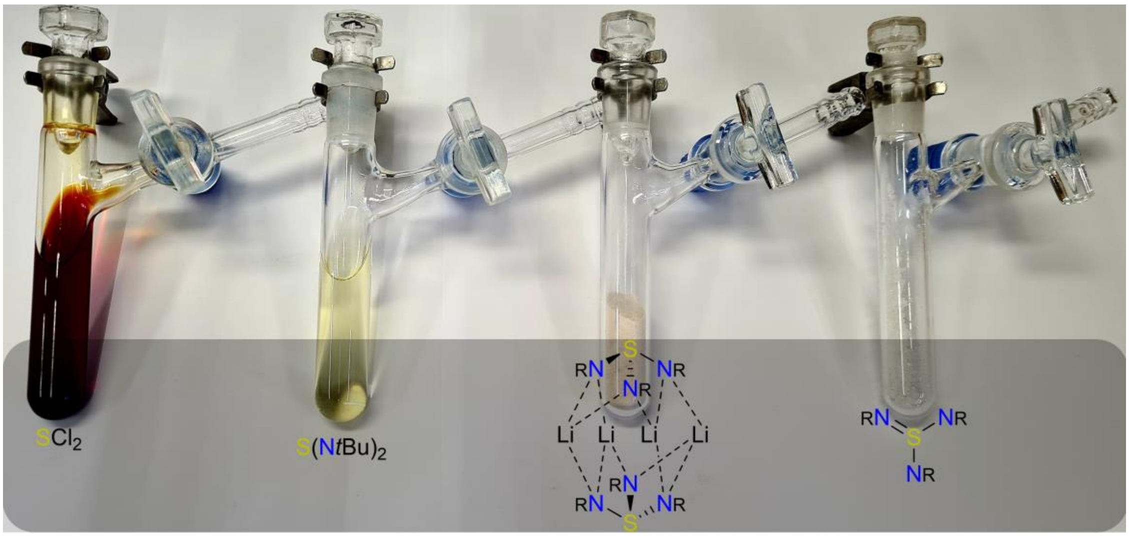

Illustration of all intermediates on the route to sulfurtriimide $S(N\textit{t}Bu)_3$ with R = *t*Bu.

3.8.1. Precursor synthesis and characterization

The general route to access sulfurtriimide $S(NtBu)_3$ (**L₁₀**) features a four-step reaction cycle, starting with the elements sulfur and chlorine that form sulfur dichloride. Initially, sulfur dichloride is freshly distilled since there is an equilibrium between sulfur di- and tetrachloride. Back in the 1960s, CLEMENS, BELL, and O'BRIEN established a convenient procedure to $S(NtBu)_2$ followed in this thesis and presented in the introduction chapter 1.9.1.[105] FLEISCHER and STALKE developed a method to retrieve $S(NtBu)_3$ without hazardous fluorine chemistry.[109] Here, $S(NtBu)_2$ is first treated with 2 equiv. LiNH*t*Bu in pentane, after removal of all volatiles, the obtained $[(Li_2(NtBu)_3S]_2$ (**L₉**) is dissolved toluene for crystallization (**Scheme 3.22.**).[109b] Importantly, it is mandatory to heat toluene to its boiling point. The final step involves controlled oxidation of **L₉** with 2 equiv. Br_2 that yields the sulfurtriimide $S(NtBu)_3$.[109a] JUNG fine-tuned this procedure and increased the yield and purity of the acquired $S(NtBu)_3$.[183] Therefore, one should remove the precipitated LiBr prior to the sublimation of $S(NtBu)_3$.[183]

Previous experience revealed that lithium-based precursors display the disadvantage of Lithium-Halide complexation, where the halide remains bound to the lanthanide center and bridges to the alkali metal..[122,123,183] The aim was to produce the higher homologs of **L₉** with sodium or potassium-based triimidosulfites. This idea started in 1993 when ILGE studied strategies to replace the lithium ions with other alkali metals and proposed $[S(tBuN)_3(thf)_3Na_3\{HNtBu)(NtBu)_2S\}]$ (**26**) and $[S(tBuN)_3(thf)_3K_3\{HNtBu)(NtBu)_2S\}]$ (**27**).[184] However, at this time, handling and isolation of these highly oxygen-sensitive compounds were not possible. Starting from the *tert*-butyl substituted sulfurdiimide $S(NtBu)_2$, complex **26,** and **27** were available from the treatment of the pure alkali metals (**Scheme 3.23.**). Instantly, a color change to dark red is observed for both reactions.

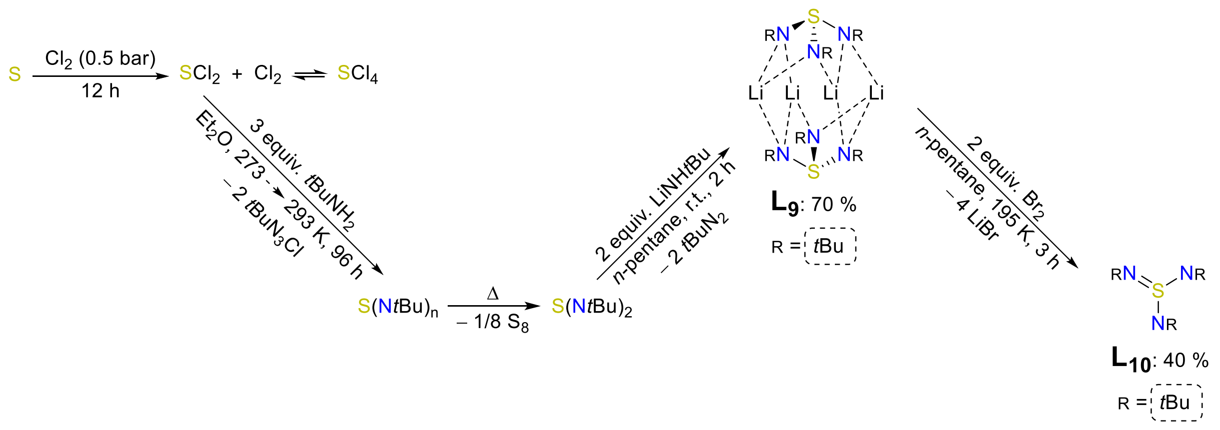

Scheme 3.22. General procedure to access $S(NtBu)_2$, $[(Li_2(NtBu)_3S]_2$ (**L₉**), and $S(NtBu)_3$ (**L₁₀**) starting from the pure elements sulfur and chlorine.

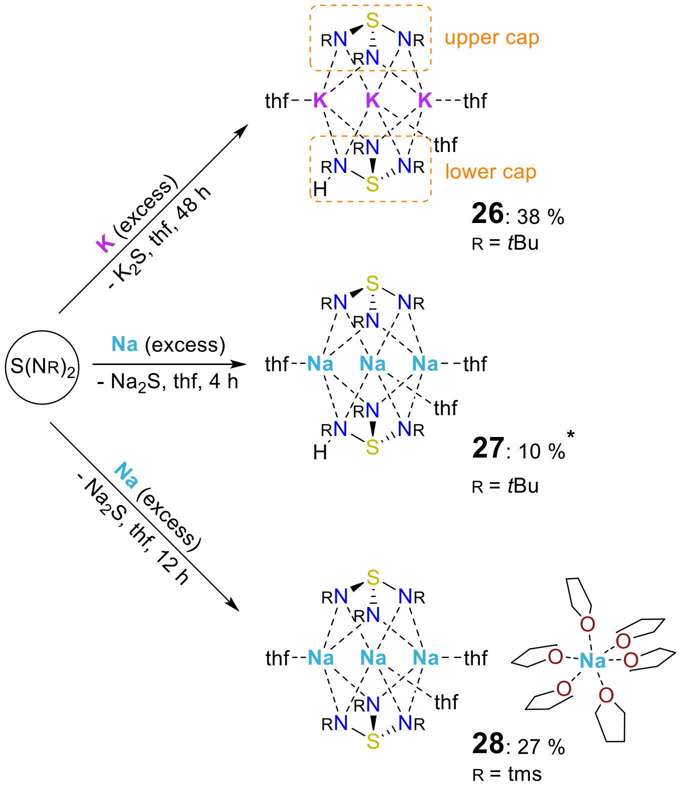

Scheme 3.23. Synthesis of $[\mathrm{S}(t\mathrm{BuN})_3(\mathrm{thf})_3\mathrm{K}_3\{\mathrm{HN}t\mathrm{Bu})(\mathrm{N}t\mathrm{Bu})_2\mathrm{S}\}]$ (**26**), $[\mathrm{S}(t\mathrm{BuN})_3(\mathrm{thf})_3\mathrm{Na}_3\{\mathrm{HN}t\mathrm{Bu})(\mathrm{N}t\mathrm{Bu})_2\mathrm{S}\}]$ (**27**), and $[\mathrm{Na}(\mathrm{thf})_6][\mathrm{S}(\mathrm{Me}_3\mathrm{SiN})_3(\mathrm{thf})_3\mathrm{Na}_3\{(\mathrm{NSiMe}_3)_3\mathrm{S}\}]$ (**28**) from $\mathrm{S}(\mathrm{NR})_2$ with the pure alkali metals in thf. ***** A route with higher yield (48 %) is obtained employing the $\mathrm{S}(\mathrm{N}t\mathrm{Bu})_3$ precursor (experimental section 5.3.27).

Similarly, **28** is obtained using the trimethylsilyl substituted $\mathrm{S}(\mathrm{SiMe}_3\mathrm{N})_2$ precursor resulting in a yellow slurry from which the sodium sodate complex **28** is isolated via centrifugation. The three aforehand mentioned complexes **26**-**28** are retrieved as block-shaped crystals suitable for X-ray diffraction experiments upon crystallizing from a saturated thf solution at 238 K. For both **26** and **27,** the orthorhombic space group $Pna2_1$ was found, with one complex molecule in the asymmetric unit, while **28** shows the monoclinic space group $C2/c$. The latter crystallizes as a three-fold twin simulating rhombohedral symmetry that was addressed with the corresponding twin law $(0.5\ -0.5\ -1\quad 0.5\ -0.5\ 1\quad -0.5\ -0.5\ 0)$ and features a solvent-separated ion pair. In each of the three complexes, two triimidosulfite ligands encapsulate three alkali metal ions and form a cage-like structure (**Figure 3.30.**). Here, the metal centers of **26**, **27**, and the anion of **28** are five-fold coordinated by four nitrogen and one oxygen donor atom. The thf separated cation of the sodium sodate motif **28** is bound to six thf donor molecules in a distorted octahedral fashion. This structural motif is unique for this ligand scaffold and a rare example of sodium sodates.[157]

In the cation, the Na–O bond lengths range from 2.344(3)-2.366(3) Å, which correlates with previously reported $[\mathrm{Na}(\mathrm{thf})_6]^+$cations.[157a–c] The distance of the sodium ions between the anion $[\mathrm{S}(\mathrm{Me}_3\mathrm{SiN})_3(\mathrm{thf})_3\mathrm{Na}_3\{(\mathrm{NSiMe}_3)_3\mathrm{S}\}]^-$ and the cation $[\mathrm{Na}(\mathrm{thf})_6]^+$ range from 10.412(2)-10.572(2) Å.

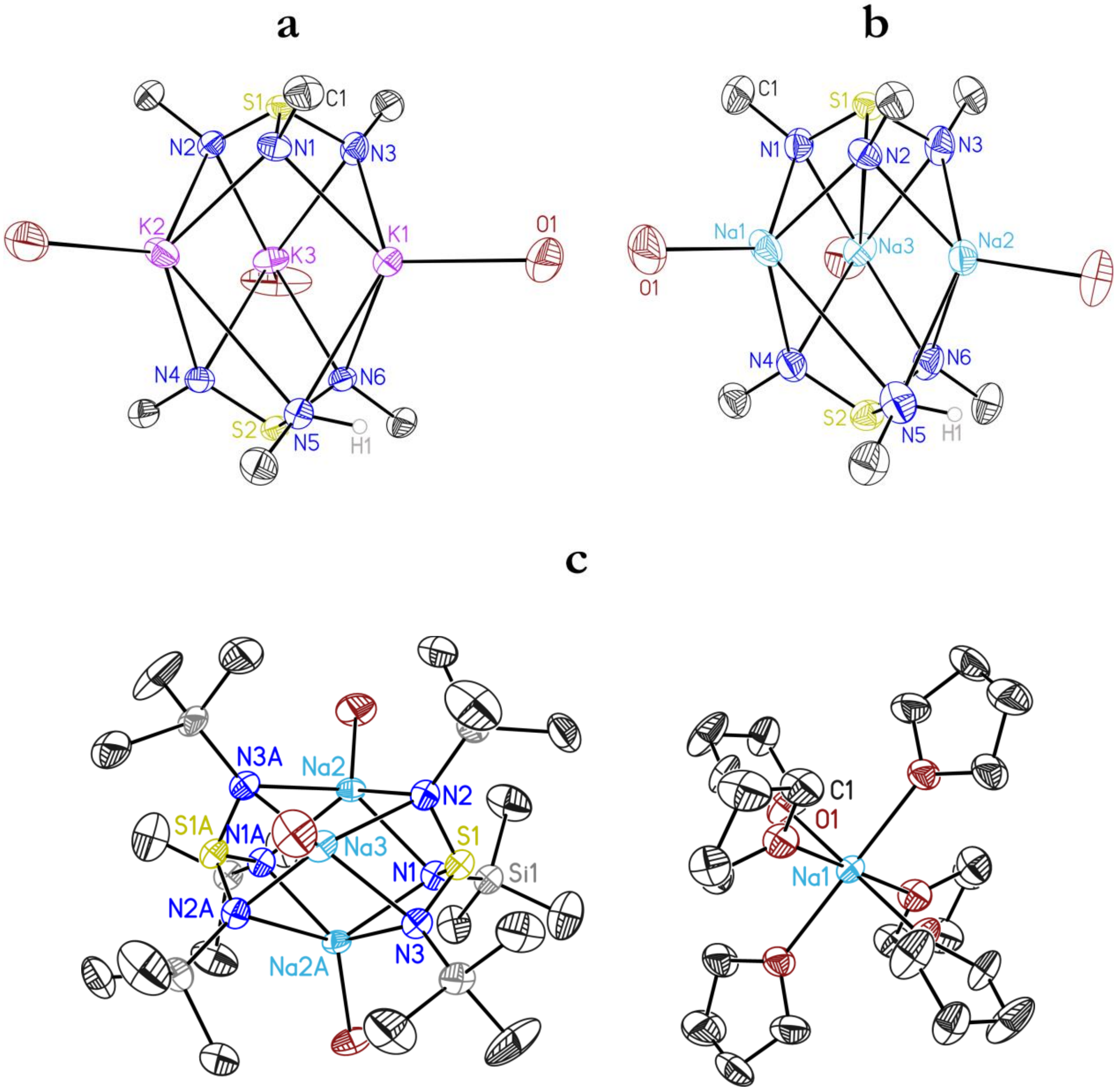

Figure 3.30. (**a**) The solid-state structure of $S(\textit{t}BuN)_3(thf)_3K_3\{HN\textit{t}Bu)(N\textit{t}Bu)_2S\}]$ (**26**), (**b**) $[S(\textit{t}BuN)_3(thf)_3Na_3\{HN\textit{t}Bu)(N\textit{t}Bu)_2S\}]$ (**27**), and (**c**) $[Na(thf)_6][S(Me_3SiN)_3(thf)_3Na_3\{(NSiMe_3)_3S\}]$ (**28**). Thermal ellipsoids are portrayed at a probability level of 50%. Lattice solvent molecules, and the thf molecules bound to each alkali metal ion are omitted for clarity. The hydrogen atoms, apart from H1 at N5 that could be taken from the Fourier map and refined freely, are omitted for clarity. The *tert*-butyl groups associated with each nitrogen atom are truncated for clarity.

According to elemental analysis data, two of the six thf moieties found in the solid-state structure are removed upon the drying process under reduced pressure. Moreover, the upper caps of **26**-**28**, and $\mathbf{L_9}$ illustrate low variations in the S(1)–N bond lengths and the N–S(1)–N angles (**Table 3.26.**). In contrast, the lower caps demonstrated high deviations in the individual bond lengths and angles for **26** and **27**. These observations confirmed the presence of the hydrogen atom at N(5), which results in an elongated S(2)–N(5) bond of 1.741(6) Å for **26** and 1.732(4) Å for **27** and significant shorter S(2)–N(4) and S(2)–N(6) bonds of 1.606(7) and 1.634(6) Å for **26** and 1.604(4) and 1.603(4) Å for **27**. Further, the N(5)–S(2)–N(4) and N(5)–S(2)–N(6) angles are narrowed to 97.4(3) and 100.6(4)° for **26** and to 96.1(2) and 102.4(2)° for **27**, while the N(6)–S(2)–N(4) angle is widened to 108.2(5)° for **26** and to 103.13(8) for **27**. The exchange of the sterically more demanding lone pair with a hydrogen atom explains this phenomenon.

Usually, detecting a hydrogen atom at this ligand class is challenging with standard NMR techniques due to its fast exchange rate. Here, the signal distribution of the *t*Bu groups of 3:2:1 in the ^{1}H-NMR indicates the presence of the protonated nitrogen, where the value of 3 corresponds to the upper cap ($S(NtBu)_3$) and the integration values of 2 and 1 to the lower cap ($S(NtBu)_2(HNtBu)$) (**Figure 3.31.**). ^{15}N-HMBC NMR data finally confirmed the protonation of one nitrogen atom also in solution (experimental section 5.3.27).

Next, shining light on the M–N distances, the reported values follow the trend of the ionic radii and increase from the lithium species **L_9** (2.006(4) Å) to the potassium complex **26** (2.630(2)-3.002(6) Å). The same trend applies to the M–M distances inside the cages, increasing from **L_9** (2.427-2.773 Å) to **27** (3.1509(19)-3.335(2) Å) and **28** (3.172(3)-3.211(2) Å), reaching 3.6510(10)-3.8419(10) Å in **26**, respectively.

Table 3.26. Selected bond lengths [Å] and angles [°] for $[S(tBuN)_3(thf)_3K_3\{HNtBu)(NtBu)_2S\}]$ (**26**), $[S(tBuN)_3(thf)_3Na_3\{HNtBu)(NtBu)_2S\}]$ (**27**), $[Na(thf)_6][S(Me_3SiN)_3(thf)_3Na_3\{(NSiMe_3)_3S\}]$ (**28**), and $[(Li_2(NtBu)_3S]_2$ (**L_9**), which is shown for comparability reasons.[109b]

	26	**27**	**28**	**L_9**[109b]
M–N$_{range}$[a]	2.630(2)-3.002(6)	2.340(4)-2.705(4)	2.462(4)-2.535(4)	2.006(4)[c]
M–O$_{range}$	2.712(6)-2.760(13)[b]		2.344(3)-2.366(3)	–
M–M$_{range}$	3.6510(10)-3.8419(10)	3.1509(19)-3.335(2)	3.172(3)-3.211(2)	2.427-2.773
M–M$_{range}$[d]	–	–	10.412(2)-10.572(2)	–
S(1)–N$_{range}$	1.644(3)-1.650(2)	1.586(4)-1.657(3)	1.615(4)-1.646(4)	1.644(2)-1.658(1)
S(2)–N(4)	1.606(7)[b]	1.604(4)	–	–
S(2)–N(5)	1.741(6)[b]	1.732(4)	–	–
S(2)–N(6)	1.634(6)[b]	1.603(4)	–	–
N–S(1)–N$_{range}$	102.77(13)-104.36(13)	99.09(18)-103.13(18)	102.13(19)-104.65(19)	100.85(7)-105.34(7)
N–S(2)–N$_{range}$	97.4(3)-108.2(5)[b]	96.1(2)-103.13(18)	–	–

[a] Disordered atoms are not considered; [b] Considering only the main component; [c] Average M–N bond length; [d] Distances of the sodium ions between the anion $[S(Me_3SiN)_3(thf)_3Na_3\{(NSiMe_3)_3S\}]^-$ and the cation $[Na(thf)_6]^+$.

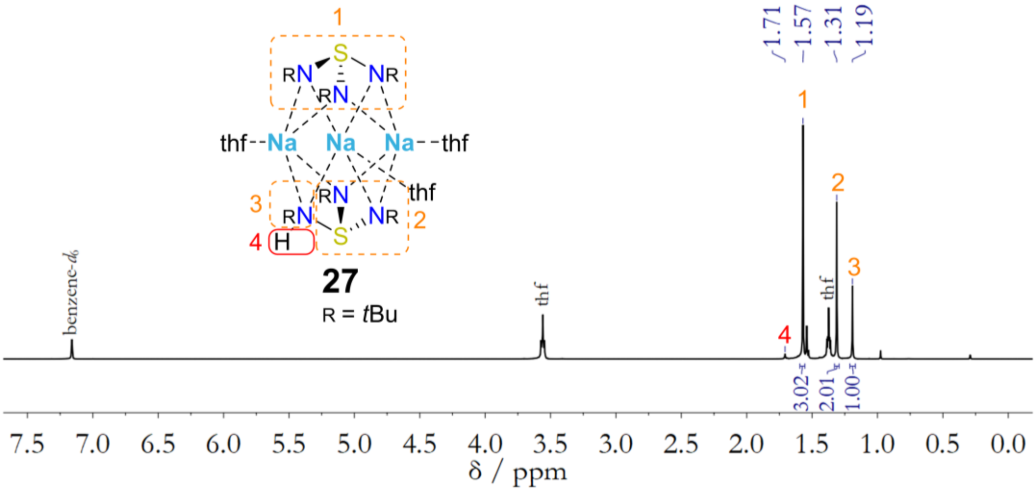

Figure 3.31. ^{1}H-NMR (500 MHz, 298 K, benzene-d_6) for **27**. δ / ppm = 1.19 (s, 9H, HNC(CH_3)), 1.31 (s, 18H, 2 NC(CH_3)), 1.57 (s, 27H, 3 NC(CH_3)), and 1.71 (s, 1H, *H*NC). The residual solvent signals are referred to coordinated thf.

3.8.2. Synthesis and solid-state structures of 29-32

Many have endeavored to exchange the alkali metal centers of $[(\mathrm{Li_2(N}t\mathrm{Bu)_3S}]_2$ (**L₉**) with lanthanide ions to obtain an encapsulated lanthanide center between two triimidosulfite ligands featuring an almost axial coordination geometry. Nevertheless, no one was successful in achieving the envisioned complexes. Henceforth, the sodium and potassium analogues **26**-**28** were prepared and characterized in the previous chapters. These precursors are anticipated to be more reactive, and the size of sodium and potassium ions matches the steric of lanthanide ions better than the lithium ones. Therefore, reactions of $[\mathrm{S}(t\mathrm{BuN})_3(\mathrm{thf})_3\mathrm{K}_3\{\mathrm{HN}t\mathrm{Bu})(\mathrm{N}t\mathrm{Bu})_2\mathrm{S}\}]$ (**26**) and the lanthanide halides were performed. Despite the several attempts in different solvents and at various temperature conditions, the high reactivity of **26** hampers the isolation of new complexes (**Scheme 3.24.**). All reactants turn into black, insoluble matter after the reaction.

The sodium species $[\mathrm{S}(t\mathrm{BuN})_3(\mathrm{thf})_3\mathrm{Na}_3\{\mathrm{HN}t\mathrm{Bu})(\mathrm{N}t\mathrm{Bu})_2\mathrm{S}\}]$ (**27**) is expected to display the ideal mixture of reactivity and selectivity. Consequently, we treated **27** with terbium(III) chloride in thf to exchange the three sodium ions from the cage and insert the lanthanide center via a metathesis reaction (**Scheme 3.25.**). After removing precipitated sodium chloride, crystallization from a saturated thf solution yielded colorless block-shaped crystals suitable for X-ray diffraction experiments. Surprisingly, this reaction forms four different terbium species (**29**-**32**) that crystallize together, featuring the same crystal habitus. Separation was achieved via measuring the individual crystals. Tremendous efforts were made to separate **29**-**32** from each other. Here, different solvents mixtures were evaluated for the crystallization cycle. Only the proportions of the obtained species changed. Isolation of a single complex species was not achieved within this thesis as they crystallized together. Changing the reaction conditions did also not lead to a single species. Nevertheless, these terbium complexes demonstrate the rich and diverse chemistry of the SN ligands and exemplify the cleavage of the S–N bond as sulfide and *tert*-butylamine form upon the reaction.

Complexes [ClTb{Na(thf)}$_2${(N*t*Bu)$_3$S}$_2$] (**29**), [{Na(thf)}$_2${S(*t*BuN)$_3$}$_2$TbSTb{Na(thf)}$_2${(N*t*Bu)$_3$S}$_2$] (**30**), and [{S(*t*BuN)$_3$}TbSTb{(N*t*Bu)$_3$S}]$_2$ (**32**) display half and [(*t*BuNH)Tb{(N*t*Bu)$_3$S}]$_2$ (**31**) an entire complex molecule in the asymmetric unit (**Figure 3.32.**). For **29** we determined a monoclinic space group ($C2/c$), while **30**-**32** share the triclinic space group $P\bar{1}$.

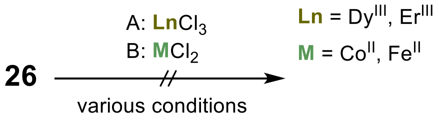

Scheme 3.24. Attempts to access d- and f-metal complexes starting from **26** and the metal halides.

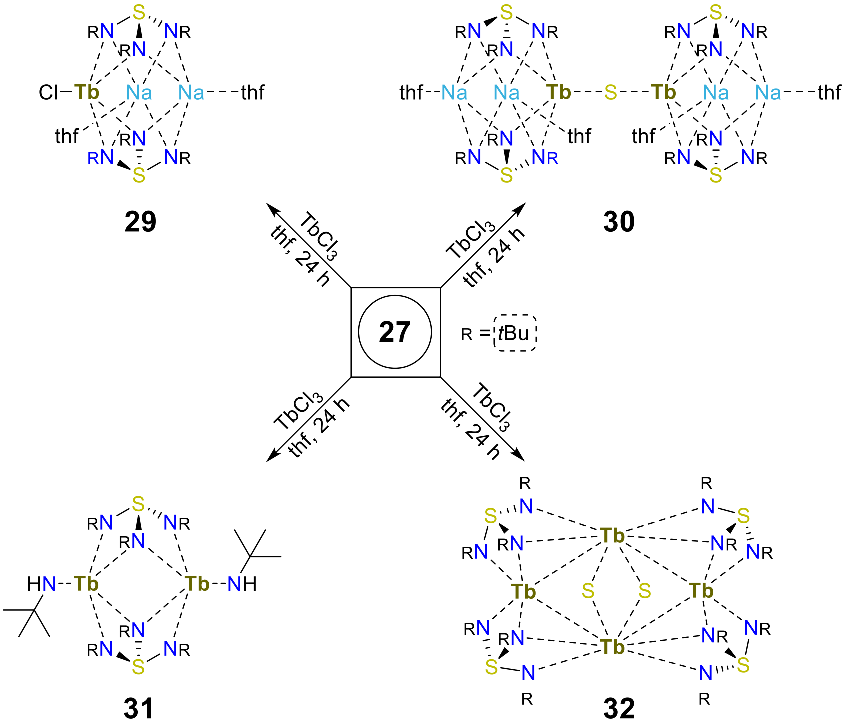

Scheme 3.25. Synthesis of [ClTb{Na(thf)}$_2${(N*t*Bu)$_3$S}$_2$] (**29**), [{Na(thf)}$_2${S(*t*BuN)$_3$}$_2$Tb STb{Na(thf)}$_2${(N*t*Bu)$_3$S}$_2$] (**30**), [(*t*BuNH)Tb{(N*t*Bu)$_3$S}]$_2$ (**31**), and [{S(*t*BuN)$_3$}TbSTb{(N*t*Bu)$_3$S}]$_2$ (**32**) from **27** and TbCl$_3$ in thf.

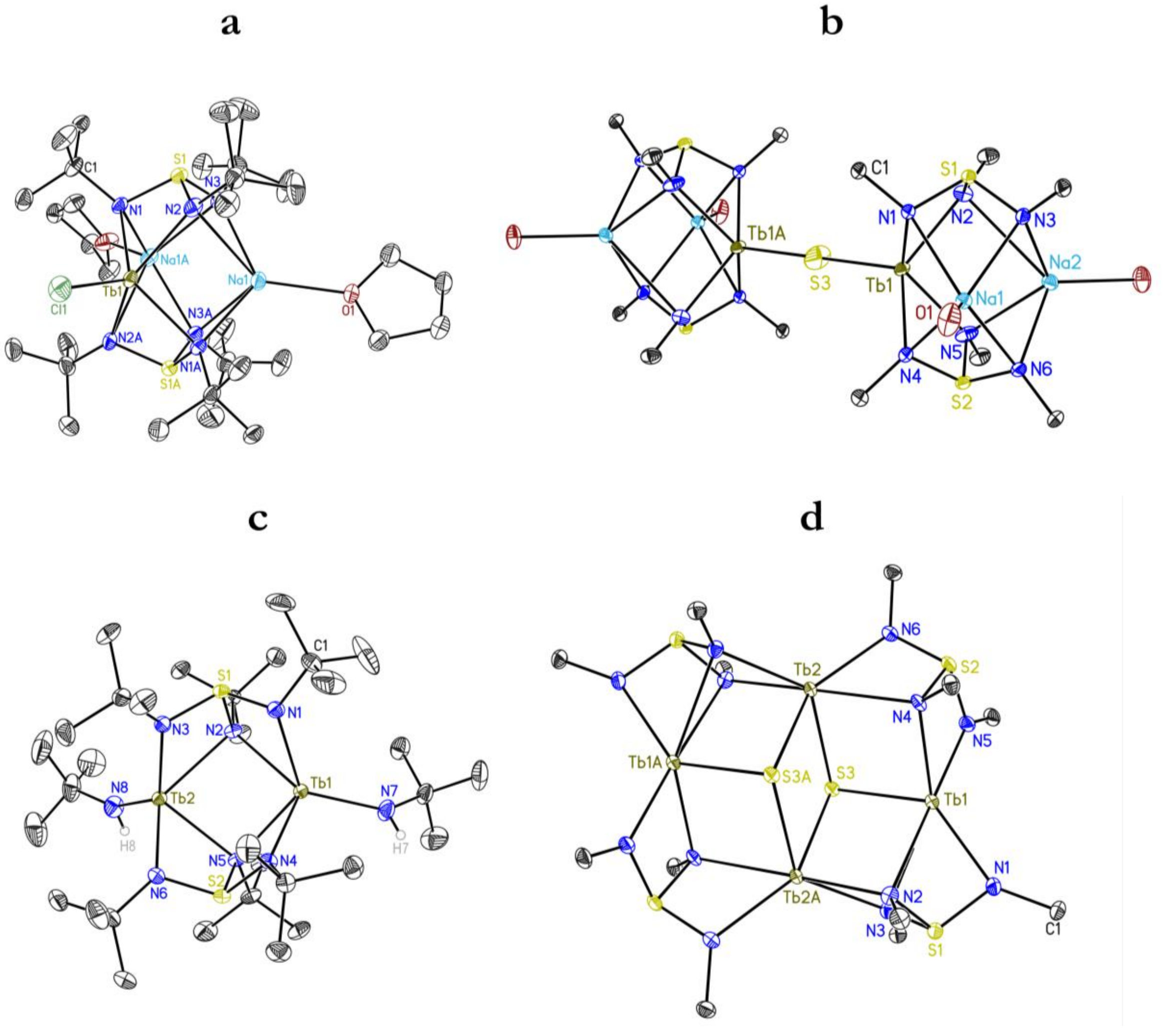

Figure 3.32. (**a**) Solid-state structures of [ClTb{Na(thf)}$_2${(N*t*Bu)$_3$S}$_2$] (**29**), (**b**) [{Na(thf)}$_2${S(*t*BuN)$_3$}$_2$Tb STb{Na(thf)}$_2${(N*t*Bu)$_3$S}$_2$] (**30**), (**c**) [(*t*BuNH)Tb{(N*t*Bu)$_3$S}]$_2$ (**31**), and (**d**) [{S(*t*BuN)$_3$}TbSTb{(N*t*Bu)$_3$S}]$_2$ (**32**). Thermal ellipsoids are displayed at a probability level of 50%. All lattice solvent molecules and hydrogen atoms, apart from H7 at N7 that could be taken from the Fourier map and refined freely, are omitted for clarity. The *tert*-butyl groups associated with each nitrogen atom are truncated for **b** and **d**, and only the donor atoms of the thf moieties are displayed in **b**.

Distances between the terbium centers and the nitrogen donors exhibit a broad range for **29**-**32** (2.263(2)-2.893(2) Å), where the deviation is strongest in the Tb$_4$-tetramer **32** (2.263(2)-2.893(2) Å) and least in the Tb monomer **29** (2.302(3)-2.371(19) Å) (**Table 3.27.**). Complex **31** features additional *t*BuNH donor sides where the Tb–N bond length is shorter as all other Tb–N bond lengths (2.1903(18)-2.1921(19) Å). The terbium ions in **31** and **32** are separated by 3.4883(18) Å (**32**) to 3.5407(6) Å (**31**), which is within the range of reported heteronuclear terbium(III) clusters. Juxtaposing the Tb–S bond lengths in **30** (2.5494(9) Å) and **32** (2.6411(10)-2.7744(8) Å), are also in good agreement with previously reported complexes. Other Ln–S–Ln analogues range from 2.503-2.622 Å, while larger clusters range between 2.738 and 3.082 Å.

Table 3.27. Selected bond lengths [Å] and angles [°] for [ClTb{Na(thf)}$_2${(N*t*Bu)$_3$S}$_2$] (**29**), [{Na(thf)}$_2${S(*t*BuN)$_3$}$_2$Tb STb{Na(thf)}$_2${(N*t*Bu)$_3$S}$_2$] (**30**), [(*t*BuNH)Tb{(N*t*Bu)$_3$S}]$_2$ (**31**), and [{S(*t*BuN)$_3$}TbSTb{(N*t*Bu)$_3$S}]$_2$ (**32**).

	29	**30**	**31**	**32**
Tb–N$_{\text{range}}$[a]	2.302(3)-2.371(19)	2.3264(16)-2.4168(15)	2.2830(15)-2.4957(15)	2.263(2)-2.893(2)
Tb–Tb	-	-	3.5407(6)	3.4883(18)
Tb–S$_{\text{range}}$	-	2.5494	-	2.6411(10)
Tb–NH$_{\text{range}}$	-	-	2.1921(19)	-
S(1)–N(1)	1.691(3)	1.6779(15)	1.6334(16)	1.636(2)
S(1)–N(2)	1.675(3)	1.6591(15)	1.6963(16)	1.658(2)
S(1)–N(3)	1.616(3)	1.6267(15)	1.6435(16)	1.669(2)
S(2)–N(4)	-	1.6781(16)	1.6398(15)	1.695(2)
S(2)–N(5)	-	1.6781(16)	1.6987(15)	1.655(2)
S(2)–N(6)	-	1.6089(16)	1.6345(17)	1.622(2)
N–S–N$_{\text{range}}$	96.44(13)-105.22(14)	97.26(8)-104.74(8)	93.73(8)-113.63(8)	89.74(10)-114.30(11)

[a] Disordered atoms are not considered; [b] Only for the main component.

Shining light on the S–N bond lengths, the shortest distance is detected for S–N(3)/(6) in **29** and **30** as this donor site does not contribute to the lanthanide bond. For **31**, two lanthanide ions are coordinated by N(2) and N(5), leading to elongated S(1)–N(2)/(5) bonds. The unique flexibility of the N–S–N angles that adjust to almost any bonding situation is exemplified in complex **32** (89.74(10)-114.30(11)°). The least range is identified for **31**, where the N–S–N angles span from 97.26(8) to 104.64(8)°. Employing the potassium precursor **26** for metathesis reactions with terbium chloride failed, as strong ligand scrambling is present and fosters the formation of insoluble products that eludes from further characterizations.

3.8.3. Summary and concluding remarks for 29-32 and their precursors 26-28

Within this chapter, three alkali metal triimidosulfites $[\mathrm{S}(t\mathrm{BuN})_3(\mathrm{thf})_3\mathrm{K}_3\{(\mathrm{HN}t\mathrm{Bu})(\mathrm{N}t\mathrm{Bu})_2\mathrm{S}\}]$ (**26**) $[\mathrm{S}(t\mathrm{BuN})_3(\mathrm{thf})_3\mathrm{Na}_3\{(\mathrm{HN}t\mathrm{Bu})(\mathrm{N}t\mathrm{Bu})_2\mathrm{S}\}]$ (**27**), and $[\mathrm{Na}(\mathrm{thf})_6][\mathrm{S}(\mathrm{Me}_3\mathrm{SiN})_3(\mathrm{thf})_3\mathrm{Na}_3\{(\mathrm{NSiMe}_3)_3\mathrm{S}\}]$ (**28**) were synthesized and characterized via X-ray diffraction experiments. Noteworthily, the latter displays the rare structure motif of a sodium sodate, which was also studied for the Mebox ligand (chapter 3.6.2). Subsequent reactions of **26** with the lanthanide halides failed. The sodium analogue **27** leads to four different terbium derivatives upon reaction with the terbium halide salts. For the resulting complexes $[\mathrm{ClTb}\{\mathrm{Na}(\mathrm{thf})\}_2\{(\mathrm{N}t\mathrm{Bu})_3\mathrm{S}\}_2]$ (**29**), $[\{\mathrm{Na}(\mathrm{thf})\}_2\{\mathrm{S}(t\mathrm{BuN})_3\}\mathrm{TbSTb}\{\mathrm{Na}(\mathrm{thf})\}_2\{(\mathrm{N}t\mathrm{Bu})_3\mathrm{S}\}]$ (**30**), $[(t\mathrm{BuNH})\mathrm{Tb}\{(\mathrm{N}t\mathrm{Bu})_3\mathrm{S}\}]_2$ (**31**), and $[\{\mathrm{S}(t\mathrm{BuN})_3\}\mathrm{TbSTb}\ \{(\mathrm{N}t\mathrm{Bu})_3\mathrm{S}\}]_2$ (**32**) the solid-state structures were determined and compared. Nevertheless, isolation of these four complexes despite from separating crystals could not be accomplish in this thesis. Looking forward, the focus should be directed toward more selective triimidosulfite precursors to minimize the number of byproducts during the reaction. This approach is followed in the following chapter.

3.9. Alkali metal based triimidosulfites in lanthanide chemistry II

Major sections of this paragraph have been published in:

[5] D. Lüert, C. M. Legendre, R. Herbst-Irmer, D. Stalke. *Chem. Eur. J.* **2022**, *28*, e202104470.[5]

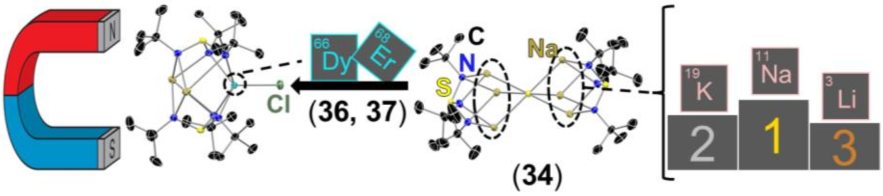

Solvent coordination is omitted.

3.9.1. Precursor synthesis and characterization

The aforementioned alkali-metal-based triimidosulfites (chapter 3.8) did not qualify for selective product formation as the obtained series of lanthanide complexes could not be separated from each other. Hence, the aim was to develop more selective precursors that process fewer side products. The initial strategy was to avoid donating solvents. However, a reaction of $\mathrm{S(N}t\mathrm{Bu)_2}$ with the pure alkali metals did not occur in non-donating solvents such as *n*-pentane or toluene. This observation suggests that the formation of alkali metal triimidosulfite cages requires a solvent with donor atoms to facilitate the reaction. For this reason, a (1:1) mixture of *n*-pentane/N,N,N',N'-tetramethylethylenediamine (tmeda) was chosen to avoid thf and slow down the reaction speed. Second, the focus was more directed toward sodium precursors as they are less reactive than the potassium analogues and sodium's ionic radius is a close fit to the radii of the lanthanides.

These precursors are accessible by treating the pure metals with sulfurdiimide, which was synthesized via established procedures.[103,105] The thf-free analogue to **26**, $[\{\mathrm{S}(t\mathrm{BuN})_2(t\mathrm{BuNH})\}_2\mathrm{K}_3(\mathrm{tmeda})\mathrm{K}_3\{(\mathrm{HN}t\mathrm{Bu})(\mathrm{N}t\mathrm{Bu})_2\mathrm{S}\}_2]$ (**33**) was prepared via an excess of potassium in a *n*-pentane/N,N,N',N'-tetramethylethylenediamine (tmeda) (1:1) mixture, by slowly adding sulfurdiimide. After stirring for 24 h, all solids were removed via filtration and **33** was obtained as a dark-red crystalline solid after doubly recrystallizing from *n*-pentane (**Scheme 3.26.**).

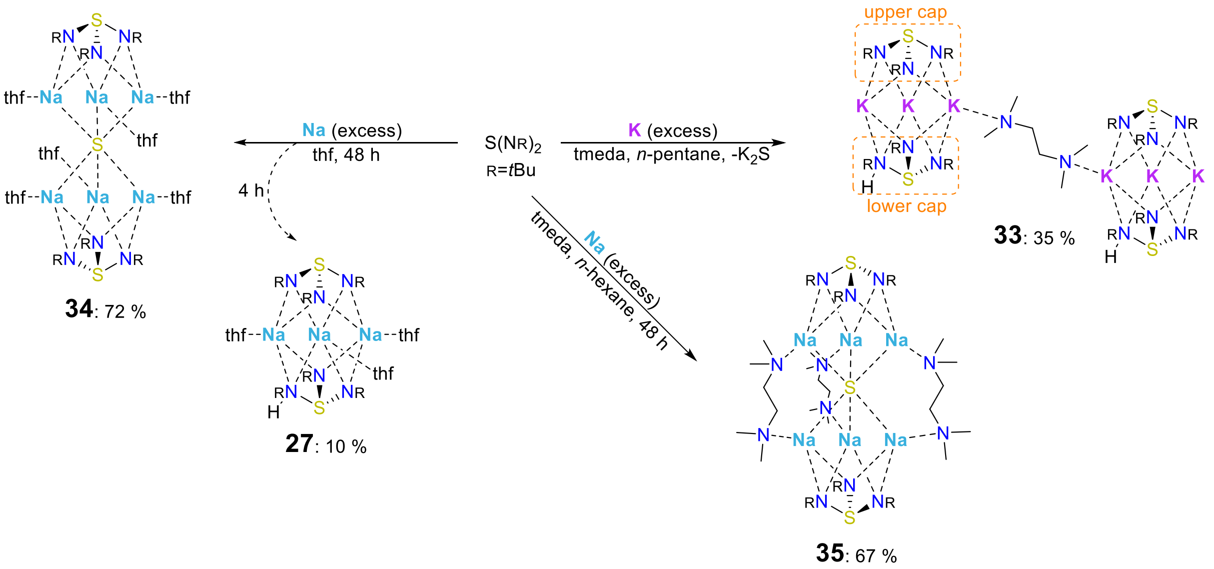

Scheme 3.26. Synthesis of potassium triimidosulfite $[\{\mathrm{S}(t\mathrm{BuN})_2(t\mathrm{BuNH})\}_2\mathrm{K}_3(\mathrm{tmeda})\mathrm{K}_3\{(\mathrm{HN}t\mathrm{Bu})(\mathrm{N}t\mathrm{Bu})_2\mathrm{S}\}_2]$ (**33**) and sodium triimidosulfites $[\mathrm{S}(t\mathrm{BuN})_3(\mathrm{thf})_3\mathrm{Na}_3\{\mathrm{HN}t\mathrm{Bu})(\mathrm{N}t\mathrm{Bu})_2\mathrm{S}\}]$ (**27**), $[\mathrm{S}(t\mathrm{BuN})_3(\mathrm{thf})_3\mathrm{Na}_3\mathrm{SNa}_3(\mathrm{thf})_3(\mathrm{N}t\mathrm{Bu})_3\mathrm{S}]$ (**34**), and $[(\mathrm{tmeda})_3\mathrm{S}\{\mathrm{Na}_3(\mathrm{N}t\mathrm{Bu})_3\mathrm{S}\}_2]$ (**35**) from sulfurdiimide and the pure alkali metals.

We assume a one-electron reduction pathway with radical intermediates as prior reported.[109,185] Furthermore, work directed toward the trimethylsilyl functionalized sulfurdiimide $\mathrm{S(Ntms)_2}$ observed radical properties upon reaction with alkali metals in lanthanide complexes.[186] Also BEWERIES and ROSENTHAL[187] reported the recombination of an amino and a sulfurdiimide fragment with a titanocene forming $\mathrm{S(Ntms)_3}$. Monitoring the reaction with NMR spectroscopy to reveal mechanistic insides was not achieved in previous studies and also failed in this thesis.[187]

Applying similar conditions with sodium yielded the $[(\mathrm{tmeda})_3\mathrm{S}\{\mathrm{Na}_3(\mathrm{N}t\mathrm{Bu})_3\mathrm{S}\}_2]$ (**34**) complex. Red impurities were extracted in *n*-hexane and **34** was obtained as a colorless solid in good yield (**Scheme 3.26.**). The treatment of sulfurdiimide with sodium fosters the formation of two products in thf. Notably, if the reaction time was stopped early, the kinetic stabilized intermediate $[\mathrm{S}(t\mathrm{BuN})_3(\mathrm{thf})_3\mathrm{Na}_3\{\mathrm{HN}t\mathrm{Bu})(\mathrm{N}t\mathrm{Bu})_2\mathrm{S}\}]$ (**27**) was isolatable in low yield (10 %). After 48 h, the thermodynamic stabilized product $[\mathrm{S}(t\mathrm{BuN})_3(\mathrm{thf})_3\mathrm{Na}_3\mathrm{SNa}_3(\mathrm{thf})_3(\mathrm{N}t\mathrm{Bu})_3\mathrm{S}]$ (**35**) was acquired and received as a colorless solid in high yield (72 %). The reader is directed to the experimental section for more details on the synthetic procedures (chapter 5.3.32).

$[\{\mathrm{S}(t\mathrm{BuN})_2(t\mathrm{BuNH})\}_2\mathrm{K}_3(\mathrm{tmeda})\mathrm{K}_3\{(\mathrm{HN}t\mathrm{Bu})(\mathrm{N}t\mathrm{Bu})_2\mathrm{S}\}_2]$ (**33**) was obtained as dark-red, block-shaped crystals, and illustrate a monoclinic crystal system ($P2_1/c$). The asymmetric unit comprises one complex molecule and half of the tmeda moiety, as depicted in the pink box (**Figure 3.33.**). One upper and one lower triimidosulfite ligand encapsulates three potassium ions, while a tmeda moiety bridges two complex units [L2 K3] through the K(3) atom. For the upper cap, low variations in S–N bond lengths and angles are found with S(1)–N distances ranging from 1.6422(14) to 1.6548(14) Å and the N–S(1)–N angles from 102.01(7)° to 105.51(7)° (**Table 3.28.**), respectively. In contrast, the lower cap illustrates a high deviation in the individual bond lengths and angles. That

Table 3.28. Selected bond lengths [Å] and angles [°] for $[\{\mathrm{S}(t\mathrm{BuN})_2(t\mathrm{BuNH})\}_2\mathrm{K}_3(\mathrm{tmeda})\mathrm{K}_3\{(\mathrm{HN}t\mathrm{Bu})(\mathrm{N}t\mathrm{Bu})_2\mathrm{S}\}_2]$ (**33**), $[(\mathrm{tmeda})_3\mathrm{S}\{\mathrm{Na}_3(\mathrm{N}t\mathrm{Bu})_3\mathrm{S}\}_2]$ (**34**), and $[\mathrm{S}(t\mathrm{BuN})_3(\mathrm{thf})_3\mathrm{Na}_3\mathrm{SNa}_3(\mathrm{thf})_3(\mathrm{N}t\mathrm{Bu})_3\mathrm{S}]$ (**35**).

	33	**34**	**35**
M–$\mathrm{N_{range}}$[a]	2.6001(14)-3.2356(16)	2.3300(17)	2.331(3)-2.562(4)
M–$\mathrm{M_{range}}$	3.6449(7)-3.9473(7)	3.1592(13)	3.151(2)-3.228(2)
S(1)–$\mathrm{N_{range}}$	1.6442(14)-1.6548(14)	1.6510(15)	1.645(3)-1.655(3)
S(2)–N(4)	1.5891(14)	1.6510(15)	1.658(3)
S(2)–N(5)	1.7590(15)	1.6510(15)	1.648(3)
S(2)–N(6)	1.6133(14)	1.6510(15)	1.653(3)
S(2/3)–$\mathrm{M_{range}}$	-	2.7691(8)	2.7232(18)-2.7623(17)
N–S(1)–$\mathrm{N_{range}}$	102.01(7)-105.51(7)	103.01(7)	102.04(16)-103.54(17)
N–S(2)–$\mathrm{N_{range}}$	95.78(7)-110.83(7)	103.01(7)	102.43(16)-103.82(17)

[a] Disordered atoms are not considered.

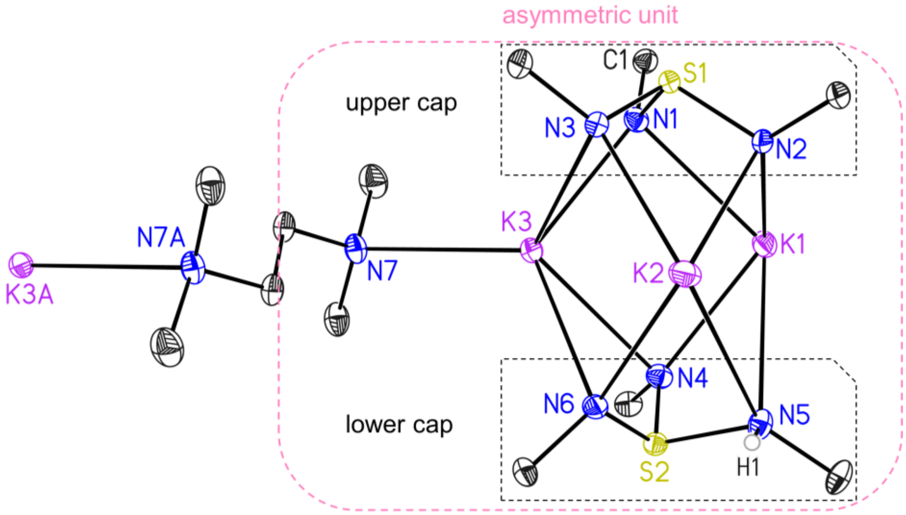

Figure 3.33. Solid-state structure of [{S(*t*BuN)$_2$(*t*BuNH)}$_2$K$_3$(tmeda)K$_3${(HN*t*Bu)(N*t*Bu)$_2$S}$_2$] (**33**) with anisotropic displacement parameters at 50 % probability level. Note: The asymmetric unit consists of only one complex molecule and half of the tmeda (pink box). The *t*Bu groups associated with each nitrogen atom from the lower and upper cap are truncated. The hydrogen atoms, apart from H1 at N5 that could be taken from the Fourier map and refined freely, are omitted for clarity.

confirms the presence of the hydrogen atom at N(5), which results in an elongated S(2)–N(5) bond of 1.7590(15) Å and significantly shorter S(2)–N(4) and S(2)–N(6) bonds with 1.5891(14) and 1.6133(14) Å. Moreover, a similar trend is detected for the N(5)–S(2)–N(4) and N(5)–S(2)–N(6) angles, which are narrowed to 99.39(7)° and 95.78(7)°, while the N(6)–S(2)–N(4) angle is widened to 110.83(7)°. This phenomenon stems from the exchange of a sterically more demanding lone pair with a hydrogen atom. All further analyses are in good agreement with the solid-state data. For [(tmeda)$_3$S{Na$_3$(N*t*Bu)$_3$S}$_2$] (**34**), we found a monoclinic space group ($P2_1/c$) with two molecules in the asymmetric unit (**Figure 3.34.**). The structure motif comprises a sulfide S^{2-} that centers a Na$_6$ distorted trigonal antiprism and two [S(N*t*Bu)$_3$]$^{2-}$ caps associated with the three sodium ions of each side. Additionally, three tmeda moieties cross-link between three sodium ions from the upper and lower cap. [S(*t*BuN)$_3$(thf)$_3$Na$_3$SNa$_3$(thf)$_3$(N*t*Bu)$_3$S] (**35**) features a similar constitution to **34**, apart from the solvent coordination, here each sodium ion is associated by one thf donor (**Figure 3.34.**). For compound **35**,[184] we determined a cubic space group ($Pa\overline{3}$), with 1/6 of the molecule in the asymmetric unit. In this high symmetry, the S^{2-} centers a non-distorted Na$_6$ trigonal antiprism. Noteworthily, the oxidation states of the sulfur atoms in the [S(N*t*Bu)$_3$]$^{2-}$ caps are +IV for all complexes, while the bridging sulfide in **34** and **35** exhibits +II and results in a neutral complex charge. Henceforth, complexes **34** and **35** can be considered as composed of a Na$_6$S^{4+} unit capped by two [S(N*t*Bu)$_3$]$^{2-}$ ligands.

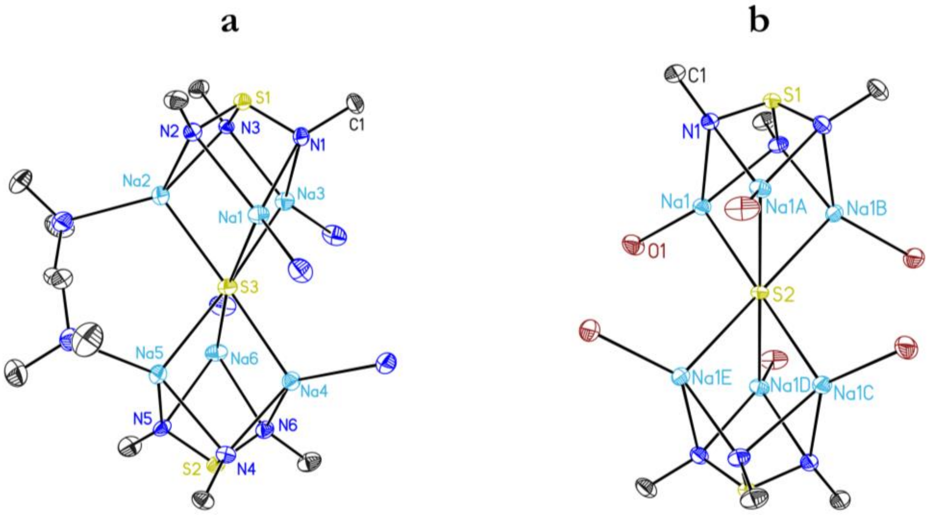

Figure 3.34. (**a**) Solid-state structure of $[(\text{tmeda})_3\text{S}\{\text{Na}_3(\text{N}t\text{Bu})_3\text{S}\}_2]$ (**34**) and (**b**) $[\text{S}(t\text{BuN})_3(\text{thf})_3\text{Na}_3\text{SNa}_3(\text{thf})_3(\text{N}t\text{Bu})_3\text{S}]$ (**35**) with anisotropic displacement parameters at 50 % probability level. Note: The asymmetric unit of **34** consists of two complex molecules, while **35** displays only 1/6 of the molecule. The *t*Bu groups associated with each nitrogen atom of the triimidosulfite are truncated. For **34,** the tmeda moieties bridging from Na1 to Na4 and Na3 to Na6 are omitted for clarity. For **35,** the thf molecules bound to each sodium ion are omitted for clarity. The hydrogen atoms are omitted for clarity.

Interestingly, comparing this central Na_6S^{4+}unit with the solid-state structure of Na_2S, we attained similar Na–S–Na angles in **35** (69.56(2), 110.44(2), 180.0°) and (70.5, 109.5 and 180.0°) in Na_2S. **34** is less symmetric than **35**, hence stronger deviations from the Na–S–Na angles are present. The coordination number in **34** and **35** is six, while the Na_2S exhibits an eight-fold coordination geometry around the sulfur atom. Consequently, the smaller coordination number leads to shorter Na–S bond lengths (2.7232(18)-2.7623(17) Å in **34** and 2.7691(8) Å in **35**) compared to 2.83 Å in Na_2S. Juxtaposing the M–N bond lengths for **34** and **35** with those in **33** assemble the expected decrease of the ionic radii from potassium to sodium. Henceforth, shorter M–N distances range from 2.331(3)-2.562(4) Å for **34** and 2.3300(17) Å for **35** compared to 3.6449(7)-3.9473(7) Å in **33** (**Table 3.28.**).

Moreover, apart from **35**, the alkali metal ions are not equally distributed from each other and exhibit a deviation of almost 0.2 Å, which may arise from the protonation of one nitrogen atom or the tmeda coordination. The cubic compound **35** illustrates identical bond lengths and angles for all symmetry-generated positions since only one-sixth of the molecule is placed in the asymmetric unit. Accordingly, all S–N bond lengths are 1.6510(15) Å and the N–S–N angles are 103.01(7)°, while the related complex **34** displays similar S–N bond distances (1.645(3)-1.663(3) Å) and N–S–N angles (102.04(16)-103.82(17)°).

3.9.2. Synthesis and SC-XRD analyses of the lanthanide(III)triimidosulfites (36-39)

All four complexes were accessible through a metathesis reaction with the corresponding lanthanide(III) chlorides. Complex [(*t*BuNH)Dy{K(0.5tmeda)}$_2${(N*t*Bu)$_3$S}$_2$]$_n$ (**36**) was obtained in *n*-pentane as a colorless solid (**Scheme 3.27.**). The dinuclear dysprosium complex [{S(*t*BuN)$_3$}$_2$Na$_2$DySDyNa$_2${(N*t*Bu)$_3$S}$_2$] (**37**) results from a reaction of **34** with DyCl$_3$ in toluene. Finally, [ClDy{Na(thf)}$_2${(N*t*Bu)$_3$S}$_2$] (**38**) and [ClEr{Na(thf)}$_2${(N*t*Bu)$_3$S}$_2$] (**39**) were obtained in thf under similar conditions. Noteworthily, the isolation of these complexes was achieved in various solvent mixture upon centrifugation (more details are reported in chapter 5.3.35).

We were able to crystalize all four complexes, while [(*t*BuNH)Dy{K(0.5tmeda)}$_2${(N*t*Bu)$_3$S}$_2$]$_n$ (**36**) displays a triclinic ($P\bar{1}$) and [{S(*t*BuN)$_3$}$_2$Na$_2$DySDyNa$_2${(N*t*Bu)$_3$S}$_2$] (**37**) a monoclinic space group. [ClLn{Na(thf)}$_2${(N*t*Bu)$_3$S}$_2$] with Ln = Dy$^{\mathrm{III}}$ (**38**) and Er$^{\mathrm{III}}$ (**39**) crystallizes in the monoclinic space group ($P2_1/n$). These mixed-metal complexes comprise two capping ligands with two alkali metal ions, one dysprosium ion (**36**-**38**), and one erbium ion for **39**.[188] In **36,** the dysprosium center is also coordinated to a negatively charged *t*BuNH amide moiety, illustrating the shortest N–Dy distance (2.199(2) Å) in this complex. This arises from ligand scrambling since the precursor (**33**) is less selective than its the sodium pendants (**34**, **35**). Despite the lowered yield from the ligand scrambling, **36** was successfully isolated as crystalline material. Furthermore, **36** forms a chain-like structure through the potassium ions bridging through tmeda donor bases (**Figure 3.35.**).

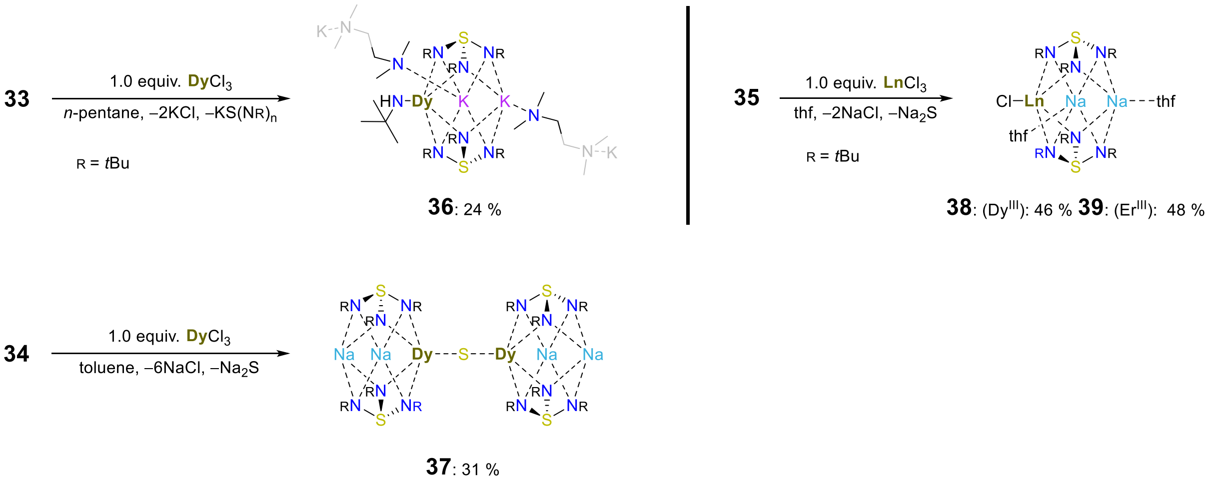

Scheme 3.27. (**top left**) Synthesis of complex [(*t*BuNH)Dy{K(0.5tmeda)}$_2${(N*t*Bu)$_3$S}$_2$]$_n$ (**36**) from **33** in *n*-pentane. (**bottom**) Preparation of [{S(*t*BuN)$_3$}$_2$Na$_2$DySDyNa$_2${(N*t*Bu)$_3$S}$_2$] (**37**) from **34**. (**top right**) Treatment of **35** with Dy$^{\mathrm{III}}$- and Er$^{\mathrm{III}}$-chloride in thf yields the desired complexes [ClDy{Na(thf)}$_2${(N*t*Bu)$_3$S}$_2$] (**38**) and [ClEr{Na(thf)}$_2${(N*t*Bu)$_3$S}$_2$] (**39**)

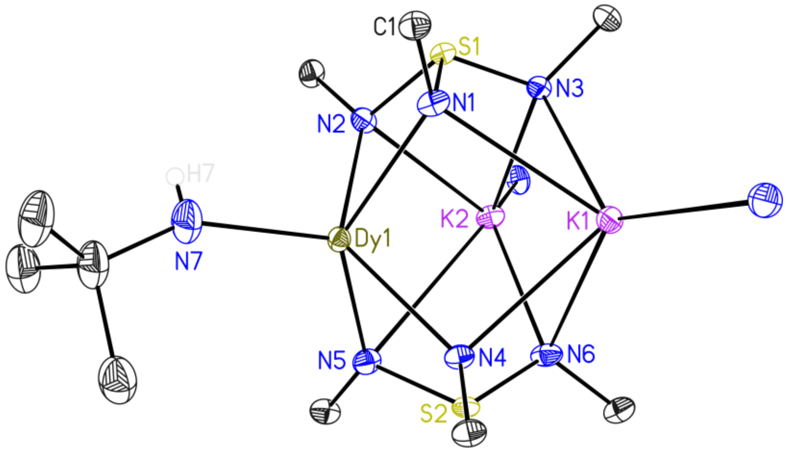

Figure 3.35. Solid-state structure of $[(t\text{BuNH})\text{Dy}\{\text{K}(0.5\text{tmeda})\}_2\{(\text{N}t\text{Bu})_3\text{S}\}_2]_n$ (**36**) with anisotropic displacement parameters at 50 % probability level. The *t*Bu groups associated with each nitrogen atom from the triimidosulfite are truncated. The hydrogen atoms, apart from H7 at N7 that could be taken from the Fourier map and refined freely, are omitted for clarity.

Complex **37** illustrates a dimeric structure pattern with two dysprosium centers bridged via a sulfide moiety. Interestingly, the sodium centers remain solvent-free and no tmeda is observed in the crystal lattice. The isomorphous complexes **38** and **39** are related but illustrate a monomeric structure and show a chloride substituent at the lanthanide center (**Figure 3.36.**). The three dysprosium complexes **36**-**38** differentiate in their individual Dy–N bond lengths. Here **37** demonstrates the broadest range (2.308(2)-2.422(2) Å), which is attributed to the missing solvent coordination at the sodium ions (**Table 3.29.**). This shortens the sodium lanthanide distance (3.4202(15)-3.4450(17) Å) and consequently leads to slightly elongated Dy–N distances for **37**. The Dy–N distances for **36** are slightly longer than for **38**, which is in good agreement with the expected ionic radii from sodium to potassium. The further Ln–N bond lengths decreased from **38** to **39** due to the lanthanide contraction. Similarly, the decrease in Ln(1)···Na(1) distance from **38** to **39** can also be explained with the decrease in ionic radii.

In the complex series from **37**-**39**, two nitrogen atoms of each triimidosulfite unit coordinate the lanthanide(III) ion with little variation for the individual S–N bond lengths, which is characteristic of the high adaptability of SN ligands in metal complexes.[121] The S–N distances span from 1.6709(17) to 1.6760(17) Å (**36**), 1.659(2) to 1.688(2) Å (**37**), 1.6667(13) to 1.6875(13) Å (**38**), 1.6632(15) to 1.6892(16) Å (**39**). However, since N(3) and N(6) do not participate in Ln–metal bonding but alkali metal bonding, their corresponding S–N bond lengths are significantly shorter (1.6097(16) and 1.6101(17) Å in **36**, 1.621(3) and 1.625(3) Å in **37**, 1.6141(13) Å in **38**, and 1.6102(16) Å in **39**). The reported Ln(1)–Cl(1) bond lengths in **38** and **39** are within the range of previously reported structures.[51a,189]

Table 3.29. Selected bond lengths [Å] and angles [°] for [(*t*BuNH)Dy{K(0.5tmeda)}$_2${(N*t*Bu)$_3$S}$_2$]$_n$ (**36**), [{S(*t*BuN)$_3$}$_2$Na$_2$DySDyNa$_2${(N*t*Bu)$_3$S}$_2$] (**37**), [ClDy{Na(thf)}$_2${(N*t*Bu)$_3$S}$_2$] (**38**) and [ClEr{Na(thf)}$_2${(N*t*Bu)$_3$S}$_2$] (**39**).

	36	**37**	**38**	**39**
Ln(1)–N$_{\text{range}}$	2.3239(17)-2.3865(17)	2.308(2)-2.422(2)	2.2985(13)-2.3702(13)	2.2868(16)-2.3403(16)
Ln(1)–M$_{\text{range}}$	3.9188(10)	3.4202(15)-3.4450(17)	3.5151(7)	3.4965(9)
Ln(1)–S(3)	-	2.5478(8)	-	-
S(1)–N(1)	1.6760(17)	1.688(2)	1.6667(13)	1.6632(15)
S(1)–N(2)	1.6724(17)	1.659(2)	1.6875(13)	1.6892(16)
S(1)–N(3)	1.6097(16)	1.625(3)	1.6141(13)	1.6102(16)
S(2)–N(4)	1.6719(16)	1.664(2)	-	-
S(2)–N(5)	1.6709(17)	1.684(3)	-	-
S(2)–N(6)	1.6101(17)	1.621(3)	-	-
Dy(1)–N(7)[a]	2.199(2)	-	-	-
N(1)–S(1)–N(2)	96.30(8)	95.55(12)	96.53(6)	96.32(8)
N(2)–S(1)–N(3)	104.80(9)	103.46(13)	106.44(7)	106.47(8)
N(3)–S(1)–N(1)	107.85(9)	107.02(13)	105.21(7)	105.32(8)
N(4)–S(2)–N(5)	95.30(8)	96.23(12)	-	-
N(5)–S(2)–N(6)	106.97(9)	105.54(13)	-	-
N(6)–S(2)–N(4)	106.75(9)	104.76(13)	-	-

[a] Disordered atoms are not considered.

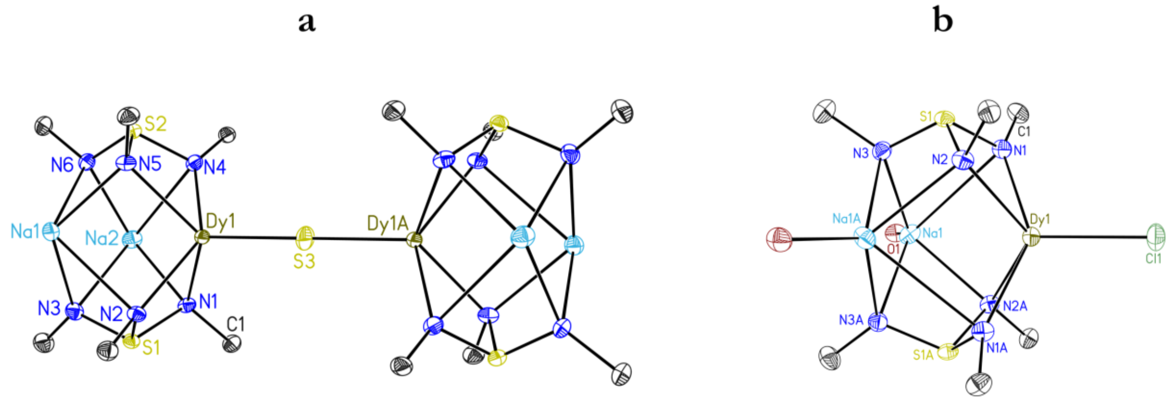

Figure 3.36. (**a**) Solid-state structure of [{S(*t*BuN)$_3$}$_2$Na$_2$DySDyNa$_2${(N*t*Bu)$_3$S}$_2$] (**37**), and (**b**) [ClDy{Na(thf)}$_2${(N*t*Bu)$_3$S}$_2$] (**38**), while the erbium(III) complex **39** is isostructural to **38**. The anisotropic displacement parameters are displayed at 50 % probability level. The *t*Bu groups associated with each nitrogen atom from the triimidosulfite are truncated. The hydrogen atoms are omitted for clarity. Only the oxygen donors of the thf moieties are depicted for **38**.

Table 3.30. Continuous Shape Measures (CShMs) of the coordination geometry for the Ln^{3+} ion environments in **36**-**39**, retrieved from the SHAPE program, displaying the lowest residue for a capped octahedron.[140]

	JTBPY-5[a]	SPY-5[b]	TBPY-5[c]	vOC-5[d]	PP-5[e]
36	10.176	3.312	6.629	7.331	27.844
37	11.787	3.981	6.727	9.333	30.459
38	10.300	3.744	5.639	8.611	32.077
39	10.058	3.530	5.541	8.287	32.021

[a] D_{3h}, Johnson trigonal bipyramid; [b] D_{4v}, Square pyramid; [c] D_{3h}, Trigonal dipyramid; [d] C_{4v}, Vacant octahedron (Johnson square pyramid, J1); [e] D_{5h}, Pentagon.

The rarely reported Dy–S–Dy motif of complex **37** illustrates a Dy–S(3) distance of 2.5478(8) Å, which agrees with other Ln–S–Ln analogues that range from 2.503 to 2.622 Å.[190] Furthermore, the N(1)–S(1)–N(2) angles are the smallest observed angles, with 96.30(8)° for **36**, 95.55(12)° for **37**, 96.56(6)° for **38**, and 96.32(8)° for **39**. This agrees with the decrease of the N(1)···N(2) distance caused by the lanthanide coordination.

Last, the SHAPE software elucidated the deviations from a trigonal bipyramidal (D_{3h}) polyhedron for **36**-**39**.[140] Here, a numerical evaluation is performed with the experimentally measured geometries of **36**-**39** to their ideal symmetries. The obtained residues range from 0 to 100, while 0 refers to a structure fully coincident in shape with the reference polyhedron. A square pyramid (D_{4v}) is the most accurate description of the symmetry of **36**-**39**, as the continuous shape measures (CShMs) exhibit the lowest residues (3.312-3.981) (**Table 3.30.**).

3.9.3. Magnetic properties of the lanthanide(III)triimidosulfites (36-39)

In this paragraph, experiments under direct current (dc) and alternating current (ac) conditions were conducted to elucidate the magnetic properties of $[(t\text{BuNH})\text{Dy}\{\text{K}(0.5\text{tmeda})\}_2\{(\text{N}t\text{Bu})_3\text{S}\}_2]_n$ (**36**), $[\{\text{S}(t\text{BuN})_3\}_2\text{Na}_2\text{DySDyNa}_2\{(\text{N}t\text{Bu})_3\text{S}\}_2]$ (**37**), and $[\text{ClLn}\{\text{Na(thf)}\}_2\{(\text{N}t\text{Bu})_3\text{S}\}_2]$ with Ln = Dy^{III} (**38**) and Ln = Er^{III} (**39**).

First, we determined the temperature-dependency of the magnetic susceptibility as the product of the temperature ($\chi_M T$), applying a direct current (dc) field of 5000 Oe. Measured values of $\chi_M T$ ($\text{cm}^3\text{mol}^{-1}$) exhibit 14.07 for **36**, 28.44 for **37**, 14.68 for **38**, and 11.31 for **39** at 210.0 K, where the calculated ones for the free trivalent ions are 14.17 for both **36** and **38**, while 28.34 for **37** and 11.48 for **39** (**Figure 3.37.**).[14] Juxtaposing these values, **36** and **39** illustrate slightly lower values than expected, whereas **37** and **38** are a little above the calculated ones, however still within the range of

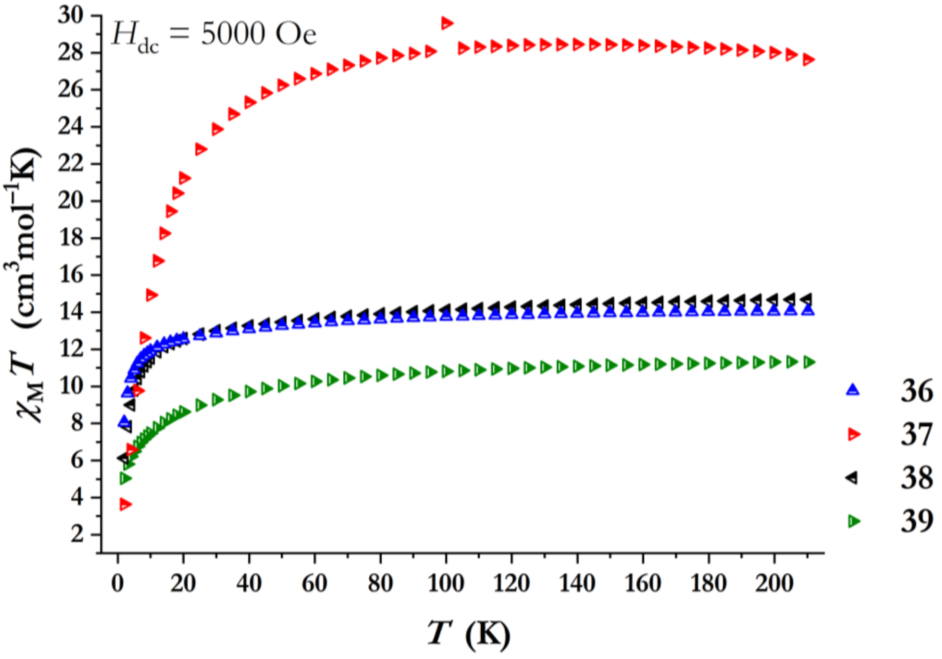

Figure 3.37. Temperature-dependency of $\chi_M T$ for **36** (blue), **37** (red), **38** (black), and **39** (green), under an applied field of H_{dc} = 5000 Oe.

related compounds. [14,52,154,163a,163b,165a] As the temperature is reduced to 25.0 K, an almost linear decay of $\chi_M T$ occurs, which correlates with the successive depopulation of the Stark subshells.[57,165a] Below 25.0 K the decrease is more rapid and displays values of 8.06 (**36**), 3.63 (**37**) 6.13 (**38**), and 5.04 (**39**) cm^{3}mol^{-1} at 2.0 K, respectively (**Figure 3.37.**). Spin-orbit coupling effects cause this phenomenon and all presented $\chi_M T$ values are in the expectancy range of previously reported complexes of this class.[14,52,154,163a,163b,165a]

The standard procedure to identify SMM properties is to search for an out-of-phase response of the magnetic susceptibility (χ''). Therefore, the first approach is to conduct magnetic susceptibility measurements under a dynamic alternating current (ac) field of 3 Oe. For the Er^{III} complex **39**, there was no χ'' signal typical for SMM behavior under zero dc field, probably due to strong QTM effects. In order to prevent such fast relaxation processes, an external dc field was applied, and the highest χ'' response was found for an optimal field of 1000 Oe. However, **39** demonstrates only a maximum slightly above 2.0 K and a rapid decay of χ'' suggests that QTM still occurs and that this type of ligand design may not be suitable for prolate-shaped lanthanide ions (see experimental part). Since dysprosium-containing molecules are more prone to illustrate SMM behavior, even under zero dc field, we expected more interesting properties for complexes **36**-**38**. Indeed, all Dy^{III} complexes respond to the dynamic out-of-phase susceptibility (χ'') under zero dc field. A drop of the in-of-phase susceptibility (χ') and the corresponding maxima in the χ'' versus frequency plot were detected up to 7.0 K for [(tBuNH)Dy{K(0.5tmeda)}$_2${(NtBu)$_3$S}$_2$]$_n$ (**36**) (**Figure 3.38.a-b**).

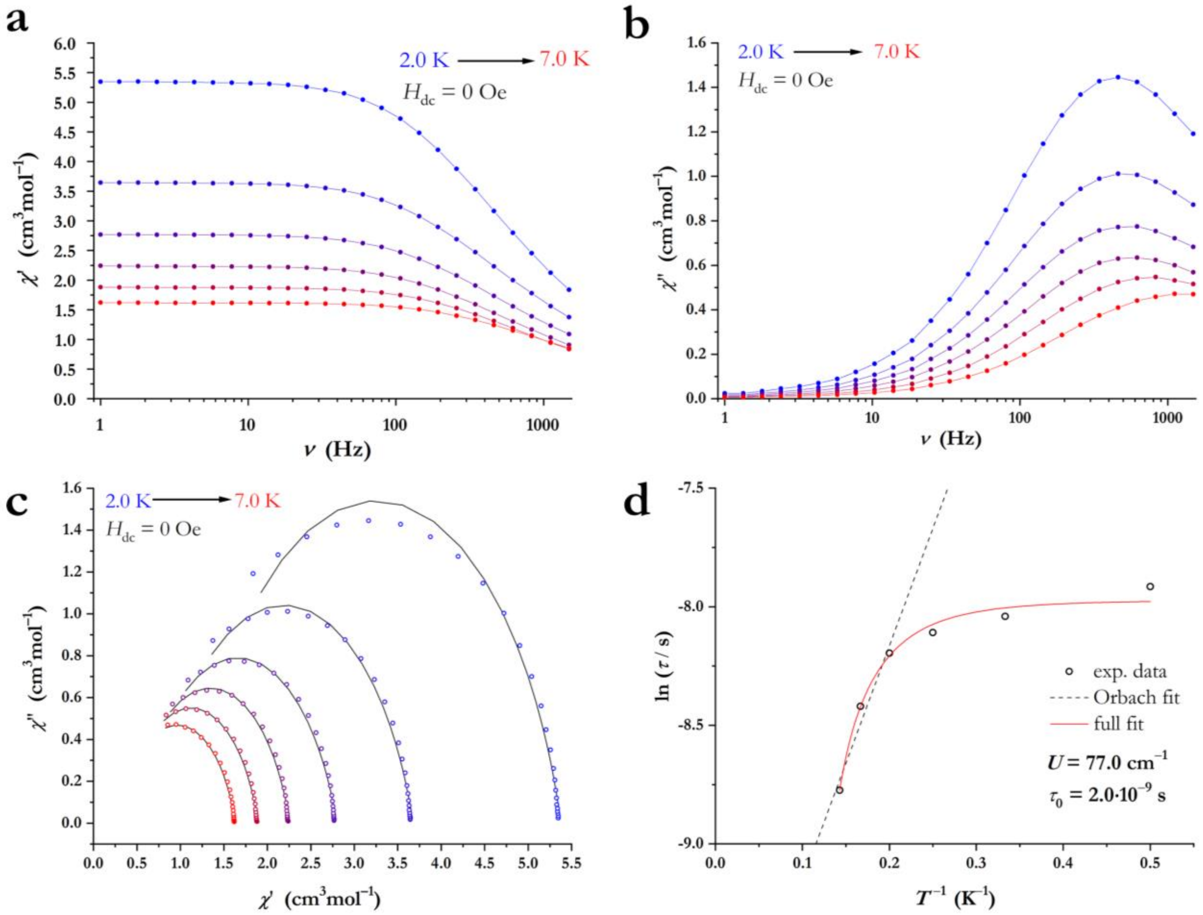

Figure 3.38. Magnetic data for of $[(t\text{BuNH})\text{Dy}\{\text{K}(0.5\text{tmeda})\}_2\{(\text{N}t\text{Bu})_3\text{S}\}_2]_n$ (**36**) under zero dc field conditions. Dynamic in-phase (**a**) and out-of-phase (**b**) susceptibilities versus variable frequencies from 2.0 to 7.0 K. Lines are guides for the eyes. (**c**) Cole-Cole plot with corresponding CC-fit data. (**d**) Arrhenius plot with the red curve exemplifying the full fit of all relaxation processes and the dashed line demonstrating a sole Orbach regression.

With the help of the Cole-Cole plot (**Figure 3.38.c**), one can extract the relaxation rates after applying a generalized Debye model within the CC-fit program to fit the data. The corresponding Arrhenius plot was constructed from the output relaxation times τ_1. Subsequently, we tried to suppress QTM, which was observable at low temperatures (**Figure 3.38.d**), by applying a dc field. The optimal field was determined to be 100 Oe, at which the χ'' values reach their highest maximum. Interestingly, the applied field initiates a second slow relaxation process, observable with a second local maximum at around 10 Hz at 3.0 K in the χ'' versus ν plot (**Figure 3.39.b**). The consequent Cole-Cole plot was best modeled with two relaxation processes in order to take the “hook-like artifacts” between 2.0-4.0 K into consideration. However, the energy barrier of the second process could not be determined as only two data points were available. Therefore, the energy barrier of the first process was fitted as stated above to be $U = 129.0\ \text{cm}^{-1}$, which is considerably higher than for zero-field conditions (77.0 cm^{-1}) (**Table 3.31.**).

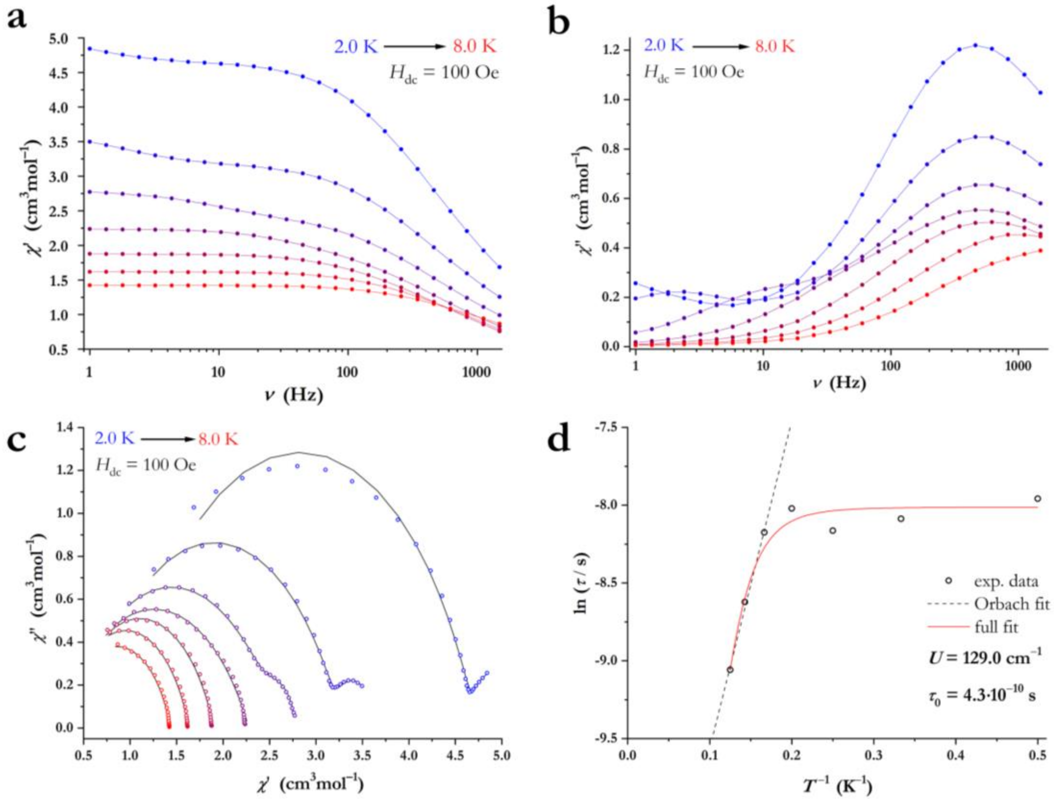

Figure 3.39. Magnetic data for of [(*t*BuNH)Dy{K(0.5tmeda)}$_2${(N*t*Bu)$_3$S}$_2$]$_n$ (**36**) under an applied dc field of 100 Oe. Dynamic in-phase (**a**) and out-of-phase (**b**) susceptibilities versus variable frequencies from 2.0 to 8.0 K. Lines are guides for the eyes. (**c**) Cole-Cole plot with corresponding CC-fit data. (**d**) Arrhenius plot with the red curve exemplifying the full fit of all relaxation processes and the dashed line demonstrating a sole Orbach regression.

Table 3.31. Best fitting parameters and their error margin for [(*t*BuNH)Dy{K(0.5tmeda)}$_2${(N*t*Bu)$_3$S}$_2$]$_n$ (**36**), [{S(*t*BuN)$_3$}$_2$Na$_2$DySDyNa$_2${(N*t*Bu)$_3$S}$_2$] (**37**), and [ClDy{Na(thf)}$_2${(N*t*Bu)$_3$S}$_2$] (**38**). R_2 gives the error of the full fit.

	36 (0 Oe)	**36** (100 Oe)	**37** (0 Oe)	**38** (0 Oe)[c]	**38** (0 Oe)[d]
U (cm^{-1})[a]	77.04 (± 8.3)	128.97 (± 14.9)	150.21 (± 12.63)	512.85 (± 74.85)	316.34 (± 3.0)
U_{eff} (cm^{-1})[b]	14.91 (± 3.3)	21.12 (± 4.9)	130.48 (± 2.79)	403.26 (± 17.86)	297.20 (± 27.9)
τ_0 (s)	$2.01\cdot10^{-6}$	$4.28\cdot10^{-10}$ (± $8.0\cdot10^{-10}$)	$4.21\cdot10^{-8}$ (± $4.2\cdot10^{-9}$)	$6.66\cdot10^{-10}$ (± $2.2\cdot10^{-11}$)	$8.25\cdot10^{-10}$ (± $1.3\cdot10^{-12}$)
	(± $8.1\cdot10^{-10}$)				
C (s^{-1}K^{-n})	0.43 (± 0.1)	3.4 10^{-3} (± $1.5\cdot10^{-4}$)	3.26 10^{-2} (± 1.20^{-2})	1.50 10^{-3} (± $1.5\cdot10^{-4}$)	$5.22\cdot10^{-4}$ (± $4.2\cdot10^{-5}$)
n	4.59 (± 0.4)	6.89 (± 0.1)	3.26 (± 2.12)	5.17 (± 0.4)	4.41 (± 0.1)
τ_{QTM} (s)	2937.5 (± 0.40)	3075.9 (± 176)	10.40 (± 40.5)	1680.13 (± 15.0)	0 (± 36.1)
R_2	0.9869	0.9828	0.9992	0.9975	0.9913

[a] U refers to the energy barrier for the full fit with equation (**3-3**); [b] U_{eff} refers to a linear approximation of a sole Orbach relaxation; [c] corresponds to the data for the first relaxation process; [d] corresponds to the data for the second relaxation process.

The same magnetic experiments were carried out for the dinuclear dysprosium complex **37**. Here, maxima of the dynamic out-of-phase susceptibility were present in the temperature range from 8.0 to 27.0 K and the first maximum occurred at a frequency of 5 Hz and shifts to higher frequencies as the temperature increases (**Figure 3.41.**). The data below 8.0 K displayed no maximum for χ'' and is therefore omitted from the plot. According to eq. **3-3**, we determined an energy barrier $U = 150.2\ \text{cm}^{-1}$ for **37**, which is almost three times higher than reported for **36**. Noteworthily, since the two dysprosium centers are linked via a sulfide moiety, we expect a weak antiferromagnetic coupling referring to previously reported complexes featuring a sulfide bridge motif. Moreover, employing the Magellan software,[174a] the two magnetic vectors of the Dy^{III} centers are determined to be exactly parallel since the bridging sulfide moiety is placed on an inversion center (**Figure 3.40.**).

Therefore, the same procedure as stated in chapter 3.6.4 was utilized, according to equation (**3-4**):[167]

$$E_{\text{dip}} = -\left\{\frac{\mu_0}{4\pi}\right\}\frac{\mu_i\mu_j}{r^3}[3cos^2(\theta) - 1] \tag{3-4}$$

Here, the θ value was determined to be 92.72°, which confirms our assumption of an antiferromagnetic interaction since θ is $> 54.75°$.[167b] Our calculation of the expected dipolar coupling of the two dysprosium centers resulted in $0.3651\ \text{cm}^{-1}$ for the dysprosium dimer **37**. These values are in the expected range of this compound class. One has to consider that this is a simplified approach and only represents a rough estimation of the dipolar interaction values.

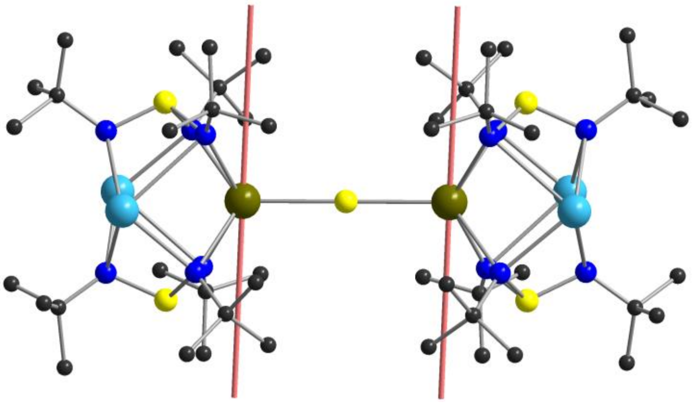

Figure 3.40. Orientation of the main magnetic axes (light coral) in $[\{S(t\text{BuN})_3\}_2\text{Na}_2\text{DySDyNa}_2\{(\text{N}t\text{Bu})_3\text{S}\}_2]$ (**37**), calculated with the program Magellan and illustrated with the program Diamond 3.[174] All hydrogen atoms are omitted for clarity. Color code: C: (black), N: (blue), O: (red), S: (yellow), Na: (sky blue), and Dy: (gold).

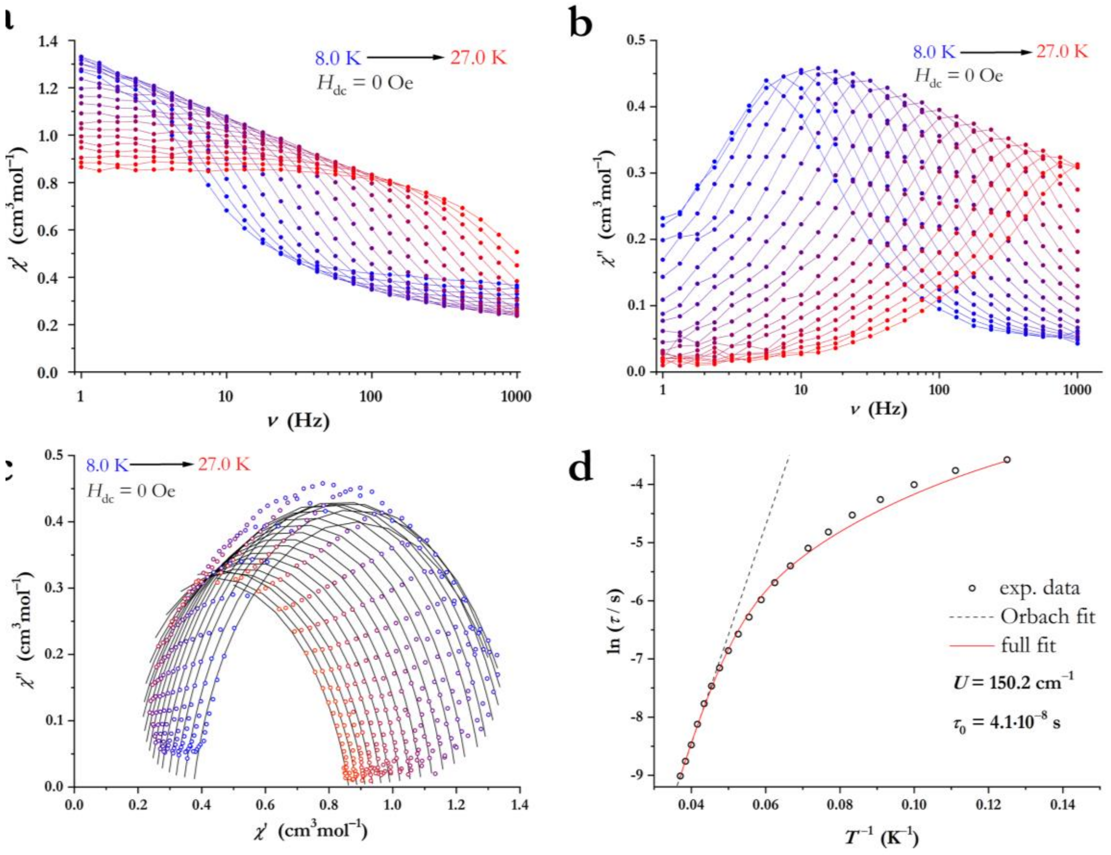

Figure 3.41. Magnetic data for of $[\{S(t\text{BuN})_3\}_2Na_2DySDyNa_2\{(Nt\text{Bu})_3S\}_2]$ (**37**) under zero-field conditions. Dynamic in-phase (**a**) and out-of-phase (**b**) susceptibilities versus variable frequencies from 8.0 to 27.0 K. Lines are guides for the eyes. (**c**) Cole-Cole plot with corresponding CC-fit data. (**d**) Arrhenius plot with the red curve exemplifying the full fit of all relaxation processes and the dashed line demonstrating a sole Orbach regression.

Therefore, the SMM behavior is rooted in the single-ion properties and is not expected to stem from the exchange coupling of both dysprosium centers. However, all attempts to synthesize the gadolinium analogue failed, which would have enabled the determination of the exact coupling value (see chapter 3.6.4). Consequently, the exact value could not be determined within this thesis.

Aforementioned complex **38** exhibits SMM behavior and displays maxima for χ'' over a broad temperature range from 16.0 to 60.0 K (**Figure 3.42.a-b**). Below 16.0 K, no maxima for the dynamic out-of-phase susceptibility (χ'' versus frequency plot) are observed, while QTM is the dominant process. Interestingly, two local maxima in the χ'' signal are detected at a frequency of 3 Hz and 34 Hz at 16 K (**Figure 3.42.b**). Increasing the temperature up to 60 K results in a characteristic shift of the maxima toward higher frequencies, indicating a true temperature-depending relaxation process and a typical SMM-like behavior. The data was processed as stated above and the Cole-Cole plot fit was performed with two relaxation processes (**Figure 3.42.c**). A sole Orbach approximation of the Arrhenius plot demonstrates a significantly higher effective energy barrier for the first process (403.3 cm^{-1}) and the second process (297.2 cm^{-1}) than observed for **36** (14.9-21.1 cm^{-1}) and **37** (130.5 cm^{-1}) (**Figure 3.42.d**). Considering the other relaxation processes (eq. **3-3**), we found even higher energy barriers of $U\tau_1$ = 512.9 cm^{-1} for the first and $U\tau_2$ = 316.3 cm^{-1} for the second relaxation process (**Figure 3.42.d**). All related fit parameters are illustrated in the table above (**Table 3.31.**). Further enhancement of the magnetic properties could not be achieved by applying an external field. Under these conditions, no maxima for the frequency dependency of χ'' did occur (see experimental, 5.3.35). Magnetization studies showed that the compounds **37** and **38** can retain their magnetization to a certain extent if the applied magnetic field is not entirely removed. Indeed, the presence of QTM at low temperatures prevents the observation of magnetic remanence at 0 dc field and results in a butterfly-shaped hysteresis (**Figure 3.43.**).[59] For **37**, this phenomenon is only present to a small extent and below 3.5 K. Excitingly, for **38**, the wings of the hysteresis are open at temperatures up to 7.0 K with a sweep rate of 185 Oe/s. A similar hysteresis was reported for $\mathrm{Cp^{ttt}{}_2DyCl}$,[51a] which makes **38** an equal contender.

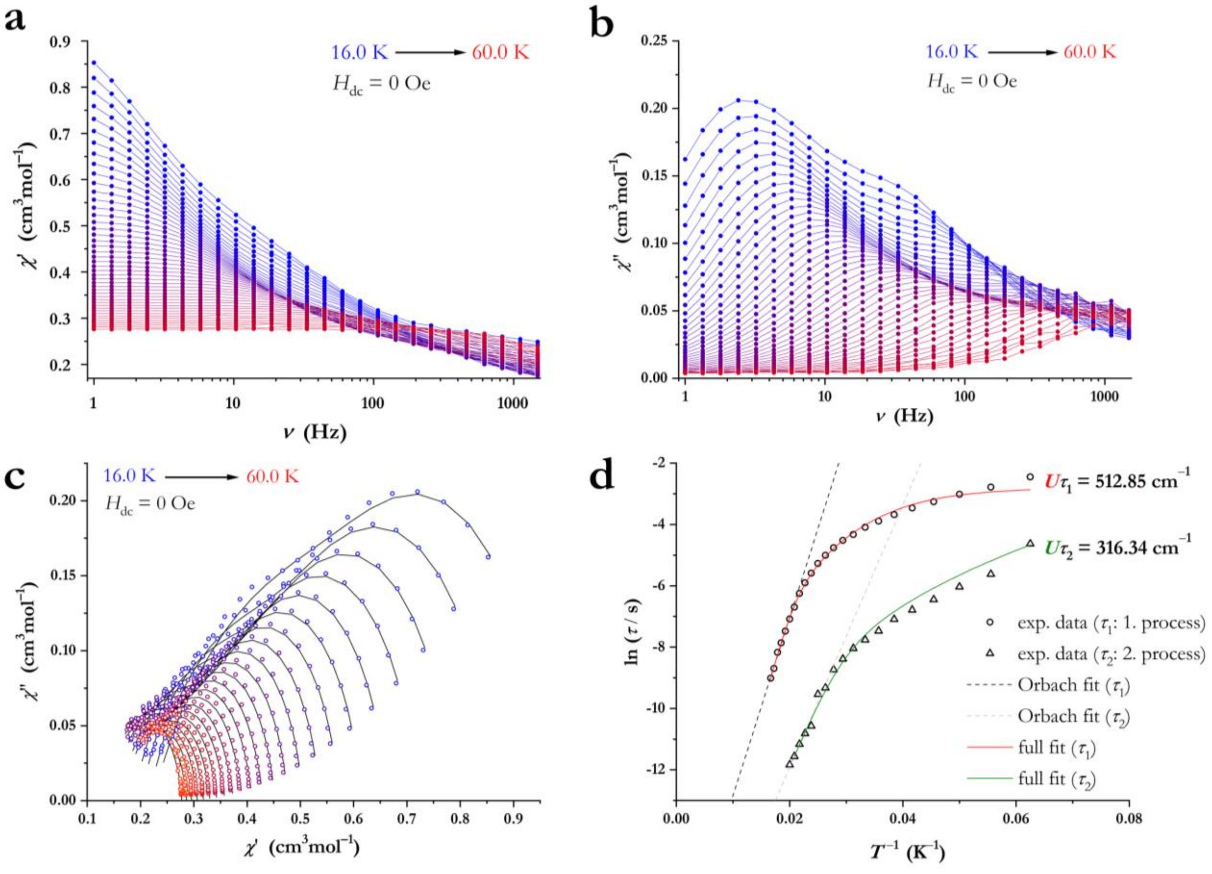

Figure 3.42. Magnetic data for of $[\mathrm{ClDy\{Na(thf)\}_2\{(N}t\mathrm{Bu)_3S\}_2}]$ (**38**) under zero field conditions. Dynamic in-phase (**a**) and out-of-phase (**b**) susceptibilities versus variable frequencies from 16.0 to 60.0 K. Lines are guides for the eyes. (**c**) Cole-Cole plot with corresponding CC-fit data. (**d**) Arrhenius plot with the red curve exemplifying the full fit of all relaxation processes and the dashed line demonstrating a sole Orbach regression.

The observation of this magnetic hysteresis suggests that the present ligand design is quite suitable for dysprosium-based SMMs, however, some improvements could potentially result in an open hysteresis and a higher blocking temperature. In order to determine the next areas of investigations toward this aim, we calculated the main magnetic axis in complexes **36**-**38** based on the electrostatic model in the program Magellan (**Figure 3.44.**).[174] Here, the main magnetic axes are oriented similarly in all complexes, displaying a small Dy–N bond deviation, which suggests a relatively high local axiality at the dysprosium center.

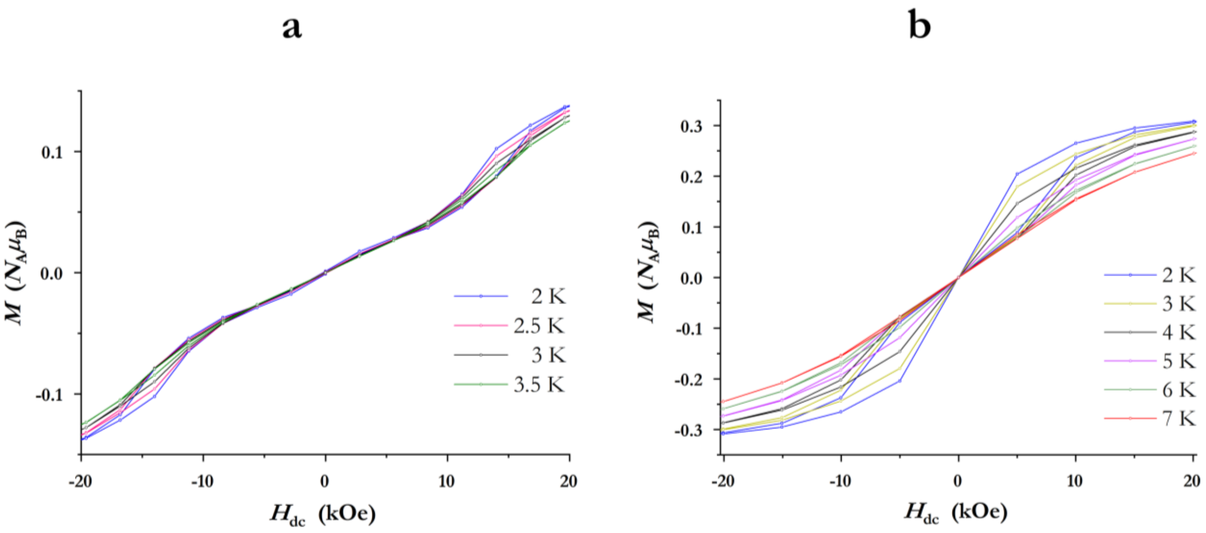

Figure 3.43. Field dependency of the magnetization for (**a**) $[\{S(tBuN)_3\}_2Na_2DySDyNa_2\{(NtBu)_3S\}_2]$ (**37**) and (**b**) $[ClDy\{Na(thf)\}_2\{(NtBu)_3S\}_2]$ (**38**) at a sweep rate of 185 Oe/s.

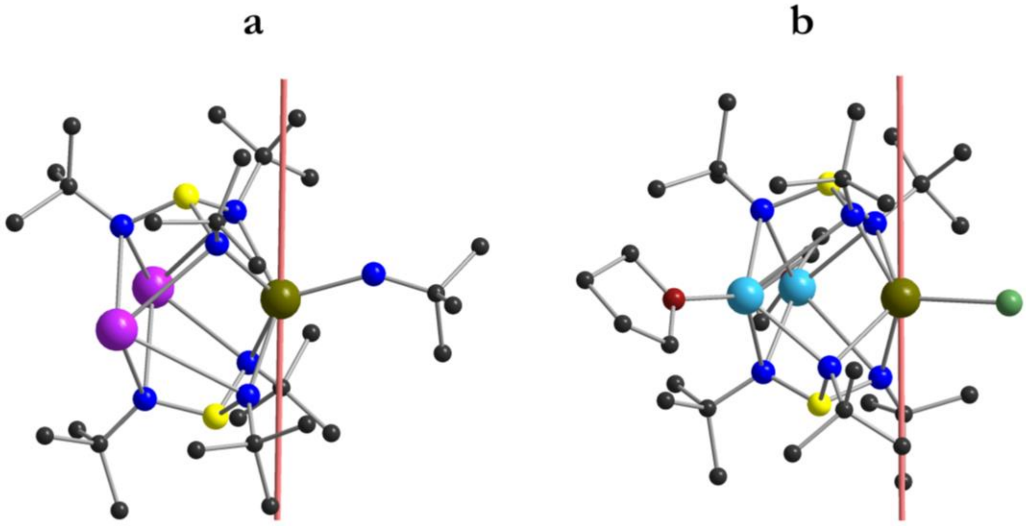

Figure 3.44. Orientation of the main magnetic axes (light coral) of the ground state for the Dy^{III} centers of: (**a**) $[(tBuNH)Dy\{K(0.5tmeda)\}_2\{(NtBu)_3S\}_2]_n$ (**36**), and (**b**) $[ClDy\{Na(thf)\}_2\{(NtBu)_3S\}_2]$ (**38**), calculated with the program Magellan and illustrated with the program Diamond 3.[174] All hydrogen atoms and the tmeda moieties in (**a**) are omitted for clarity. Color code: C: (black), N: (blue), O: (red), S: (yellow), Na: (sky blue), K: (pink), Cl: (green), and Dy: (gold).

If translated to the analogous Er(III)-complex, this observation might further explain why no SMM behavior is detected for **39** and confirms that the present ligands generate a ligand field beneficial to oblate-shaped lanthanides as the Dy^{3+} ion.

The main magnetic axes are also located perpendicular to the nitrogen atom of the *tert*-butylamide in **36**, to the sulfide bridge in **37**, and to the halide atom in **38**, respectively, resulting in substantial transverse anisotropy. Thus, the next steps should focus on removing these additional donors, which likely hamper the achievement of optimal axial anisotropy in the present complexes.

3.9.4. Summary and concluding remarks for 36-39 and their precursors 33-35

Within this chapter one potassium and two sodium triimidosulfite precursors, in particular the $[\{\mathrm{S}(t\mathrm{BuN})_2(t\mathrm{BuNH})\}_2\mathrm{K}_3(\mathrm{tmeda})\mathrm{K}_3\{(\mathrm{HN}t\mathrm{Bu})(\mathrm{N}t\mathrm{Bu})_2\mathrm{S}\}_2]$ (**33**), $[(\mathrm{tmeda})_3\mathrm{S}\{\mathrm{Na}_3(\mathrm{N}t\mathrm{Bu})_3\mathrm{S}\}_2]$ (**34**), and $[\mathrm{S}(t\mathrm{BuN})_3(\mathrm{thf})_3\mathrm{Na}_3\mathrm{SNa}_3(\mathrm{thf})_3(\mathrm{N}t\mathrm{Bu})_3\mathrm{S}]$ (**35**) were successfully synthesized and characterized via SC-XRD, NMR, and EA. The previously discussed potassium precursor $[\mathrm{S}(t\mathrm{BuN})_3(\mathrm{thf})_3\mathrm{K}_3\{\mathrm{HN}t\mathrm{Bu})(\mathrm{N}t\mathrm{Bu})_2\mathrm{S}\}]$ (**26**) is identified as highly reactive resulting in decomposition upon all reactions attempted. However, most of the ligand scrambling has been sufficiently suppressed by modifying this compound accordingly. Similar improvements were employed for the sodium precursors **34** and **35**. The $[\mathrm{S}(t\mathrm{BuN})_3(\mathrm{thf})_3\mathrm{Na}_3\{\mathrm{HN}t\mathrm{Bu})(\mathrm{N}t\mathrm{Bu})_2\mathrm{S}\}]$ (**27**) compound resulted in an interesting complex series (**29**-**32**), nevertheless the reaction was not selective enough to isolate these complexes. Therefore, the sodium precursors **34** and **35** were engineered to provide an enhanced selectivity.

The subsequent lanthanide(III) complexes $[(t\mathrm{BuNH})\mathrm{Dy}\{\mathrm{K}(0.5\mathrm{tmeda})\}_2\{(\mathrm{N}t\mathrm{Bu})_3\mathrm{S}\}_2]_n$ (**36**), $[\{\mathrm{S}(t\mathrm{BuN})_3\}_2\mathrm{Na}_2\mathrm{DySDyNa}_2\{(\mathrm{N}t\mathrm{Bu})_3\mathrm{S}\}_2]$ (**37**), and $[\mathrm{ClLn}\{\mathrm{Na}(\mathrm{thf})\}_2\{(\mathrm{N}t\mathrm{Bu})_3\mathrm{S}\}_2]$ with Ln = $\mathrm{Dy}^{\mathrm{III}}$ (**38**), and $\mathrm{Er}^{\mathrm{III}}$ (**39**) were analyzed via SC-XRD and SQUID magnetometry. None of these complexes display an alkali metal halide co-complexation, which turned out to be the main hindrance for SN ligands to enhance toe SMM properties. Excitingly, complexes **36**-**38** portrayed a true SMM signature with energy barriers of 72.0 cm^{-1} (**36**), 150.2 cm^{-1} (**37**), 512.9 cm^{-1} (**38**, U_1), and 316.3 cm^{-1} (**38**, U_2) under zero-field conditions. Assumingly, the additional tBuNH coordination is crucial in lowering the energy barrier U of **36** to only 72.0 cm^{-1}. Remarkably, **37** and **38** illustrate the best magnetic performance upon all previously reported SN systems, while **38** also illustrates maxima of the dynamic out-of-phase susceptibility up to 60 K and a butterfly-shaped hysteresis up to 7 K. Looking forward, the abstraction of the remaining chloride from **38** could lead to $[(\mathrm{thf})_2\mathrm{Na}_2\mathrm{Dy}\{\mathrm{S}(\mathrm{N}t\mathrm{Bu})_3\}_2]^+$ and substantially increase the axial anisotropy. Consequently, this approach could lead to better overall magnetic properties.

4. Summary and Outlook

This thesis focused on the tailor-made development of various mono- and dinuclear lanthanide complexes in the light of their magnetic properties, featuring the Box and SN ligand scaffold. Furthermore, another research strand was dedicated to the magnetic properties of d-metal complexes comprising both ligand motives. In addition, major affords were directed toward suitable precursor design, avoiding lithium compounds to exclude lithium halide co-complexation in the subsequent d- and f-metal complexes. A breakthrough in the field of SN chemistry was achieved with the dysprosium(III) triimidosulfite series (**36**-**38**) that exhibit major improvements in their overall magnetic performance. Moreover, the rare structure motif of sodium sodates was studied in solution and the solid-state and hence utilized to engineer new SMMs. Last, air-stable SMMs based on d-metals that are suitable for spectroscopic and magnetic benchmarking were introduced. The main findings are outlined below and the interested reader is directed to the summary and concluding remarks section of the individual chapters.

In the first part of this thesis, research emphasizing the Box ligand platform resulted in a series of air-stable SMMs (**3**, **1***, **3***) featuring the bis(benzoxazol-2-yl)methanide and bis(4-methyl-benzoxazol-2-yl)methanide ligand (**Figure 4.1.**). Various relaxation processes with a coexisting phonon bottleneck contribution were identified in this context. The entire series (**1**-**4**, **1***-**4***) is offering a versatile and tunable platform to facilitate spectroscopic and magnetic benchmarking and is supported by computational methods. Additionally, high-resolution X-ray diffraction experiments provide further insight to magneto-structural correlations for the **3** and **3*** and were conducted by KÖHLER within the STALKE group.

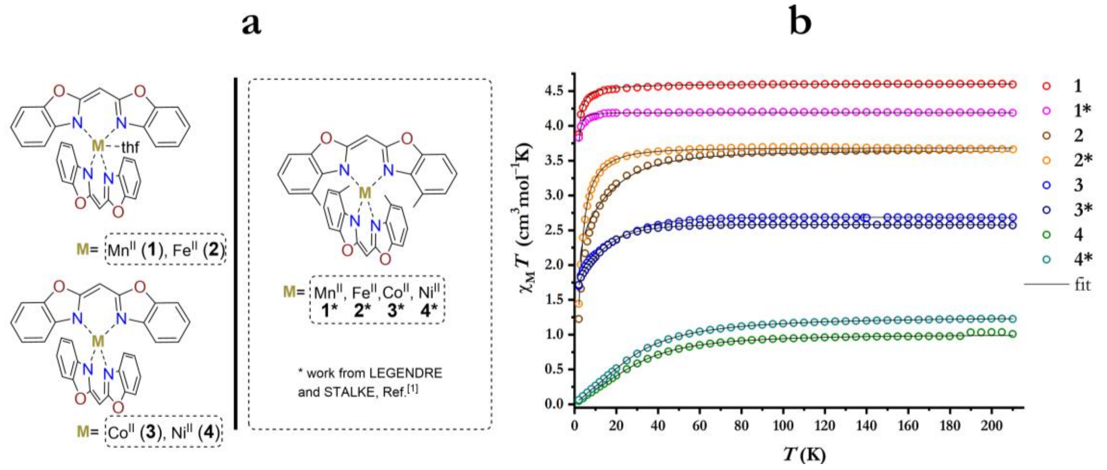

Figure 4.1. (**a**) Overview of 3d metal complexes featuring the bis(4-*R*-benzoxazol-2-yl)methanide ligand. (**b**) Temperature dependency of $\chi_M T$ for **1**-**4** and **1***-**4*** from 210 to 2 K. Reproduced from Ref.[1] with permission from the Royal Society of Chemistry.

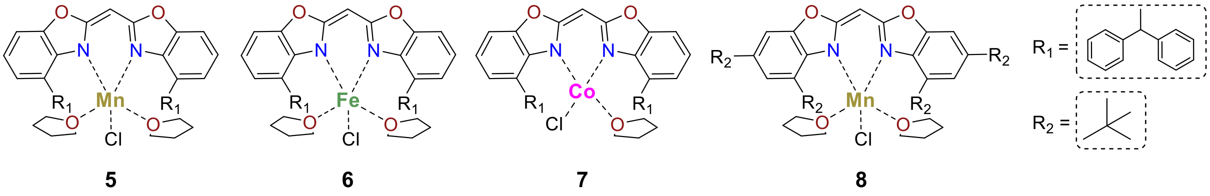

Scheme 4.1. Overview on the [(thf)$_n$MCl{(4-benzhydryl-NCOC$_6$H$_3$)$_2$CH}] with M = Mn^{II} (**5**), n = 2; Fe^{II} (**6**), n = 2; and Co^{II} (**7**), n = 1; and the [(thf)$_2$MnCl{(4,6-*t*Bu-NCOC$_6$H$_3$)$_2$CH}] complex series.

Next, we aimed to juxtapose the coordination chemistry and the magnetic properties of the d-metal bis(4,6-*R,R*'-benzoxazol-2-yl)methanide series (**1**-**4** and **1***-**4***) with sterically more demanding BOX ligands featuring benzhydryl (**L$_2$**, *R* = benzhydryl, *R*' = H) or *tert*-butyl (**L$_3$**, *R* = *R*' = *t*Bu) functionalization. However, all attempts with a (1:2) or (1:1) stoichiometry resulted in monosubstituted complexes (**5**-**9**) (**Scheme 4.1.**). SMM behavior was observable for none of these complexes. Moreover, the remaining chlorido ligand most likely hampers the magnetic performance.

Switching the focus toward f-metal-based systems, the versatile [Ln(HMDS)$_3$] precursors are prepared. These were first described 50 years ago, however within this thesis we could finally report the two missing solid-state structures of Ln = Gd (**9**), and Ho (**10**) (**Scheme 4.2.**). In the derived Box complexes **11**-**15**, the coordination polyhedron is best described by a capped octahedron, as confirmed by continuous shape measures with the SHAPE software.[140a,140b,155] Magnetic studies on **12**-**15** revealed no SMM-like behavior due to the absence of an out-of-phase response of the susceptibility. An enhancement of the magnetic performance should be achieved with lower coordination numbers, which could be realized by applying Box ligands with increased steric demand and the use of non-donating solvents. The next section focuses on the methyl-substituted Box ligand and its derived lanthanide complexes.

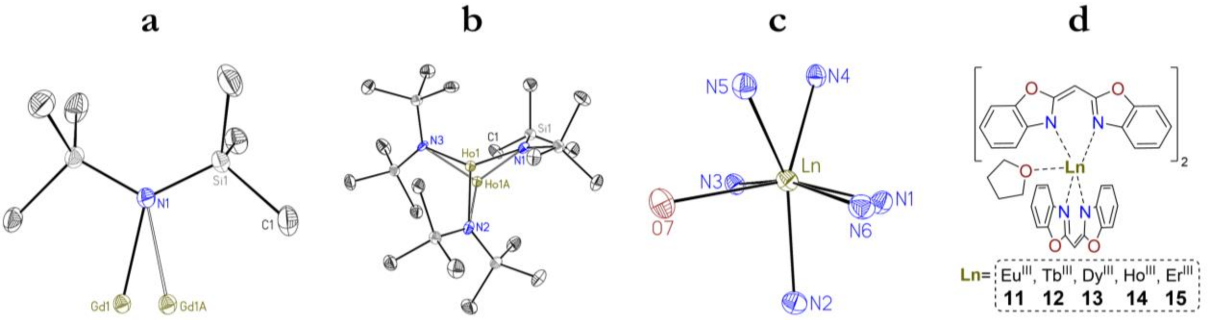

Scheme 4.2. (**a**-**b**) The solid-state structure of [Ln(HMDS)$_3$] with Ln = Gd (**9**), and Ho (**10**). (**c**) First coordination sphere of [(thf)Ln^{III}{(NCOC$_6$H$_4$)$_2$CH}$_3$] series and depiction of the entire molecule (**d**).

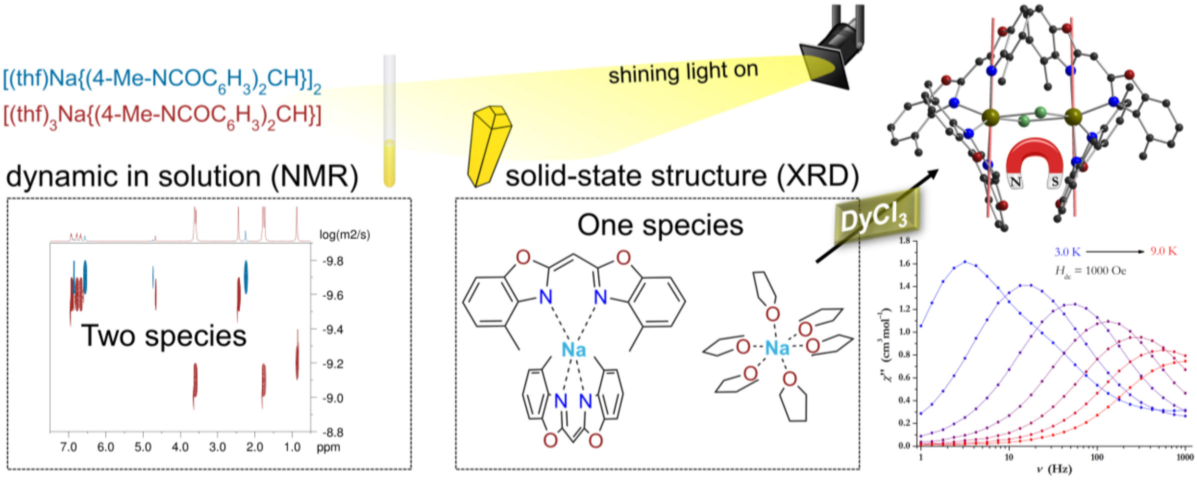

Figure 4.2. (**left**) Illustration of the DOSY-NMR versus the solid-state picture. (**right**) Depiction of [(μ-Cl)Dy^{III}{4-Me-NCOC$_6$H$_3$)$_2$CH}$_2$]$_2$ (**20**), its susceptibility χ'' versus frequency plot, and the orientation of the main magnetic axes (light coral) calculated with the program Magellan and illustrated with the program Diamond 3.[174] All hydrogen atoms are omitted for clarity. Color code: C: (black), N: (blue), O: (red), Cl: (green), and Dy: (gold).

Within this chapter two sodium precursors, in particular, the sodium sodate [Na(thf)$_6$][Na{4-Me-NCOC$_6$H$_3$)$_2$CH}$_2$] (**17**) and the [(thf)$_3$Na{(NCOC$_6$H$_4$)$_2$CH}] (**18**) are studied. **17** represents the first reported example of an alkali metal Box derivative featuring a solvent separated ion pair, which is in general a rarely observed structure motif. DOSY-NMR studies unequivocally demonstrated that under r.t. condition, the solvent separated ion pair is not maintained, while the equilibrium is shifted toward the dimer at low temperatures (**Figure 4.2.**). The subsequent dinuclear lanthanide(III) complexes [(μ-Cl)Ln^{III}{4-Me-NCOC$_6$H$_3$)$_2$CH}$_2$]$_2$ (**19**-**21**) with Ln = Gd^{III} (**19**), Dy^{III} (**20**), and Er^{III} (**21**) were analyzed via SC-XRD and SQUID magnetometry, while the Dy^{III}-complex **20** exhibits a true SMM signature with an energy barrier of 315.7 cm^{-1} (0 Oe) and 378.9 cm^{-1} (1000 Oe), respectively. Further, the Gd^{III}-complex (**19**) provides insights into the magnetic interaction between both Dy^{III} centers, best described by a weak antiferromagnetic coupling with a value of -0.035 cm^{-1}. However, the main contribution to the observed SMM behavior stems from the single ion properties as the coupling is weak. Perspectives for improvement should focus on optimizing the coordination environment to attain a tetrahedral mode with a bulky non-coordinating counter ion. Studies with more bulky Box systems such as *tert*-butyl- or benzhydryl-groups are envisioned. Removing the remaining halide with KC$_8$ or Mg should be evaluated as well.

The second part of this thesis emphasizes sulfur-nitrogen-based ligands. Based on the methyl- [(thf)Li{MeS(NSiMe$_3$)$_2$}]$_2$ (**L$_8$**) and *tert*-butyl- [Li{*t*BuS(NSiMe$_3$)$_2$}]$_2$ (**L$_7$**) substituted diimidosulfinate ligands (**L$_5$**), two field-induced dysprosium SMMs are reported (**Figure 4.3.**). The solid-state analysis reveals the presence of lithium chloride co-complexation, as reported for the aforementioned complexes in chapter 3.7.

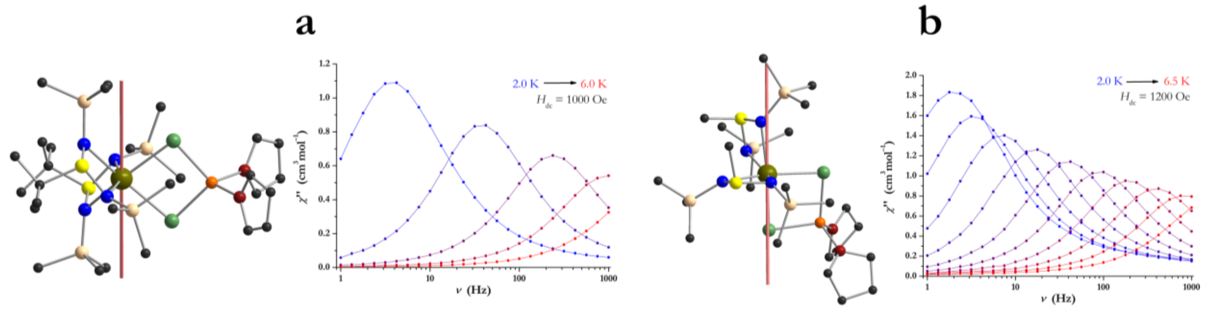

Figure 4.3. (**a**) Orientation of the main magnetic axes (light coral) and susceptibility χ'' versus frequency plot for (**a**) [(thf)$_2$LiCl$_2$Dy{MeS(NSiMe$_3$)$_2$}$_2$] (**DL_MR17**) and (**b**) [(thf)$_2$LiCl$_2$Dy{*t*BuS(NSiMe$_3$)$_2$}$_2$] (**DL_MR16**). Magnetic axes are calculated with the program Magellan and illustrated with the program Diamond 3.[174] All hydrogen atoms are omitted for clarity. Color code: C: (black), N: (blue), O: (red), S: (yellow), Si: (light brown) Li: (orange), and Dy: (gold).

Despite the lack of pure axial ligand symmetry, maxima in the out-of-phase susceptibility stemming from SMM behavior were detected up to 5.0 K for [(thf)$_2$LiCl$_2$Dy{MeS(NSiMe$_3$)$_2$}$_2$] (**DL_MR17**) and up to 6.0 K for [(thf)$_2$LiCl$_2$Dy{*t*BuS(NSiMe$_3$)$_2$}$_2$] (**DL_MR16**). As mentioned above, further magnetic improvements are feasible upon avoiding the lithium precursors and removing the remaining chloride ligands. Therefore, **L$_7$** is protonated giving ([*t*BuS(NHSiMe$_3$)(NSiMe$_3$)] (**23**) and further studies will be carried out by P. KALLENBACH.

Last, two chapters are dedicated to several potassium and sodium triimidosulfite precursors. The potassium precursor [S(*t*BuN)$_3$(thf)$_3$K$_3${HN*t*Bu)(N*t*Bu)$_2$S}] (**26**) is identified as highly reactive resulting in decomposition upon all reaction attempts. However, most of the ligand scrambling has been sufficiently suppressed by modifying this compound accordingly. The [S(*t*BuN)$_3$(thf)$_3$Na$_3${HN*t*Bu)(N*t*Bu)$_2$S}] (**27**) precursor gives access to an interesting complex series (**29**-**32**), but the reaction was not selective enough to isolate these complexes. Henceforth, the sodium precursors [(tmeda)$_3$S{Na$_3$(N*t*Bu)$_3$S}$_2$] (**34**), and [S(*t*BuN)$_3$(thf)$_3$Na$_3$SNa$_3$(thf)$_3$(N*t*Bu)$_3$S] (**35**) were engineered to provide an enhanced selectivity. The derived lanthanide$^{\mathrm{III}}$ complexes [(*t*BuNH)Dy{K(0.5tmeda)}$_2${(N*t*Bu)$_3$S}$_2$]$_n$ (**36**), [{S(*t*BuN)$_3$}$_2$Na$_2$DySDyNa$_2${(N*t*Bu)$_3$S}$_2$] (**37**), and [ClLn{Na(thf)}$_2${(N*t*Bu)$_3$S}$_2$] with Ln = Dy$^{\mathrm{III}}$ (**38**), and Er$^{\mathrm{III}}$ (**39**) are analyzed via SC-XRD and SQUID magnetometry. None of these complexes display a NaHal co-complexation, which turned out to be the main hindrance for SN ligands in enhancing their SMM properties. Excitingly, complexes **36**-**38** portrayed a true SMM signature with energy barriers of 72.0 cm^{-1} (**36**), 150.2 cm^{-1} (**37**), 512.9 cm^{-1} (**38**, U_1), and 316.3 cm^{-1} (**38**, U_2) under zero-field conditions. Assumingly, the additional *t*BuNH coordination is crucial in lowering the anisotropy and the energy barrier U of **36** to only 72.0 cm^{-1}, compared to a halide coordination. Remarkably, **37** and **38** illustrate the best magnetic performance upon all previously reported SN systems and **38** shows maxima of the dynamic out-of-phase susceptibility up to 60.0 K and a butterfly-shaped hysteresis up to 7.0 K.

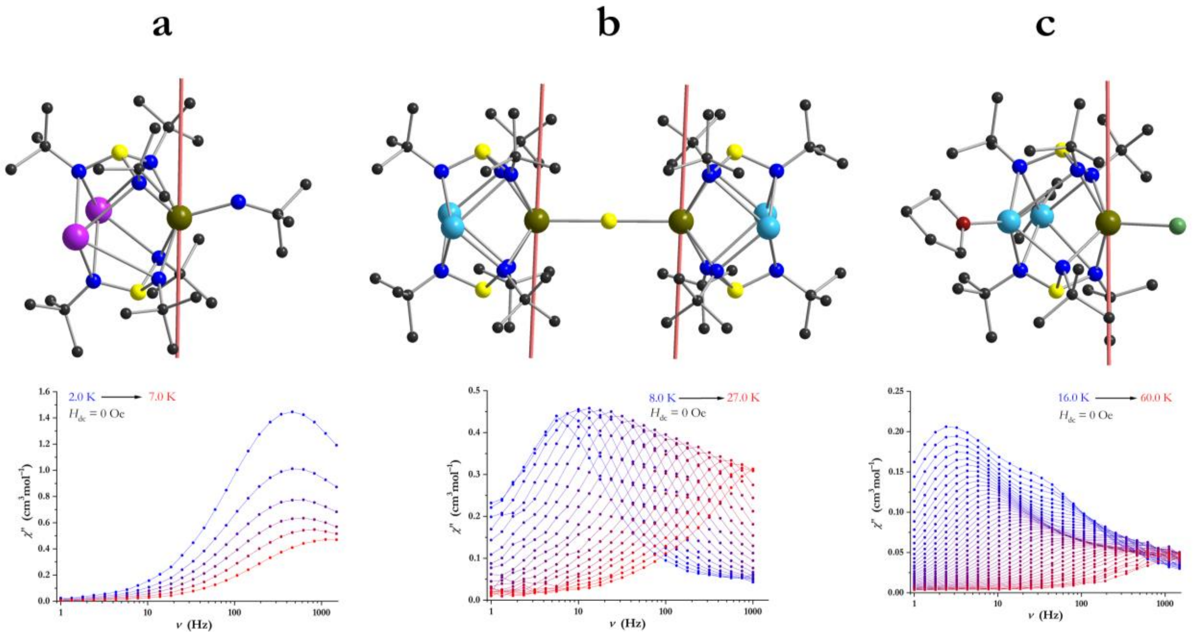

Figure 4.4. (**a**) Orientation of the main magnetic axes (light coral) (top) and susceptibility χ'' versus frequency plot (bottom) in $[(t\text{BuNH})\text{Dy}\{\text{K}(0.5\text{tmeda})\}_2\{(\text{N}t\text{Bu})_3\text{S}\}_2]_n$ (**36**), (**b**) $[\{\text{S}(t\text{BuN})_3\}_2\text{Na}_2\text{DySDyNa}_2\{(\text{N}t\text{Bu})_3\text{S}\}_2]$ (**37**), and (**c**) $[\text{ClDy}\{\text{Na}(\text{thf})\}_2\{(\text{M}t\text{Bu})_3\text{S}\}_2]$ (**38**). The magnetic axes are calculated with the program Magellan and illustrated with the program Diamond 3.[174] All hydrogen atoms and the tmeda moieties attached to each potassium ion in (**a**) are omitted for clarity. Color code: C: (black), N: (blue), O: (red), S: (yellow), K: (purple) Na: (sky blue), and Dy: (gold).

Looking forward, the abstraction of the remaining chloride from **38** could lead to $[(\text{thf})_2\text{Na}_2\text{Dy}\{\text{S}(\text{N}t\text{Bu})_3\}_2]^+$ and substantially increase the axial anisotropy, consequently leading to better overall magnetic properties (**Figure 4.4.**).

In the light of the presented results, two strategies seem feasible for magnetic enhancements of the systems in this thesis. Firstly, the focus should shift toward the diimidosulfinate compounds since they are more robust and accessible in a more straightforward approach than their higher substituted polyimido congeners. Therefore, these systems are ideal models to systematically investigate procedures for abstracting the remaining halides that significantly hamper an axial coordination geometry and the subsequent the magnetic performance of our complexes. Once the methods are developed for sulfinates, they should be transferred to the complexes mentioned in this thesis.

Secondly, many SN systems hosting f-metal centers were investigated. No computational studies to correlate experimental and theoretical data exist so far. A systematic ligand screening study should provide new strategies for tailor-made ligand design for the synthetic chemist.

Both approaches could help to identify new avenues to access better performing SMMs featuring the SN motif.

5. Experimental Information

5.1. General procedures

All reactions were performed in oven-dried glassware under dry argon or nitrogen conditions, using Schlenk techniques, or an argon dry box.[191] Chlorinated solvents were distilled from calcium hydride, while all other solvents were distilled from sodium or potassium, and stored over 3 Å/4 Å molecular sieve prior to use. Filtrations were performed with Whatman™ glass microfiber filters GF/B standard, a LabMini™ 8M Mini Centrifuge, or glass fritted filters with Celite ranging from P2 to P4. All d- and f-metal halide salts were purchased from Sigma-Aldrich at a 99.999 % purity level and used as received. Other starting materials were ordered from ABCR, Acros Organics, and VWR.

5.2. Analytical methods

5.2.1. Elemental analysis

All elemental analysis measurements for the mass fractions of C, H, N, and S were recorded on an Elementar Vario EL3 device at the mikroanalytische Labor, institute of inorganic chemistry, University of Göttingen. As demonstrated by SC-XRD analysis, some complexes contain additional solvent molecules in the crystal lattice since the crystals were grown in the mother liquor. Even overnight drying under reduced pressure of these samples could not remove the entire amount of lattice solvents. Henceforth, slight deviations are found for the values of C and H.

5.2.2. NMR spectroscopy

All ^{1}H-, ^{13}C-, and ^{15}N-NMR experiments were performed on Bruker Avance III 500 , 400 , and 300 MHz spectrometers. NMR data were referenced to the deuterated solvent (thf-d_8 , benzene-d_6, and toluene-d_8), which was dried over activated molecular sieves.[192] The chemical shifts δ are illustrated in ppm, relative to the residual proton signal of the employed deuterated standard and the coupling constants J in Hz. Signals were assigned using conventional 2D correlations (COSY, HSQC, HMBC). ^{1}H-DOSY-NMR-ECC-*MW* measurements were performed in collaboration with A.-K. KREYENSCHMIDT within the group of STALKE. The samples were prepared with 20 µmol of 2,2,3,3-tetramethylbutane (TMB) as an internal standard for the sample material in thf-d_8. Temperature-dependent measurements were carried out at 323, 298, and 243 K. For each compound, the magnetic field pulse was fine-tuned in the range of 400-3500 µs. The subsequent diffusion coefficients are calculated by Gaussian fits with the T1/T2 interface in Topspin 3.1.

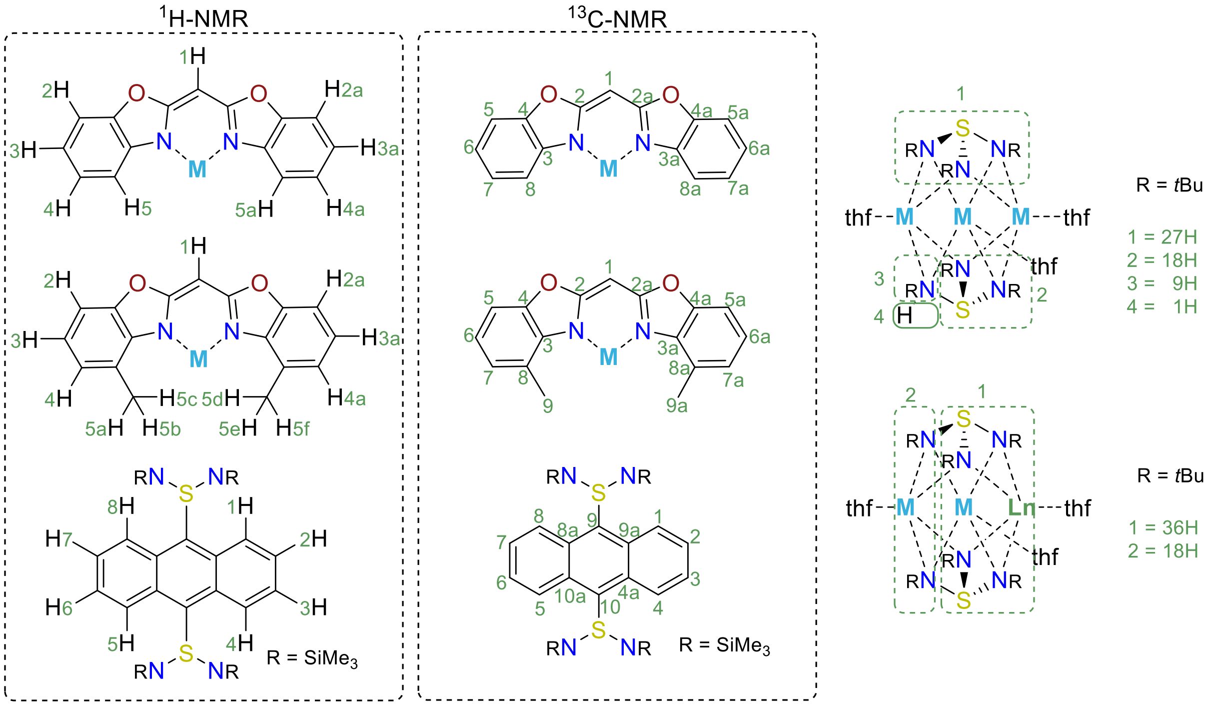

Figure 5.1. Signal assignment for all Box and SN NMR data.

For all paramagnetic NMR data, the line broadening is displayed as $\Delta\nu_{A}^{FWHH}$ (abbrv.: $W_{1/2}$) in Hz and other relevant parameters such as spectral width (sw), acquisition time (aq), relaxation delay (d1), and number of scans (ns) are provided for each experiment.

5.2.3. Mass spectrometry

The mass spectrometry data was collected from the Central Analysis Department, located at the organic chemistry institute, University of Göttingen. The experiments applying the ESI-MS method were recorded with a Bruker MicroTOF and the LIFDI-MS data with a *Jeol* AccuTOF spectrometer. Peaks are illustrated as mass to charge ratio (*m*/*z*) of the fragmented ions and refer to their isotopes with the highest natural abundancies.

5.2.4. Magnetic susceptibility measurements

The magnetic property measurements were performed with a Quantum Design MPMS XL 5 SQUID magnetometer equipped with a 5 T magnet and a frequency range of 1 to 1488 Hz or a Quantum Design MPMS 3 SQUID magnetometer equipped with a 7 T magnet and a frequency range of 1 to 1000 Hz. The procedure stated below is based on the on-device training from LEGENDRE and DEMESHKO at the University of Göttingen.

The sample was prepared from crystalline material, which was crushed and transferred into a galantine capsule. In order to prevent magnetic torquing, the sample was covered with Fomblin Y45 oil and sealed with a smaller gel bucket. Next, the sealed sample is charged into a sample holder (a non-paramagnetic drinking straw) and closed with two rubber septa. Transportation to the SQUID device was facilitated in a Schlenk tube to avoid exposure to air and moisture.

Inside the SQUID magnetometer, the sample was centered first, which is an automatic process (chapter 1.6.2). The Fomblin Y45 oil freezes below 210 K. Therefore, the direct current (dc) susceptibility measurement is conducted in the temperature range between 210 to 2 K. Usually, a dc field of 0.5 T is employed. However, some measurements with gadolinium compounds require smaller dc fields. This experiment provides the contribution of the orbital angular momentum to the magnetic properties and further confirms the multiplicity and nuclearity of the compound. Second, the sample is probed for hysteresis behavior, searching for remnant magnetization at 2 K via a field sweep from 7 to 0 T, 0 to −7 T, −7 to 0 T, and back to 7 T. Slow relaxation of magnetization was identified within an alternating current (ac) test at the highest frequency (1488/1000 Hz) under zero-field conditions and an applied dc field of 1000 Oe. Subsequent field-depending measurements were carried out at the optimal temperature to identify the field strength with the highest out-of-phase response. For all SMMs, additional measurements within the temperature range were performed under the ideal field conditions. In the case of a transition metal SMM, variable temperature variable field (VTVH) experiments were carried out to assert the zero-field splitting parameters D and E.

OriginPro 8.5 served as the work-up user face for all data.[193] The first step in processing the data was a correction of the diamagnetic contribution from the Y45 oil ($\chi_g = -5.70 \cdot 10^{-7}$ emu/(g Oe)) and the gel capsules ($\chi_g = -3.51 \cdot 10^{-7}$ emu/(g Oe)) according to $M_{dia} = \chi_g\, m\, H$ as well as correction for temperature-independent paramagnetic (TIP) were applied. The standard procedure to correct the molar susceptibility χ_M is obtained via $\chi_M = -0.5\, M\, 10^{-6}$ cm^3 mol^{-1}. An approximation for the $\chi_M T$ and VTVH data was achieved with the JulX-2s package suite available from E. Bill located at the MPI in Mülheim.[131] Furthermore, the CC-fit program was employed to fit the relaxation rate in the Cole-Cole plot and the MAGELLAN program to determine the main magnetic axis in all dysprosium complexes, both developed by CHILTON, University of Manchester.[136,174a]

5.3. Compound synthesis and characterization

5.3.1. Synthesis of [(thf)Mn{(NCOC$_6$H$_4$)$_2$CH}$_2$] (1)

	M [g mol^{-1}]	*n* [mmol]	*m* [mg]	equiv.	*V* [ml]
MnCl$_2$	125.48	0.07	8.70	1	-
KBox	360.45	0.14	50	2	-
thf	-	-	-	-	5

KBox (2 equiv., 50 mg, 0.14 mmol) was dissolved in thf and upon adding MnCl$_2$ (1 equiv., 8.70 mg, 0.07 mmol), a color change to green was noticed. After stirring the reaction mixture for 12h at r.t., precipitated KCl was removed via filtration and all remaining solvent was removed under reduced pressure. Recrystallization from a saturated solution in 1 ml thf, allowing 3 ml pentane to evaporate into the thf solution at 238 K, afforded green-block-shaped crystals.

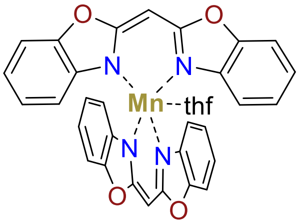

Empirical formula: $C_{34}H_{26}MnN_4O_5$

Molecular weight: 625.54 g mol^{-1}

Yield: 20.2 mg, 32.4 µmol, 46 %

^{1}H NMR {sw: 263 ppm; aq: 0.996 s; d1: 0.1 s; ns: 128}

(500.25 MHz, thf-d_8): δ = −19.55 (bs, 2H, H5, H5a $W_{1/2}$ = 2262 Hz), −3.48 (bs, 2H, H3, H3a $W_{1/2}$ = 430 Hz), 8.43 (bs, 1H, H1, $W_{1/2}$ = 413 Hz), 11.83 (bs, 2H, H4, H4a $W_{1/2}$ = 628 Hz), 29.66 (bs, 2H, H2, H2a $W_{1/2}$ = 1740 Hz) ppm.

^{13}C {^{1}H} NMR

(125.80 MHz, thf-d_8): Strong paramagnetic center, no signals detectable.

Elemental analysis

(calc. in %): **C**: 65.28 (65.38); **H**: 4.19 (4.07); **N**: 8.96 (8.81).

MS (LIFDI)

m/*z* (%): 553.3 (100) [M – thf]$^+$

All experimental data can be retrieved from the supplementary information, available under: https://www.rsc.org/suppdata/d1/dt/d1dt03230e/d1dt03230e1.pdf

5.3.2. Synthesis of $[(thf)Fe\{(NCOC_6H_4)_2CH\}_2]$ (2)

	M [g mol^{-1}]	*n* [mmol]	*m* [mg]	equiv.	*V* [ml]
$FeCl_2$	126.75	0.07	8.79	1	-
$Fe(HMDS)_2$	376.62	0.07	26.1	1	-
KBox	360.45	0.14	50	2	-
Box	250.26	0.14	35.0	2	-
thf	-	-	-	-	5

KBox (2 equiv., 50 mg, 0.14 mmol) was dissolved in thf and upon adding $FeCl_2$ (1 equiv., 8.79 mg, 0.07 mmol), a color change to yellow was observed. After stirring 24h at r.t., precipitated KCl was removed via filtration and all remaining solvent was removed under reduced pressure. Recrystallization from a saturated solution in 1 ml thf, allowing 3 ml pentane to evaporate into the thf solution at 238 K, afforded yellow-block-shaped crystals. A higher yield of 51 % is attained using $Fe(HMDS)_2$ (1 equiv., 26.1 mg, 0.07 mmol) and the Box ligand (2 equiv., 35.0 mg, 0.14 mmol). Forming (H)HMDS is removed under reduced pressure and the purification process is analog to the first method.

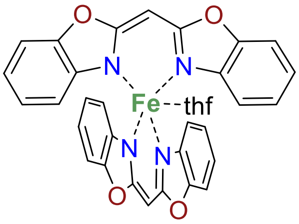

Empirical formula: $C_{34}H_{26}FeN_4O_5$

Molecular weight: 626.45 g mol^{-1}

Yield: I: 12.6 mg, 20.1 µmol, 29 %
II: 22.0 mg, 35.1 µmol, 51 %

^{1}H NMR (500.25 MHz, thf-d_8): {sw: 200 ppm; aq: 0.655 s; d1: 0.1 s; ns: 128}
δ = −55.29 (bs, 2H, H5, H5a, $W_{½}$ = 793 Hz), −15.07 (bs, 2H, H3, H3a, $W_{½}$ = 28 Hz), −9.24 (bs, 2H, H4, H4a, $W_{½}$ = 150 Hz), 36.24 (s, 2H, H2, H2a, $W_{½}$ = 27 Hz) ppm. (Note: H1 is only resolved for $[Co(Box)_2]$ (**3**))

^{13}C {^{1}H} NMR (125.80 MHz, thf-d_8): {sw: 1806 ppm; aq: 0.655 s; d1: 0.1 s; ns: 1024}
δ = 7.37 (s, 1C, C7), 234.63 (s, 1C, C), 235.93 (s, 1C, C6), 308.18 (s, 1C, C), 390.01 (s, 1C, C), 606.66 (s, 1C, 1C), 625.23 (s, 1C, C), 1047.75 (s, 1C, C8) ppm.

Elemental analysis (calc. in %): **C**: 65.53 (65.19); **H**: 4.09 (4.18); **N**: 8.99 (8.94).

MS (LIFDI) *m/z* (%): 554.3 (100) [M – thf]$^+$

All experimental data can be retrieved from the supplementary information, available under: https://www.rsc.org/suppdata/d1/dt/d1dt03230e/d1dt03230e1.pdf

5.3.3. Synthesis of [Co{(NCOC$_6$H$_4$)$_2$CH}$_2$] (3)

	M [g mol^{-1}]	*n* [mmol]	*m* [mg]	equiv.	*V* [ml]
CoCl$_2$	129.83	0.06	8.33	1	-
KBox	360.45	0.14	50	2	-
thf	-	-	-	-	5

KBox (2 equiv., 50 mg, 0.14 mmol) and CoCl$_2$ (1 equiv., 8.33 mg, 0.07 mmol) were mixed and stirred for 24h in thf at r.t. The resulting red solution was filtrated and all remaining thf was removed under reduced pressure. **3** was then extracted in toluene (3 x 2 ml). Recrystallization from a saturated solution in 2 ml toluene, allowing 2 ml hexane to evaporate into the toluene solution at 238 K, afforded red-needle-shaped crystals.

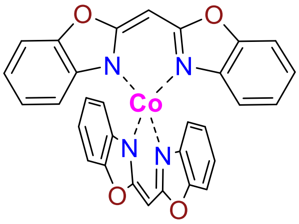

Empirical formula:	C$_{34}$H$_{26}$CoN$_4$O$_5$
Molecular weight:	557.43 g mol^{-1}
Yield:	27.1 mg, 48.6 µmol, 70 %

^{1}H NMR {sw: 234 ppm; aq: 0.559 s; d1: 0.1 s; ns: 128}
(500.25 MHz, thf-*d*$_8$): δ = −74.98 (bs, 2H, H5, H5a, $W_{½}$ = 1493 Hz), −24.64 (s, 2H, H3, H3a, $W_{½}$ = 71 Hz), −16.23 (bs, 1H, H1, H1a, $W_{½}$ = 400 Hz), 2.51 (s, 2H, H4, H4a, $W_{½}$ = 44 Hz), 40.65 (s, 2H, H2, H2a, $W_{½}$ = 75 Hz) ppm.

^{13}C {^{1}H} NMR {sw: 1806 ppm; aq: 0.288 s; d1: 0.2 s; ns: 1024}
(125.80 MHz, thf-*d*$_8$): δ = −37.62 (s, 1C, C7), −33.32 (s, 1C, C5), 270.58 (s, 1C, C6), 369.01 (s, 1C, C4), 401.11 (s, 1C, C2/C3), 591.95 (s, 1C, C1), 750.88 (s, 1C, C2/C3), 1031.0 (s, 1C, C8) ppm.

Elemental analysis
(calc. in %): **C**: 64.34 (64.64); **H**: 3.15 (3.25); **N**: 10.43 (10.05).

MS (LIFDI)
m/*z* (%): 557.3 (100) [M]$^+$

All experimental data can be retrieved from the supplementary information, available under: https://www.rsc.org/suppdata/d1/dt/d1dt03230e/d1dt03230e1.pdf

5.3.4. Synthesis of [Ni{(NCOC$_6$H$_4$)$_2$CH}$_2$] (4)

	M [g mol^{-1}]	*n* [mmol]	*m* [mg]	equiv.	*V* [ml]
NiCl$_2$	129.59	0.07	7.80	1	-
KBox	360.45	0.14	50	2	-
thf	-	-	-	-	5

KBox (2 equiv., 50 mg, 0.14 mmol) and NiCl$_2$ (1 equiv., 7.80 mg, 0.07 mmol) were weight in a Schlenk flask and refluxed for 2h in thf. The resulting blue solution was filtrated and all remaining thf was removed under reduced pressure. **4** was then extracted in toluene (3 x 2 ml). Recrystallization from a saturated toluene solution (2 ml), allowing 2 ml hexane to evaporate into the toluene solution at 238 K, afforded dark-green needle-shaped crystals.

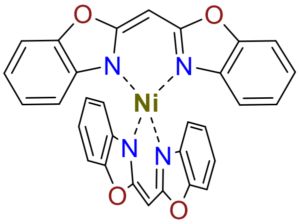

Empirical formula:	C$_{34}$H$_{26}$NiN$_4$O$_5$
Molecular weight:	557.19 g mol^{-1}
Yield:	21.0 mg, 37.7 µmol, 50 %

^{1}H NMR (500.25 MHz, thf-*d*$_8$): {sw: 298 ppm; aq: 0.367 s; d1: 0.05 s; ns: 128}
δ = −109.63 (s, 2H, H5, H5a, $W_{1/2}$ = 120 Hz), −13.68 (s, 2H, H3, H3a, $W_{1/2}$ = 100 Hz), 18.28 (bs, 2H, H4, H4a, $W_{1/2}$ = 75 Hz), 40.65 (s, 2H, H2, H2a, $W_{1/2}$ = 91 Hz) ppm. (Note: H1 is only resolved for [Co(Box)$_2$] (**3**))

^{13}C {^{1}H} NMR (125.80 MHz, thf-*d*$_8$): {sw: 1987 ppm; aq: 0.262 s; d1: 0.2 s; ns: 21217}
δ = −94.40 (s, 1C, C7), −6.03 (s, 1C, C5), 36.58 (s, 1C, C6), 289.46 (s, 1C, C4), 404.34 (s, 1C, C2/C3), 447.45 (s, 1C, C1), 536.04 (s, 1C, C2/C3) 748.25 (s, 1C, C8) ppm.

Elemental analysis
(calc. in %): **C**: 64.41 (64.67); **H**: 3.43 (3.26); **N**: 10.32 (10.06).
MS (LIFDI)
m/*z* (%): 556.3 (100) [M]$^+$

All experimental data can be retrieved from the supplementary information, available under: https://www.rsc.org/suppdata/d1/dt/d1dt03230e/d1dt03230e1.pdf

5.3.5. Synthesis of [(thf)$_2$MnCl{(4-benzhydryl-NCOC$_6$H$_3$)$_2$CH}] (5)

	M [g mol^{-1}]	*n* [mmol]	*m* [mg]	equiv.	*V* [ml]
MnCl$_2$	125.48	0.17	21.3	1.0	-
KH	40.11	0.22	8.9	1.3	-
Bzhbox	582.70	0.17	100	1.0	-
thf					5

Bzhbox (1.0 equiv., 100 mg, 0.17 mmol) and KH (1.3 equiv., 8.9 mg, 0.22 mmol) were transferred into a Schlenk flask and stirred in thf at r.t. for 24h. The resulting red suspension was filtrated and dropwise added to MnCl$_2$ (1.0 equiv., 21.3 mg, 0.17 mmol) and stirred for 24h. All volatiles were removed under reduced pressure, and **6** was extracted in toluene (3 x 2 ml). Yellow block-shaped crystals suitable for SC-XRD were obtained from hexane (2 ml) evaporation into a saturated toluene solution (1.5 ml).

Empirical formula: $C_{49}H_{45}ClMnN_2O_2$

Molecular weight: 816.30 g mol^{-1}

Yield: 55.6 mg, 68.1 µmol, 40 %

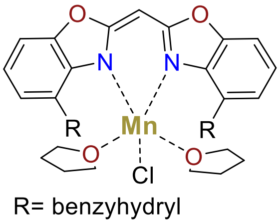

^{1}H NMR {sw: 238 ppm; aq: 0.551 s; d1: 0.1 s; ns: 256}

(500.25 MHz, thf-*d*$_8$): δ = −7.79 (bs, 1H, H1, $W_{½}$ = 1504 Hz), 1.73 (m, 8H, OCH$_2$C***H***$_2$), 3.58 (m, 8H, OC***H***$_2$CH$_2$), 4.62 (bs, 2H, H, $W_{½}$ = 103 Hz), 5.33 (bs, 2H, H, $W_{½}$ = 150 Hz), 6.27 (bs, 2H, H, $W_{½}$ = 80 Hz), 7.14 (bs, 20H, (CH***Ph***$_2$)$_2$), $W_{½}$ = 130 Hz), 11.51 (bs, 2H, (C***H***Ph$_2$)$_2$), $W_{½}$ = 604 Hz) ppm.

^{13}C {^{1}H} NMR

(125.80 MHz, thf-*d*$_8$): Strong paramagnetic center, no signals detectable.

Elemental analysis

(calc. in %): **C**: 71.79 (72.10); **H**: 5.21 (5.56); **N**: 3.82 (3.43).

MS (LIFDI)

m/*z* (%): 1222.1 (100) [2 Ligand, 1 Mn + Li]$^+$

5.3.6. Synthesis of [(thf)$_2$FeCl{(4-benzhydryl-NCOC$_6$H$_3$)$_2$CH}] (6)

	M [g mol^{-1}]	*n* [mmol]	*m* [mg]	equiv.	*V* [ml]
FeCl$_2$	126.75	0.17	21.6	1.0	-
KH	40.11	0.22	8.9	1.3	-
Bzhbox	582.70	0.17	100	1.0	-
thf					5

Bzhbox (1.0 equiv., 100 mg, 0.17 mmol) and KH (1.3 equiv., 8.9 mg, 0.22 mmol) were transferred into a Schlenk flask and stirred in thf at r.t. for 24h. The resulting red suspension was filtrated and dropwise added to FeCl$_2$ (1.0 equiv., 21.6 mg, 0.17 mmol) and stirred for 24h. All volatiles were removed under reduced pressure, and **6** was extracted in toluene (3 x 2 ml). Red needle-shaped crystals suitable for SC-XRD were obtained from hexane (2 ml) evaporation into a saturated toluene solution (1.5 ml).

Empirical formula: $C_{49}H_{45}ClFeN_2O_4$

Molecular weight: 817.20 g mol^{-1}

Yield: 59.4 mg, 72.7 µmol, 42 %

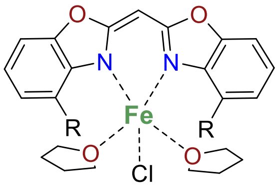

R= benzhydryl

^{1}H NMR {sw: 319 ppm; aq: 1.022 s; d1: 0.5 s; ns: 1024}

(500.25 MHz, thf-*d*$_8$): δ = −10.53 (s, 1H, H1, $W_{1/2}$ = 50 Hz), 1.69 (m, 8H, $\mathrm{OCH_2C}\boldsymbol{H}_2$), 3.83 (m, 8H, $\mathrm{OC}\boldsymbol{H}_2\mathrm{CH_2}$), 5.67 (s, 2H, H, $W_{1/2}$ = 17 Hz), 6.40 (s, 2H, H, $W_{1/2}$ = 12 Hz), 7.84 (bs, 20H, $(\mathrm{CH}\boldsymbol{Ph}_2)_2$), $W_{1/2}$ = 10 Hz), 12.78 (bs, 2H, H, $W_{1/2}$ = 48 Hz), 36.26 (bs, 2H, $(\mathrm{C}\boldsymbol{H}\mathrm{Ph_2})_2$), $W_{1/2}$ = 37 Hz) ppm.

^{13}C {^{1}H} NMR

(125.80 MHz, thf-*d*$_8$): Strong paramagnetic center, no signals detectable.

Elemental analysis

(calc. in %): **C**: 71.1 (72.02); **H**: 5.16 (5.55); **N**: 3.57 (3.43).

MS (LIFDI)

m/*z* (%): 672.1 (100) [M – thf]$^+$

5.3.7. Synthesis of [(thf)CoCl{(4-benzhydryl-NCOC$_6$H$_3$)$_2$CH}] (7)

	M [g mol^{-1}]	*n* [mmol]	*m* [mg]	equiv.	*V* [ml]
CoCl$_2$	129.83	0.17	22.3	1.0	-
KH	40.11	0.22	8.9	1.3	-
Bzhbox	582.70	0.17	100	1.0	-
thf	-	-	-	-	5

Bzhbox (1.0 equiv., 100 mg, 0.17 mmol) and KH (1.3 equiv., 8.9 mg, 0.22 mmol) were transferred into a Schlenk flask and stirred in thf at r.t. for 24h. The resulting red suspension was filtrated and dropwise added to CoCl$_2$ (1.0 equiv., 22.3 mg, 0.22 mmol) and stirred for 24h. All volatiles were removed under reduced pressure, and **7** was extracted in toluene (3 x 2 ml). Brown block-shaped crystals suitable for SC-XRD were obtained from hexane (2 ml) evaporation into a saturated toluene solution (1.5 ml).

Empirical formula: C$_{45}$H$_{37}$ClCoN$_2$O$_3$

Molecular weight: 748.19 g mol^{-1}

Yield: 47.8 mg, 63.9 µmol, 37 %

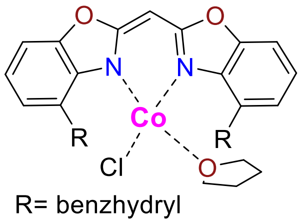

^{1}H NMR {sw: 178 ppm; aq: 0.367 s; d1: 0.05 s; ns: 128}

(500.25 MHz, thf-*d*$_8$): $\delta = -18.71$ (bs, 1H, H, $W_{1/2}$ = 78 Hz), 0.98 (bs, 2H, H, $W_{1/2}$ = 70 Hz), 1.78 (m, 4H, OCH$_2$C***H***$_2$), 3.87 (m, 4H, OC***H***$_2$CH$_2$), 5.46 (s, 2H, H, $W_{1/2}$ = 40 Hz), 6.44 (bs, 2H, H, $W_{1/2}$ = 32 Hz), 8.08 (bs, 20H, (CH***Ph***$_2$)$_2$), $W_{1/2}$ = 41 Hz), 42.20 (bs, 2H, (C***H***Ph$_2$)$_2$), $W_{1/2}$ = 148 Hz) ppm.

^{13}C {^{1}H} NMR

(125.80 MHz, thf-*d*$_8$): Strong paramagnetic center, no signals detectable.

Elemental analysis

(calc. in %), [M + 1thf]: **C**: 71.87 (72.24); **H**: 5.27 (4.98); **N**: 3.52 (3.74).

MS (LIFDI)

m/*z* (%): 675.1 (100) [M – thf]$^+$

5.3.8. Synthesis of [(thf)$_2$MnCl{(4,6-*t*Bu-NCOC$_6$H$_2$)$_2$CH}] (8)

	M [g mol^{-1}]	*n* [mmol]	*m* [mg]	equiv.	*V* [ml]
MnCl$_2$	125.48	0.20	24.5	1	-
K*t*Bubox	512.77	0.20	100	1	-
thf	-	-	-	-	5

KBzhbox (1 equiv., 100 mg, 0.20 mmol) and MnCl$_2$ (1 equiv., 24.5 mg, 0.20 mmol) were transferred into a Schlenk flask and stirred in thf at r.t. for 24h. The resulting greenish suspension was filtrated and all remaining thf was removed under reduced pressure. **8** was then extracted in toluene (3 x 2 ml). Recrystallization from a saturated solution in 1 ml toluene at 238 K afforded green block-shaped crystals.

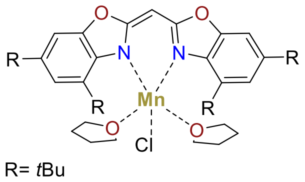

Empirical formula: $C_{39}H_{57}ClMnN_2O_4$
Molecular weight: 708.28 g mol^{-1}
Yield: 59.5 mg, 84.0 µmol, 42 %

^{1}H NMR
(500.25 MHz, thf-*d*$_8$): Strong paramagnetic center, no signals detectable.
^{13}C {^{1}H} NMR
(125.80 MHz, thf-*d*$_8$): Strong paramagnetic center, no signals detectable.
Elemental analysis
(calc. in %), [M – thf]: **C**: 65.41 (66.08); **H**: 7.21 (7.76); **N**: 4.21 (4.40).
MS (LIFDI)
m/*z* (%): 528.2 (100) [M – Cl, 2 thf]$^+$

5.3.9. Synthesis of [Gd{N(SiCH$_3$)$_2$}$_3$] (9)

	M [g mol^{-1}]	*n* [mmol]	*m* [mg]	equiv.	*V* [ml]
GdCl$_3$	263.61	0.50	132	1	-
KHMDS	199.48	1.50	300	3	-
thf	-	-	-	-	10

KHMDS (3 equiv., 300 mg, 1.50 mmol) and GdCl$_3$ (1 equiv., 132 mg, 0.50 mmol) were transferred into a Schlenk flask and stirred in thf at r.t. for 24h. All volatiles were removed under reduced pressure and the resulting product was extracted with *n*-pentane (5 x 5 ml). After removal of volatiles, the white solid was sublimated at 446 K and 5·10^{-2} mbar. Colorless needle-shaped crystals suitable for X-ray diffraction experiments were obtained from a saturated solution in *n*-pentane.

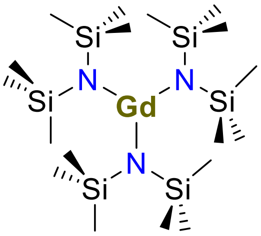

Empirical formula: $C_{18}H_{54}GdN_3Si_6$

Molecular weight: 638.22 g mol^{-1}

Yield: 194.9 mg, 305 µmol, 61 %

^{1}H NMR {sw: 99 ppm; aq: 1.65 s; d1: 0.1 s; ns: 8}

(500.25 MHz, thf-*d*$_8$): δ = –10.94 (bs, 54H, (Si(C***H***$_3$)$_3$)$_6$, $W_{1/2}$ = 3055 Hz) ppm.

^{13}C {^{1}H} NMR

(125.80 MHz, thf-*d*$_8$): Strong paramagnetic center, no signals detectable.

Elemental analysis

(calc. in %): **C**: 33.29 (33.87); **H**: 8.82 (8.53); **N**: 6.34 (6.58).

MS (LIFDI)

m/*z* (%): 638.2 (100) [M]$^+$

This synthesis is a modified procedure of BRADLEY, GHOTRA, and HART. **9** was prior published with low-quality SC-XRD data in the master thesis of D. Lüert.[144]

5.3.10. Synthesis of [Ho{N(SiCH$_3$)$_2$}$_3$] (10)

	M [g mol^{-1}]	*n* [mmol]	*m* [mg]	equiv.	*V* [ml]
HoCl$_3$	271.28	0.74	200	1	-
KHMDS	199.48	2.21	440	3	-
thf	-	-	-	-	10

KHMDS (3 equiv., 440 mg, 2.21 mmol) and HoCl$_3$ (1 equiv., 200 mg, 0.74 mmol) were transferred into a Schlenk flask and stirred in thf at r.t. for 24h. All volatiles were removed under reduced pressure and the resulting product was extracted with *n*-pentane (5 x 5 ml). After removal of volatiles, the light pink solid was sublimated at 446 K and 5·10^{-2} mbar. Colorless needle-shaped crystals suitable for X-ray diffraction experiments were obtained from a saturated solution in *n*-pentane.

Empirical formula: C$_{18}$H$_{54}$HoN$_3$Si$_6$
Molecular weight: 645.22 g mol^{-1}
Yield: 295.0 mg, 447 µmol, 61 %

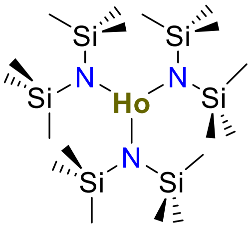

^{1}H NMR {sw: 200 ppm; aq: 1.311 s; d1: 0.1 s; ns: 8}
(500.25 MHz, toluene-*d*$_8$): δ = –72.46 (bs, 54H, Si(C***H***$_3$)$_3$)$_6$, *W*$_{½}$ = 938 Hz) ppm.

^{13}C {^{1}H} NMR {sw: 1193 ppm; aq: 0.323 s; d1: 0.2 s; ns: 64}
(125.80 MHz, thf-*d*$_8$): δ = 5.57.46 (s, 18C, Si(***C***H$_3$)$_3$)$_6$) ppm.
Elemental analysis
(calc. in %): **C**: 34.02 (33.46); **H**: 8.42 (8.42); **N**: 6.51 (6.50).
MS (LIFDI)
m/*z* (%): 645.3 (100) [M]$^+$

This synthesis is a modified procedure of BRADLEY, GHOTRA, and HART. **10** was prior published with low-quality SC-XRD data in the master thesis of D. Lüert.[144]

5.3.11. Synthesis of [(thf)Eu{(NCOC$_6$H$_4$)$_2$CH}$_3$] (11)

	M [g mol^{-1}]	n [mmol]	m [mg]	equiv.	V [ml]
[Eu(HMDS)$_3$]	633.12	0.13	84.3	1	-
Box	250.26	0.40	100	3	-
thf	-	-	-	-	3

[Eu(HMDS)$_3$] (1 equiv., 84.3 mg, 0.13 mmol) was dropwise added to Box (3 equiv., 100 mg, 0.40 mmol) in thf and stirred at r.t. for 24h. H(HMDS) was removed under reduced pressure, and blue block-shaped crystals suitable for X-ray diffraction experiments were obtained from slow evaporation of pentane (3 ml) into a saturated thf solution (1.5 ml) at 238 K. High purity was achieved after two cycles of recrystallization.

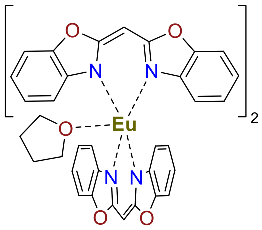

Empirical formula: $C_{49}H_{35}EuN_6O_7$

Molecular weight: 971.82 g mol^{-1}

Yield: 50.5 mg, 51.9 µmol, 39 %

^{1}H NMR {sw: 263 ppm; aq: 0.996 s; d1: 0.1 s; ns: 128}

(500.25 MHz, thf-d_8): δ = 1.75 (m, 4H, $\mathrm{OCH_2C}\boldsymbol{H}_2$), 2.82 (s, 1H, H1), 3.61 (m, 4H, $\mathrm{OC}\boldsymbol{H}_2\mathrm{CH_2}$), 4.75 (d, 2H, H2, H2a, $^3J_{\mathrm{HH}}$ = 7.43), 7.64 (s, 2H, H4, H4a), 7.86 (t, 2H, H3, H3a, $^3J_{\mathrm{HH}}$ = 7.06), 10.60 (s, 2H, H5, H5a) ppm.

^{13}C {^{1}H} NMR {sw: 602 ppm; aq: 0.432 s; d1: 0.3 s; ns: 32}

(125.80 MHz, thf-d_8): δ = 31.69 (s, 2C, C2), 25.30 (m, 4C, $\mathrm{OCH_2}\boldsymbol{C}\mathrm{H_2}$), 67.45 (m, 4H, $\mathrm{O}\boldsymbol{C}\mathrm{H_2CH_2}$) 102.75 (s, 1C, C1), 110.50 (s, 2C, C6), 118.99 (s, 2C, C8), 120.83 (s, 2C, C9), 129.86 (s, 2C, C7), 149.66 (s, 1C, C5) 155.23 (s, 2C, C4) ppm.

Elemental analysis

(calc. in %): **C**: 60.31 (60.56); **H**: 3.88 (3.63); **N**: 8.26 (8.65).

MS (LIFDI)

m/z (%): 900.1 (100) [M]$^+$

5.3.12. Synthesis of [(thf)Tb{$(NCOC_6H_4)_2CH$}$_3$] (12)

	M [g mol⁻¹]	*n* [mmol]	*m* [mg]	equiv.	*V* [ml]
[Tb(HMDS)$_3$]	640.09	0.13	85.3	1	-
Box	250.26	0.40	100	3	-
thf	-	-	-	-	3

[Tb(HMDS)$_3$] (1 equiv., 85.3 mg, 0.13 mmol) was dropwise added to Box (3 equiv., 100 mg, 0.40 mmol) in thf and stirred at r.t. for 24h. H(HMDS) was removed under reduced pressure and yellow block-shaped crystals suitable for X-ray diffraction experiments were obtained from slow evaporation of pentane (3 ml) into a saturated thf solution (1.5 ml) at 238 K. High purity was achieved after two cycles of recrystallization.

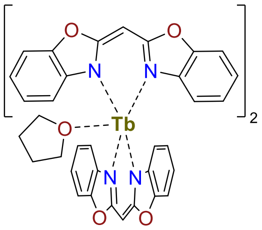

Empirical formula:	$C_{49}H_{35}TbN_6O_7$
Molecular weight:	1050.24 g mol⁻¹
Yield:	50.2 mg, 47.8 µmol, 36 %

^{1}H NMR	{sw: 250 ppm; aq: 1.05 s; d1: 0.1 s; ns: 128}
(500.25 MHz, thf-d_8):	δ = −63.14 (bs, 2H, H, $W_{½}$ = 2408 Hz), −9.50 (bs, 2H, H, $W_{½}$ = 195 Hz), 3.38 (s, 2H, H, $W_{½}$ = 82 Hz), 9.56 (s, 2H, H, $W_{½}$ = 97 Hz), 88.80 (s, 1H, H1, $W_{½}$ = 405 Hz) ppm.
^{13}C {^{1}H} NMR	
(125.80 MHz, thf-d_8):	Strong paramagnetic center, no signals detectable.
Elemental analysis	
(calc. in %):	**C**: 60.88 (60.58); **H**: 4.36 (4.12); **N**: 7.71 (8.00).
MS (LIFDI)	
m/*z* (%):	906.13 (100) [M]⁺

All experimental data can be retrieved from the supplementary information, available under: https://chemistry-europe.onlinelibrary.wiley.com/action/downloadSupplement?doi=10.1002%2Fejic.202100822&file=ejic202100822-sup-0001-misc_information.pdf

5.3.13. Synthesis of [(thf)Dy{(NCOC$_6$H$_4$)$_2$CH}$_3$] (13)

	M [g mol^{-1}]	*n* [mmol]	*m* [mg]	equiv.	*V* [ml]
[Dy(HMDS)$_3$]	643.66	0.13	85.7	1	-
Box	250.26	0.40	100	3	-
thf	-	-	-	-	3

[Dy(HMDS)$_3$] (1 equiv., 85.7 mg, 0.13 mmol) was dropwise added to Box (3 equiv., 100 mg, 0.40 mmol) in thf and stirred at r.t. for 24h. H(HMDS) was removed under reduced pressure and yellow block-shaped crystals suitable for X-ray diffraction experiments were obtained from slow evaporation of pentane (3 ml) into a saturated thf solution (1.5 ml) at 238 K. High purity was achieved after two cycles of recrystallization. The solvent-free analogue **13'** was obtained by applying the procedure above with toluene.

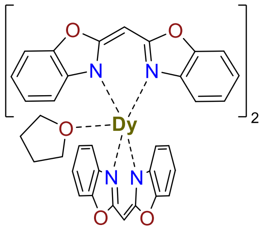

Empirical formula: $C_{49}H_{35}DyN_6O_7$

Molecular weight: 1054.24 g mol^{-1}

Yield: 57.7 mg, 54.7 µmol, 41 %

^{1}H NMR {sw: 300 ppm; aq: 0.874 s; d1: 0.1 s; ns: 128}
(500.25 MHz, thf-*d*$_8$): δ = −41.68 (bs, 2H, H, $W_{½}$ = 3069 Hz), −2.72 (s, 2H, H, $W_{½}$ = 253 Hz), 7.24 (bs, 2H, H, $W_{½}$ = 95 Hz), 13.36 (s, 2H, H, $W_{½}$ = 100 Hz), 77.18 (s, 1H, H1, $W_{½}$ = 102 Hz) ppm.

^{13}C {^{1}H} NMR
(125.80 MHz, thf-*d*$_8$): Strong paramagnetic center, no signals detectable.

Elemental analysis
(calc. in %): **C**: 60.54 (60.37); **H**: 4.42 (4.11); **N**: 7.67 (7.97).

MS (LIFDI)
m/*z* (%): 911.1 (100) [M]$^+$

All experimental data can be retrieved from the supplementary information, available under: https://chemistry-europe.onlinelibrary.wiley.com/action/downloadSupplement?doi=10.1002%2Fejic.202100822&file=ejic202100822-sup-0001-misc_information.pdf

5.3.14. Synthesis of [(thf)Ho{(NCOC$_6$H$_4$)$_2$CH}$_3$] (14)

	M [g mol^{-1}]	*n* [mmol]	*m* [mg]	equiv.	*V* [ml]
[Ho(HMDS)$_3$]	646.09	0.13	86.1	1	-
Box	250.26	0.40	100	3	-
thf	-	-	-	-	3

[Ho(HMDS)$_3$] (1 equiv., 86.1 mg, 0.13 mmol) was dropwise added to Box (3 equiv., 100 mg, 0.40 mmol) in thf and stirred at r.t. for 24h. H(HMDS) was removed under reduced pressure and yellow block-shaped crystals suitable for X-ray diffraction experiments were obtained from slow evaporation of pentane (3 ml) into a saturated thf solution (1.5 ml) at 238 K. High purity was achieved after two cycles of recrystallization.

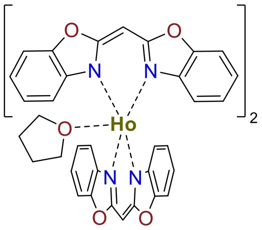

Empirical formula: $C_{49}H_{35}HoN_6O_7$

Molecular weight: 1056.24 g mol^{-1}

Yield: 51.7 mg, 48.9 µmol, 37 %

^{1}H NMR (500.25 MHz, thf-*d*$_8$): {sw: 263 ppm; aq: 0.996 s; d1: 0.1 s; ns: 128} δ = −47.84 (bs, 2H, H, $W_{1/2}$ = 2135 Hz), −6.13 (s, 2H, H, $W_{1/2}$ = 138 Hz), 2.99 (s, 2H, H, $W_{1/2}$ = 52 Hz), 8.33 (s, 2H, H, $W_{1/2}$ = 78 Hz), 61.98 (s, 1H, H1, $W_{1/2}$ = 367 Hz) ppm.

^{13}C {^{1}H} NMR (125.80 MHz, thf-*d*$_8$): Strong paramagnetic center, no signals detectable.

Elemental analysis (calc. in %): **C**: 60.56 (60.23); **H**: 4.31 (4.10); **N**: 8.01 (7.95).

MS (LIFDI) *m*/*z* (%): 912.1 (100) [M]$^+$

All experimental data can be retrieved from the supplementary information, available under: https://chemistry-europe.onlinelibrary.wiley.com/action/downloadSupplement?doi=10.1002%2Fejic.202100822&file=ejic202100822-sup-0001-misc_information.pdf

5.3.15. Synthesis of [(thf)Er{(NCOC$_6$H$_4$)$_2$CH}$_3$] (15)

	M [g mol⁻¹]	*n* [mmol]	*m* [mg]	equiv.	*V* [ml]
[Er(HMDS)$_3$]	648.42	0.13	86.4	1	-
Box	250.26	0.40	100	3	-
thf	-	-	-	-	3

[Er(HMDS)$_3$] (1 equiv., 86.4 mg, 0.13 mmol) was dropwise added to Box (3 equiv., 100 mg, 0.40 mmol) in thf and stirred at r.t. for 24h. H(HMDS) was removed under reduced pressure and yellow block-shaped crystals suitable for X-ray diffraction experiments were obtained from slow evaporation of pentane (3 ml) into a saturated thf solution (1.5 ml) at 238 K. High purity was achieved after two cycles of recrystallization.

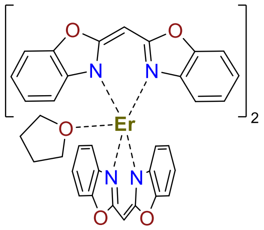

Empirical formula: $C_{49}H_{35}HoN_6O_7$

Molecular weight: 1059.24 g mol⁻¹

Yield: 48.1 mg, 45.4 µmol, 34 %

^{1}H NMR
(500.25 MHz, thf-*d*$_8$): {sw: 200 ppm; aq: 1.31 s; d1: 0.1 s; ns: 128}
δ = −22.64 (bs, 2H, H, $W_{½}$ = 251 Hz), 4.35 (s, 2H, H, $W_{½}$ = 53 Hz), 10.79 (s, 2H, H, $W_{½}$ = 47 Hz), 17.66 (s, 2H, H, $W_{½}$ = 114 Hz), 55.82 (s, 1H, H1, $W_{½}$ = 1207 Hz) ppm.

^{13}C {^{1}H} NMR
(125.80 MHz, thf-*d*$_8$): Strong paramagnetic center, no signals detectable.

Elemental analysis
(calc. in %): **C**: 60.32 (60.10); **H**: 4.21 (4.09); **N**: 8.21 (7.93).

MS (LIFDI)
m/z (%): 912.1 (100) [M]⁺

All experimental data can be retrieved from the supplementary information, available under: https://chemistry-europe.onlinelibrary.wiley.com/action/downloadSupplement?doi=10.1002%2Fejic.202100822&file=ejic202100822-sup-0001-misc_information.pdf

5.3.16. Synthesis of [Er{$(NCSC_6H_4)_2CH$}$_3$] (16)

	M [g mol⁻¹]	*n* [mmol]	*m* [mg]	equiv.	*V* [ml]
[Er(HMDS)$_3$]	648.42	0.12	76.5	1	-
Sbox	282.38	0.35	100	3	-
thf	-	-	-	-	3

[Er(HMDS)$_3$] (1 equiv., 76.5 mg, 0.12 mmol) in thf was dropwise added to Sbox (3 equiv., 100 mg, 0.35 mmol) in thf and stirred at r.t. for 24h. H(HMDS) was removed under reduced pressure and yellow block-shaped crystals suitable for X-ray diffraction experiments were obtained from slow evaporation of pentane (3 ml) into a saturated thf solution (1.5 ml) at 238 K after 19 weeks.

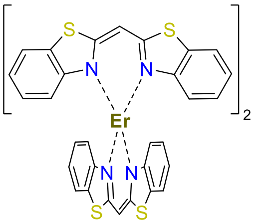

Empirical formula: $C_{49}H_{35}ErN_6S_6$

Molecular weight: 1011.37 g mol^{-1}

Yield: 43.7 mg, 43.4 µmol, 36 %

^{1}H NMR

(500.25 MHz, thf-d_8): $\delta = -26.44$ (bs, 2H, H, $W_{½}$ = 232 Hz), 3.42 (s, 2H, H, $W_{½}$ = 51 Hz), 8.32 (bs, 2H, H, $W_{½}$ = 51 Hz), 19.84 (bs, 2H, H, $W_{½}$ = 90 Hz), 62.43 (bs, 1H, H1, $W_{½}$ = 1032 Hz) ppm.

^{13}C {^{1}H} NMR

(125.80 MHz, thf-d_8): Strong paramagnetic center, no signals detectable.

Elemental analysis

(calc. in %): **C**: 54.02 (53.44); **H**: 3.11 (2.69); **N**: 8.04 (8.31).

MS (LIFDI)

m/*z* (%): 1009.9 (100) [M + H$^+$]$^+$

5.3.17. Synthesis of [Na(thf)$_6$][Na{(4-Me-NCOC$_6$H$_3$)$_2$CH}$_2$] (17)

	M [g mol^{-1}]	*n* [mmol]	*m* [mg]	equiv.	*V* [ml]
NaHMDS	183.37	1.08	197.6	1	-
Mebox	278.31	1.08	300	1	-
thf	-	-	-	-	8

NaHMDS (1 equiv., 197.6 mg, 1.08 mmol) in thf was dropwise added to Mebox (1 equiv., 300 mg, 1.08 mmol) in thf and stirred at r.t. for 24h. Formed H(HMDS) was removed under reduced pressure and suitable crystals for X-ray diffraction experiments were obtained saturated thf solution (2.0 ml) at 238 K. High purity was achieved after two cycles of recrystallization.

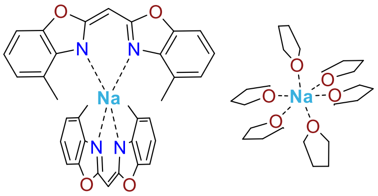

Empirical formula: $C_{58}H_{74}NNa_2O_{10}$

Molecular weight: 1033.23 g mol^{-1}(6 thf)

890.02 g mol^{-1}(4 thf)

Yield: 362 mg, 0.35 mmol, 76 %

^{1}H NMR

(500.25 MHz, thf-*d*$_8$): δ = 1.77 (m, 12H, OCH$_2$C***H***$_2$), 2.41 (s, 6H, H5a-f), 3.62 (m, 12H, OC***H***$_2$CH$_2$), 4.70 (s, 1H, H1), 6.65 (t, 2H, H7, H7a, $^3J_{HH}$ = 7.57 Hz), 6.74 (d, 2H, H4, H4a, $^3J_{HH}$ = 7.26 Hz), 6.88 (d, 2H, H2, H2a, $^3J_{HH}$ = 7.46 Hz) ppm.

^{13}C {^{1}H} NMR

(125.80 MHz, thf-*d*$_8$): 16.97 (s, 2C, C9, C9a), 26.26 (m, 2C, ***C***H$_2$, thf), 58.85 (s, 1C, C1), 68.10 (m, 2C, OCH$_2$, thf), 105.64 (s, 2C, C5, C5a), 118.60 (s, 2C, C6, C6a), 122.25 (s, 2C, C7, C7a), 123.85 (s, 2C, C8, C8a), 145.29 (s, 2C, C3, C3a), 149.46 (s, 2C, C4, C4a), 170.10 (s, 2C, C2, C2a) ppm.

Elemental analysis

(calc. in %): [M - 2 thf] **C**: 66.95 (67.55); **H**: 6.71 (6.58); **N**: 6.40 (6.73).

MS (ESI [+])

m/*z* (%): 301.09(100) [0.5 M -3 thf]$^+$, 302.10 (19) [0.5 M -3 thf]$^+$.

All experimental data can be retrieved from the supplementary information, available under: https://pubs.acs.org/doi/suppl/10.1021/acs.inorgchem.1c03714/suppl_file/ic1c03714_si_001.pdf

5.3.18. Synthesis of [(thf)$_3$Na(NCOC$_6$H$_4$)$_2$CH] (18)

	M [g mol^{-1}]	*n* [mmol]	*m* [mg]	equiv.	*V* [ml]
NaHMDS	183.37	2.00	366.4	1	-
Box	250.26	2.00	500	1	-
thf	-	-	-	-	10

NaHMDS (1 equiv., 366.4 mg, 2.00 mmol) in thf was dropwise added to Box (1 equiv., 500 mg, 2.00 mmol) in thf and stirred at r.t. for 24h. Formed H(HMDS) was removed under reduced pressure and suitable crystals for X-ray diffraction experiments were obtained saturated thf solution (2.5 ml) at 238 K. High purity was achieved after two cycles of recrystallization.

Empirical formula:	$C_{27}H_{33}N_2NaO_5$
Molecular weight:	488.56 g mol^{-1}
Yield:	512 mg, 1.05 mmol, 62 %

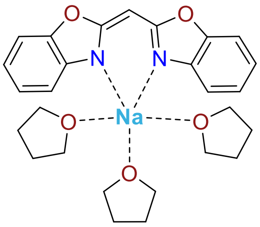

^{1}H NMR

(500.25 MHz, thf-*d*$_8$): δ = 1.77 (m, 12H, OCH$_2$C***H***$_2$), 3.62 (m, 12H, OC***H***$_2$CH$_2$), 4.69 (s, 1H, H1), 6.72 (td, 2H, H3, H3a, J_{HH} = 7.44, 0.91 Hz), 6.89 (td, 2H, H4, H4a, J_{HH} = 7.76, 0.91 Hz), 7.01 (m, 2H, H2, H6), 7.04 (m, 2H, H5, H9) ppm.

^{13}C {^{1}H} NMR

(125.80 MHz, thf-*d*$_8$): 25.48 (m, 2C, ***C***H$_2$, thf), 67.57 (m, 2C, OCH$_2$, thf), 108.03 (s, 2C, C6, C13), 113.56 (m, 2C, C9, C16), 119.06 (m, 2C, C7, C14), 122.97 (s, 2C, C8, C15), 147.15 (s, 2C, C4, C11), 150.43 (s, 2C, C5, C12), 171.10 (s, 2C, C1, C3) ppm.

Elemental analysis

(calc. in %): [M - thf] **C**: 66.15 (66.33); **H**: 6.31 (6.05); **N**: 6.51 (6.73).

MS (ESI [+])

m/*z* (%): 273.05(100) [M - thf]$^+$, 274.06 (16), [M - thf]$^+$

All experimental data can be retrieved from the supplementary information, available under: https://pubs.acs.org/doi/suppl/10.1021/acs.inorgchem.1c03714/suppl_file/ic1c03714_si_001.pdf

5.3.19. Synthesis of $[(\mu\text{-Cl})Gd\{(4\text{-Me-NCOC}_6H_3)_2CH\}_2]_2$ (19)

	M [g mol⁻¹]	*n* [mmol]	*m* [mg]	equiv.	*V* [ml]
$GdCl_3$	263.61	0.11	26.7	1	-
NaMebox	890.02	0.21	90	2	-
toluene	-	-	-	-	4

$GdCl_3$ (1 equiv., 26.7 mg, 0.11 mmol) and NaMebox (2 equiv., 90 mg, 0.21 mmol) were dissolved in toluene and stirred at r.t. for 24 h. Precipitating sodium chloride was removed with a GF/B WHATMAN™ filter and the filtrate was treated under reduced pressure until a level of 0.5 ml toluene. Storing at r.t. conditions resulted in yellow block-shaped crystals suitable for X-ray diffraction. Additional washing with cold toluene 2 x 0.5 ml) led to a high purity of **19**.

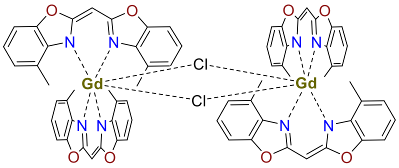

Empirical formula: $C_{58}H_{52}Cl_2Gd_2N_8O_8$

Molecular weight: 1494.61 g mol⁻¹

Yield: 28.0 mg, 18.7 µmol, 35 %

¹H NMR

(500.25 MHz, thf-*d*₈): Strong paramagnetic center, no signals detectable.

¹³C {¹H} NMR

(125.80 MHz, thf-*d*₈): Strong paramagnetic center, no signals detectable.

Elemental analysis

(calc. in %): **C**: 57.08 (56.77); **H**: 4.00 (3.81); **N**: 7.33 (7.06).

[M + 1 toluene]

All experimental data can be retrieved from the supplementary information, available under: https://pubs.acs.org/doi/suppl/10.1021/acs.inorgchem.1c03714/suppl_file/ic1c03714_si_001.pdf

5.3.20. Synthesis of [(μ-Cl)Dy{(4-Me-NCOC$_6$H$_3$)$_2$CH}$_2$]$_2$ (20)

	M [g mol^{-1}]	*n* [mmol]	*m* [mg]	equiv.	*V* [ml]
DyCl$_3$	268.85	0.11	27.2	1	-
NaMebox	890.02	0.21	90	2	-
toluene	-	-	-	-	4

DyCl$_3$ (1 equiv., 27.2 mg, 0.11 mmol) and NaMebox (2 equiv., 90 mg, 0.21 mmol) were dissolved in toluene and stirred at r.t. for 24 h. Precipitating sodium chloride was removed with a GF/B WHATMAN™ filter and the filtrate was treated under reduced pressure until a level of 0.5 ml toluene. Storing at r.t. conditions resulted in yellow block-shaped crystals suitable for X-ray diffraction. Additional washing with cold toluene 2 x 0.5 ml) led to a high purity of **20**.

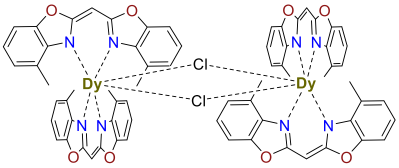

Empirical formula: C$_{58}$H$_{52}$Cl$_2$Dy$_2$N$_8$O$_8$

Molecular weight: 1505.11 g mol^{-1}

Yield: 31.1 mg, 20.7 µmol, 36 %

^{1}H NMR (500.25 MHz, thf-*d*$_8$): {sw: 300 ppm; aq: 0.100 s; d1: 0.1 s; ns: 32}
δ = −71.64 (bs, 1H, H1, $W_{1/2}$ = 172 Hz), 25.47 (bs, 2H, H, $W_{1/2}$ = 128 Hz), 36.26 (bs, 2H, H, $W_{1/2}$ = 221 Hz), 75.33 (bs, 2H, H, $W_{1/2}$ = 229 Hz), 132.97 (bs, 6H, C***H***$_3$, $W_{1/2}$ = 413 Hz) ppm..

^{13}C {^{1}H} NMR (125.80 MHz, thf-*d*$_8$): Strong paramagnetic center, no signals detectable.

Elemental analysis (calc. in %): [M + 2 toluene] **C**: 57.93 (58.30); **H**: 4.06 (4.06); **N**: 6.63 (6.63).

All experimental data can be retrieved from the supplementary information, available under: https://pubs.acs.org/doi/suppl/10.1021/acs.inorgchem.1c03714/suppl_file/ic1c03714_si_001.pdf

5.3.21. Synthesis of [(*µ*-Cl)Er{(4-Me-NCOC$_6$H$_3$)$_2$CH}$_2$]$_2$ (21)

	M [g mol^{-1}]	*n* [mmol]	*m* [mg]	equiv.	*V* [ml]
ErCl$_3$	273.61	0.11	27.7	1	-
NaMebox	890.02	0.21	90	2	-
toluene	-	-	-	-	4

ErCl$_3$ (1 equiv., 27.7 mg, 0.11 mmol) and NaMebox (2 equiv., 90 mg, 0.21 mmol) were dissolved in toluene and stirred at r.t. for 24 h. Precipitating sodium chloride was removed with a GF/B WHATMAN™ filter and the filtrate was treated under reduced pressure until a level of 0.5 ml toluene. Storing at r.t. conditions resulted in yellow block-shaped crystals suitable for X-ray diffraction. Additional washing with cold toluene 2 x 0.5 ml) led to a high purity of **21**.

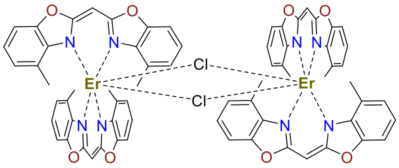

Empirical formula: C$_{58}$H$_{52}$Cl$_2$Er$_2$N$_8$O$_8$

Molecular weight: 1514.63 g mol^{-1}

Yield: 34.2 mg, 22.6 µmol, 40 %

^{1}H NMR {sw: 179 ppm; aq: 0.367 s; d1: 0.05 s; ns: 128}

(500.25 MHz, thf-*d*$_8$): δ = -20.54 (bs, 1H, H1, $W_{½}$ = 84 Hz), 8.33 (bs, 2H, H, $W_{½}$ = 39 Hz), 13.69 (bs, 2H, H, $W_{½}$ = 169 Hz), 16.85 (bs, 2H, H, $W_{½}$ = 190 Hz), 45.34 (bs, 6H, C***H***$_3$, $W_{½}$ = 997 Hz) ppm.

^{13}C {1H} NMR

(125.80 MHz, thf-*d*$_8$): Strong paramagnetic center, no signals detectable.

Elemental analysis

(calc. in %): **C**: 57.57 (57.97); **H**: 4.05 (4.03); **N**: 6.59 (6.60).

[M + 2 toluene]

All experimental data can be retrieved from the supplementary information, available under: https://pubs.acs.org/doi/suppl/10.1021/acs.inorgchem.1c03714/suppl_file/ic1c03714_si_001.pdf

5.3.22. Synthesis of [An{S(NSiMe$_3$)(NHSiMe$_3$)}$_2$] (22)

	M [g mol^{-1}]	*n* [mmol]	*m* [mg]	equiv.	*V* [ml]
[{(thf)$_2$Li(NSiMe$_3$)$_2$S}$_2$An] (**L$_6$**)	891.43	1.68	1500	1	-
*t*BuNH$_3$Cl	109.60	3.83	424	2.3	-
n-pentane	-	-	-	-	40

L$_6$ (1 equiv., 1.5 g, 1.68 mmol) and *t*BuNH$_3$Cl (2.3 equiv., 424 mg, 3.83 mmol) were transferred into a Schlenk flask and stirred in *n*-pentane at r.t. for 24h. The precipitated solid was removed via filtration, and the product was extracted in *n*-pentane (3 x 5 ml). Most of the *n*-pentane was removed under reduced pressure and yellow needle-shaped crystals suitable for X-ray diffraction experiments were obtained from a saturated *n*-pentane solution (7.5 ml) at 238 K. High purity was achieved after two cycles of recrystallization.

Empirical formula: $C_{26}H_{46}N_4S_2Si_4$

Molecular weight: 591.14 g mol^{-1}

Yield: 708.5 mg, 1.20 mmol, 71 %

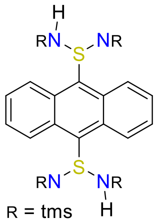

^{1}H NMR

(400.25 MHz, benzene-*d*$_6$): δ = 0.08 (s, 36H, Si(C***H***$_3$)$_3$), 5.64 (d, 2H, N***H***), 7.57 (m, 4H, H7, H6, H3, H2), 9.63 (m, 4H, H8, H5, H4, H1) ppm.

^{13}C {^{1}H} NMR

(125.76 MHz, benzene-*d*$_6$): δ = 0.84 (s, 6C, NSi(***C***H$_3$)$_3$), 2.75 (s, 6C, HNSi(***C***H$_3$)$_3$), 124.57 (m, 4C, C7, C6, C2, C3), 125.84 (m, 4C, C10a, C9a, C8a, C4a), 129.90 (br, 2C, C8, C5, C4, C1), 144.61 (br, 2C, C10, C9) ppm.

Elemental analysis

(calc. in %): **C**: 52.66 (52.83); **H**: 7.88 (7.84); **N**: 8.92 (9.48); **S**: 10.81 (10.85).

MS (LIFDI)

m/*z* (%): 590.3 (100) [M]$^+$

5.3.23. Synthesis of [*t*BuS(NSiMe$_3$)(NHSiMe$_3$)] (23)

	M [g mol^{-1}]	*n* [mmol]	*m* [mg]	equiv.	*V* [ml]
[Li{*t*BuS(NSiMe$_3$)$_2$S}$_2$]$_2$ (**L$_7$**)	541.02	0.56	300	1.0	-
*t*BuNH$_3$Cl	109.60	1.15	128	2.1	-
n-pentane	-	-	-	-	5

L$_7$ (1 equiv., 0.3 g, 0.56 mmol) and *t*BuNH$_3$Cl (2.1 equiv., 0.13 g, 1.15 mmol) were transferred into a Schlenk flask and stirred in *n*-pentane at r.t. for 24h. The precipitated solid was removed via filtration and the product was extracted in *n*-pentane (3 x 1 ml). Most of the *n*-pentane was removed under reduced pressure and colorless block-shaped crystals suitable for X-ray diffraction experiments were obtained from a saturated *n*-pentane solution (1.5 ml) at 238 K. High purity was achieved after two cycles of recrystallization.

Empirical formula: $C_{10}H_{28}N_2SSi_2$

Molecular weight: 264.58g mol^{-1}

Yield: 35.2 mg, 133 µmol, 24 %

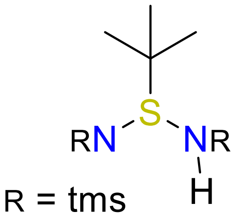

^{1}H NMR

(400.25 MHz, thf-*d*$_8$): $\delta = -0.04$ (s, 18H, $\mathrm{Si(C\boldsymbol{H}_3)_3}$), 0.93 (s, 9H, $\mathrm{C(CH_3)_3}$), 1.29 (s, 1H, $\mathrm{N\boldsymbol{H}}$) ppm.

^{13}C {^{1}H} NMR

(125.76 MHz, thf-*d*$_8$): $\delta = 3.74$ (s, 6C, $\mathrm{NSi(\boldsymbol{C}H_3)_3}$), 23.11 (s, 3C, $\mathrm{C(\boldsymbol{C}H_3)_3}$), 54.26 (s, 1C, $\mathrm{\boldsymbol{C}(CH_3)_3}$) ppm.

Elemental analysis

(calc. in %): **C**: 44.96 (45.40); **H**: 7.88 (10.67); **N**: 10.34 (10.59); **S**: 11.86 (12.12).

MS (ESI)

m/*z* (%): 265.16 (100) [M+H]$^+$

5.3.24. Synthesis of $[An_{0.5}\{S(SiMe_3N)_2(thf)_2Na_2(NSiMe_3)_2S\}An_{0.5}]_n$ (24)

	M [g mol⁻¹]	*n* [mmol]	*m* [mg]	equiv.	*V* [ml]
$[An\{S(NSiMe_3)(NHSiMe_3)\}_2]$ (**22**)	591.14	0.14	83.3	1.0	-
NaH	23.99	0.31	7.4	2.2	-
thf	-	-	-	-	5

22 (1 equiv., 83.3 mg, 0.14 mmol) and NaH (2.2 equiv., 7.4 mg, 0.31 mmol) were transferred into a Schlenk flask and stirred in thf at r.t. for 24h. All solids were removed via filtration and the volatiles were removed under reduced pressure and red block-shaped crystals suitable for X-ray diffraction experiments were obtained from a saturated thf solution (1.5 ml) at 238 K. High purity was achieved after two cycles of recrystallization.

Empirical formula:	$C_{34}H_{60}N_4Na_2O_2S_2Si_4$
Molecular weight:	779.32g mol⁻¹
Yield:	98.19 mg, 126 µmol, 90 %

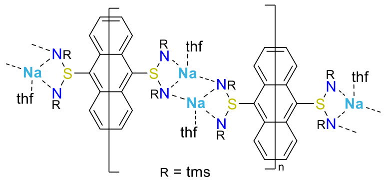

¹H NMR	
(400.25 MHz, thf-*d*₈):	$\delta = -0.33$ (m, 36H, Si(C***H***₃)₃), 1.73 (m, OCH₂C***H***₂), 3.58 (m, OC***H***₂CH₂) 7.21 (m, 4H, H2, H3, H6, H7), 9.78 (m, 4H, H1, H4, H5, H8) ppm.
¹³C {¹H} NMR	
(125.76 MHz, thf-*d*₈):	$\delta = 2.39$ (s, 12C, NSi(***C***H₃)₃), 24.42 (6C, OCH₂***C***H₂), 66.46 (6C, O***C***H₂CH₂), 123.87-122.68 (m, 2C2, C7, C6, C2, C3), 126.95-125.61 (m, 4C, C10a, C9a, C8a, C4a), 129.42 (br, 2C, C8, C5, C4, C1), 153.01 (br, 2C, C10, C9) ppm.
Elemental analysis	
(calc. in %):	**C**: 50.21 (50.95); **H**: 7.93 (7.41); **N**: 7.93 (7.92); **S**: 10.75 (10.33).
[M − thf]	
MS (LIFDI)	
m/*z* (%):	Only ligand fragment detectable: 590.3 (100).

5.3.25. Synthesis of [(thf)$_2$K(NSiMe$_3$)$_2$S}An{S(SiMe$_3$N)$_2$K(thf)$_2$}] (25)

	M [g mol^{-1}]	*n* [mmol]	*m* [mg]	equiv.	*V* [ml]
[An{S(NSiMe$_3$)(NHSiMe$_3$)}$_2$] (**22**)	591.14	0.85	500	1.0	-
KH	40.11	1.86	75	2.2	-
thf	-	-	-	-	10

22 (1 equiv., 500 mg, 0.85 mmol) and KH (2.2 equiv., 75 mg, 1.86 mmol) were transferred into a Schlenk flask and stirred in thf at r.t. for 24h. All solids were removed via filtration and the volatiles were removed under reduced pressure and red block-shaped crystals suitable for X-ray diffraction experiments were obtained from a saturated thf solution (2.5 ml) at 238 K. High purity was achieved after two cycles of recrystallization.

Empirical formula: $C_{42}H_{76}K_2N_4O_4S_2Si_4$

Molecular weight: 955.75 g mol^{-1}

Yield: 576.8 mg, 0.60 mmol, 71 %

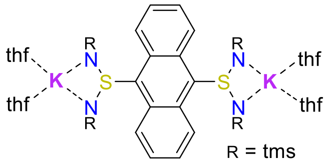

^{1}H NMR

(400.25 MHz, thf-*d*$_8$): $\delta = -0.34$ (m, 36H, Si(C$\boldsymbol{H}_3$)$_3$), 1.81 (m, OCH$_2$C$\boldsymbol{H}_2$), 3.58 (m, OC$\boldsymbol{H}_2$CH$_2$), 7.22 (m, 4H, H2, H3, H6, H7), 9.91 (m, 4H, H1, H4, H5, H8) ppm.

^{13}C {^{1}H} NMR

(100.64 MHz, thf-*d*$_8$): $\delta = 2.08$ (s, 12C, NSi($\boldsymbol{C}$H$_3$)$_3$), 121.97 (m, 2C2, C6, C2, C3,C7), 125.51 (m, 4C, C10a, C4a, C9a, C8a), 128.24 (br, 2C, C1, C4,C5, C8), 143.67 (s, 2C, C9, C10) ppm.

Elemental analysis

(calc. in %): **C**: 50.57 (50.32); **H**: 7.31 (7.45); **N**: 6.80 (6.90); **S**: 7.81 (7.90).

[M – 2 thf]

MS (LIFDI)

m/*z* (%): Only ligand fragment detectable: 590.3 (100).

5.3.26. Synthesis of $[S(t\mathrm{BuN})_3(\mathrm{thf})_3K_3(\mathrm{HN}t\mathrm{Bu})(\mathrm{N}t\mathrm{Bu})_2S\}]$ (26)

	M [g mol⁻¹]	*n* [mmol]	*m* [mg]	equiv.	*V* [ml]
$S(t\mathrm{BuN})_2$	174.34	10.32	1800	1.0	2
K	39.10	24.1	941	2.33	-
thf	-	-	-	-	8

Potassium (2.33 equiv., 0.94 g, 24.1 mmol) was transferred into a Schlenk flask and melted for an increased reaction surface. Upon the potassium mirror, thf (8 ml) was added, and then the $S(t\mathrm{BuN})_2$ (1 equiv., 2 ml, 10.32 mmol) was inserted dropwise, displaying a color change to dark red. Notably, conventional filtration methods do not work to separate the solids from the obtained suspension. Therefore, the reaction mixture was centrifuged (5 min, 8000 rpm), which resulted in a clear red solution. Crystals suitable for X-ray diffraction analysis were gained from a saturated solution of **26** in thf at 238 K. High purity was achieved after two cycles of recrystallization.

Empirical formula: $C_{36}H_{79}N_6K_3O_3S_2$

Molecular weight: 825.48 g mol⁻¹

Yield: 1.08 g, 1.31 mmol, 38 %

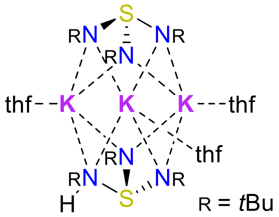

^{1}H NMR
(500 MHz, benzene-*d*$_6$): δ = 1.04 (s, 1H, N***H***), 1.10 (s, 9H, HNC(C***H***$_3$)$_3$), 1.19 (s, 18H, NC(C***H***$_3$)$_3$), 1.41 (m, 12H, OCH$_2$C***H***$_2$), 1.48 (s, 27H, NC(C***H***$_3$)$_3$), 3.56 (m, 12H, OC***H***$_2$CH$_2$) ppm.

^{13}C {^{1}H} NMR
(125.76 MHz, benzene-*d*$_6$): δ = 25.85 (6C, OCH$_2$***C***H$_2$), 31.74 (3C, HNC(***C***H$_3$)$_3$), 34.64 (6C, NC(***C***H$_3$)$_3$), 35.59 (9C, NC(***C***H$_3$)$_3$), 52.08 (1C, N***C***), 53.42 (3C, N***C***), 53.66 (2C, N***C***), 67.87 (6C, O***C***H$_2$CH$_2$) ppm.

^{15}N-HMBC NMR
(40 MHz, benzene-*d*$_6$): δ = −240.22 (***N***C(CH$_3$)$_3$), −235.45 (***N***C(CH$_3$)$_3$), −230.88 (d, H***N***C(CH$_3$)$_3$).

Elemental analysis
(calc. in %): **C**: 52.67 (52.38); **H**: 9.83 (9.65); **N**: 10.73 (10.18); **S**: 7.58 (7.77).

5.3.27. Synthesis of $[\mathrm{S}(t\mathrm{BuN})_3(\mathrm{thf})_3\mathrm{Na}_3(\mathrm{HN}t\mathrm{Bu})(\mathrm{N}t\mathrm{Bu})_2\mathrm{S}\}]$ (27)

	M [g mol^{-1}]	*n* [mmol]	*m* [mg]	equiv.	*V* [ml]
$\mathrm{S}(t\mathrm{BuN})_2$	174.34	25.81	-	1.0	5
$\mathrm{S}(t\mathrm{BuN})_3$	245.15				
Na	23.99	60.14	1380	2.33	-

Method A: Sodium (2.33 equiv., 1.38 g, 60.14 mmol) was transferred into a Schlenk flask and melted for an increased reaction surface. Next, thf (10 ml) was added and then the $\mathrm{S}(t\mathrm{BuN})_2$ (1 equiv., 5 ml, 25.81 mmol) was inserted dropwise, displaying a color change to red. After 4h, filtration via a glass fritted filter (P4) over celite and dual crystallization from thf (6 ml) gave the red product. Crystals suitable for X-ray diffraction analysis were gained from a saturated solution of **27** in thf at 238 K. **Method B**: Sodium (2.33 equiv., 0.27 g, 11.65 mmol) was prepared as described under method A and $\mathrm{S}(t\mathrm{BuN})_3$ in thf (2 ml) was slowly added at r.t. and stirred for 48h. Promptly, a color change to dark blue is observable. After 48h, a red solution is obtained. Filtration via a glass fitted filter (P4) over celite and dual crystallization from thf (3 ml) yielded the red product.

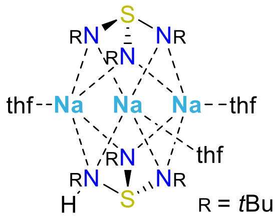

Empirical formula: $\mathrm{C_{36}H_{79}N_6Na_3O_3S_2}$

Molecular weight: 777.16g mol^{-1}

Yield: Method A: 0.21 g, 0.27 mmol, 10 %

Method B: 0.94 g, 1.21 µmol, 48 %

^{1}H NMR

(500.25 MHz, benzene-*d*$_6$): δ = 1.19 (s, 9H, HNC(C$\boldsymbol{H}_3$)$_3$), 1.31 (s, 18H, NC(C$\boldsymbol{H}_3$)$_3$), 1.37 (m, 12H, OCH$_2$C$\boldsymbol{H}_2$), 1.57 (27H, NC(C$\boldsymbol{H}_3$)$_3$), 1.71 (s, 1H, N$\boldsymbol{H}$), 3.56 (m, 12H, OC$\boldsymbol{H}_2$CH$_2$), ppm.

^{13}C {^{1}H} NMR

(125.76 MHz, benzene-*d*$_6$): δ = 25.26 (6C, OCH$_2$$\boldsymbol{C}H_2$), 31.12 (3C, HNC($\boldsymbol{C}H_3$)$_3$), 34.10 (6C, NC($\boldsymbol{C}H_3$)$_3$), 35.22 (9C, NC($\boldsymbol{C}H_3$)$_3$), 52.25 (1C, N$\boldsymbol{C}$), 52.80 (3C, N$\boldsymbol{C}$), 53.33 (2C, N$\boldsymbol{C}$), 67.67 (6C, O$\boldsymbol{C}H_2CH_2$) ppm.

^{15}N-HMBC NMR

(40 MHz, benzene-*d*$_6$): δ = −241.66 ($\boldsymbol{N}$C(CH$_3$)$_3$), −234.78 ($\boldsymbol{N}$C(CH$_3$)$_3$), −231.40 (d, H$\boldsymbol{N}$C(CH$_3$)$_3$).

Elemental analysis

(calc. in %): **C**: 55.25 (55.64); **H**: 9.72 (10.25); **N**: 10.63 (10.81); **S**: 8.64 (8.25).

All experimental data can be retrieved from the supplementary information, available under: https://chemistry-europe.onlinelibrary.wiley.com/action/downloadSupplement?doi=10.1002%2Fchem.202104470&file=chem202104470-sup-0001-misc_information.pdf

5.3.28. Synthesis of $[Na(thf)_6][S(Me_3SiN)_3(thf)_3Na_3(NSiMe_3)_3S]$ (28)

	M [g mol⁻¹]	*n* [mmol]	*m* [mg]	equiv.	*V* [ml]
$S(SiMe_3N)_2$	206.45	8.72	1800	1.0	2
Na	22.99	20.31	467	2.33	-
thf	-	-	-	-	5

Sodium (2.33 equiv., 467 mg, 20.31 mmol) was transferred into a Schlenk flask and melted to increase the reaction surface. Next, thf (5 ml) was added, and then the $S(SiMe_3N)_2$ (1 equiv., 1.8 g, 8.72 mmol) was inserted dropwise, displaying a color change to red, which faded after 10 min. After 12h of stirring at r.t., a yellow gel-like mixture was obtained. Extracting the slurry with thf (3 x 3 ml) and centrifuging (3 min, 8000 rpm) resulted in a clear yellow solution. Crystals suitable for X-ray diffraction experiments were obtained from a concentrated solution of **28** in thf.

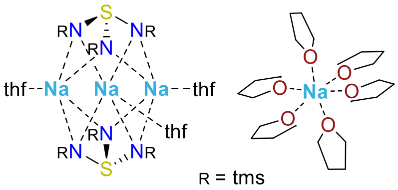

Empirical formula: $C_{54}H_{126}N_6Na_4O_9S_2Si_6$

Molecular weight: 1328.22g mol⁻¹

Yield: 1.04 g, 0.78 mmol, 27 %

¹H NMR

(400.25 MHz, thf-*d*₈): *δ* = −0.04 (s, 18H, $Si(C\boldsymbol{H}_3)_3$), 1.69 (m, 12H, $OC\boldsymbol{H}_2CH_2$), 3.54 (m, 12H, $OCH_2C\boldsymbol{H}_2$), ppm.

¹³C {¹H} NMR

(125.76 MHz, thf-*d*₈): *δ* = 6.76 (s, 18C, $Si(\boldsymbol{C}H_3)_3$), 25.36 (6C, $OCH_2\boldsymbol{C}H_2$), 67.38 (6C, $O\boldsymbol{C}H_2CH_2$) ppm.

Elemental analysis

(calc. in %): **C**: 47.17 (46.66); **H**: 10.01 (9.36); **N**: 6.76 (7.10); **S**: 4.97 (5.42).

[M – 2 thf]

5.3.29. Synthesis of Tb$_n$Clusters with n= 1, 2, and 4 (29-32)

	M [g mol^{-1}]	*n* [mmol]	*m* [mg]	equiv.	*V* [ml]
$[\mathrm{S}(t\mathrm{BuN})_3(\mathrm{thf})_3\mathrm{Na}_3(\mathrm{HN}t\mathrm{Bu})(\mathrm{N}t\mathrm{Bu})_2\mathrm{S}\}]$ (**27**)	777.16	0.13	100	1	-
TbCl_3	265.28	0.13	34	1	-
thf	-	-	-	-	4

27 (1 equiv., 100 mg, 0.13 mmol) and TbCl_3 (1 equiv., 34 mg, 0.13 mmol) were transferred into a Schlenk flask and stirred in thf at r.t. for 24h. All solids were removed via filtration and the terbium species (29-32) were crystallized from a saturated thf solution at 238 K. Despite the tremendous efforts to separate the four terbium species from each other, we were not able to do so. However, we only accomplished to change the ratios of **29**-**31** in the obtained crystalline material, and the separation of these complex series failed.

$[\mathrm{ClTb}\{\mathrm{Na}(\mathrm{thf})\}_2\{(\mathrm{N}t\mathrm{Bu})_3\mathrm{S}\}_2]$ (**29**):

The most successful approach is to employ a ligand/metal ratio of 1:1 and perform the reaction in pure thf. Crystallization was carried out in thf, allowing *n*-pentane to evaporate into the concentrated thf solution.

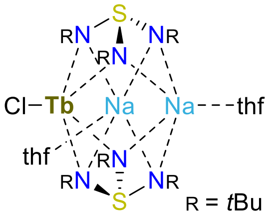

$[\{\mathrm{Na}(\mathrm{thf})\}_2\{\mathrm{S}(t\mathrm{BuN})_3\}_2\mathrm{TbSTb}\{(\mathrm{N}t\mathrm{Bu})_3\mathrm{S}\}_2\{\mathrm{Na}(\mathrm{thf})\}_2]$ (**30**):

Most successful approach is to employ a ligand/metal ratio of 1:2 and perform the reaction and crystallization in pure toluene.

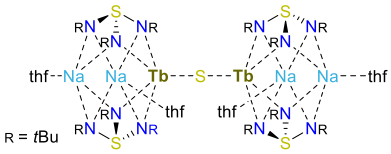

$[(t\mathrm{BuNH})\mathrm{Tb}\{(\mathrm{N}t\mathrm{Bu})_3\mathrm{S}\}]_2$ (**31**):

The most successful approach is to employ a ligand/metal ratio of 1:2 and perform the reaction and crystallization in pure thf.

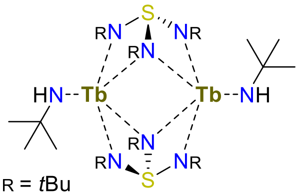

$[\{\mathrm{S}(t\mathrm{BuN})_3\}\mathrm{TbSTb}\{(\mathrm{N}t\mathrm{Bu})_3\mathrm{S}\}]_2$ (**32**):

The most successful approach is to employ a ligand/metal ratio of 1:4 and perform the reaction and crystallization in pure thf.

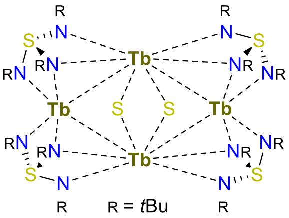

5.3.30. Synthesis of $[\{S(t\mathrm{BuN})_2(t\mathrm{BuNH})\}_2K_3(\mathrm{tmeda})K_3\{(\mathrm{HN}t\mathrm{Bu})(\mathrm{N}t\mathrm{Bu})_2S\}_2]$ (33)

	M [g mol⁻¹]	*n* [mmol]	*m* [mg]	equiv.	*V* [ml]
$S(t\mathrm{BuN})_2$	174.34	10.32	1800	1	2
K	39.10	24.06	940	2.33	-
n-pentane					5
tmeda					5

Potassium (2.33 equiv., 0.94 g, 24.1 mmol) was transferred into a Schlenk flask and melted for an increased reaction surface. Upon the potassium mirror, an *n*-pentane/tmeda mixture (1:1, 10 ml) was added and then the $S(t\mathrm{BuN})_2$ (1 equiv., 2 ml, 10.32 mmol) was inserted dropwise. Instantaneously, a color change to red is observable and after 24h a dark red solution is obtained. Filtration via a glass fritted filter (P4) over celite and crystallizing twice from *n*-pentane (3 ml) yielded the red product. Crystals suitable for X-ray diffraction analysis were gained from a saturated solution of **33** in *n*-pentane at 238 K. High purity was achieved after two cycles of recrystallization.

Empirical formula:	$C_{54}H_{126}K_6N_{14}S_4$
Molecular weight:	1334.53 g mol⁻¹
Yield:	0.81 g, 0.61 mmol, 35 %

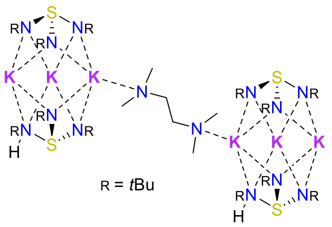

^{1}H NMR

(500 MHz, benzene-*d*₆): δ =1.08 (s, 9H, $HNC(C\boldsymbol{H}_3)_3$), 1.16 (s, 18H, $NC(C\boldsymbol{H}_3)_3$), 1.45 (s, 27H, $NC(C\boldsymbol{H}_3)_3$), 2.13 (s, 12H, $N(C\boldsymbol{H}_3)_2$), 2.38 (m, 4H, $C\boldsymbol{H}_2$) ppm.

^{13}C {^{1}H} NMR

(125 MHz, benzene-*d*₆): δ = 30.90 (3C, $HNC(\boldsymbol{C}H_3)_3$), 33.79 (6C, $NC(\boldsymbol{C}H_3)_3$), 34.74 (9C, $NC(\boldsymbol{C}H_3)_3$), 45.26 (4C, $N(CH_3)_2$, tmeda), 51.20 (1C, $HN\boldsymbol{C}(CH_3)_3$), 52.33 (3C, $N\boldsymbol{C}(CH_3)_3$), 52.77 (3C, $N\boldsymbol{C}(CH_3)_3$) 57.56 (2C, $\boldsymbol{C}H_2$, tmeda) ppm.

^{15}N-HMBC NMR

(40 MHz, benzene-*d*₆): δ = −240.31 ($\boldsymbol{N}C(CH_3)_3$), −235.37 ($\boldsymbol{N}C(CH_3)_3$), −230.84 ($H\boldsymbol{N}C(CH_3)_3$), −227.65 (tmeda) ppm.

Elemental analysis

(calc. in %): **C**: 49.45 (48.60); **H**: 10.42 (9.52); **N**: 14.13 (14.69); **S**: 9.21 (9.61).

All experimental data can be retrieved from the supplementary information, available under: https://chemistry-europe.onlinelibrary.wiley.com/action/downloadSupplement?doi=10.1002%2Fchem.202104470&file=chem202104470-sup-0001-misc_information.pdf

5.3.31. Synthesis of $[\{(\mathrm{tmeda})_3\mathrm{S}\{\mathrm{Na}_3(\mathrm{N}t\mathrm{Bu})_3\mathrm{S}\}_2]$ (34)

	M [g mol⁻¹]	*n* [mmol]	*m* [mg]	equiv.	*V* [ml]
$\mathrm{S}(t\mathrm{BuN})_2$	174.34	5.16	900	1	1
Na	22.99	12.03	280	2.33	-
n-hexane					2.5
tmeda					2.5

Sodium (2.33 equiv., 0.28 g, 12.03 mmol) was transferred into a Schlenk flask and melted to increase the reaction surface. Upon the sodium mirror, an *n*-hexane/tmeda mixture (1:1, 5 ml) was added and then the $\mathrm{S}(t\mathrm{BuN})_2$ (1 equiv., 1 ml, 5.16 mmol) was inserted dropwise. Instantaneously, a color change to light red was observable, which faded after 12 h. Impurities (red) of the crude product were extracted in n-hexane (6 x2 ml) in a centrifuge (2min, 8000 rpm). Crystals suitable for X-ray diffraction analysis were gained from a saturated solution of **35** in *n*-hexane/tmeda at 238 K. The purified product appears as a colorless solid.

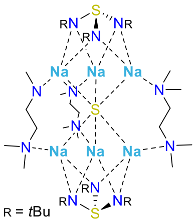

Empirical formula:	$C_{42}H_{102}N_{12}Na_6S_3$
Molecular weight:	1009.48 g mol⁻¹
Yield:	1.05 g, 1.04 mmol, 67 %

¹H NMR

(500 MHz, toluene-d_8): δ = 1.45 (s, 54H, $\mathrm{NC(C}\boldsymbol{H}_3)_6$), 2.04 (s, 36H, $\mathrm{N(C}\boldsymbol{H}_3)_2$, tmeda), 2.23 (m, 12H, $\mathrm{C}\boldsymbol{H}_2$, tmeda) ppm. (313 K)

¹³C {¹H} NMR

(125 MHz, toluene-d_8): δ = 39.95 (18C, $\mathrm{NC(}\boldsymbol{C}\mathrm{H}_3)_6$), 46.38 (12C, $\mathrm{N(CH_3)_2}$, tmeda), 53.31 (6C, $\mathrm{N}\boldsymbol{C}\mathrm{(CH_3)_3)_6}$), 58.70 (6C, $\boldsymbol{C}\mathrm{H}_2$, tmeda) ppm.

¹⁵N-HMBC NMR

(40 MHz, toluene-d_8): δ = −236.35 ($\boldsymbol{N}\mathrm{C(CH_3)_3}$), −58.52 ($\boldsymbol{N}\mathrm{C(CH_3)_2}$) ppm.

Elemental analysis

(calc. in %): **C**: 49.75 (49.97); **H**: .9.72 (10.01); **N**: 16.63 (16.65); **S**: 10.22 (9.84).

All experimental data can be retrieved from the supplementary information, available under: https://chemistry-europe.onlinelibrary.wiley.com/action/downloadSupplement?doi=10.1002%2Fchem.202104470&file=chem202104470-sup-0001-misc_information.pdf

5.3.32. Synthesis of [{S(*t*BuN)$_3$(thf)$_3$Na$_3$SNa$_3$(thf)$_3$(N*t*Bu)$_3$S] (35)

	M [g mol^{-1}]	*n* [mmol]	*m* [mg]	equiv.	*V* [ml]
S(*t*BuN)$_2$	174.34	25.81	4500	1	5
Na	22.99	60.14	1380	2.33	-
thf					10

Sodium (2.33 equiv., 1.38 g, 60.14 mmol) was transferred into a Schlenk flask and melted to increase the reaction surface. Upon the sodium mirror, thf (10 ml) was added and then the S(*t*BuN)$_2$ (1 equiv., 5 ml, 25.81 mmol) was inserted dropwise. Instantaneously, a color change to red is observable and after 48h an orange solution is obtained. Filtration via a glass fritted filter (P4) over celite and crystallizing twice thf (6 ml) yielded the colorless product. Crystals suitable for X-ray diffraction analysis were gained from a saturated solution of **34** in thf at 238 K. High purity was achieved after two cycles of recrystallization.

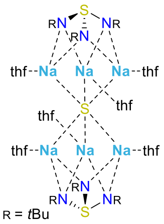

Empirical formula: $C_{48}H_{102}N_6Na_6O_6S_3$

Molecular weight: 1093.50 g mol^{-1}

Yield: 6.81 g, 6.23 mmol, 72 %

^{1}H NMR

(400.25 MHz, toluene-*d*$_8$): δ = 1.16 (s, 54H, NC(C$\boldsymbol{H}_3$)$_6$), 1.43 (m, 24H, OCH$_2$C$\boldsymbol{H}_2$), 3.53 (m, 24H, OC$\boldsymbol{H}_2$CH$_2$), ppm.

^{13}C {^{1}H} NMR

(125.76 MHz, toluene-*d*$_8$): δ = 25.26 (12C, OCH$_2$$\boldsymbol{C}H_2$), 35.55 (18C, NC($\boldsymbol{C}H_3$)$_3$), 53.08 (6C, N$\boldsymbol{C}$(CH$_3$)$_3$), 68.04 (12C, O$\boldsymbol{C}H_2CH_2$) ppm.

^{15}N-HMBC NMR

(40 MHz, toluene-*d*$_8$): $\delta = -233.74$ ($\boldsymbol{N}$C(CH$_3$)$_3$ ppm.

Elemental analysis

(calc. in %): **C**: 53.25 (52.72); **H**: 9.82 (9.40); **N**: 7.93 (7.69); **S**: 8.34 (8.80).

All experimental data can be retrieved from the supplementary information, available under: https://chemistry-europe.onlinelibrary.wiley.com/action/downloadSupplement?doi=10.1002%2Fchem.202104470&file=chem202104470-sup-0001-misc_information.pdf

5.3.33. Synthesis of [(*t*BuNH)}Dy{K(0.5tmeda)}$_2${N*t*Bu)$_3$S}$_2$]$_n$ (36)

	M [g mol⁻¹]	*n* [mmol]	*m* [mg]	equiv.	*V* [ml]
33	1324.53	0.15	100	1	-
$DyCl_3$	268.86	0.16	44	1.1	-
n-pentane					6

33 (1 equiv., 100 mg, 0.15 mmol) and $DyCl_3$ were transferred into a Schlenk flask and suspended in *n*-pentane. Promptly, a color change to dark blue was observable. After 24h a yellow suspension was received and filtered via a glass fritted filter (P4) over celite, and crystallizing twice from *n*-pentane (3 ml) yielded the white product.

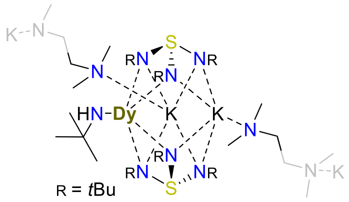

Empirical formula: $C_{34}H_{80}N_9DyK_2S_2$

Molecular weight: 920.45 g mol⁻¹

Yield: 33 mg, 35.9 µmol, 24 %

^{1}H NMR {sw: 223 ppm; aq: 0.367 s; d1: 0.05 s; ns: 128}

(400.25 MHz, thf-d_8): δ = −7.06 (s, 18H, $\mathrm{NC(C}\boldsymbol{H}_3)_3$, $W_{1/2}$ = 56 Hz), 2.35 (s, 12H, $\mathrm{N(C}\boldsymbol{H}_3)_2$, $W_{1/2}$ = 15 Hz), 2.51 (m, 4H, $\mathrm{C}\boldsymbol{H}_2$, $W_{1/2}$ = 15 Hz) 27.24(bs, 18H, $\mathrm{NCC}\boldsymbol{H}_3$, $W_{1/2}$ = 523 Hz) 63.97 (bs, 36H, $\mathrm{NC(C}\boldsymbol{H}_3)_3$, $W_{1/2}$ = 401 Hz) ppm.

^{13}C {^{1}H} NMR

(125.76 MHz, thf-d_8): Strong paramagnetic center, no signals detectable.

Elemental analysis

(calc. in %): **C**: 44.65 (44.39); **H**: 8.82 (8.77); **N**: 14.33 (13.70); **S**: 7.41 (6.97).

All experimental data can be retrieved from the supplementary information, available under: https://chemistry-europe.onlinelibrary.wiley.com/action/downloadSupplement?doi=10.1002%2Fchem.202104470&file=chem202104470-sup-0001-misc_information.pdf

5.3.34. Synthesis of [$Na_2\{S(t\mathrm{BuN})_3\}_2DySDy\{(Nt\mathrm{Bu})_3S\}_2Na_2$] (37)

	M [g mol^{-1}]	*n* [mmol]	*m* [mg]	equiv.	*V* [ml]
[{tmeda)$_3$S{$Na_3(Nt\mathrm{Bu})_3S$}$_2$] (**35**)	1009.48	0.2	200	1	-
$DyCl_3$	268.86	0.2	53.3	1	-
toluene					5

Both **35** (1 equiv., 200 mg, 0.2 mmol) and $DyCl_3$ (1 equiv., 53.3 mg, 0.2 mmol) were combined in a Schlenk flask and stirred 24 h in toluene. Instantaneously, a color change to light blue is observable and after 24 h, a yellow suspension is obtained. The solvent is removed under reduced pressure to a total volume of 2 ml and then filtered via a GF/B WHATMAN™ filter. Crystals suitable for X-ray diffraction analysis were gained from a saturated solution of **37** in toluene, allowing *n*-hexane to evaporate at 238 K.

Empirical formula: $C_{48}H_{108}Dy_2N_{12}Na_4S_5$

Molecular weight: 1430.74 g mol^{-1}

Yield: 43.9 mg, 30.71 µmol, 31 %

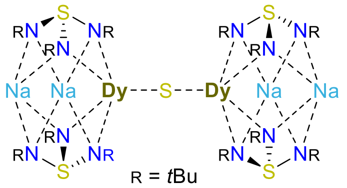

^{1}H NMR {sw: 250 ppm; aq: 1.311 s; d1: 0.1 s; ns: 128}

(400.25 MHz, toluene-d_8): δ = −61.14 (bs, 36H, NC(C***H***)$_3$)$_8$, $W_{1/2}$ = 2394 Hz), 69.89 (bs, 18H, NC(C***H***)$_3$)$_4$, $W_{1/2}$ = 665 Hz) ppm.

^{13}C {^{1}H} NMR

(125.76 MHz, toluene-d_8): Strong paramagnetic center, no signals detectable.

Elemental analysis

(calc. in %): **C**: 40.81 (40.30); **H**: 7.33 (7.61); **N**: 11.93 (11.75); **S**: 11.65 (11.20).

5.3.35. Synthesis of [ClDy{Na(thf)}$_2${(N*t*Bu)$_3$S}$_2$] (38)

	M [g mol^{-1}]	*n* [µmol]	*m* [mg]	equiv.	*V* [ml]
[{S(*t*BuN)$_3$(thf)$_3$Na$_3$SNa$_3$(thf)$_3$(N*t*Bu)$_3$S] (**34**)	1093.50	91.5	100	1	-
DyCl$_3$	268.86	91.5	25	1	-
thf					4

Both **34** (1 equiv., 100 mg, 91.5 µmol) and DyCl$_3$ (1 equiv., 25 mg, 91.5 µmol) were combined in a Schlenk flask and stirred 24 h in toluene. Instantaneously, a color change to dark blue is observable and after 24 h a yellow suspension is obtained. Centrifugation in a thf/toluene/pentane mixture (2:1:1) in 4 ml total volume and crystallization from a thf/toluene mixture (1:1) in 1 ml yielded the white product. Crystals suitable for X-ray diffraction experiments were obtained from slow pentane (3 ml) evaporation into a saturated thf solution at 238 K.

Empirical formula: $C_{32}H_{70}ClDyN_6Na_2S_2$

Molecular weight: 879.00 g mol^{-1}

Yield: 37 mg, 42 µmol, 46 %

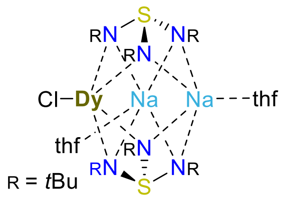

^{1}H NMR (400.25 MHz, thf-*d*$_8$): {sw: 550 ppm; aq: 0.594 s; d1: 0.1 s; ns: 128}
δ = −59.27 (bs, 18H, NC(C***H***$_3$)$_3$, *W*$_{½}$ = 3638 Hz), 1.94 (m, 8H, OCH$_2$C***H***$_2$), 3.64 (m, 8H, OC***H***$_2$CH$_2$), 160.33 (bs, 36H, NC(C***H***$_3$)$_3$, *W*$_{½}$ = 346 Hz) ppm.

^{13}C {^{1}H} NMR (125.76 MHz, thf-*d*$_8$): {sw: 1987 ppm; aq: 0.262 s; d1: 0.2 s; ns: 102400}
δ = −41.50 (12C, NC(***C***H$_3$)$_3$) −17.04 (6C, C(***C***H$_3$)$_3$), 24.72 (8C, OCH$_2$***C***H$_2$), 67.54 (8C, O***C***H$_2$CH$_2$), 151.18 (2C, ***C***(CH$_3$)$_3$), 300.11 (4C, ***C***(CH$_3$)$_3$) ppm.

Elemental analysis (calc. in %): **C**: 43.45 (43.73); **H**: 8.43 (8.03); **N**: 9.79 (9.56); **S**: 7.67 (7.29).

All experimental data can be retrieved from the supplementary information, available under: https://chemistry-europe.onlinelibrary.wiley.com/action/downloadSupplement?doi=10.1002%2Fchem.202104470&file=chem202104470-sup-0001-misc_information.pdf

5.3.36. Synthesis of $[\mathrm{ClEr}\{\mathrm{Na(thf)}\}_2\{(\mathrm{N}t\mathrm{Bu})_3\mathrm{S}\}_2]$ (39)

	M [g mol^{-1}]	*n* [µmol]	*m* [mg]	equiv.	*V* [ml]
$[\{\mathrm{S}(t\mathrm{BuN})_3(\mathrm{thf})_3\mathrm{Na}_3\mathrm{SNa}_3(\mathrm{thf})_3(\mathrm{N}t\mathrm{Bu})_3\mathrm{S}]$ (**34**)	1093.50	91.5	100	1	-
$\mathrm{ErCl_3}$	273.62	91.5	25	1	-
thf					4

Both **34** (1 equiv., 100 mg, 91.5 µmol) and $\mathrm{ErCl_3}$ (1 equiv., 25 mg, 91.5 µmol) were combined in a Schlenk flask and stirred 24 h in toluene. Instantaneously, a color change to dark blue is observable and after 24 h a yellow suspension is obtained. Centrifugation in a thf/toluene/pentane mixture (2:1:1) in 4 ml total volume and crystallization from a thf/toluene mixture (1:1) in 1 ml yielded the white product. Crystals suitable for X-ray diffraction experiments were obtained from slow pentane (3 ml) evaporation into a saturated thf (1 ml) solution at 238 K.

Empirical formula: $\mathrm{C_{32}H_{70}ClErN_6Na_2S_2}$

Molecular weight: 883.38 g mol^{-1}

Yield: 39 mg, 44 µmol, 48 %

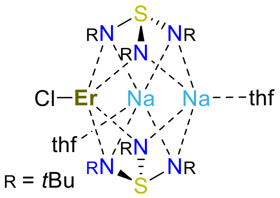

^{1}H NMR {sw: 64 ppm; aq: 4.089 s; d1: 0.1 s; ns: 32}

(500 MHz, thf-d_8): $\delta = -38.06$ (bs, 18H, $\mathrm{NC(C}\boldsymbol{H}_3)_3$, $W_{1/2} = 347$ Hz), 1.54 (m, 8H, $\mathrm{OCH_2C}\boldsymbol{H}_2$), 3.55 (m, 8H, $\mathrm{OC}\boldsymbol{H}_2\mathrm{CH_2}$), 15.60 (s, 36H, $\mathrm{NC(C}\boldsymbol{H})_3)_3$, $W_{1/2} = 61$ Hz) ppm.

^{13}C {^{1}H} NMR {sw: 526 ppm; aq: 0.996 s; d1: 0.2 s; ns: 40960}

(125 MHz, thf-d_8): $\delta = -34.94$ (12C, $\mathrm{NC(}\boldsymbol{C}\mathrm{H_3)_3}$) 26.21 (8C, $\mathrm{OCH_2}\boldsymbol{C}\mathrm{H_2}$), 49.63 (6C, $\mathrm{C(}\boldsymbol{C}\mathrm{H_3)_3}$), 49.63 (2C, $\mathrm{N}\boldsymbol{C}\mathrm{(CH_3)_3}$), 68.24 (8C, $\mathrm{O}\boldsymbol{C}\mathrm{H_2CH_2}$), 99.91 (4C, $\boldsymbol{C}\mathrm{(CH_3)_3}$) ppm.

Elemental analysis

(calc. in %): **C**: 43.65 (43.49); **H**: 8.31 (7.98); **N**: 9.24 (9.51); **S**: 6.71 (7.26).

All experimental data can be retrieved from the supplementary information, available under: https://chemistry-europe.onlinelibrary.wiley.com/action/downloadSupplement?doi=10.1002%2Fchem.202104470&file=chem202104470-sup-0001-misc_information.pdf

6. Crystallographic Section

6.1. Crystallization – practice and procedure

All ligands and precursors were crystallized in a standard one-solvent approach, applying a temperature gradient. For the subsequent complexes, more advanced procedures were employed and can be categorized by the following methods:

The slow evaporation technique[194]

The compound is dissolved in an appropriate solvent and filtrated into a small screw-cap vial. Next, this small glass container is equipped with a cannula and placed in a big screw-cap vial (**Figure 6.1.**). The big screw-cap vial contains a solvent that can evaporate into the sample's mother liquor and decrease the sample's solubility in its mother liquor. There are two major benefits of using a cannula rather than a standard stir bar or relying on the rough surface of your glassware to initiate crystal growth. First, the size of single crystals for SC-XRD experiments is crucial, and the sizing of the crystals grown on the cannula is ideal for these experiments. Further, larger crystals usually sprout at the bottom and feature various domains, which either hamper SC-XRD data refinements or do not allow SC-XRD studies in the first place. Second, extracting the single crystals from the mother liquor is challenging. The attached crystals can directly be transferred into the perfluorinated oil by removing the cannula. The most significant benefit is avoiding any perfluorinated oil contamination to the remaining crystals in the mother liquor. Therefore, the precious sample will be available for all other analysis procedures.

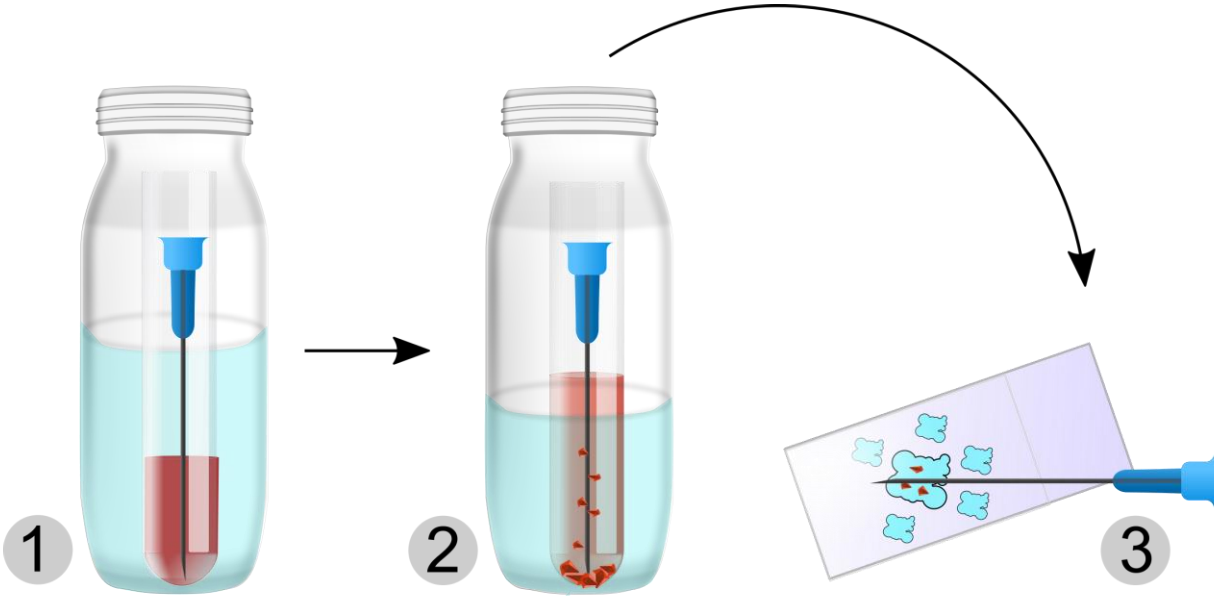

Figure 6.1. Procedures of the slow evaporation technique to grow and extract single crystals for SC-XRD experiments.

The layering technique[194]

For this method, the sample is concentrated in the desired solvent and then carefully layered with a solvent, illustrating a low solubility for the corresponding sample. The top layer will then diffuse into the phase sample and slowly decrease the solubility of the dissolved sample. Crystal growth is initiated and produces suitable crystals for SC-XRD experiments.

6.2. Crystal selection and application

All crystals were extracted from the mother liquor into perfluorinated oil on a microscope slide via an oil-coated spatula under an argon condition. Most crystals were prepared inside the glove box. Therefore all used equipment (spatula, perfluorinated oil, microscope slide, and transport container) were precooled to 243 K. This approach provided a higher probability of sensitive crystals not melting or decomposing in the diffractometer room. Next, the microscope slide was safely removed from the container and placed under a cooling nitrogen gas flow facilitated by the X-Temp2 device.[195] Appling polarized light under a microscope elucidated the best crystals for X-ray diffraction experiments. The selected crystal was then transferred to the tip of a *MiTeGen©MicroMount*, which was positioned on the goniometer head of the diffractometer and shock cooled to 100 K.[196]

6.3. Data collection and processing

The data sets were recorded on a BRUKER SMART APEX diffractometer equipped with an INCOATEC Mo-IμS Microsource (λ= 0.71073 Å), a BRUKER Mo-TXS rotating anode (λ= 0.71073 Å) or a BRUKER SMART APEX with an INOATEC Ag-IμS Microsource (λ= 0.56086 Å).[197] The diffractometers had a built-in OXFORD CYOSYSTEM crystal cooling apparatus. For all measurements, either an INCOATEC QUAZAR or HELIOS mirror optics mounted on a D8-goniometer with an APEX II CCD detector were used.

The APEX2 program interface was used on all diffractometers, while a matrix scan was performed to determine crystal quality and cell parameters prior to the measurement cycle.[198] For each measurement, a ω-scan mode with 0.5 ° steps was chosen. Next, all collected data was integrated with SAINT, and a semi-empirical absorption correction was achieved with the SADABS program.[199] For some data sets, a 3λ correction was required.[200] Followed by employing XPREP for data statistics, preliminary space group determination, and file setup for structure solution and refinement cycles.[201]

6.4. Structure solution and refinement

All received structures were solved by direct methods with SHELXT[202] and refined on F^2 using the full-matrix least-squares modes of SHELXL in the graphical user interface SHELXLE.[124,203] If not stated differently, a riding model was used to refine all C-bonded hydrogen atoms isotropically with geometrically optimized positions. The U_{iso} were constrained to 1.2 U_{eq} of the pivot atom or 1.5 U_{eq} of the methyl carbon atom. Quality of the refinement cycle was evaluated by comparing the calculated (F_{c}) and observed (F_{o}) structure factors. Therefore, generally employed criteria R_1 and $R_{2,w}$ estimate the quality of the structure model, calculated according to equations (**6-1**) and (**6-2**).

$$R_1 = \frac{\Sigma\left||F_{\text{o}}| - |F_{\text{c}}|\right|}{\Sigma|F_{\text{o}}|} \tag{6-1}$$

$$R_{2,w} = \sqrt{\frac{\Sigma w(F_{\text{o}}^2 - F_{\text{c}}^2)^2}{\Sigma F_{\text{o}}^4}} \tag{6-2}$$

An additional quality criterium is the goodness of fit on F^2 (GooF), which displays the deviation between observed and calculated structure factors and is illustrated in equation (**6-3**) with m = number of reflections and n = number of parameters.

$$GoF = \sqrt{\frac{\Sigma_{hkl} w(F_{\text{o}}^2 - F_{\text{c}}^2)^2}{m - n}} \tag{6-3}$$

The residual densities from Fourier analysis should be located in the bonding regions and be at a minimum. Especially for lanthanides, as being heavy scatterers, higher residuals next to the metal ion are appropriate since they stem from absorption effects. The atomic displacement parameters' size, orientation, and ellipticity (ADPs) is another standard for judging model quality. A final model should display ADPs equal in size with a slight ellipticity and oriented perpendicular to the bond. All graphics were either created with the program XP or Mercury, with a depiction of 50 % for the anisotropic displacement parameters, and all hydrogen atoms bonded to carbon atoms were removed for clarity.[204]

6.5. Crystallographic data during this thesis

6.5.1. Crystal structure of $[(thf)Mn\{(NCOC_6H_4)_2CH\}_2]$ (1)

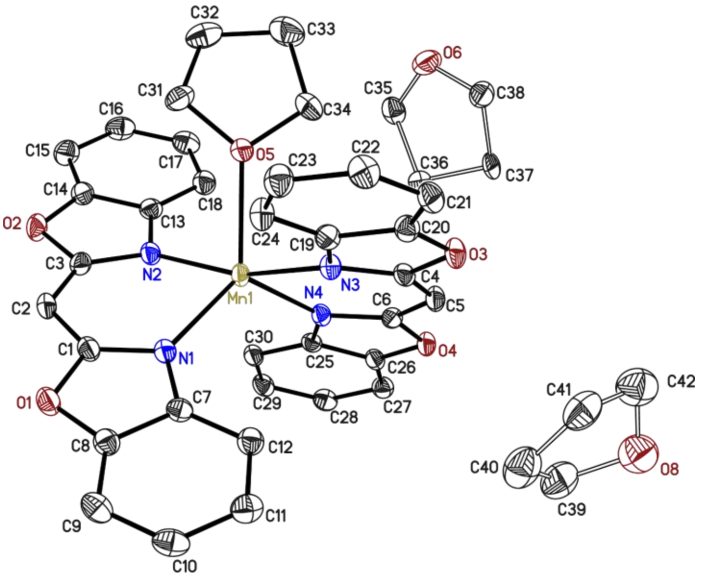

Figure 6.2. The asymmetric unit of **1** with thermal ellipsoids at 50% probability level. The hydrogen atoms are omitted for clarity. The non-coordinating lattice thf units were disordered about symmetry elements and were refined with distance restraints and restraints for the anisotropic displacement parameters. Reproduced from Ref.[1] with permission from the Royal Society of Chemistry.

Table 6.1. Crystallographic data for **1**.

Compound	1_DL_MnBox		*Z*	8
CCDC no.	2095985		ρ_{calc} [Mg m^{-3}]	1.427
Empirical formula	$C_{38}H_{34}MnN_4O_6$		μ [mm^{-1}]	0.462
Formula weight [g mol^{-1}]	697.63		*F*(000)	2904
Temperature [K]	100(2)		Crystal size [mm]	0.332 x 0.233 x 0.218
Wavelength [Å]	0.71073		θ range [°]	2.035 to 26.497
Crystal system	Monoclinic		Reflections collected	56345
Space group	*C*2/*c*		Unique reflections	6684
Unit cell parameters	*a* [Å]	36.870(4)	R_{int}	0.0393
	b [Å]	8.799(2)	Restraints / parameters	146 / 487
	c [Å]	22.995(3)	Goodness-of-fit on F^2	1.052
	α [°]	90	R_1 [I>2σ(I)]	0.0308
	β [°]	119.49(3)	$R_{2,w}$ (all data)	0.0822
	γ [°]	90	$\Delta\varrho_{\text{max}}/\Delta\varrho_{\text{min}}$ [e Å^{-3}]	0.301 / −0.328
Volume [Å^3]	6494(2)		Color and shape	Light green blocks

6.5.2. Crystal structure of [(thf)Fe{(NCOC$_6$H$_4$)$_2$CH}$_2$] (2)

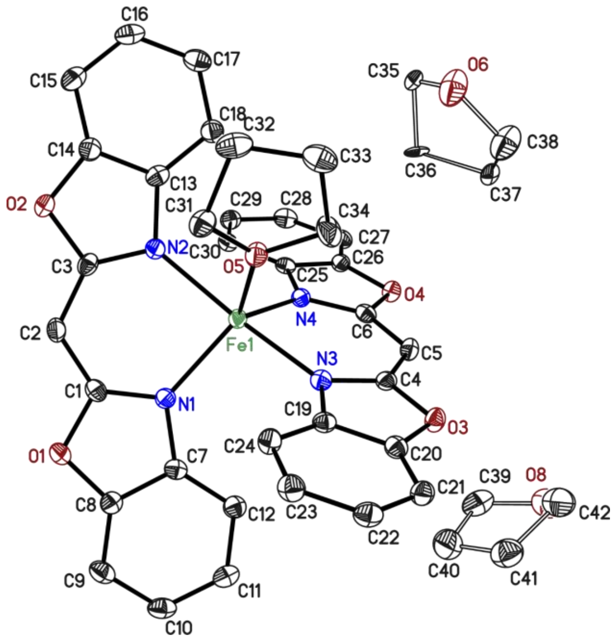

Figure 6.3. The asymmetric unit of **2** with thermal ellipsoids at 50% probability level. The hydrogen atoms are omitted for clarity. The non-coordinating lattice thf units were disordered about symmetry elements and were refined with distance restraints and restraints for the anisotropic displacement parameters. Reproduced from Ref.[1] with permission from the Royal Society of Chemistry.

Table 6.2. Crystallographic data for **2**.

Compound	2_DL_FeBox		Z	8
CCDC no.	2095986		ρ_{calc} [Mg m^{-3}]	1.440
Empirical formula	$C_{38}H_{34}FeN_4O_6$		μ [mm^{-1}]	0.524
Formula weight [g mol^{-1}]	698.54		F(000)	2912
Temperature [K]	100(2)		Crystal size [mm]	0.450 x 0.347 x 0.061
Wavelength [Å]	0.71073		θ range [°]	1.280 to 26.043
Crystal system	Monoclinic		Reflections collected	88097
Space group	$C2/c$		Unique reflections	6361
Unit cell parameters	a [Å]	36.725(4)	R_{int}	0.0610
	b [Å]	8.803(2)	Restraints / parameters	146 / 487
	c [Å]	23.004(3)	Goodness-of-fit on F^2	1.049
	α [°]	90	R_1 [$I>2\sigma(I)$]	0.0311
	β [°]	119.97(3)	$R_{2,w}$ (all data)	0.0703
	γ [°]	90	$\Delta\varrho_{\max}/\Delta\varrho_{\min}$ [e Å^{-3}]	0.298 / −0.347
Volume [Å^3]	6443(2)		Color and shape	Yellow needles

6.5.3. Crystal structure of $[Co\{(NCOC_6H_4)_2CH\}_2]$ (3)

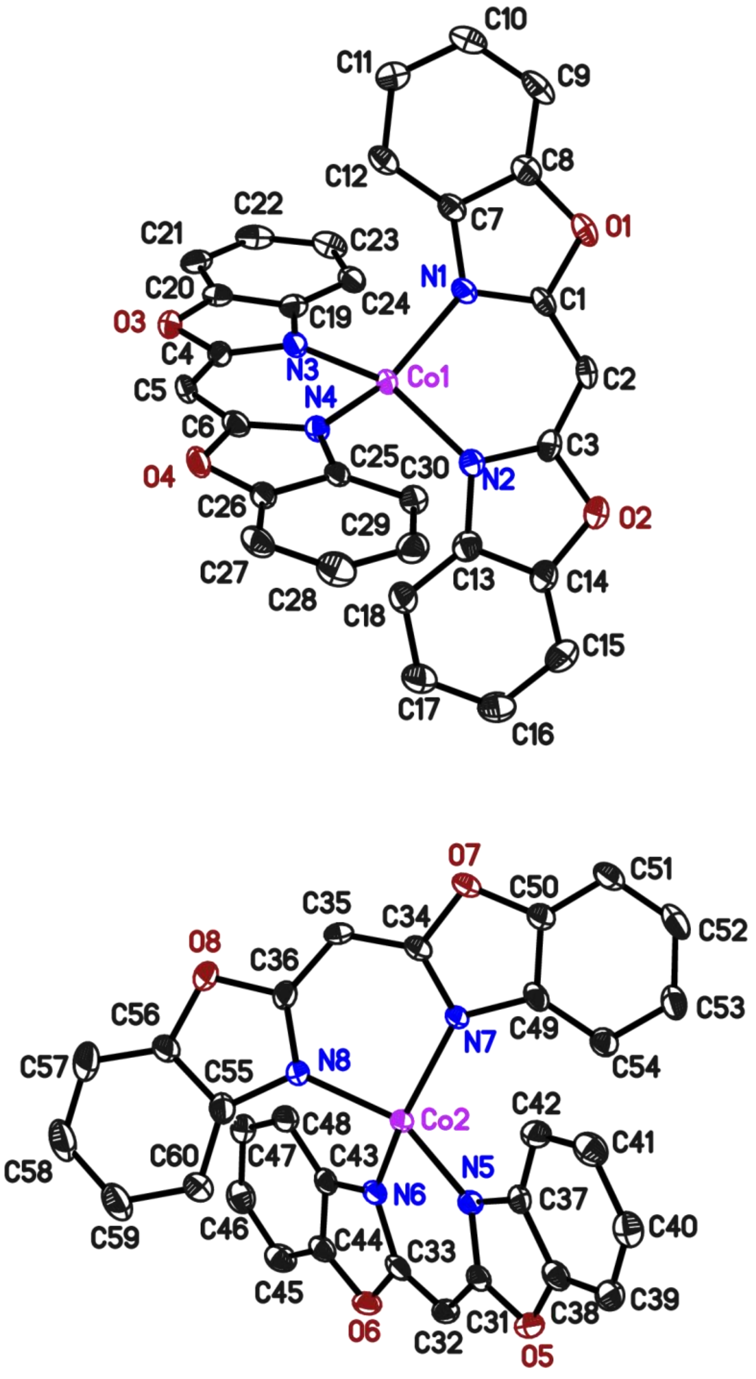

Figure 6.4. The asymmetric unit of **3** with thermal ellipsoids at 50% probability level. The hydrogen atoms are omitted for clarity. The asymmetric unit contains two complex molecules and no solvent molecules. The measured crystal was non-merohedrally twinned with the twin law 1 0 0 0 −1 0 −0.68 0 −1. The fractional contribution refines to 0.0515(6). Reproduced from Ref.[1] with permission from the Royal Society of Chemistry.

Table 6.3. Crystallographic data for **3**.

Compound	3_DL_CoBox		Z	8
CCDC no.	2095987		ρ_{calc} [Mg m^{-3}]	1.526
Empirical formula	$C_{30}H_{18}CoN_4O_4$		μ [mm^{-1}]	0.754
Formula weight [g mol^{-1}]	557.41		F(000)	2280
Temperature [K]	100(2)		Crystal size [mm]	0.245 x 0.143 x 0.118
Wavelength [Å]	0.71073		θ range [°]	1.104 to 27.526
Crystal system	Monoclinic		Reflections collected	158194
Space group	$P2_1/n$		Unique reflections	11334
Unit cell parameters	a [Å]	20.023(3)	R_{int}	0.0999
	b [Å]	7.758(2)	Restraints / parameters	0 / 704
	c [Å]	31.980(4)	Goodness-of-fit on F^2	1.104
	α [°]	90	R_1 [I>2σ(I)]	0.0615
	β [°]	102.30(2)	$R_{2,w}$ (all data)	0.01584
	γ [°]	90	$\Delta\varrho_{\mathrm{max}}/\Delta\varrho_{\mathrm{min}}$ [e Å^{-3}]	1.218 / −1.158
Volume [Å^3]	4854(2)		Color and shape	Red needles

6.5.4. Crystal structure of [Ni{$(NCOC_6H_4)_2CH$}$_2$] (4)

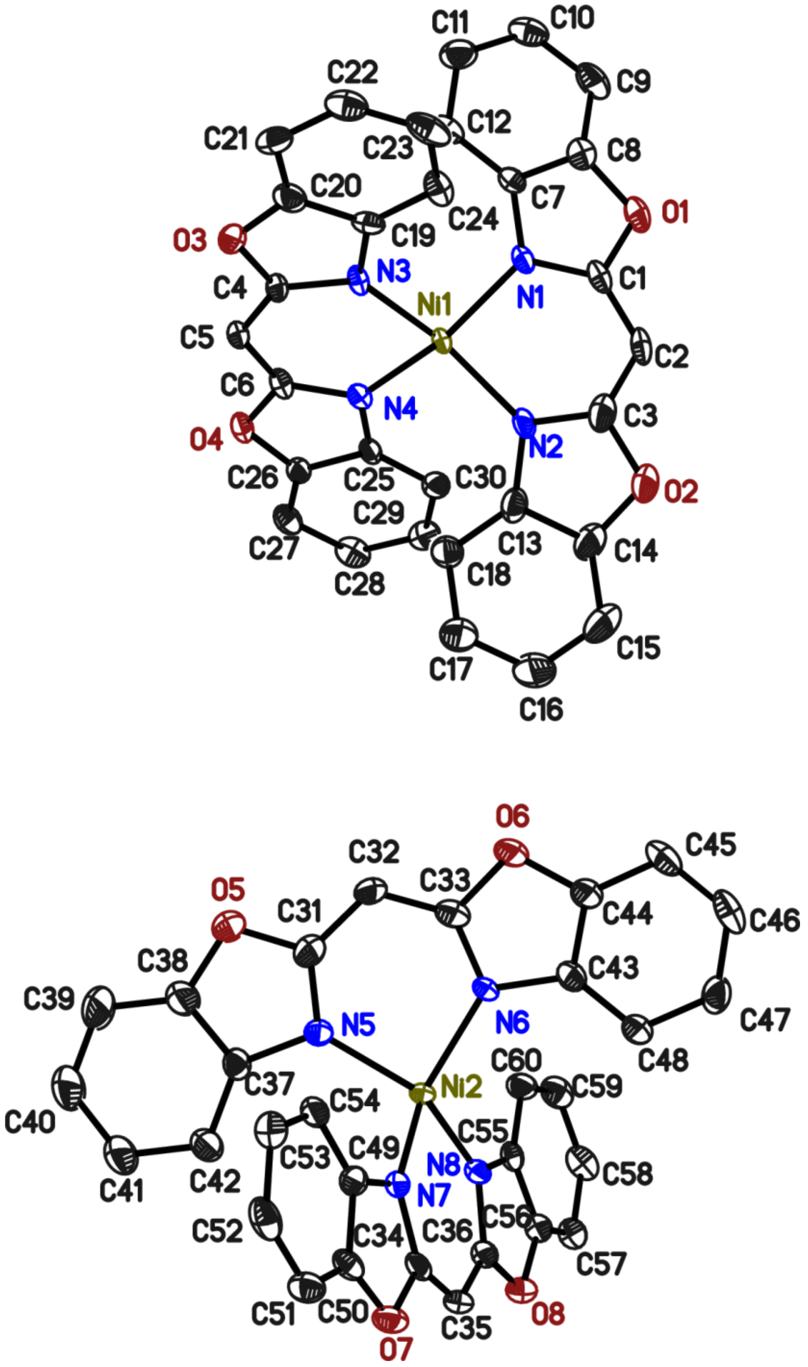

Figure 6.5. The asymmetric unit of **4** with thermal ellipsoids at 50% probability level. The hydrogen atoms are omitted for clarity. The SC-XRD data was relatively weak compared to the other complexes in general. The asymmetric unit contains two complex molecules and no solvent molecules. The measured crystal was non-merohedrally twinned with the twin law 1 0 0 0 −1 0 −0.68 0 −1. However, integration with two orientation matrices did not lead to an improvement in the data. Therefore, the integration was performed with a fixed integration box (x = y = z = 0.4).

Table 6.4. Crystallographic data for **4**.

Compound	4_DL_NiBox		Z	8
CCDC no.	2095988		ρ_{calc} [Mg m^{-3}]	1.528
Empirical formula	$C_{30}H_{18}NiN_4O_4$		μ [mm^{-1}]	0.848
Formula weight [g mol^{-1}]	557.19		$F(000)$	2288
Temperature [K]	100(2)		Crystal size [mm]	0.234 x 0.132 x 0.050
Wavelength [Å]	0.71073		θ range [°]	1.112 to 25.389
Crystal system	Monoclinic		Reflections collected	74403
Space group	$P2_1/n$		Unique reflections	8912
Unit cell parameters	a [Å]	19.780(3)	R_{int}	0.0971
	b [Å]	7.760(2)	Restraints / parameters	0 / 703
	c [Å]	32.304(4)	Goodness-of-fit on F^2	1.247
	α [°]	90	R_1 [$I>2\sigma(I)$]	0.0881
	β [°]	102.24(3)	$R_{2,w}$ (all data)	0.2243
	γ [°]	90	$\Delta\varrho_{\text{max}}/\Delta\varrho_{\text{min}}$ [e Å^{-3}]	1.430 / −1.010
Volume [Å^3]	4846(2)		Color and shape	Dark green needles

6.5.5. Crystal structure of [(thf)$_2$MnCl(4-benzhydryl-NCOC$_6$H$_4$)$_2$CH] (5)

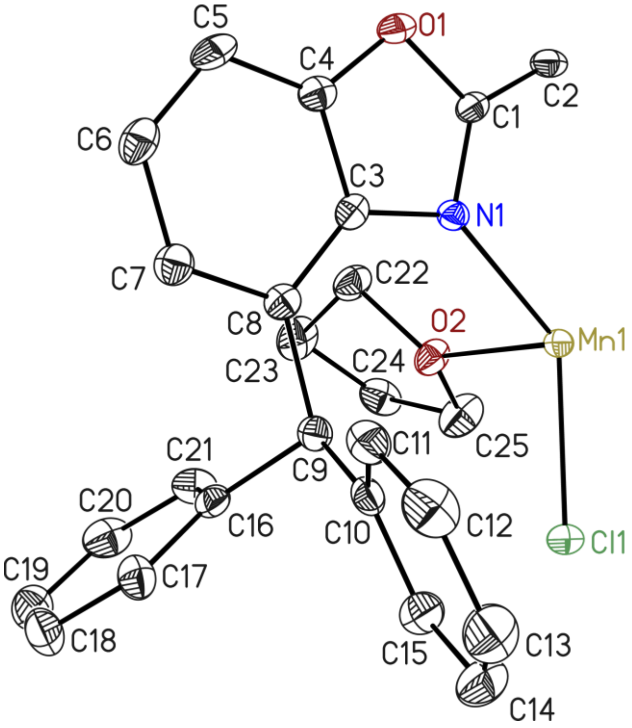

Figure 6.6. The asymmetric unit of **5** illustrates half a complex molecule with thermal ellipsoids at 50% probability level. The hydrogen atoms are omitted for clarity.

Table 6.5. Crystallographic data for **5**.

Compound	5_DL_MnBZH		*Z*	4
CCDC no.			ρ_{calc} [Mg m^{-3}]	1.379
Empirical formula	$C_{49}H_{45}ClMnN_2O_4$		μ [mm^{-1}]	0.454
Formula weight [g mol^{-1}]	816.26		*F*(000)	1708
Temperature [K]	100(2)		Crystal size [mm]	0.169 x 0.141 x 0.078
Wavelength [Å]	0.71073		θ range [°]	1.558 to 26.411
Crystal system	Monoclinic		Reflections collected	92676
Space group	*C*2/*c*		Unique reflections	4032
Unit cell parameters	*a* [Å]	15.380(2)	R_{int}	0.0453
	b [Å]	9.778(2)	Restraints / parameters	0 / 259
	c [Å]	26.305(4)	Goodness-of-fit on F^2	1.041
	α [°]	90	R_1 [$I>2\sigma(I)$]	0.0294
	β [°]	96.42(2)	$R_{2,w}$ (all data)	0.0717
	γ [°]	90	$\Delta\varrho_{max}/\Delta\varrho_{min}$ [e Å^{-3}]	0.283 / −0.294
Volume [Å^3]	3931.1(11)		Color and shape	Yellow blocks

6.5.6. Crystal structure of [(thf)$_2$FeCl{(4-benzhydryl-NCOC$_6$H$_3$)$_2$CH}] (6)

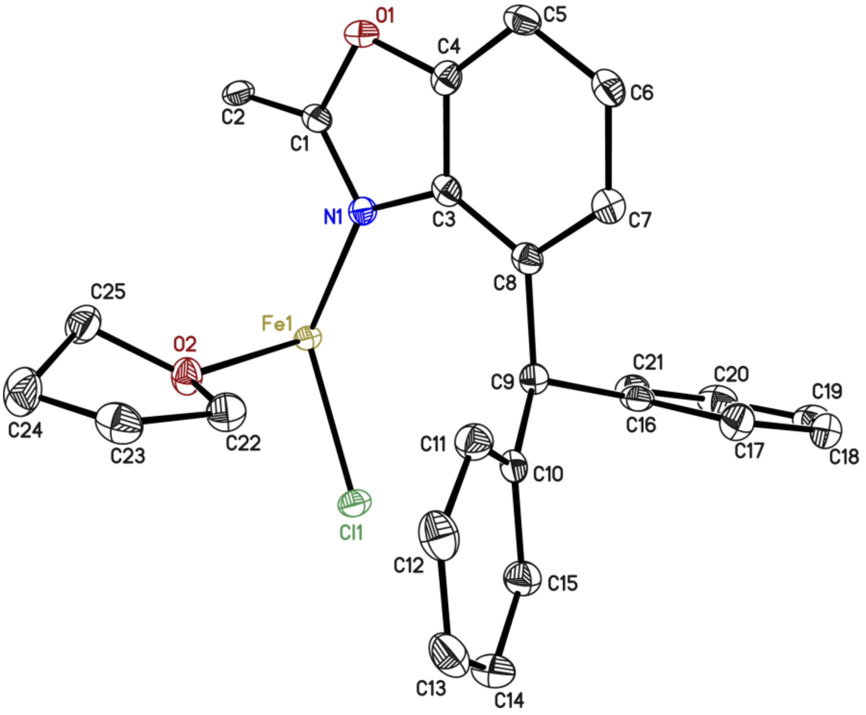

Figure 6.7. The asymmetric unit of **6** displays half a complex molecule with thermal ellipsoids at 50% probability level. The hydrogen atoms are omitted for clarity.

Table 6.6. Crystallographic data for **6**.

Compound	6_DL_FeBZH		Z	4
CCDC no.			ρ_{calc} [Mg m^{-3}]	1.440
Empirical formula	$C_{49}H_{45}ClFeN_2O_4$		μ [mm^{-1}]	0.523
Formula weight [g mol^{-1}]	817.17		F(000)	1712
Temperature [K]	100(2)		Crystal size [mm]	0.342 x 0.283 x 0.138
Wavelength [Å]	0.71073		θ range [°]	1.578 to 26.646
Crystal system	Monoclinic		Reflections collected	31401
Space group	$C2/c$		Unique reflections	3951
Unit cell parameters	a [Å]	14.649(2)	R_{int}	0.0479
	b [Å]	9.973(2)	Restraints / parameters	0 / 259
	c [Å]	25.99(3)	Goodness-of-fit on F^2	1.052
	α [°]	90	R_1 [I>2σ(I)]	0.0335
	β [°]	96.82(2)	$R_{2,w}$ (all data)	0.0846
	γ [°]	90	$\Delta\varrho_{\mathrm{max}}/\Delta\varrho_{\mathrm{min}}$ [e Å^{-3}]	0.315 / −0.374
Volume [Å^3]	3770(7)		Color and shape	Red needles

6.5.7. Crystal structure of [(thf)CoCl{(4-benzhydryl-NCOC$_6$H$_3$)$_2$CH}] (7)

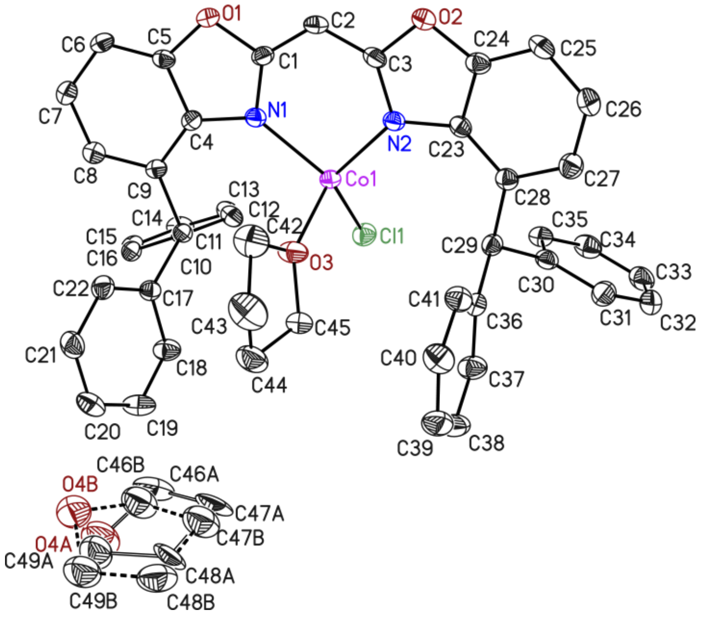

Figure 6.8. The asymmetric unit of **7** with thermal ellipsoids at 50% probability level. The hydrogen atoms are omitted for clarity. The thf unit was disordered about 2 positions (O4A/O4B-unit) and was refined with distance restraints and restraints for the anisotropic displacement parameters. The occupancy of the minor position refined to 0.483(13), respectively.

Table 6.7. Crystallographic data for **7**.

Compound	7_DL_CoBZH		Z	4
CCDC no.			ρ_{calc} [Mg m^{-3}]	1.371
Empirical formula	$C_{49}H_{41}ClCoN_2O_{3.5}$		μ [mm^{-1}]	0.569
Formula weight [g mol^{-1}]	784.20		F(000)	1636
Temperature [K]	100(2)		Crystal size [mm]	0.560 x 0.374 x 0.184
Wavelength [Å]	0.71073		θ range [°]	1.535 to 26.411
Crystal system	Monoclinic		Reflections collected	51745
Space group	$P2_1/c$		Unique reflections	7772
Unit cell parameters	a [Å]	13.9004(3)	R_{int}	0.0565
	b [Å]	12.504(3)	Restraints / parameters	236 / 560
	c [Å]	22.897(6)	Goodness-of-fit on F^2	1.038
	α [°]	90	R_1 [I>2σ(I)]	0.0385
	β [°]	107.37(2)	$R_{2,w}$ (all data)	0.1010
	γ [°]	90	$\Delta\varrho_{\max}/\Delta\varrho_{\min}$ [e Å^{-3}]	1.245 / −0.738
Volume [Å^3]	3798.1(16)		Color and shape	Brown blocks

6.5.8. Crystal structure of [(thf)$_2$MnCl{(4,6-*t*Bu-NCOC$_6$H$_2$)$_2$CH}] (8)

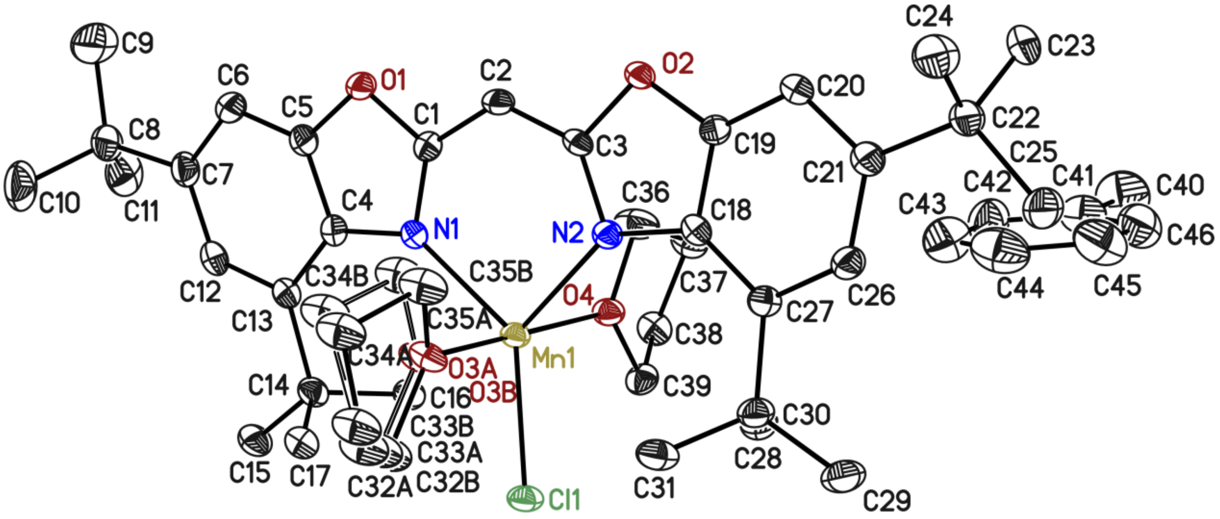

Figure 6.9. The asymmetric unit of **8** with thermal ellipsoids at 50% probability level. The hydrogen atoms are omitted for clarity. The thf unit was disordered about 2 positions (O3A/O3B-unit) and was refined with distance restraints and restraints for the anisotropic displacement parameters. The occupancy of the major position refined to 0.793(6), respectively.

Table 6.8. Crystallographic data for **8**.

Compound	8_DL_Mn*t*Bubox		*Z*	4
CCDC no.	-		ρ_{calc} [Mg m^{-3}]	1.229
Empirical formula	$C_{46}H_{65}ClMnN_2O_4$		μ [mm^{-1}]	0.410
Formula weight [g mol^{-1}]	800.39		*F*(000)	1716
Temperature [K]	100(2)		Crystal size [mm]	0.213 x 0.185 x 0.142
Wavelength [Å]	0.71073		θ range [°]	2.040 to 25.036
Crystal system	Monoclinic		Reflections collected	149269
Space group	$P2_1/n$		Unique reflections	7639
Unit cell parameters	*a* [Å]	10.770(2)	R_{int}	0.0449
	b [Å]	26.632(4)	Restraints / parameters	158 / 546
	c [Å]	15.080(3)	Goodness-of-fit on F^2	1.034
	α [°]	90	R_1 [$I>2\sigma(I)$]	0.0361
	β [°]	89.97(3)	$R_{2,w}$ (all data)	0.0953
	γ [°]	90	$\Delta\varrho_{\max}/\Delta\varrho_{\min}$ [e Å^{-3}]	1.245 / −0.738
Volume [Å^3]	4325(2)		Color and shape	Yellow blocks

6.5.9. Crystal structure of [Gd{N(SiCH$_3$)$_2$}$_3$] (9)

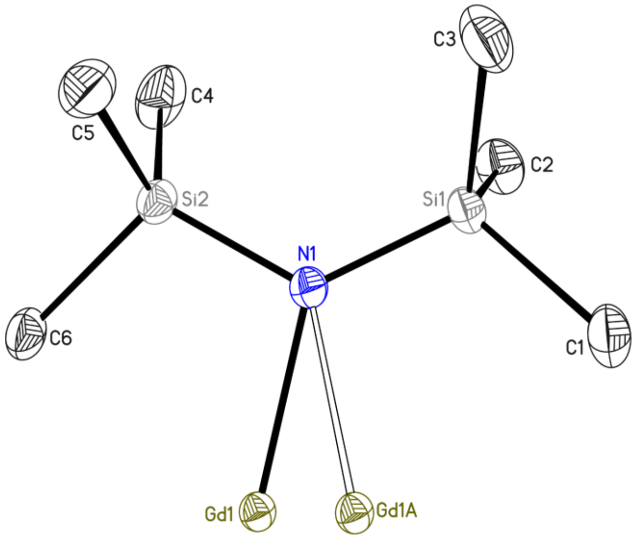

Figure 6.10. The asymmetric unit of **9** shows 1/3 of the entire molecule with thermal ellipsoids at 50% probability level. The hydrogen atoms are omitted for clarity. We found a strong disorder of the metal center, which was addressed with a disorder about 2 positions. The displacement parameters were constrained to be identical. The occupancies refined to 0.3005(3) and 0.0328(3), respectively. Further, the following twin law was employed to refine the structure: TWIN −1 0 0 1 1 0 0 0 −1. The fractional contribution refined to 0.4391(13) for the minor domain. The squeeze command was then applied to remove the electron density of severely disordered solvent molecules along the three-fold axis.

Table 6.9. Crystallographic data for **9.**

Compound	9_DL_GdHMDS		Z	2
CCDC no.	2109791		ρ_{calc} [Mg m^{-3}]	1.108
Empirical formula	$C_{18}H_{54}GdN_3Si_6$		μ [mm^{-1}]	1.031
Formula weight [g mol^{-1}]	638.43		F(000)	662
Temperature [K]	100(2)		Crystal size [mm]	0.190 x 0.023 x 0.016
Wavelength [Å]	0.71073		θ range [°]	1.933 to 22.114
Crystal system	Trigonal		Reflections collected	15661
Space group	$P\bar{3}$		Unique reflections	3134
Unit cell parameters	a [Å]	16.301(3)	R_{int}	0.0391
	b [Å]	16.301(3)	Restraints / parameters	0 / 88
	c [Å]	8.313(3)	Goodness-of-fit on F^2	1.049
	α [°]	90	R_1 [I>2σ(I)]	0.0268
	β [°]	90	$R_{2,w}$ (all data)	0.0669
	γ [°]	120	$\Delta\varrho_{\max}/\Delta\varrho_{\min}$ [e Å^{-3}]	2.119 / −2.271
Volume [Å^3]	1913.0(8)		Color and shape	Colorless needles

6.5.10. Crystal structure of $[\mathrm{Ho}\{\mathrm{N}(\mathrm{SiCH}_3)_2\}_3]$ (10)

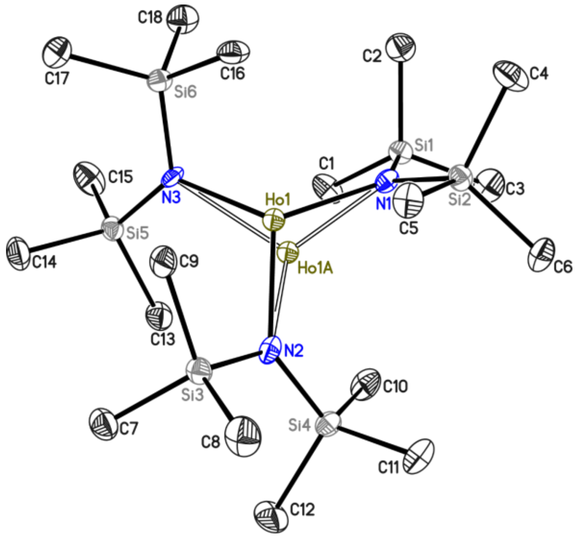

Figure 6.11. The asymmetric unit of **10** with thermal ellipsoids at 50% probability level. The hydrogen atoms are omitted for clarity. We found a strong disorder of the metal center, which was addressed with a disorder about 2 positions. The displacement parameters were constrained to be identical. The occupancies refined to 0.9760(6) and 0.0240(3), respectively. Further, the following two twin operations describing a three-fold axis were employed to refine the structure: −1 0 0 0 −0.5 1.5 0 −0.5 −0.5 and −1 0 0 0 −0.5 −1.5 0 0.5 −0.5. The fractional contributions refined to 0.3079(9) and 0.2987(13) for the minor domains. The squeeze command was then applied to remove the electron density of the severely disordered solvent molecule.

Table 6.10. Crystallographic data for **10.**

Compound	10_DL_HoHMDS		Z	4
CCDC no.	2109790		ρ_{calc} [Mg m^{-3}]	1.134
Empirical formula	$C_{18}H_{54}HoN_3Si_6$		μ [mm^{-1}]	1.220
Formula weight [g mol^{-1}]	646.11		F(000)	1336
Temperature [K]	100(2)		Crystal size [mm]	0.251 x 0.092 x 0.021
Wavelength [Å]	0.71073		θ range [°]	1.514 to 21.385
Crystal system	Monoclinic		Reflections collected	84067
Space group	$P2_1/n$		Unique reflections	13236
Unit cell parameters	a [Å]	8.302(2)	R_{int}	0.0707
	b [Å]	27.999(8)	Restraints / parameters	0 / 277
	c [Å]	16.275(4)	Goodness-of-fit on F^2	1.048
	α [°]	90	R_1 [I>2σ(I)]	0.0316
	β [°]	99.05(2)	$R_{2,w}$ (all data)	0.0647
	γ [°]	90	$\Delta\varrho_{\max}/\Delta\varrho_{\min}$ [e Å^{-3}]	0.759 / −0.970
Volume [Å^3]	3783.0(17)		Color and shape	Colorless needles

6.5.11. Crystal structure of [(thf)Eu{(NCOC$_6$H$_4$)$_2$CH}$_3$] (11)

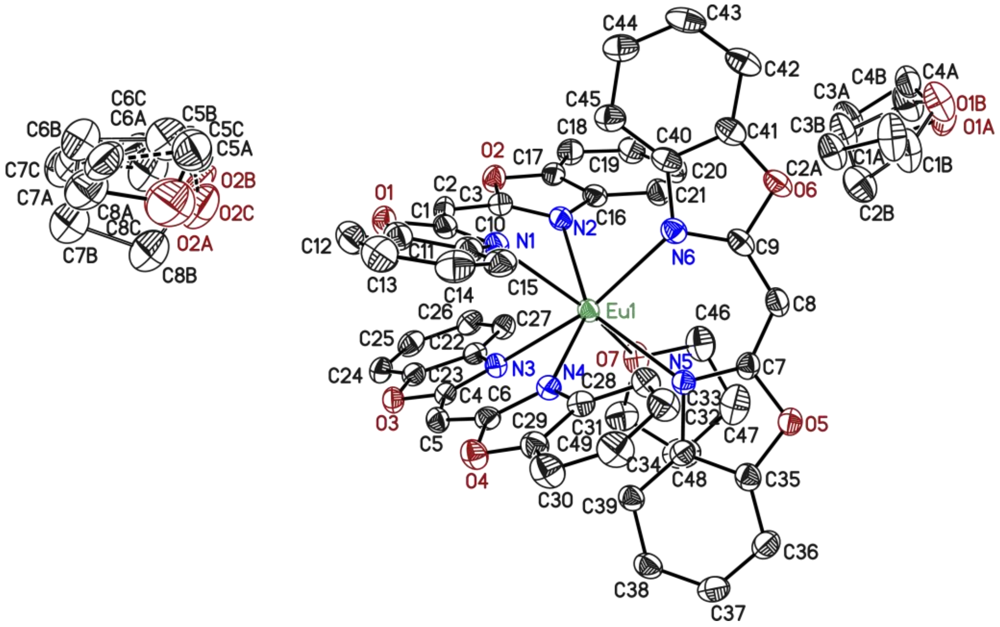

Figure 6.12. The asymmetric unit of **11** with thermal ellipsoids at 50% probability level. The hydrogen atoms are omitted for clarity. The non-coordinating lattice thf units were disordered about 2 positions (O1A/O1B-units) and about 3 positions (O2A/O2B/O2C-units). They were refined with distance restraints and restraints for the anisotropic displacement parameters. The occupancies of the minor positions refined to 0.489(3), 0.235(3), and 0.254(3), respectively.

Table 6.11. Crystallographic data for **11**.

Compound	11_DL_EuBox		Z	4
CCDC no.	-		ρ_{calc} [Mg · m^{-3}]	1.532
Empirical formula	$C_{57}H_{51}N_6O_9Eu$		μ [mm^{-1}]	1.364
Formula weight [g mol^{-1}]	1115.99		F(000)	2280
Temperature [K]	100(2)		Crystal size [mm]	0.231 x 0.216 x 0.183
Wavelength [Å]	0.71073		θ range [°]	1.442 to 26.833
Crystal system	Monoclinic		Reflections collected	123291
Space group	$P2_1/c$		Unique reflections	10347
Unit cell parameters	a [Å]	12.028(2)	R_{int}	0.0324
	b [Å]	18.821(3)	Restraints / parameters	867 / 797
	c [Å]	21.412(3)	Goodness-of-fit on F^2	1.091
	α [°]	90	R_1 [$I>2\sigma(I)$]	0.0285
	β [°]	93.51(2)	$R_{2,w}$ (all data)	0.0739
	γ [°]	90	$\Delta\varrho_{\mathrm{max}}/\Delta\varrho_{\mathrm{min}}$ [e Å^{-3}]	1.293 / −0.744
Volume [Å^3]	4838.1(13)		Color and shape	Blue blocks

6.5.12. Crystal structure of [(thf)Tb{(NCOC$_6$H$_4$)$_2$CH}$_3$] (12)

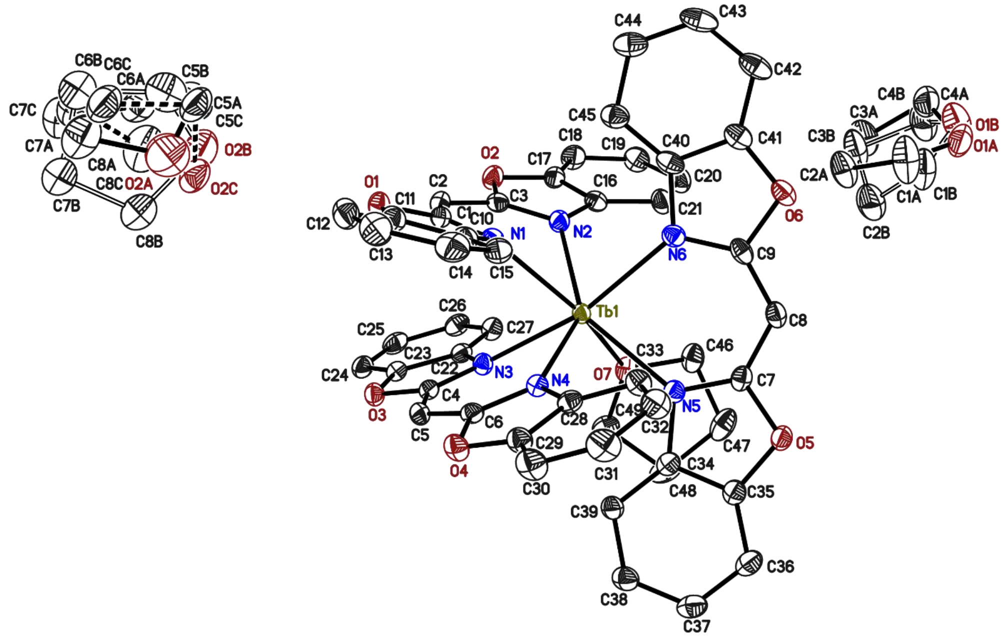

Figure 6.13. The asymmetric unit of **12** with thermal ellipsoids at 50% probability level. The hydrogen atoms are omitted for clarity. The non-coordinating lattice thf units were disordered about 2 positions (O1A/O1B-units) and about 3 positions (O2A/O2B/O2C-units). They were refined with distance restraints and restraints for the anisotropic displacement parameters. The occupancies of the minor positions refined to 0.311(12), 0.286(3), and 0.181(3), respectively.

Table 6.12. Crystallographic data for **12**.

Compound	12_DL_TbBox		*Z*	4
CCDC no.	2109784		ρ_{calc} [Mg m^{-3}]	1.534
Empirical formula	$C_{57}H_{51}N_6O_9Tb$		μ [mm^{-1}]	1.521
Formula weight [g mol^{-1}]	1122.95		*F*(000)	2288
Temperature [K]	100(2)		Crystal size [mm]	0.346 x 0.253 x 0.152
Wavelength [Å]	0.71073		θ range [°]	1.441 to 26.818
Crystal system	Monoclinic		Reflections collected	142209
Space group	$P2_1/c$		Unique reflections	10406
Unit cell parameters	*a* [Å]	12.085(2)	R_{int}	0.0277
	b [Å]	18.899(3)	Restraints / parameters	873 / 797
	c [Å]	21.333(3)	Goodness-of-fit on F^2	1.153
	α [°]	90	R_1 [I>2σ(I)]	0.0253
	β [°]	93.53(2)	$R_{2,w}$ (all data)	0.0610
	γ [°]	90	$\Delta\varrho_{\max}/\Delta\varrho_{\min}$ [e Å^{-3}]	1.027 / −0.696
Volume [Å^3]	4863.1(13)		Color and shape	Yellow blocks

6.5.13. Crystal structure of $[(thf)Dy\{(NCOC_6H_4)_2CH\}_3]$ (13)

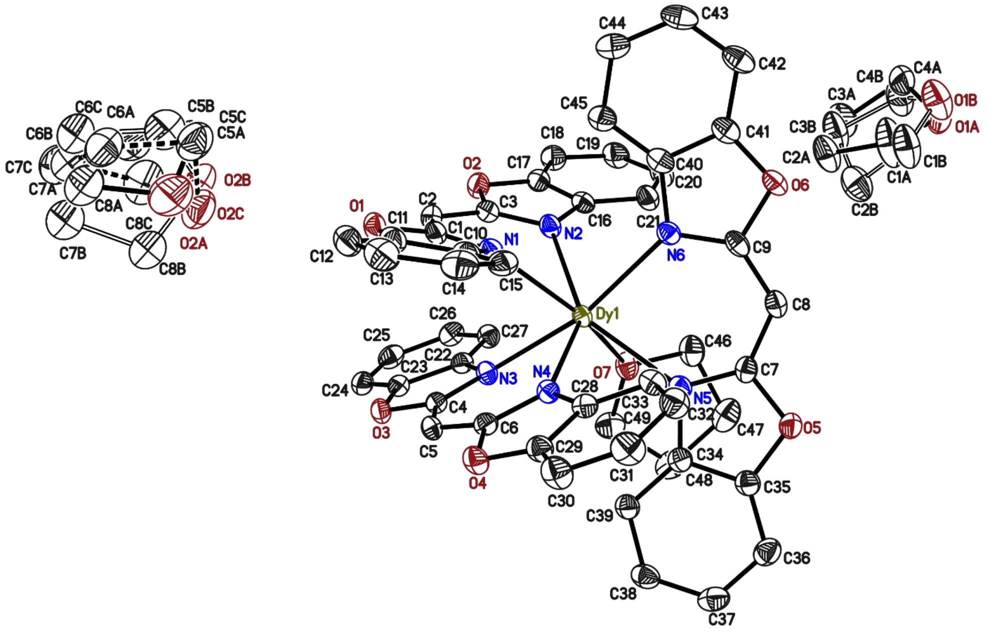

Figure 6.14. The asymmetric unit of **13** with thermal ellipsoids at 50% probability level. The hydrogen atoms are omitted for clarity. The non-coordinating lattice thf units were disordered about 2 positions (O1A/O1B-units) and about 3 positions (O2A/O2B/O2C-units). They were refined with distance restraints and restraints for the anisotropic displacement parameters. The occupancies of the minor positions refined to 0.320(12), 0.189(3), and 0.139(3), respectively.

Table 6.13. Crystallographic data for **13**.

Compound	13_DL_DyBox		*Z*	4
CCDC no.	2109785		ρ_{calc} [Mg m^{-3}]	1.546
Empirical formula	$C_{57}H_{51}N_6O_9Dy$		μ [mm^{-1}]	1.611
Formula weight [g mol^{-1}]	1122.95		*F*(000)	2292
Temperature [K]	100(2)		Crystal size [mm]	0.231 x 0.216 x 0.183
Wavelength [Å]	0.71073		θ range [°]	1.446 to 26.803
Crystal system	Monoclinic		Reflections collected	144039
Space group	$P2_1/c$		Unique reflections	10337
Unit cell parameters	*a* [Å]	12.0970(2)	R_{int}	0.0353
	b [Å]	18.753(3)	Restraints / parameters	879 / 797
	c [Å]	21.390(3)	Goodness-of-fit on F^2	1.126
	α [°]	90	R_1 [$I > 2\sigma(I)$]	0.0248
	β [°]	93.87(2)	$R_{2,w}$ (all data)	0.0629
	γ [°]	90	$\Delta\varrho_{max}/\Delta\varrho_{min}$ [e Å^{-3}]	1.099 / −0.583
Volume [Å^3]	4841.4(13)		Color and shape	Yellow blocks

6.5.14. Crystal structure of [Dy{(NCOC$_6$H$_4$)$_2$CH}$_3$] (13’)

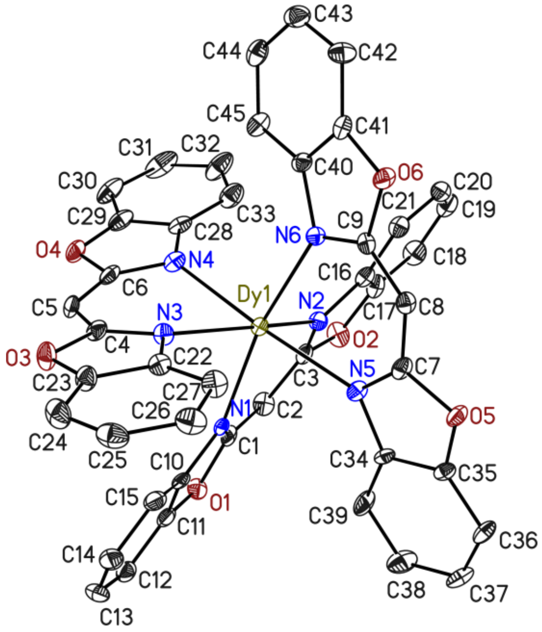

Figure 6.15. The asymmetric unit of **13’** with thermal ellipsoids at 50% probability level. The hydrogen atoms are omitted for clarity. No lattice solvent is present.

Table 6.14. Crystallographic data for **13’**.

Compound	13_1_DyBox		*Z*	4
CCDC no.	-		ρ_{calc} [Mg m^{-3}]	1.672
Empirical formula	$C_{45}H_{27}N_6O_6Dy$		μ [mm^{-1}]	2.129
Formula weight [g mol^{-1}]	910.22		*F*(000)	1812
Temperature [K]	100(2)		Crystal size [mm]	0.125 x 0.117 x 0.067
Wavelength [Å]	0.71073		θ range [°]	1.649 to 26.176
Crystal system	Monoclinic		Reflections collected	9756
Space group	$P2_1/c$		Unique reflections	6120
Unit cell parameters	*a* [Å]	11.856(2)	R_{int}	0.0349
	b [Å]	17.809(3)	Restraints / parameters	0 / 523
	c [Å]	18.073(3)	Goodness-of-fit on F^2	1.014
	α [°]	90	R_1 [$I>2\sigma(I)$]	0.0339
	β [°]	108.59(3)	$R_{2,w}$ (all data)	0.0783
	γ [°]	90	$\Delta\varrho_{\max}/\Delta\varrho_{\min}$ [e Å^{-3}]	0.876 / −0.545
Volume [Å^3]	3616.9(12)		Color and shape	Yellow blocks

6.5.15. Crystal structure of [(thf)Ho{(NCOC$_6$H$_4$)$_2$CH}$_3$] (14)

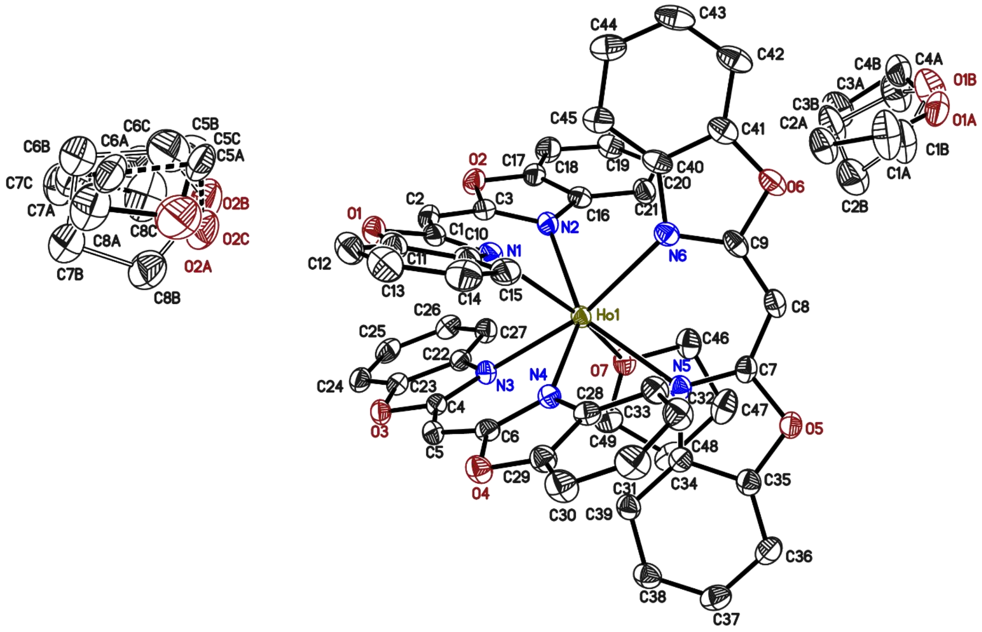

Figure 6.16. The asymmetric unit of **14** with thermal ellipsoids at 50% probability level. The hydrogen atoms are omitted for clarity. The non-coordinating lattice thf units were disordered about 2 positions (O1A/O1B-units) and about 3 positions (O2A/O2B/O2C-units). They were refined with distance restraints and restraints for the anisotropic displacement parameters. The occupancies of the minor positions refined to 0.293(10), 0.306(3), and 0.211(3), respectively.

Table 6.15. Crystallographic data for **14**.

Compound	14_DL_HoBox		*Z*	4
CCDC no.	2109786		ρ_{calc} [Mg m^{-3}]	1.551
Empirical formula	C$_{57}$H$_{51}$N$_6$O$_9$Ho		μ [mm^{-1}]	1.704
Formula weight [g mol^{-1}]	1128.96		*F*(000)	2296
Temperature [K]	100(2)		Crystal size [mm]	0.264 x 0.256 x 0.206
Wavelength [Å]	0.71073		θ range [°]	1.443 to 26.767
Crystal system	Monoclinic		Reflections collected	144305
Space group	*P*2$_1$/*c*		Unique reflections	10281
Unit cell parameters	*a* [Å]	12.055(2)	R_{int}	0.0235
	b [Å]	18.879(3)	Restraints / parameters	873 / 797
	c [Å]	21.286(3)	Goodness-of-fit on F^2	1.073
	α [°]	90	R_1 [I>2σ(I)]	0.02115
	β [°]	93.62(2)	$R_{2,w}$ (all data)	0.0550
	γ [°]	90	$\Delta\varrho_{\max}/\Delta\varrho_{\min}$ [e Å^{-3}]	0.766 / −0.524
Volume [Å^3]	4834.7(13)		Color and shape	Yellow blocks

6.5.16. Crystal structure of [(THF)Er{$(NCOC_6H_4)_2CH$}$_3$] (15)

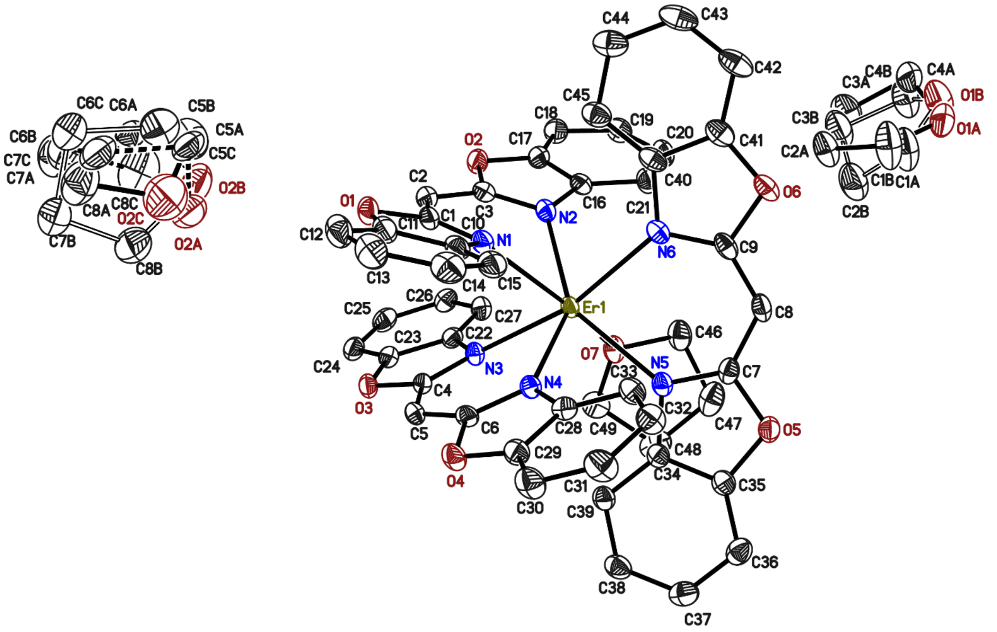

Figure 6.17. The asymmetric unit of **15** with thermal ellipsoids at 50% probability level. The hydrogen atoms are omitted for clarity. The non-coordinating lattice thf units were disordered about 2 positions (O1A/O1B-units) and about 3 positions (O2A/O2B/O2C-units). They were refined with distance restraints and restraints for the anisotropic displacement parameters. The occupancies of the minor positions refined to 0.254(12), 0.335(3), and 0.247(3), respectively.

Table 6.16. Crystallographic data for **15**.

Compound	15_DL_ErBox		*Z*	4
CCDC no.	2109786		ρ_{calc} [Mg m^{-3}]	1.560
Empirical formula	$C_{57}H_{51}N_6O_9Er$		μ [mm^{-1}]	1.810
Formula weight [g mol^{-1}]	1131.29		*F*(000)	2300
Temperature [K]	100(2)		Crystal size [mm]	0.303 x 0.230 x 0.133
Wavelength [Å]	0.71073		θ range [°]	1.443 to 26.877
Crystal system	Monoclinic		Reflections collected	144922
Space group	$P2_1/c$		Unique reflections	10346
Unit cell parameters	*a* [Å]	12.024(2)	R_{int}	0.0437
	b [Å]	18.909(3)	Restraints / parameters	867 / 797
	c [Å]	21.231(3)	Goodness-of-fit on F^2	1.127
	α [°]	90	R_1 [$I>2\sigma(I)$]	0.0262
	β [°]	93.53(3)	$R_{2,w}$ (all data)	0.0662
	γ [°]	90	$\Delta\varrho_{max}/\Delta\varrho_{min}$ [e Å^{-3}]	1.245 / -0.738
Volume [Å^3]	4818.0(13)		Color and shape	Yellow blocks

6.5.17. Crystal structure of [Er{(NCSC$_6$H$_4$)$_2$CH}$_3$] (16)

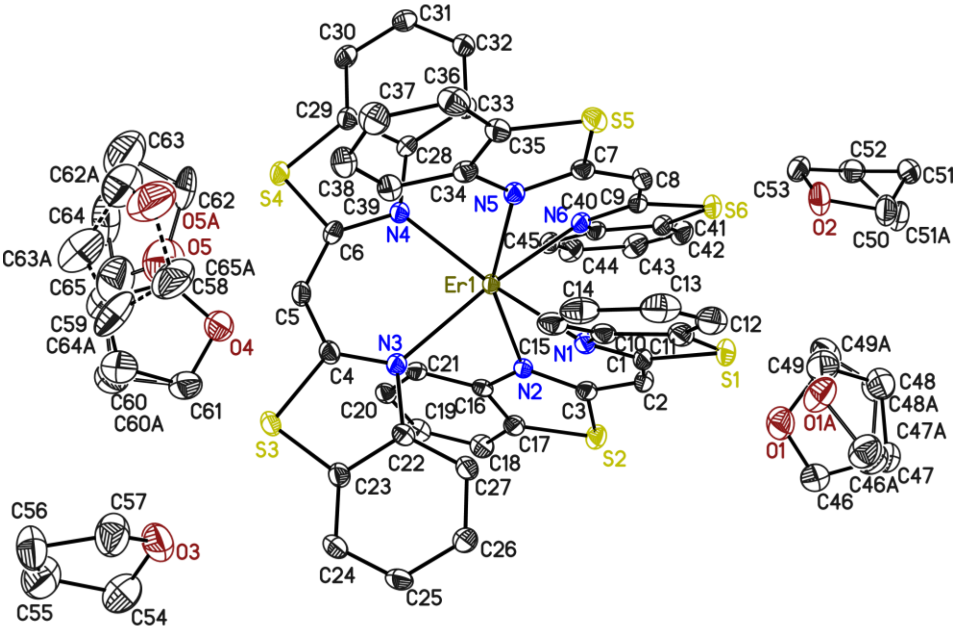

Figure 6.18. The asymmetric unit of **16** with thermal ellipsoids at 50% probability level and the hydrogen atoms are omitted for clarity. The non-coordinating lattice thf units were disordered about 2 positions (O1/O1B-, O5/O5A-units) and were refined with distance restraints and restraints for the anisotropic displacement parameters. The occupancies of the major positions refined to 0.832(4), and 0.648(14), respectively.

Table 6.17. Crystallographic data for **16**.

Compound	16_DL_ErSBox		Z	8
CCDC no.	-		ρ_{calc} [Mg m^{-3}]	1.535
Empirical formula	$C_{63}H_{63}ErN_6O_{4.5}S_6$		μ [mm^{-1}]	1.724
Formula weight [g mol^{-1}]	1335.81		F(000)	5464
Temperature [K]	100(2)		Crystal size [mm]	0.376 x 0.289 x 0.233
Wavelength [Å]	0.71073		θ range [°]	1.449 to 26.880
Crystal system	Monoclinic		Reflections collected	100965
Space group	$C2/c$		Unique reflections	12442
Unit cell parameters	a [Å]	23.156(3)	R_{int}	0.0199
	b [Å]	17.796(3)	Restraints / parameters	1048 / 860
	c [Å]	28.346(3)	Goodness-of-fit on F^2	1.055
	α [°]	90	R_1 [I>2σ(I)]	0.0204
	β [°]	98.114(2)	$R_{2,w}$ (all data)	0.0517
	γ [°]	90	$\Delta\varrho_{max}/\Delta\varrho_{min}$ [e Å^{-3}]	0.729 / -0.350
Volume [Å^3]	11563(2)		Color and shape	Orange blocks

6.5.18. Crystal structure of [Na(thf)$_6$][Na{(4-Me-NCOC$_6$H$_3$)$_2$CH}$_2$] (17)

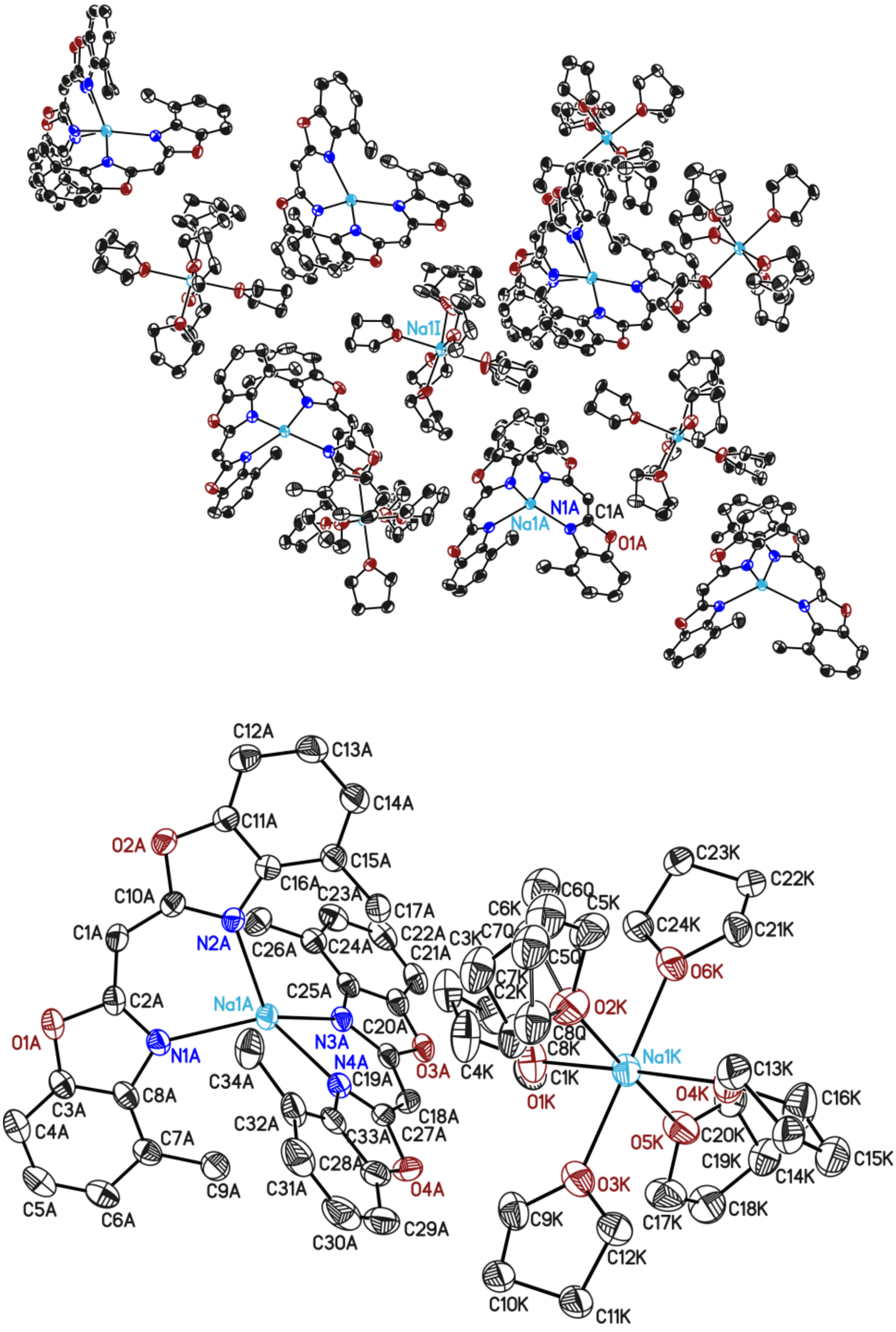

Figure 6.19. The asymmetric unit of **17** with thermal ellipsoids at 50% probability level. The hydrogen atoms are omitted for clarity. The upper illustration shows the six non-identical molecules in the asymmetric unit, while the lower figure portrays one complex moiety with its solvent-separated ion pair. Two of the twelve ligands and ten of the 36 thf molecules are disordered over two positions, and restraints on the anisotropic displacement parameters and on distances and angle distances were applied. The occupancies of the minor positions of the ligands refined to 0.377(7) and 0.484(5), respectively. The occupancies of the minor positions of the thf molecules refined from 0.092(4) to 0.498(5).

Table 6.18. Crystallographic data for **17**.

Compound	17_DL_NaMeBox		Z	24
CCDC no.	2122903		ρ_{calc} [Mg m^{-3}]	1.243
Empirical formula	$C_{58}H_{74}N_4Na_2O_{10}$		μ [mm^{-1}]	0.098
Formula weight [g mol^{-1}]	1033.19		F(000)	13248
Temperature [K]	100(2)		Crystal size [mm]	0.544 x 0.358 x 0.272
Wavelength [Å]	0.71073		θ range [°]	0.724 to 25.093
Crystal system	Monoclinic		Reflections collected	221822
Space group	$P2_1/c$		Unique reflections	58664
Unit cell parameters	a [Å]	20.837(2)	R_{int}	0.0810
	b [Å]	38.066(3)	Restraints / parameters	44969 / 4733
	c [Å]	41.783(4)	Goodness-of-fit on F^2	1.018
	α [°]	90	R_1 [I>2σ(I)]	0.0590
	β [°]	91.69(2)	$R_{2,w}$ (all data)	0.1724
	γ [°]	90	$\Delta\varrho_{\text{max}}/\Delta\varrho_{\text{min}}$ [e Å^{-3}]	0.303 / -0.331
Volume [Å^3]	33127(5)		Color and shape	Colorless blocks

6.5.19. Crystal structure of $[(thf)_3Na(NCOC_6H_4)_2CH\}]$ (18)

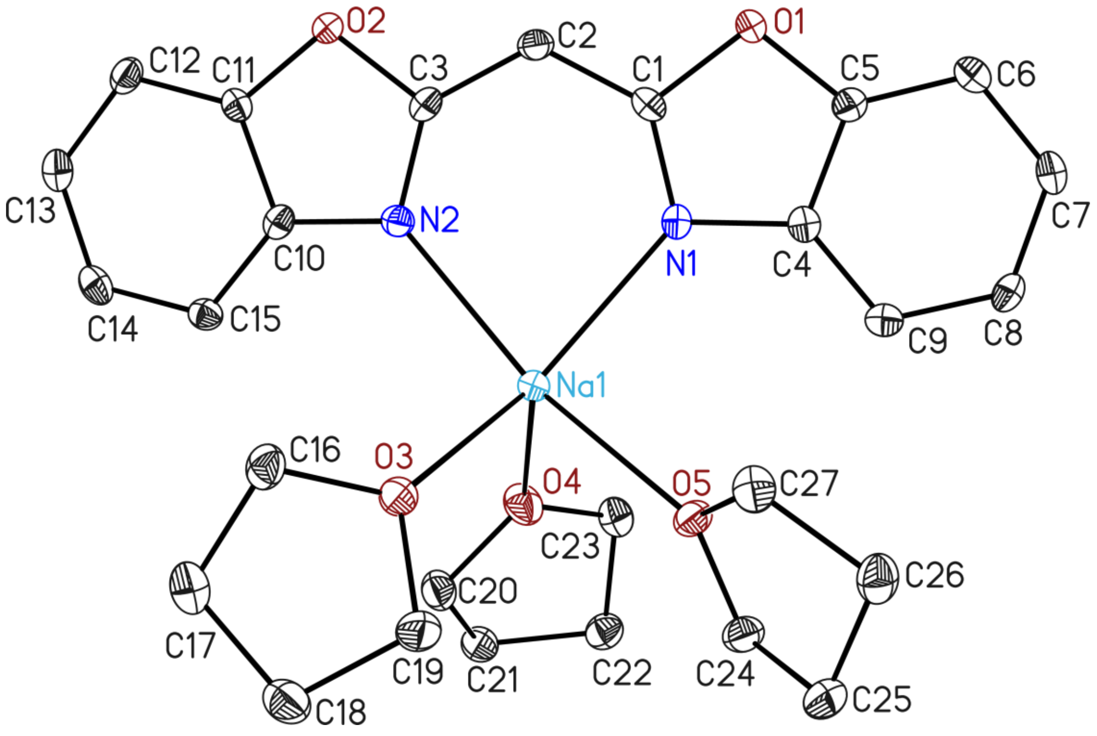

Figure 6.20. The asymmetric unit of **18** with thermal ellipsoids at 50% probability level. The hydrogen atoms are omitted for clarity.

Table 6.19. Crystallographic data for **18**.

Compound	18_DL_NaBox		*Z*	4
CCDC no.	2122904		ρ_{calc} [Mg m^{-3}]	1.295
Empirical formula	$C_{27}H_{33}N_2NaO_5$		μ [mm^{-1}]	0.104
Formula weight [g mol^{-1}]	488.54		*F*(000)	1040
Temperature [K]	100(2)		Crystal size [mm]	0.275 x 0.191 x 0.113
Wavelength [Å]	0.71073		θ range [°]	1.998 to 26.855
Crystal system	Orthorhombic		Reflections collected	90106
Space group	*Pna*2$_1$		Unique reflections	5394
Unit cell parameters	*a* [Å]	16.393(2)	R_{int}	0.0471
	b [Å]	7.496(2)	Restraints / parameters	1/ 319
	c [Å]	20.389(3)	Goodness-of-fit on F^2	1.035
	α [°]	90	R_1 [I>2σ(I)]	0.0261
	β [°]	90	$R_{2,w}$ (all data)	0.0654
	γ [°]	90	$\Delta\varrho_{max}/\Delta\varrho_{min}$ [e Å^{-3}]	0.213 / -0.176
Volume [Å^3]	2505.4(8)		Color and shape	Colorless blocks

6.5.20. Crystal structure of $[(\mu\text{-Cl})\text{Gd}\{4\text{-MeNCOC}_6\text{H}_3)_2\text{CH}\}_2]_2$ (19)

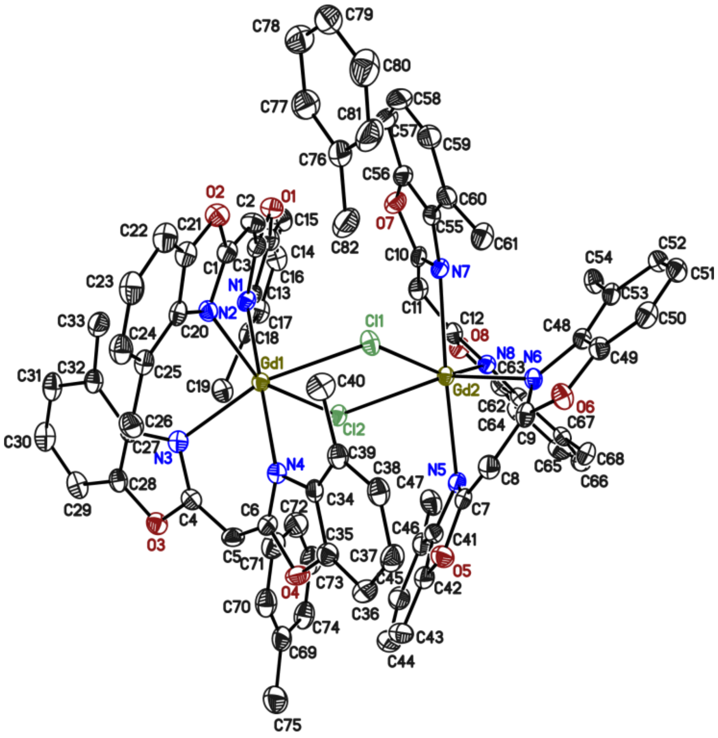

Figure 6.21. The asymmetric unit of **19** with thermal ellipsoids at 50% probability level. The hydrogen atoms are omitted for clarity.

Table 6.20. Crystallographic data for **19**.

Compound	19_DL_GdMeBox		*Z*	2
CCDC no.	2122905		ρ_calc [Mg m^{-3}]	1.586
Empirical formula	$C_{82}H_{68}Cl_2Gd_2N_8O_8$		μ [mm^{-1}]	2.012
Formula weight [g mol^{-1}]	1678.84		*F*(000)	1684
Temperature [K]	100(2)		Crystal size [mm]	0.257 x 0.180 x 0.077
Wavelength [Å]	0.71073		θ range [°]	0.902 to 26.505
Crystal system	Triclinic		Reflections collected	110467
Space group	$P\bar{1}$		Unique reflections	14551
Unit cell parameters	*a* [Å]	12.105(2)	R_int	0.0407
	b [Å]	12.878(2)	Restraints / parameters	0 / 929
	c [Å]	23.054(4)	Goodness-of-fit on F^2	1.241
	α [°]	80.47(2)	R_1 [$I>2\sigma(I)$]	0.0340
	β [°]	82.81(2)	$R_{2,w}$ (all data)	0.0770
	γ [°]	87.55(3)	$\Delta\varrho_\text{max}/\Delta\varrho_\text{min}$ [e Å^{-3}]	1.402 / -1.786
Volume [Å^3]	3515.5(10)		Color and shape	Yellow blocks

6.5.21. Crystal structure of $[(\mu\text{-Cl})\text{Dy}\{4\text{-MeNCOC}_6\text{H}_3)_2\text{CH}\}_2]_2$ (20)

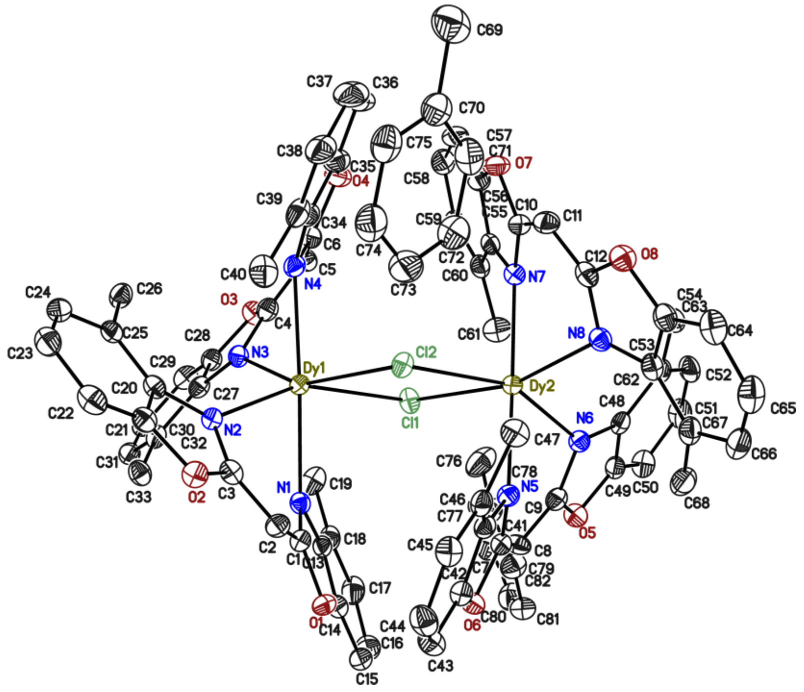

Figure 6.22. The asymmetric unit of **20** with thermal ellipsoids at 50% probability level. The hydrogen atoms are omitted for clarity.

Table 6.21. Crystallographic data for **20**.

Compound	XYZ		Z	2
CCDC no.	2122906		ρ_{calc} [Mg m^{-3}]	1.600
Empirical formula	$C_{82}H_{68}Cl_2Dy_2N_8O_8$		μ [mm^{-1}]	2.256
Formula weight [g mol^{-1}]	1689.34		F(000)	1692
Temperature [K]	100(2)		Crystal size [mm]	0.226 x 0.168 x 0.135
Wavelength [Å]	0.71073		θ range [°]	0.905 to 26.899
Crystal system	Triclinic		Reflections collected	129629
Space group	$P\bar{1}$		Unique reflections	15046
Unit cell parameters	a [Å]	12.103(2)	R_{int}	0.0367
	b [Å]	12.884(2)	Restraints / parameters	0 / 929
	c [Å]	22.999(3)	Goodness-of-fit on F^2	1.016
	α [°]	80.27(2)	R_1 [I>2σ(I)]	0.0246
	β [°]	82.83(2)	$R_{2,w}$ (all data)	0.0571
	γ [°]	87.58(3)	$\Delta\varrho_{\max}/\Delta\varrho_{\min}$ [e Å^{-3}]	1.704 / -0.690
Volume [Å^3]	3506.3(10)		Color and shape	Yellow blocks

6.5.22. Crystal structure of $[(\mu\text{-Cl})\text{Er}\{4\text{-MeNCOC}_6\text{H}_3)_2\text{CH}\}_2]_2$ (21)

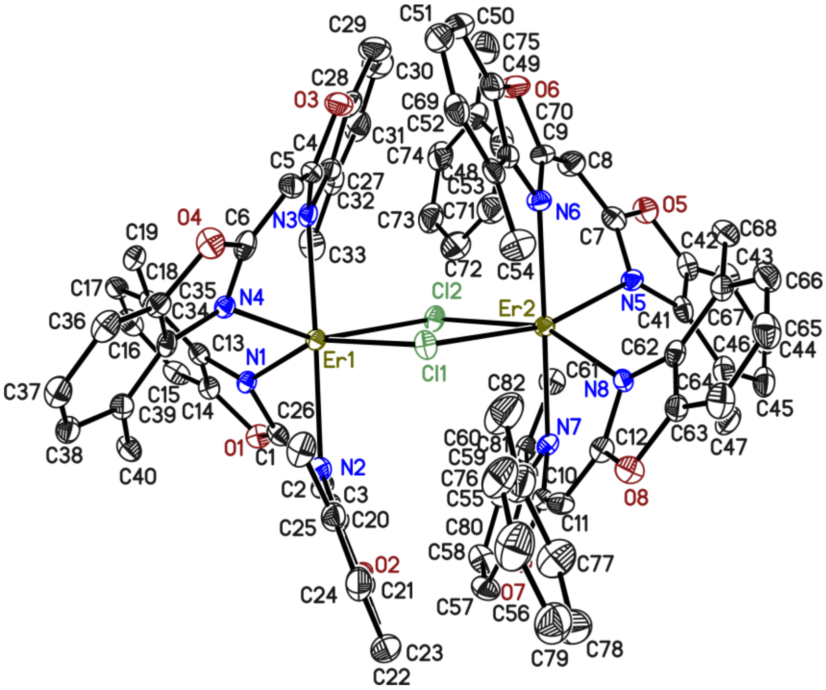

Figure 6.23. The asymmetric unit of **21** with thermal ellipsoids at 50% probability level. The hydrogen atoms are omitted for clarity.

Table 6.22. Crystallographic data for **21**.

Compound	21_DL_ErMeBox		Z	2
CCDC no.	2122907		ρ_{calc} [Mg m^{-3}]	1.601
Empirical formula	$C_{82}H_{68}Cl_2Er_2N_8O_8$		μ [mm^{-1}]	2.507
Formula weight [g mol^{-1}]	1698.86		$F(000)$	1700
Temperature [K]	100(2)		Crystal size [mm]	0.172 x 0.154 x 0.088
Wavelength [Å]	0.71073		θ range [°]	0.904 to 26.372
Crystal system	Triclinic		Reflections collected	77456
Space group	$P\bar{1}$		Unique reflections	14409
Unit cell parameters	a [Å]	12.127(2)	R_{int}	0.0519
	b [Å]	12.908(2)	Restraints / parameters	0 / 929
	c [Å]	23.026(3)	Goodness-of-fit on F^2	1.032
	α [°]	80.32(2)	R_1 [$I>2\sigma(I)$]	0.0291
	β [°]	82.66(2)	$R_{2,w}$ (all data)	0.0637
	γ [°]	87.57(2)	$\Delta\varrho_{\text{max}}/\Delta\varrho_{\text{min}}$ [e Å^{-3}]	0.913 / −0.755
Volume [Å^3]	3523.1(10)		Color and shape	Yellow blocks

6.5.23. Crystal structure of [An{S(NSiMe$_3$)(NHSiMe$_3$)}$_2$] (22)

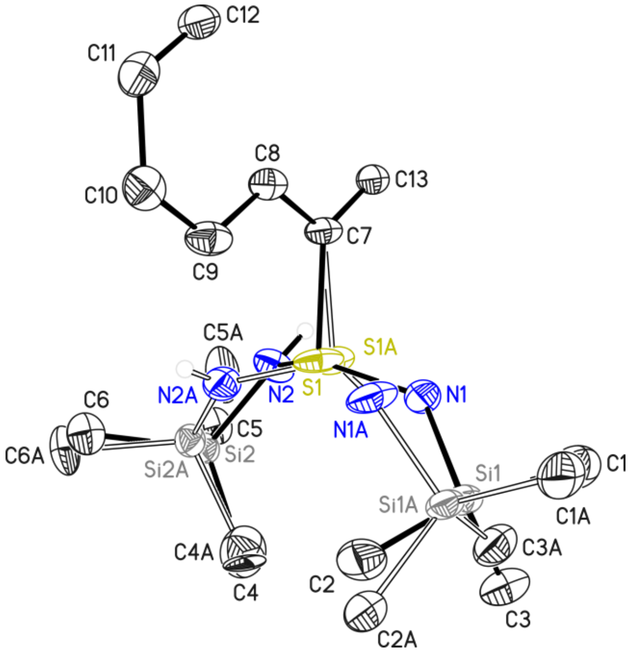

Figure 6.24. The asymmetric unit of **22** with thermal ellipsoids at 50% probability level. The hydrogen atoms are omitted for clarity. The sulfiniminamine unit was disordered over two positions and restraints on the anisotropic displacement parameters and on distances and angle distances were applied. The occupancies of the minor positions refined to 0.439(3), respectively.

Table 6.23. Crystallographic data for **22**.

Compound	22_DL_HAn		*Z*	2
CCDC no.	-		ρ_{calc} [Mg m^{-3}]	1.189
Empirical formula	$C_{26}H_{46}N_4S_2Si_4$		μ [mm^{-1}]	0.328
Formula weight [g mol^{-1}]	591.15		*F*(000)	636
Temperature [K]	100(2)		Crystal size [mm]	0.427 x 0.108 x 0.101
Wavelength [Å]	0.71073		θ range [°]	1.405 to 26.164
Crystal system	Monoclinic		Reflections collected	46887
Space group	$P2_1/c$		Unique reflections	3300
Unit cell parameters	*a* [Å]	6.216(2)	R_{int}	0.0517
	b [Å]	28.980(4)	Restraints / parameters	504 / 238
	c [Å]	9.172(2)	Goodness-of-fit on F^2	1.152
	α [°]	90	R_1 [I>2σ(I)]	0.0385
	β [°]	91.27(2)	$R_{2,w}$ (all data)	0.0844
	γ [°]	90	$\Delta\varrho_{\text{max}}/\Delta\varrho_{\text{min}}$ [e Å^{-3}]	0.273 / −0.186
Volume [Å^3]	1651.8(11)		Color and shape	Yellow needles

6.5.24. Crystal structure of [*t*BuS(NSiMe$_3$)(NHSiMe$_3$)] (23)

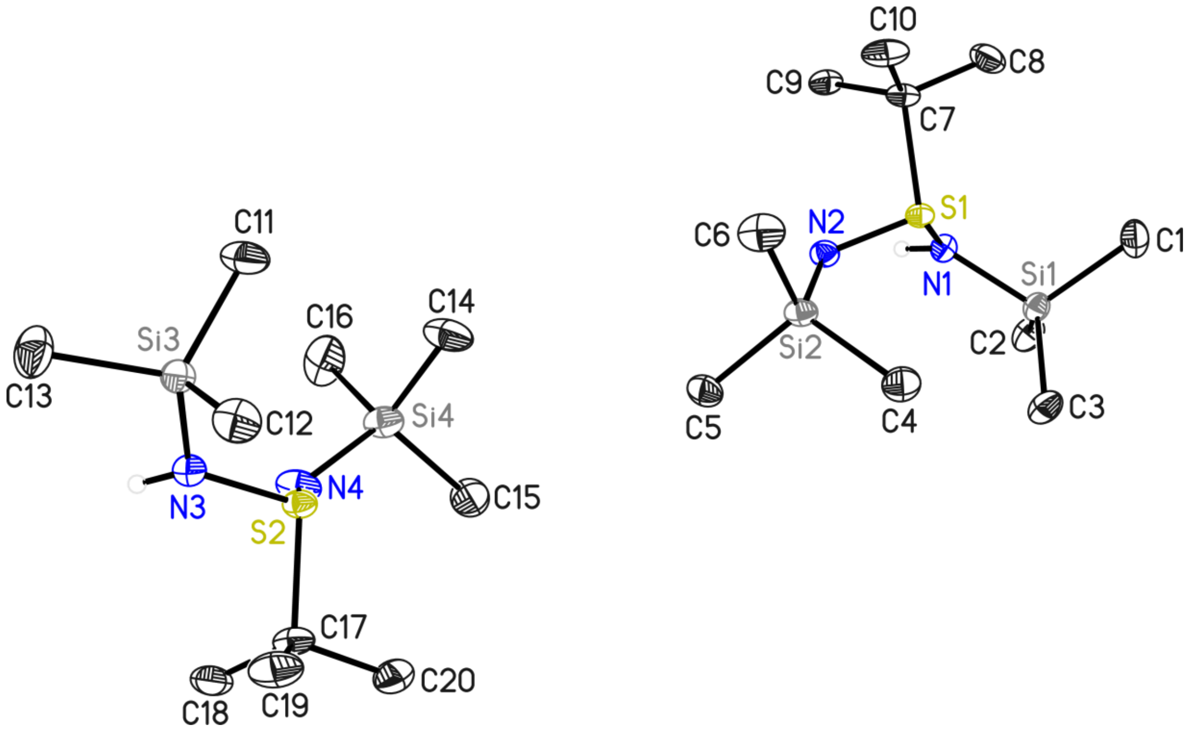

Figure 6.25. Asymmetric unit of **23** with thermal ellipsoids at 50% probability level. The hydrogen atoms are omitted for clarity.

Table 6.24. Crystallographic data for **23**.

Compound	23_DL_HtBuSN		Z	4
CCDC no.	-		ρ_{calc} [Mg m^{-3}]	1.084
Empirical formula	$C_{10}H_{28}N_2SSi_2$		μ [mm^{-1}]	0.326
Formula weight [g mol^{-1}]	264.58		F(000)	584
Temperature [K]	100(2)		Crystal size [mm]	0.297 x 0.275 x 0.222
Wavelength [Å]	0.71073		θ range [°]	1.132 to 26.408
Crystal system	Triclinic		Reflections collected	55471
Space group	$P\bar{1}$		Unique reflections	6635
Unit cell parameters	a [Å]	8.931(2)	R_{int}	0.0278
	b [Å]	10.327(2)	Restraints / parameters	0 / 297
	c [Å]	18.074(3)	Goodness-of-fit on F^2	1.152
	α [°]	95.04	R_1 [$I>2\sigma(I)$]	0.0299
	β [°]	91.54(2)	$R_{2,w}$ (all data)	0.0788
	γ [°]	102.12(3)	$\Delta\varrho_{max}/\Delta\varrho_{min}$ [e Å^{-3}]	0.710 / −0.557
Volume [Å^3]	1621.8(6)		Color and shape	Colorless blocks

6.5.25. Crystal structure of $[An_{0.5}\{S(SiMe_3N)_2(thf)_2Na_2(NSiMe_3)_2S\}An_{0.5}]_n$ (24)

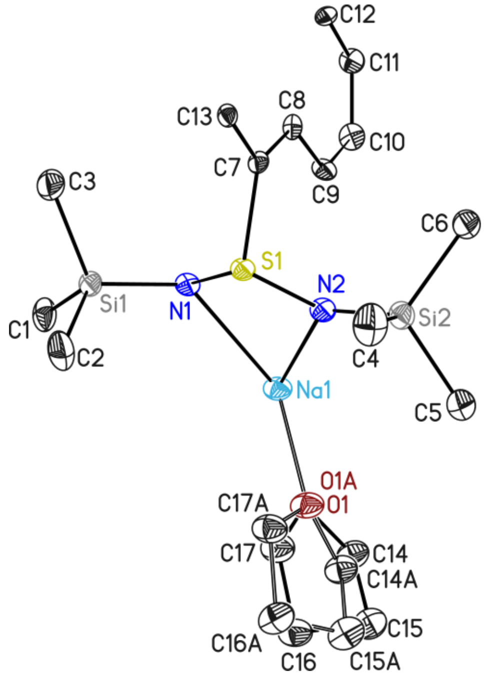

Figure 6.26. The asymmetric unit of **24** with thermal ellipsoids at 50% probability level. The hydrogen atoms are omitted for clarity. The thf unit was disordered over two positions and restraints on the anisotropic displacement parameters and on distances and angle distances were applied. The occupancies of the minor positions refined to 0.49(2), respectively.

Table 6.25. Crystallographic data for **24**.

Compound	24_DL_NaAn		*Z*	4
CCDC no.	-		ρ_{calc} [Mg m^{-3}]	1.203
Empirical formula	$C_{17}H_{30}N_2SNaOSSi_2$		μ [mm^{-1}]	0.289
Formula weight [g mol^{-1}]	389.66		*F*(000)	836
Temperature [K]	100(2)		Crystal size [mm]	0.142 x 0.137 x 0.094
Wavelength [Å]	0.71073		θ range [°]	1.979 to 25.109
Crystal system	Monoclinic		Reflections collected	18223
Space group	$P2_1/n$		Unique reflections	3057
Unit cell parameters	*a* [Å]	10.023(2)	R_{int}	0.0962
	b [Å]	13.521(2)	Restraints / parameters	236 / 263
	c [Å]	15.924(33)	Goodness-of-fit on F^2	1.152
	α [°]	90	R_1 [$I>2\sigma(I)$]	0.0478
	β [°]	94.77(2)	$R_{2,w}$ (all data)	0.1009
	γ [°]	90	$\Delta\varrho_{max}/\Delta\varrho_{min}$ [e Å^{-3}]	0.263 / −0.287
Volume [Å^3]	2150.6(7)		Color and shape	Red blocks

6.5.26. Crystal structure of $[(thf)_2K(NSiMe_3)_2S\}An\{S(SiMe_3N)_2K(thf)_2\}]$ (25)

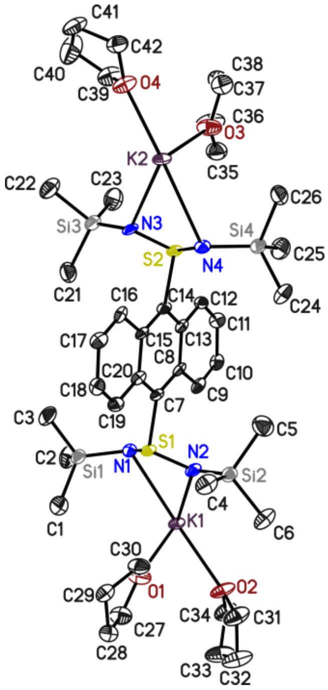

Figure 6.27. The asymmetric unit of **25** with thermal ellipsoids at 50% probability level. The hydrogen atoms are omitted for clarity.

Table 6.26. Crystallographic data for **25**.

Compound	25_DL_KAn		Z	4
CCDC no.	-		ρ_{calc} [Mg m^{-3}]	1.222
Empirical formula	$C_{42}H_{75}K_2N_4O_4S_2Si_4$		μ [mm^{-1}]	0.396
Formula weight [g mol^{-1}]	954.74		F(000)	2052
Temperature [K]	100(2)		Crystal size [mm]	0.257 x 0.180 x 0.077
Wavelength [Å]	0.71073		θ range [°]	1.426 to 26.448
Crystal system	Monoclinic		Reflections collected	55447
Space group	$P2_1/c$		Unique reflections	10629
Unit cell parameters	a [Å]	14.340(2)	R_{int}	0.1154
	b [Å]	19.851(2)	Restraints / parameters	0 / 534
	c [Å]	18.301(2)	Goodness-of-fit on F^2	1.022
	α [°]	90	R_1 [I>2σ(I)]	0.0642
	β [°]	95.12(2)	$R_{2,w}$ (all data)	0.1759
	γ [°]	90	$\Delta\varrho_{max}/\Delta\varrho_{min}$ [e Å^{-3}]	0.775 / −0.602
Volume [Å^3]	5188.8(12)		Color and shape	Red blocks

6.5.27. Crystal structure of [S(*t*BuN)$_3$(thf)$_3$K$_3$(HN*t*Bu)(N*t*Bu)$_2$S}] (26)

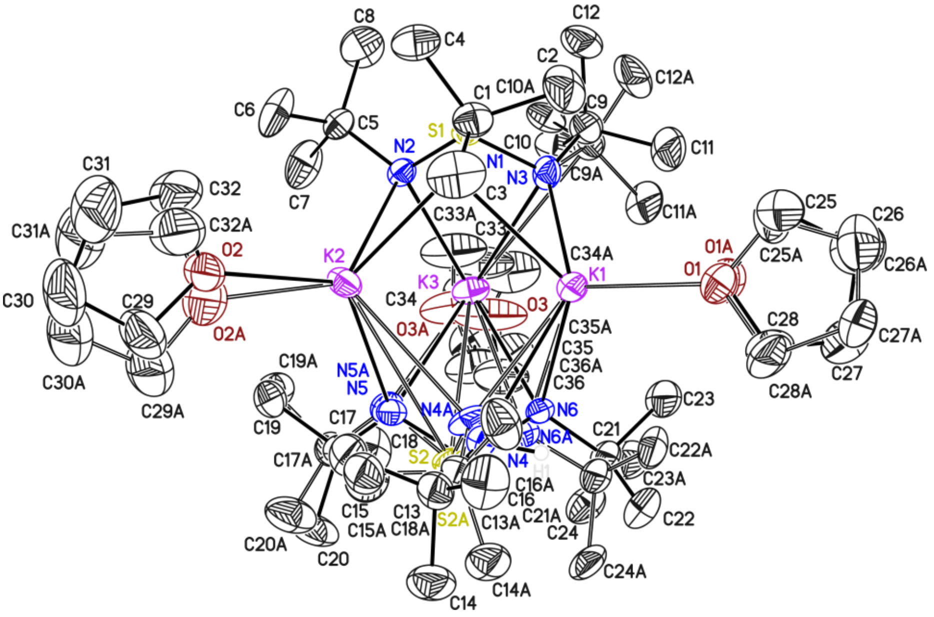

Figure 6.28. The asymmetric unit of **26** with thermal ellipsoids at 50% probability level. The hydrogen atoms are omitted for clarity, except the hydrogen at N5. Treatment of disordered groups was required for each thf, for *tert*-butyl groups and one entire triimidosulfite ligand. These groups were best described with a disorder over two positions. Therefore, restraints were applied on the anisotropic displacement parameters and on distances and angle distances. The occupancies of the major positions refined to 0.745(5), 0.516(14), 0.811(7), 0.788(9), and 0.711(13), respectively.

Table 6.27. Crystallographic data for **26**.

Compound	26_DL_KCage		*Z*	4
CCDC no.	-		ρ_{calc} [Mg m^{-3}]	1.135
Empirical formula	$C_{36}H_{79}K_3N_6O_3S_2$		μ [mm^{-1}]	0.405
Formula weight [g mol^{-1}]	825.47		Absolute structure parameter	0.007(12)
Temperature [K]	100(2)		Crystal size [mm]	0.635 x 0.312 x 0.152
Wavelength [Å]	0.71073		θ range [°]	1.606 to 27.191
Crystal system	Orthorhombic		Reflections collected	50381
Space group	*Pna*2$_1$		Unique reflections	10670
Unit cell parameters	*a* [Å]	15.015(2)	R_{int}	0.0330
	b [Å]	18.154(3)	Restraints / parameters	3835 / 793
	c [Å]	17.724(3)	Goodness-of-fit on F^2	1.027
	α [°]	90	R_1 [I>2σ(I)]	0.0344
	β [°]	90	$R_{2,w}$ (all data)	0.0862
	γ [°]	90	$\Delta\varrho_{max}/\Delta\varrho_{min}$ [e Å^{-3}]	0.347 / −0.178
Volume [Å^3]	4831.2(13)		Color and shape	Colorless blocks

6.5.28. Crystal structure of [S(*t*BuN)$_3$(thf)$_3$K$_3$(HN*t*Bu)(N*t*Bu)$_2$S}] (27)

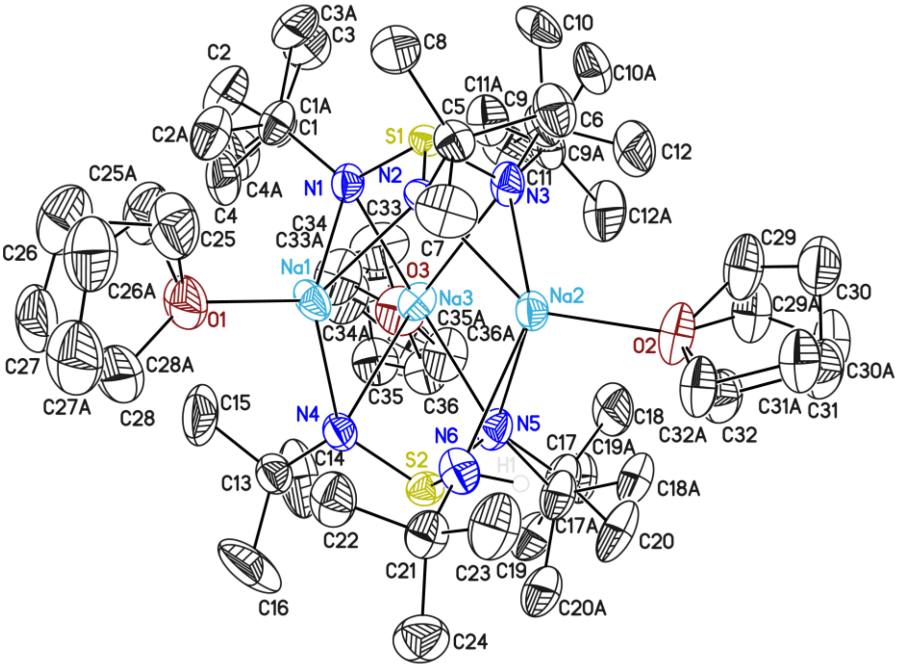

Figure 6.29. The asymmetric unit of **27** with thermal ellipsoids at 50% probability level. The hydrogen atoms are omitted for clarity. The thf- and the *t*Bu-units were disordered about 2 positions and were refined with distance restraints and restraints for the anisotropic displacement parameters. The occupancies of the major position refined to 0.788(9), 0.64(3), 0.620(11), 0.762(10), 0.564(14), and 0.899(7), respectively.

Table 6.28. Crystallographic data for **27**.

Compound	27_DL_NaCage		*Z*	4
CCDC no.	2128426		ρ_{calc} [Mg m^{-3}]	1.133
Empirical formula	$C_{36}H_{79}N_6Na_3O_3S_2$		μ [mm^{-1}]	0.184
Formula weight [g mol^{-1}]	777.14		*F*(000)	1704
Temperature [K]	100(2)		Crystal size [mm]	0.355 x 0.283 x 0.272
Wavelength [Å]	0.71073		θ range [°]	1.657 to 26.715
Crystal system	Orthorhombic		Reflections collected	73524
Space group	*Pna*2$_1$		Unique reflections	8681
Unit cell parameters	*a* [Å]	15.072(2)	R_{int}	0.0414
	b [Å]	17.049(3)	Restraints / parameters	2399 / 684
	c [Å]	17.726(3)	Goodness-of-fit on F^2	1.053
	α [°]	90	R_1 [I>2σ(I)]	0.0454
	β [°]	90	$R_{2,w}$ (all data)	0.1193
	γ [°]	90	$\Delta\varrho_{max}/\Delta\varrho_{min}$ [e Å^{-3}]	0.397 / −0.212
Volume [Å^3]	4554.9(13)		Color and shape	Red blocks

6.5.29. Crystal structure of $[Na(thf)_6][S(Me_3SiN)_3(thf)_3Na_3(NSiMe_3)_3S]$ (28)

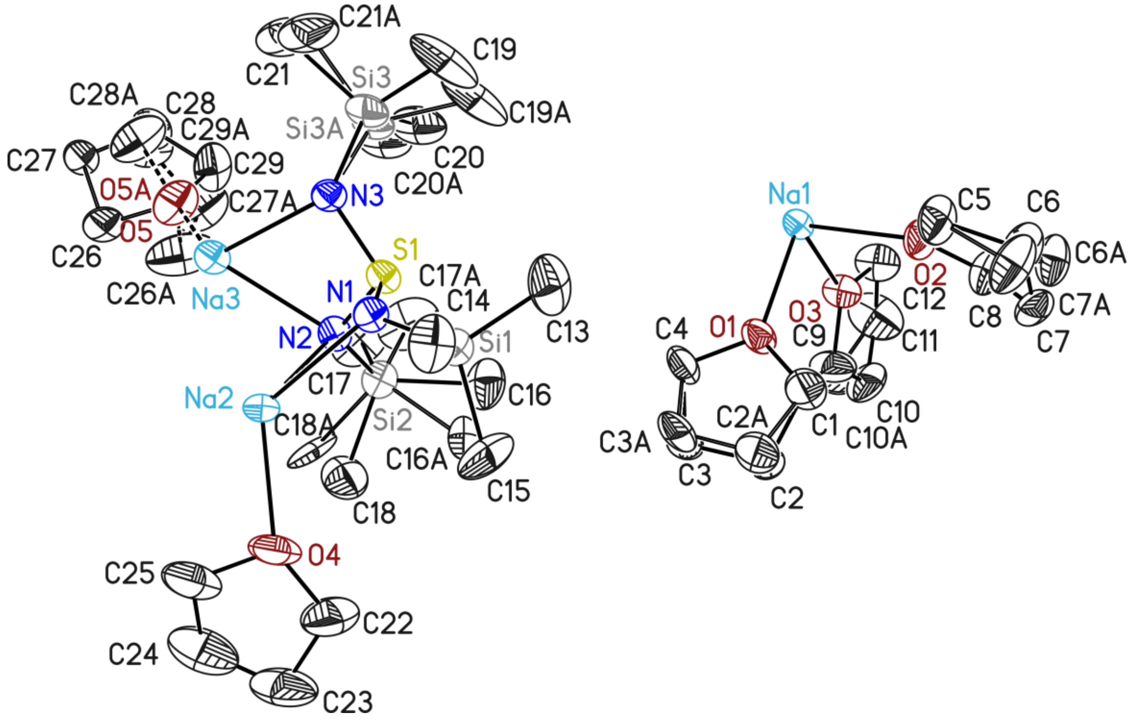

Figure 6.30. The asymmetric unit of **28** with thermal ellipsoids at 50% probability level. The hydrogen atoms are omitted for clarity. The crystals crystallize as three-fold twins simulating rhombohedral symmetry with the twin law 0.5 −0.5 −1 0.5 −0.5 1 −0.5 −0.5 0. The fractional contributions refine to 0.3424(19), 0.3270(17), and 0.3306(19).

Table 6.29. Crystallographic data for **28**.

Compound	28_DL_NatmsCage		*Z*	4
CCDC no.	-		ρ_{calc} [Mg m^{-3}]	1.129
Empirical formula	$C_{54}H_{126}N_6Na_4O_9S_2Si_6$		μ [mm^{-1}]	0.230
Formula weight [g mol^{-1}]	1328.22		*F*(000)	2896
Temperature [K]	100(2)		Crystal size [mm]	0.548 x 0.327 x 0.316
Wavelength [Å]	0.71073		θ range [°]	1.389 to 26.518
Crystal system	Monoclinic		Reflections collected	65351
Space group	*C*2/*c*		Unique reflections	8347
Unit cell parameters	*a* [Å]	29.410(8)	R_{int}	0.0540
	b [Å]	18.118(5)	Restraints / parameters	1986 / 524
	c [Å]	17.268(5)	Goodness-of-fit on F^2	1.024
	α [°]	90	R_1 [I>2σ(I)]	0.0485
	β [°]	121.89(2)	$R_{2,w}$ (all data)	0.1301
	γ [°]	90	$\Delta\varrho_{max}$/$\Delta\varrho_{min}$ [e Å^{-3}]	0.382 / −0.945
Volume [Å^3]	7812(4)		Color and shape	Yellow blocks

6.5.30. Crystal structure of [ClTb{Na(thf)}$_2${(N*t*Bu)$_3$S}$_2$] (29)

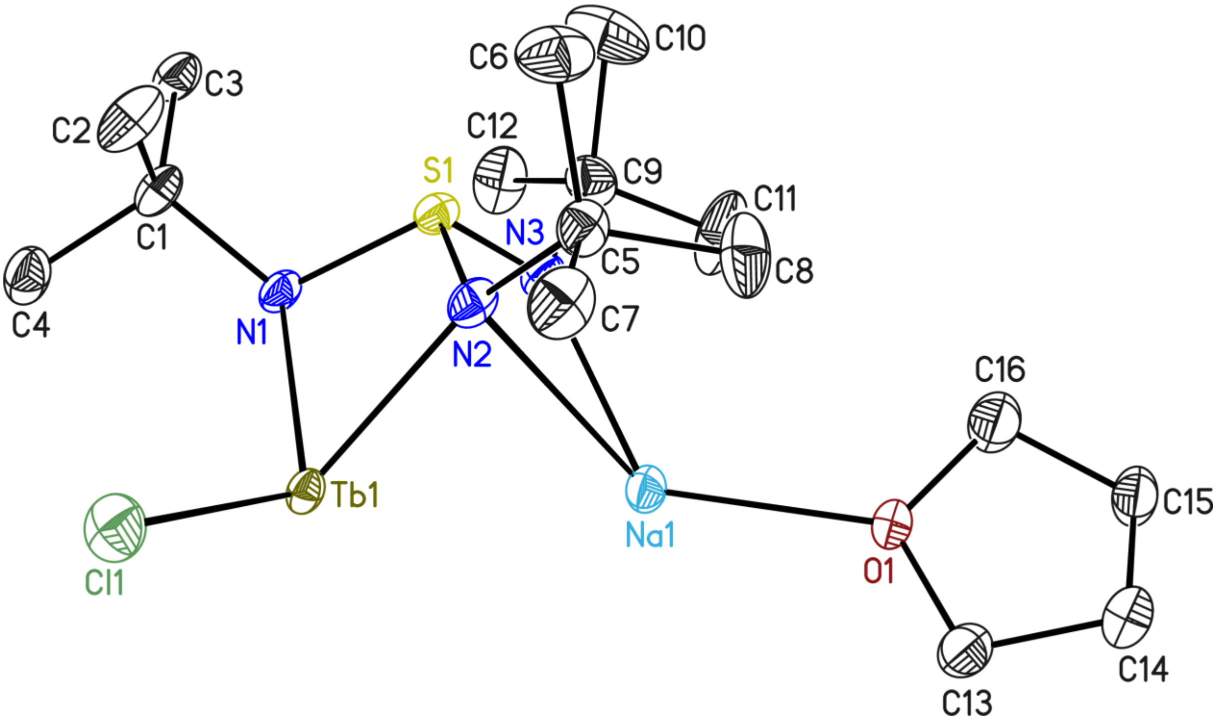

Figure 6.31. The asymmetric unit of **29** with thermal ellipsoids at 50% probability level. The hydrogen atoms are omitted for clarity.

Table 6.30. Crystallographic data for **29**.

Compound	29_DL_TbCage		*Z*	4
CCDC no.	-		ρ_{calc} [Mg m^{-3}]	1.374
Empirical formula	$C_{32}H_{70}ClN_6Na_2O_2S_2Tb$		μ [mm^{-1}]	1.887
Formula weight [g mol^{-1}]	875.41		*F*(000)	1824
Temperature [K]	100(2)		Crystal size [mm]	0.595 x 0.315 x 0.185
Wavelength [Å]	0.71073		θ range [°]	2.042 to 26.741
Crystal system	Monoclinic		Reflections collected	35256
Space group	*C*2/*c*		Unique reflections	4496
Unit cell parameters	*a* [Å]	11.880(2)	R_{int}	0.0316
	b [Å]	18.362(3)	Restraints / parameters	0 / 218
	c [Å]	19.401(3)	Goodness-of-fit on F^2	1.053
	α [°]	90	R_1 [I>2σ(I)]	0.0295
	β [°]	90.29(2)	$R_{2,w}$ (all data)	0.0721
	γ [°]	90	$\Delta\varrho_{max}/\Delta\varrho_{min}$ [e Å^{-3}]	2.331 / −1.737
Volume [Å^3]	4232.1(12)		Color and shape	Colorless blocks

6.5.31. Crystal structure of $[\{Na(thf)_2\{S(\textit{t}BuN)_3\}_2TbSTb\{(N\textit{t}Bu)_3S\}_2\{Na(thf)\}_2]$ (30)

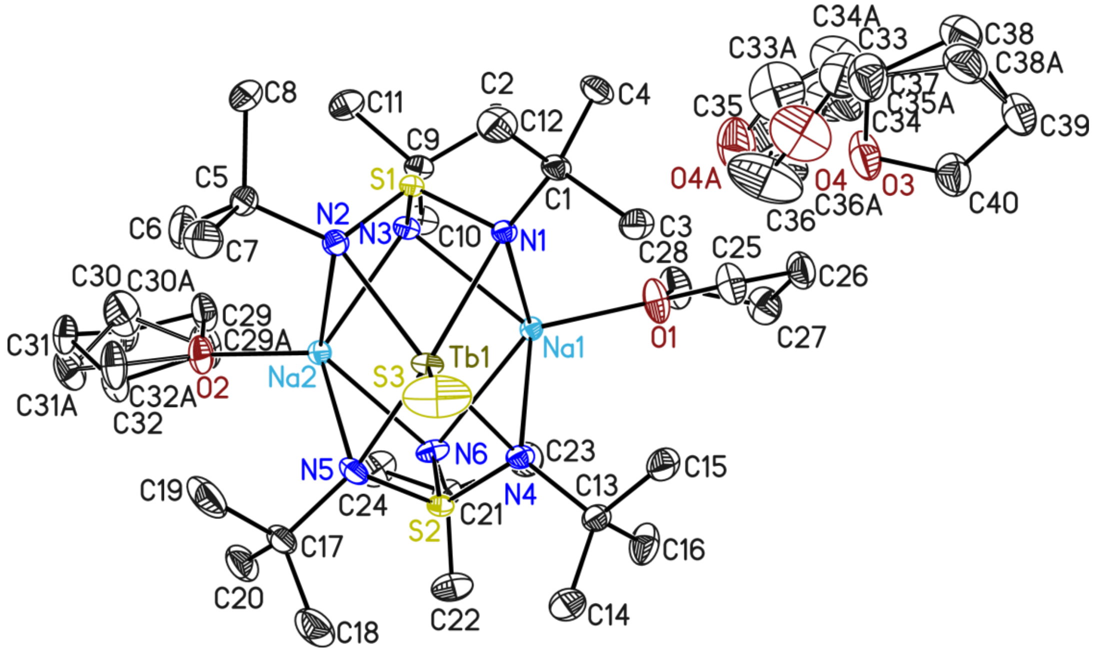

Figure 6.32. The asymmetric unit of **30** with thermal ellipsoids at 50% probability level. The hydrogen atoms are omitted for clarity. Treatment of disordered groups was required for two thf moieties and best describes with a disorder over two positions. Therefore, Restraints on the anisotropic displacement parameters and on distances and angle distances were applied. The occupancies of the major positions refine to 0.721 (10), 0.901 (8), and 0.684(9).

Table 6.31. Crystallographic data for **30**.

Compound	30_DL_TbSTbCage		*Z*	1
CCDC no.	-		ρ_{calc} [Mg m^{-3}]	1.325
Empirical formula	$C_{80}H_{172}N_{12}Na_4O_8S_5Tb_2$		μ [mm^{-1}]	0.842
Formula weight [g mol^{-1}]	2000.39		*F*(000)	1054
Temperature [K]	100(2)		Crystal size [mm]	0.370 x 0.364 x 0.222
Wavelength [Å]	0.56086		θ range [°]	1.496 to 21.957
Crystal system	Triclinic		Reflections collected	175798
Space group	$P\bar{1}$		Unique reflections	12418
Unit cell parameters	*a* [Å]	11.107(2)	R_{int}	0.0335
	b [Å]	13.723(2)	Restraints / parameters	816 / 614
	c [Å]	17.446(3)	Goodness-of-fit on F^2	1.186
	α [°]	102.80(3)	R_1 [$I>2\sigma(I)$]	0.0199
	β [°]	101.03(2)	$R_{2,w}$ (all data)	0.0488
	γ [°]	97.06(2)	$\Delta\rho_{\text{max}}/\Delta\rho_{\text{min}}$ [e Å^{-3}]	0.768 / −0.614
Volume [Å^3]	2506.9(8)		Color and shape	Red blocks

6.5.32. Crystal structure of [(*t*BuNH)}Tb{(N*t*Bu)$_3$S}]$_2$ (31)

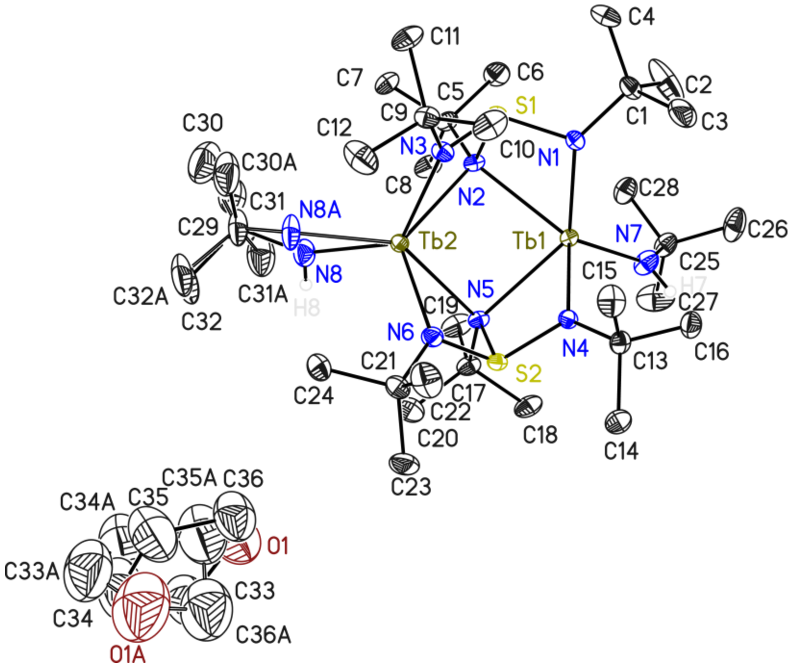

Figure 6.33. The asymmetric unit of **31** with thermal ellipsoids at 50% probability level. The hydrogen atoms are omitted for clarity. Treatment of disordered groups was required for two tBu-groups and the lattice thf moiety, which are best described with a disorder over two positions. Therefore, restraints on the anisotropic displacement parameters and on distances and angle distances were applied. The occupancies of the major positions refine to 0.729(4) and 0.911(3).

Table 6.32. Crystallographic data for **31**.

Compound	31_DL_Tb2Cage		Z	2
CCDC no.	-		ρ_{calc} [Mg m^{-3}]	1.440
Empirical formula	$C_{36}H_{82}N_8OS_2Tb_2$		μ [mm^{-1}]	1.650
Formula weight [g mol^{-1}]	1025.05		$F(000)$	1048
Temperature [K]	100(2)		Crystal size [mm]	0.414 x 0.336 x 0.248
Wavelength [Å]	0.56086		θ range [°]	1.589 to 24.285
Crystal system	Triclinic		Reflections collected	141350
Space group	$P\bar{1}$		Unique reflections	15019
Unit cell parameters	a [Å]	10.122(2)	R_{int}	0.0264
	b [Å]	11.178(2)	Restraints / parameters	440 / 557
	c [Å]	23.274(3)	Goodness-of-fit on F^2	1.158
	α [°]	98.19(2)	R_1 [I>2σ(I)]	0.0195
	β [°]	96.84(2)	$R_{2,w}$ (all data)	0.0426
	γ [°]	112.47(3)	$\Delta\varrho_{\text{max}}/\Delta\varrho_{\text{min}}$ [e Å^{-3}]	1.327 / −1.454
Volume [Å^3]	2364.8(9)		Color and shape	Colorless blocks

6.5.33. Crystal structure of [S(*t*BuN)$_3$}TbSTb{(N*t*Bu)$_3$S}]$_2$ (32)

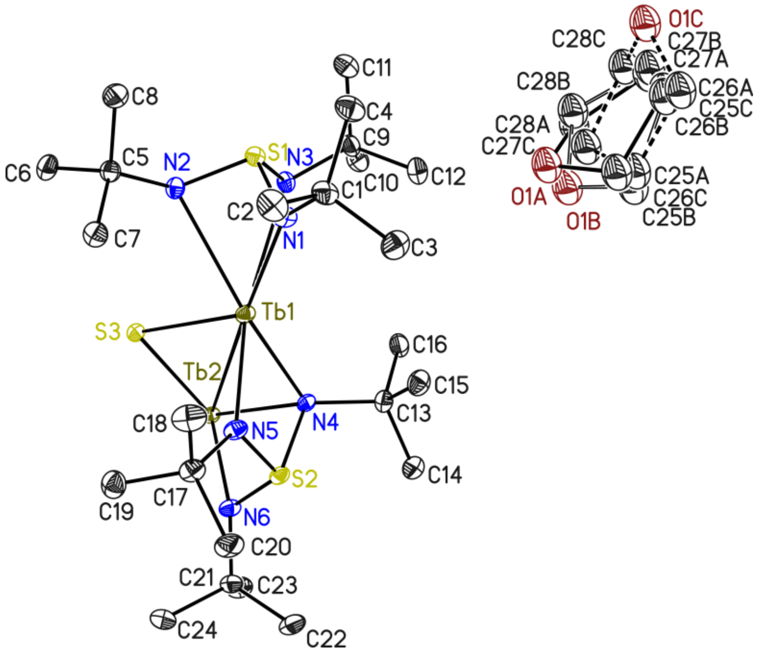

Figure 6.34. The asymmetric unit of **32** with thermal ellipsoids at 50% probability level. The hydrogen atoms are omitted for clarity. In the crystal lattice, a thf moiety was found and is best described with a disorder over three positions and restraints on the anisotropic displacement parameters and on distances, and angle distances were applied. The occupancies refine to 0.464(3), 0.371(3), and 0.165(2).

Table 6.33. Crystallographic data for **32**.

Compound	32_DL_Tb4Cage		*Z*	1
CCDC no.	-		ρ_{calc} [Mg m^{-3}]	1.669
Empirical formula	$C_{56}H_{124}N_{12}O_2S_6Tb_4$		μ [mm^{-1}]	4.063
Formula weight [g mol^{-1}]	1825.70		*F*(000)	916
Temperature [K]	100(2)		Crystal size [mm]	0.232 x 0.124 x 0.043
Wavelength [Å]	0.71073		θ range [°]	1.764 to 26.925
Crystal system	Triclinic		Reflections collected	52840
Space group	$P\bar{1}$		Unique reflections	7813
Unit cell parameters	*a* [Å]	12.401(2)	R_{int}	0.0474
	b [Å]	13.668(3)	Restraints / parameters	523 / 442
	c [Å]	13.808(3)	Goodness-of-fit on F^2	1.046
	α [°]	119.13(3)	R_1 [I>2σ(I)]	0.0193
	β [°]	112.75(2)	$R_{2,w}$ (all data)	0.0506
	γ [°]	91.56(2)	$\Delta\varrho_{\max}/\Delta\varrho_{\min}$ [e Å^{-3}]	1.014 / −0.776
Volume [Å^3]	1816.6(8)		Color and shape	Colorless blocks

6.5.34. Crystal structure of [{S(tBuN)$_2$(tBuNH)}$_2$K$_3$(tmeda)K$_3${(HNtBu)(NtBu)$_2$S}$_2$] (33)

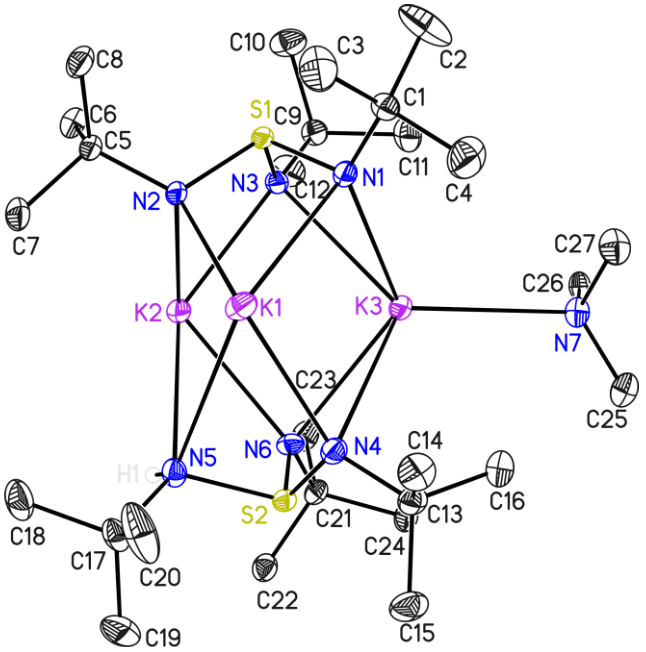

Figure 6.35. The asymmetric unit of **33** with thermal ellipsoids at 50% probability level. The hydrogen atoms are omitted for clarity, except the hydrogen at N5. Half a molecule of the bridging tetramethylethylenediamine moiety at K3 is located in the asymmetric unit and connects two complex molecules. No disorder treatment is required, and the hydrogen associated with N5 is refined freely with thermal ellipsoids at 50% probability level. The hydrogen atoms are omitted for clarity.

Table 6.34. Crystallographic data for **33**.

Compound	33_DL_KtmedaC		Z	2
CCDC no.	2128424		ρ_{calc} [Mg m^{-3}]	1.165
Empirical formula	$C_{54}H_{126}K_6N_{14}S_4$		μ [mm^{-1}]	0.258
Formula weight [g mol^{-1}]	1334.52		F(000)	1452
Temperature [K]	100(2)		Crystal size [mm]	0.377 x 0.281 x 0.190
Wavelength [Å]	0.56086		θ range [°]	1.467 to 20.256
Crystal system	Monoclinic		Reflections collected	141047
Space group	$P2_1/c$		Unique reflections	7484
Unit cell parameters	a [Å]	15.380(2)	R_{int}	0.0722
	b [Å]	13.885(2)	Restraints / parameters	0 / 376
	c [Å]	17.912(3)	Goodness-of-fit on F^2	1.046
	α [°]	90	R_1 [I>2σ(I)]	0.0296
	β [°]	95.74(2)	$R_{2,w}$ (all data)	0.0722
	γ [°]	90	$\Delta\varrho_{\max}/\Delta\varrho_{\min}$ [e Å^{-3}]	0.306 / -0.353
Volume [Å^3]	3806.0(10)		Color and shape	Red blocks

6.5.35. Crystal structure of [{(tmeda)$_3$S{Na$_3$(N*t*Bu)$_3$S}$_2$] (34)

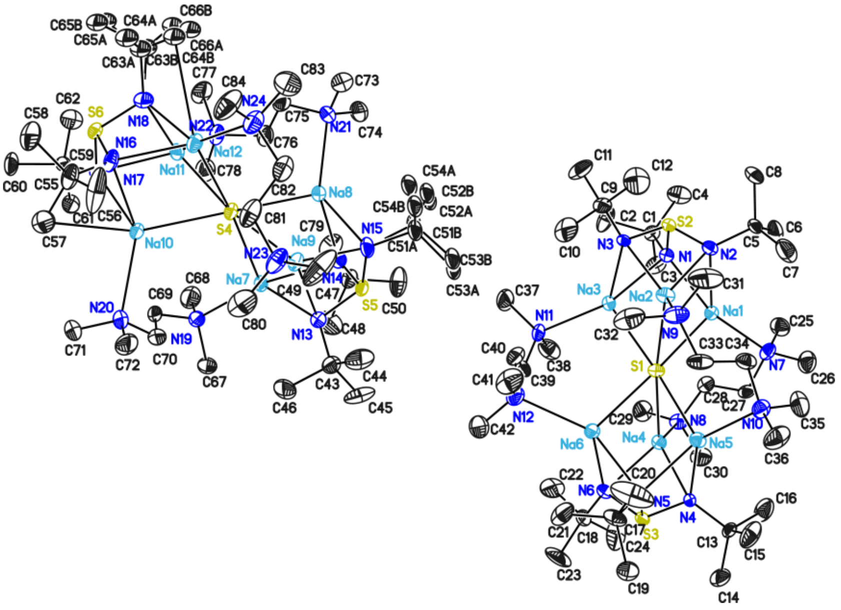

Figure 6.36. The asymmetric unit of **34** with thermal ellipsoids at 50% probability level. The hydrogen atoms are omitted for clarity. The two *tert*-butyl groups were disordered about 2 positions and refined with distance restraints and restraints for the anisotropic displacement parameters. The occupancies of the minor positions refined to 0.389(8), and 0.147(4), respectively. The measured crystal was pseudo-merohedrally twinned with the twin law −1 0 0 0−1 0 0 0 1, with the fractional contribution refined to 0.4166(10).

Table 6.35. Crystallographic data for **34**.

Compound	34_DL_Na6tmedaC		*Z*	8
CCDC no.	2128427		ρ_{calc} [Mg m^{-3}]	1.034
Empirical formula	$C_{42}H_{102}N_{12}Na_6S_3$		μ [mm^{-1}]	0.190
Formula weight [g mol^{-1}]	1009.47		*F*(000)	4416
Temperature [K]	100(2)		Crystal size [mm]	0.254 x 0.212 x 0.145
Wavelength [Å]	0.71073		θ range [°]	1.024 to 25.693
Crystal system	Monoclinic		Reflections collected	126730
Space group	$P2_1/c$		Unique reflections	24641
Unit cell parameters	*a* [Å]	19.880(3)	R_{int}	0.0655
	b [Å]	17.651(2)	Restraints / parameters	729 / 1255
	c [Å]	36.973(3)	Goodness-of-fit on F^2	1.009
	α [°]	90	R_1 [I>2σ(I)]	0.0456
	β [°]	90.00(2)	$R_{2,w}$ (all data)	0.0938
	γ [°]	90	$\Delta\varrho_{\max}/\Delta\varrho_{\min}$ [e Å^{-3}]	0.328 / −0.304
Volume [Å^3]	12974(3)		Color and shape	Colorless blocks

6.5.36. Crystal structure of [{S(*t*BuN)$_3$(thf)$_3$Na$_3$SNa$_3$(thf)$_3$(N*t*Bu)$_3$S] (35)

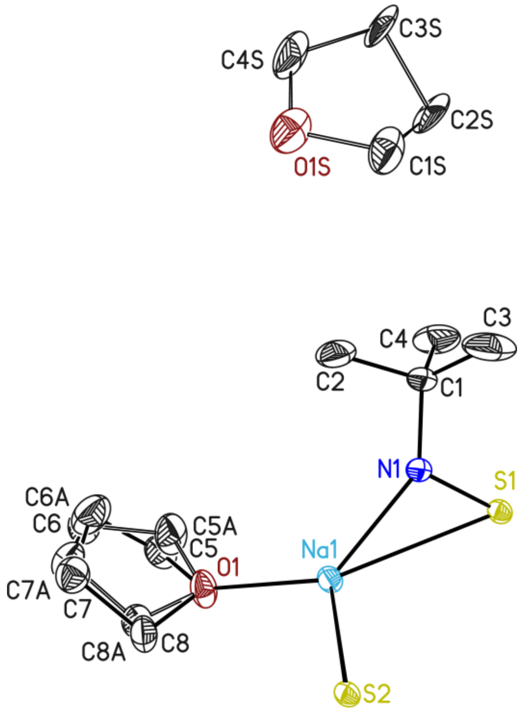

Figure 6.37. The asymmetric unit of **35** with thermal ellipsoids at 50% probability level. The hydrogen atoms are omitted for clarity. The thf unit was disordered about 2 positions and refined with distance restraints and restraints for the anisotropic displacement parameters. The occupancies of the major position refined to 0.64(2) respectively.

Table 6.36. Crystallographic data for **35**.

Compound	35_DL_Na6Cage		*Z*	4
CCDC no.	2128425		ρ_{calc} [Mg m^{-3}]	1.144
Empirical formula	$C_{52}H_{110}N_6Na_6O_7S_3$		μ [mm^{-1}]	0.107
Formula weight [g mol^{-1}]	1165.57		*F*(000)	2536
Temperature [K]	100(2)		Crystal size [mm]	0.407 x 0.400 x 0.305
Wavelength [Å]	0.56086		θ range [°]	1.699 to 19.994
Crystal system	Cubic		Reflections collected	32527
Space group	$Pa\bar{3}$		Unique reflections	2148
Unit cell parameters	*a* [Å]	18.917(2)	R_{int}	0.0722
	b [Å]	18.917(2)	Restraints / parameters	306 / 190
	c [Å]	18.917(2)	Goodness-of-fit on F^2	1.062
	α [°]	90	R_1 [I>2σ(I)]	0.0370
	β [°]	90	$R_{2,w}$ (all data)	0.0942
	γ [°]	90	$\Delta\varrho_{\max}/\Delta\varrho_{\min}$ [e Å^{-3}]	0.250 / -0.225
Volume [Å^3]	6770(2)		Color and shape	Colorless blocks

6.5.37. Crystal structure of $[(t\text{BuNH})\}\text{Dy}\{\text{K}(0.5\text{tmeda})\}_2\{\text{N}t\text{Bu})_3\text{S}\}_2]_n$ (36)

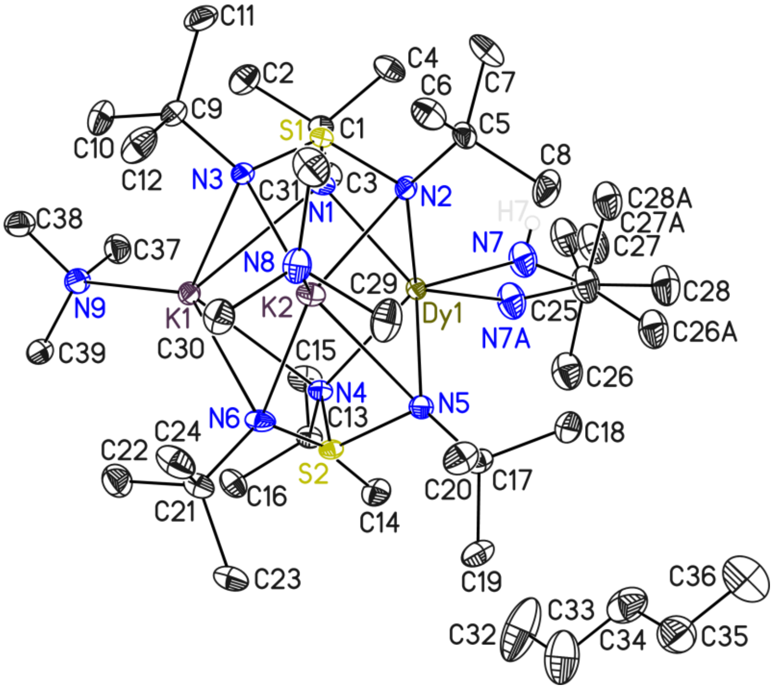

Figure 6.38. The asymmetric unit of **36** with thermal ellipsoids at 50% probability level. The hydrogen atoms are omitted for clarity.

Table 6.37. Crystallographic data for **36**.

Compound	36_DL_DyKCage		*Z*	1
CCDC no.	2128428		ρ_{calc} [Mg m^{-3}]	1.287
Empirical formula	$C_{78}H_{184}Dy_2K_4N_{18}S_4$		μ [mm^{-1}]	0.930
Formula weight [g mol^{-1}]	1984.06		*F*(000)	1050
Temperature [K]	100(2)		Crystal size [mm]	0.241 x 0.231 x 0.184
Wavelength [Å]	0.56086		θ range [°]	1.464 to 21.787
Crystal system	Triclinic		Reflections collected	150125
Space group	$P\bar{1}$		Unique reflections	12369
Unit cell parameters	*a* [Å]	11.149(2)	R_{int}	0.0406
	b [Å]	12.947(2)	Restraints / parameters	250 / 558
	c [Å]	18.319(3)	Goodness-of-fit on F^2	1.072
	α [°]	82.43(2)	R_1 [$I>2\sigma(I)$]	0.0227
	β [°]	79.11(2)	$R_{2,w}$ (all data)	0.0524
	γ [°]	82.64(3)	$\Delta\varrho_{\max}/\Delta\varrho_{\min}$ [e Å^{-3}]	2.483 / -1.160
Volume [Å^3]	2559.5(8)		Color and shape	Colorless blocks

6.5.38. Crystal structure of $[Na_2\{S(\textit{t}BuN)_3\}_2DySDy\{(N\textit{t}Bu)_3S\}_2Na_2]$ (37)

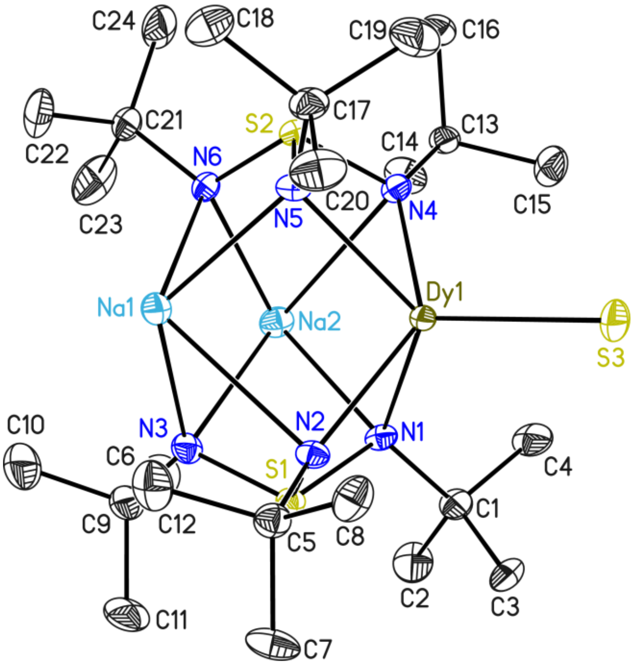

Figure 6.39. The asymmetric unit of **37** with thermal ellipsoids at 50% probability level. The hydrogen atoms are omitted for clarity. Half a complex molecule is displayed in the asymmetric unit.

Table 6.38. Crystallographic data for **37**.

Compound	37_DL_Dy2Cage		Z	2
CCDC no.	-		ρ_{calc} [Mg m^{-3}]	1.400
Empirical formula	$C_{48}H_{108}Dy_2N_{12}Na_4S_5$		μ [mm^{-1}]	2.404
Formula weight [g mol^{-1}]	1430.72		F(000)	1472
Temperature [K]	100(2)		Crystal size [mm]	0.135 x 0.115 x 0.090
Wavelength [Å]	0.71073		θ range [°]	1.655 to 26.787
Crystal system	Monoclinic		Reflections collected	48134
Space group	$P2_1/n$		Unique reflections	7226
Unit cell parameters	a [Å]	11.141(4)	R_{int}	0.0581
	b [Å]	16.543(6)	Restraints / parameters	0 / 340
	c [Å]	18.920(7)	Goodness-of-fit on F^2	1.0445
	α [°]	90	R_1 [$I>2\sigma(I)$]	0.0266
	β [°]	103.32(3)	$R_{2,w}$ (all data)	0.0572
	γ [°]	90	$\Delta\varrho_{max}/\Delta\varrho_{min}$ [e Å^{-3}]	0.618 / −0.513
Volume [Å^3]	3393(2)		Color and shape	Colorless blocks

6.5.39. Crystal structure of $[\mathrm{ClDy}\{\mathrm{Na(thf)}\}_2\{(\mathrm{N}t\mathrm{Bu})_3\mathrm{S}\}_2]$ (38)

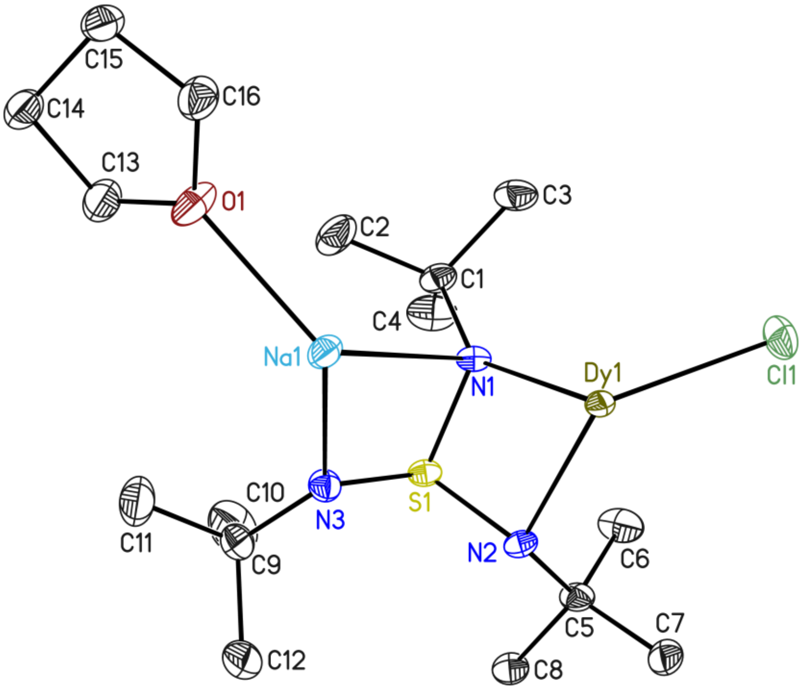

Figure 6.40. The asymmetric unit of **38** with thermal ellipsoids at 50% probability level. The hydrogen atoms are omitted for clarity.

Table 6.39. Crystallographic data for **38**.

Compound	38_DL_DyCage		Z	4
CCDC no.	2128429		ρ_{calc} [Mg m^{-3}]	1.387
Empirical formula	$C_{32}H_{70}ClDyN_6Na_2O_2S_2$		μ [mm^{-1}]	1.992
Formula weight [g mol^{-1}]	878.99		F(000)	1828
Temperature [K]	100(2)		Crystal size [mm]	0.355 x 0.138 x 0.134
Wavelength [Å]	0.71073		θ range [°]	2.459 to 26.796
Crystal system	Monoclinic		Reflections collected	60115
Space group	$C2/c$		Unique reflections	4490
Unit cell parameters	a [Å]	11.858(2)	R_{int}	0.0722
	b [Å]	18.318(2)	Restraints / parameters	0 / 218
	c [Å]	19.385(3)	Goodness-of-fit on F^2	1.087
	α [°]	90	R_1 [$I>2\sigma(I)$]	0.0152
	β [°]	90.26(2)	$R_{2,w}$ (all data)	0.0405
	γ [°]	90	$\Delta\varrho_{\max}/\Delta\varrho_{\min}$ [e Å^{-3}]	0.789 / −0.272
Volume [Å^3]	4210.7(11)		Color and shape	Colorless blocks

6.5.40. Crystal structure of [ClEr{Na(thf)}$_2${(N*t*Bu)$_3$S}$_2$] (39)

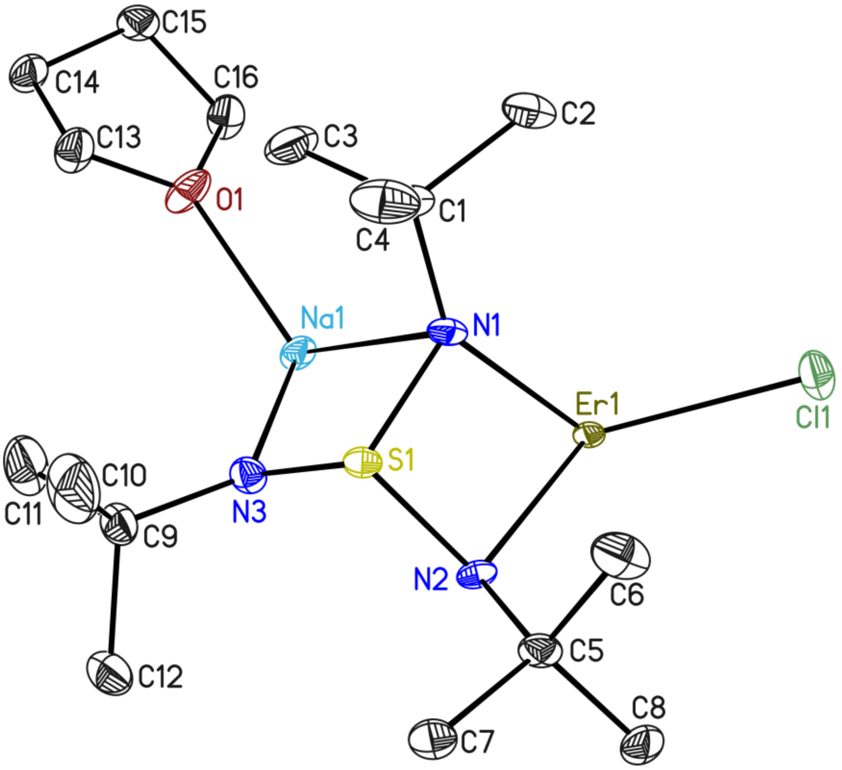

Figure 6.41. The asymmetric unit of **39** with thermal ellipsoids at 50% probability level. The hydrogen atoms are omitted for clarity.

Table 6.40. Crystallographic data for **39**.

Compound	39_DL_ErCage		*Z*	4
CCDC no.	2128430		ρ_{calc} [Mg m^{-3}]	1.404
Empirical formula	$C_{32}H_{70}ClErN_6Na_2O_2S_2$		μ [mm^{-1}]	1.194
Formula weight [g mol^{-1}]	883.75		*F*(000)	1836
Temperature [K]	100(2)		Crystal size [mm]	0.454 x 0.430 x 0.360
Wavelength [Å]	0.56086		θ range [°]	1.658 to 21.932
Crystal system	Monoclinic		Reflections collected	65058
Space group	*C*2/*c*		Unique reflections	5148
Unit cell parameters	*a* [Å]	11.822(2)	R_{int}	0.0370
	b [Å]	18.247(2)	Restraints / parameters	0 / 218
	c [Å]	19.388(3)	Goodness-of-fit on F^2	1.126
	α [°]	90	R_1 [I>2σ(I)]	0.0210
	β [°]	90.41(2)	$R_{2,w}$ (all data)	0.0546
	γ [°]	90	$\Delta\varrho_{\max}/\Delta\varrho_{\min}$ [e Å^{-3}]	1.523 / −1.219
Volume [Å^3]	4182.2(11)		Color and shape	Colorless blocks

6.5.41. Crystal structure of [(*t*BuNH)}Lu{K(0.5tmeda)}$_2${N*t*Bu)$_3$S}$_2$]$_n$ (40)

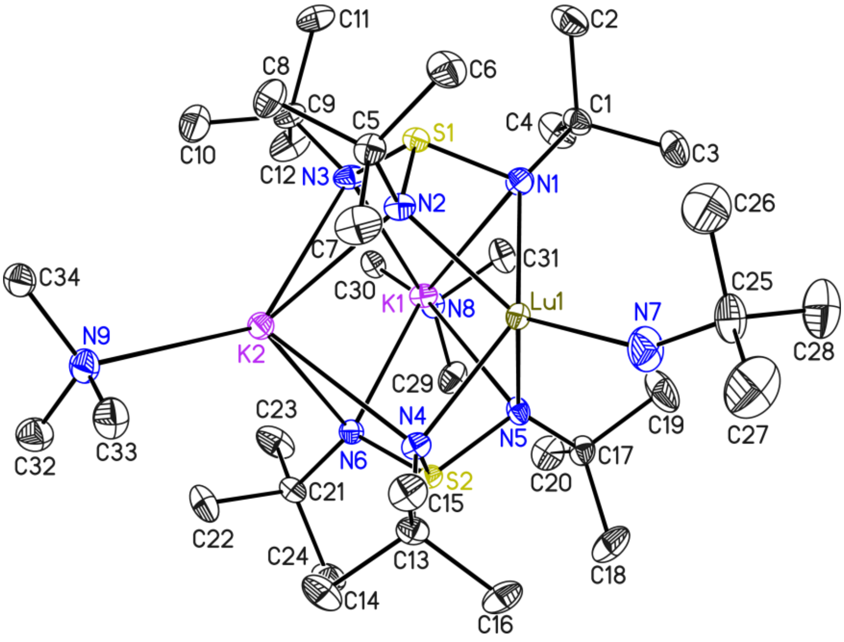

Figure 6.42. The asymmetric unit of **40** with thermal ellipsoids at 50% probability level. The hydrogen atoms are omitted for clarity.

Table 6.41. Crystallographic data for **40**.

Compound	40_DL_LuKCage		*Z*	2
CCDC no.	-		ρ_{calc} [Mg m^{-3}]	1.299
Empirical formula	$C_{39}H_{88}LuK_2N_9S_2$		μ [mm^{-1}]	0.930
Formula weight [g mol^{-1}]	1000.47		*F*(000)	1052
Temperature [K]	100(2)		Crystal size [mm]	0.417 x 0.226 x 0.140
Wavelength [Å]	0.56086		θ range [°]	1.466 to 23.768
Crystal system	Triclinic		Reflections collected	281650
Space group	$P\bar{1}$		Unique reflections	15824
Unit cell parameters	*a* [Å]	11.144(2)	R_{int}	0.0473
	b [Å]	12.933(2)	Restraints / parameters	0 / 502
	c [Å]	18.317(3)	Goodness-of-fit on F^2	1.072
	α [°]	82.58(2)	R_1 [$I>2\sigma(I)$]	0.0279
	β [°]	79.25(2)	$R_{2,w}$ (all data)	0.0718
	γ [°]	82.62(2)	$\Delta\varrho_{\text{max}}/\Delta\varrho_{\text{min}}$ [e Å^{-3}]	5.301 / −1.268
Volume [Å^3]	2557.1(8)		Color and shape	Colorless blocks

6.6. Crystallographic cooperation

Overview of subsequent crystal structures:

SC-XRD data recorded for Marvin Redecker within the group of Prof. Dr. D. Stalke

- Crystal structure of **DL_MR38**
- Crystal structure of **DL_MR23**
- Crystal structure of **DL_MR15**
- Crystal structure of **DL_MR37**
- Crystal structure of **DL_MR16**
- Crystal structure of **DL_MR17**

SC-XRD data recorded for Dr. S. K. Sarkar within the group of Prof. Dr. H. W. Roesky

- Crystal structure of **DL_SK1**

SC-XRD data recorded for Dr. A. Harinath within the group of Prof. H. W. Roesky

- Crystal structure of **DL_AHN1**
- Crystal structure of **DL_AHN2**
- Crystal structure of **DL_AHN3**
- Crystal structure of **DL_AHN4**

Some of the displayed solid-state structures have been published or will soon be submitted in the following articles:

DL_SK1 in:

[6] Y. Ding, S. K. Sarkar, M. Nazish, S. Muhammed, D. Lüert, P. N. Ruth, C. M. Legendre, R. Herbst-Irmer, P. Parameswaran, D. Stalke, Z. Yang, H. W. Roesky. Stabilization of Reactive Nitrene by Silylenes without Using a Reducing Metal. *Angew. Chem. Int. Ed.* **2021**, *60*, 27206-27211.[6]

DL_AHN1-4 in:

[7] M. Nazish, A. Harinath, D. Lüert, C. Köhler, R. Herbst-Irmer, D. Stalke, H. W. Roesky. Reactivity of silylene with gallium- and boron tribromide under reducing conditions resulted in a completely unforeseen product. **2022**, *manuscript in preparation*.[7]

6.6.1. Crystal structure of DL_MR38

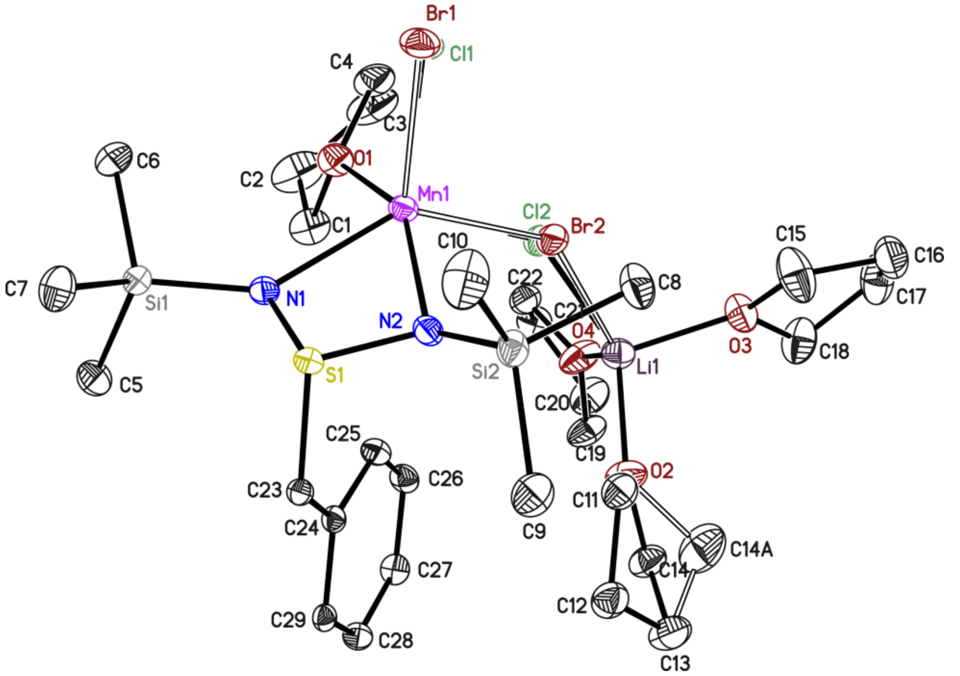

Figure 6.43. The asymmetric unit of **DL_MR38** with thermal ellipsoids at 50% probability level. The hydrogen atoms are omitted for clarity. The Cl1 and Cl2 atoms were disordered about 2 positions with bromide, which was employed in prior reactions. They were refined with distance restraints and restraints for the anisotropic displacement parameters. The occupancies of the minor positions refined to 0.1418(14), and 0.0441(14), respectively.

Table 6.42. Crystallographic data for **DL_MR38**.

Compound	**DL_MR38**		*Z*	1
CCDC no.	-		ρ_{calc} [Mg m^{-3}]	1.301
Empirical formula	$C_{58}H_{108}Br_{0.37}Cl_{3.63}Li_2Mn_2N_4O_8SSi_4$		μ [mm^{-1}]	0.844
Formula weight [g mol^{-1}]	1448.04		*F*(000)	767
Temperature [K]	100(2)		Crystal size [mm]	0.452 x 0.250 x 0.160
Wavelength [Å]	0.71073		θ range [°]	1.136 to 26.737
Crystal system	Triclinic		Reflections collected	107348
Space group	$P\bar{1}$		Unique reflections	7863
Unit cell parameters	*a* [Å]	9.967(2)	R_{int}	0.0244
	b [Å]	11.314(3)	Restraints / parameters	10 / 403
	c [Å]	18.802(3)	Goodness-of-fit on F^2	1.040
	α [°]	74.45(2)	R_1 [$I>2\sigma(I)$]	0.0248
	β [°]	76.34(3)	$R_{2,w}$ (all data)	0.0674
	γ [°]	66.09(2)	$\Delta\varrho_{\max}/\Delta\varrho_{\min}$ [e Å^{-3}]	1.245 / -0.738
Volume [Å^3]	1847.7(7)		Color and shape	Brown blocks

6.6.2. Crystal structure of DL_MR23

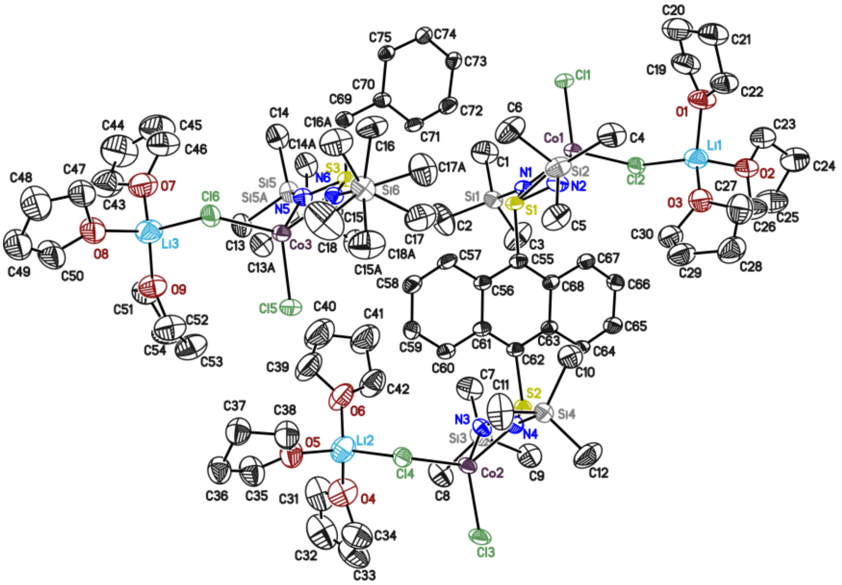

Figure 6.44. The asymmetric unit of **DL_MR23** with thermal ellipsoids at 50% probability level. The hydrogen atoms are omitted for clarity. The trimethylsilyl groups were disordered about 2 positions and refined with distance restraints and restraints for the anisotropic displacement parameters. The occupancies of the major positions refined to 0.643(11) and 0.860(8). The measured crystal was pseudo-merohedral twinned with the twin law −1 0 0 −1 0 0 0 0 1 with the fractional contribution refined to 0.0688(11). Moreover, the reciprocal lattice of both domains differs slightly from each other, however the deviation is too small to determine the second orientation matrix.

Table 6.43. Crystallographic data for **DL_MR23**.

Compound	**DL_MR23**		Z	6
CCDC no.	-		ρ_{calc} [Mg m^{-3}]	1.279
Empirical formula	$C_{50}H_{90}Br_{0.}Cl_4Li_2Co_2N_4O_6S_2Si_4$		μ [mm^{-1}]	0.831
Formula weight [g mol^{-1}]	1292.60		F(000)	4088
Temperature [K]	100(2)		Crystal size [mm]	0.411 x 0.272 x 0.094
Wavelength [Å]	0.71073		θ range [°]	1.128 to 26.349
Crystal system	Monoclinic		Reflections collected	131287
Space group	$P2_1/c$		Unique reflections	18442
Unit cell parameters	a [Å]	14.232(2)	R_{int}	0.0796
	b [Å]	32.698(4)	Restraints / parameters	2616 / 1089
	c [Å]	21.754(3)	Goodness-of-fit on F^2	1.079
	α [°]	90	R_1 [I>2σ(I)]	0.0925
	β [°]	95.96(2)	$R_{2,w}$ (all data)	0.2664
	γ [°]	90	$\Delta\varrho_{\max}/\Delta\varrho_{\min}$ [e Å^{-3}]	1.143 / −0.886
Volume [Å^3]	10069(2)		Color and shape	Green plates

6.6.3. Crystal structure of DL_MR15

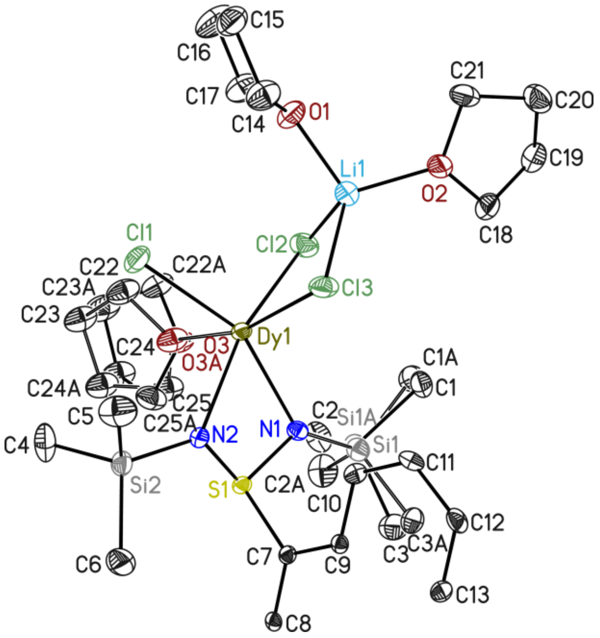

Figure 6.45. The asymmetric unit of **DL_MR15** with thermal ellipsoids at 50% probability level. The hydrogen atoms are omitted for clarity. One thf and trimethylsilyl moiety were disordered about 2 positions They were refined with distance restraints and restraints for the anisotropic displacement parameters. The occupancies of the minor positions refined to 0.65(2), and 0.0093(8), respectively. The measured crystal was non-merohedrally twinned with the twin law −1 0 −0.833   0 −1 0   0 0 1, with the fractional contribution refined to 0.2631(5).

Table 6.44. Crystallographic data for **DL_MR15**.

Compound	**DL_MR15**		*Z*	2
CCDC no.	-		ρ_{calc} [Mg m^{-3}]	1.504
Empirical formula	$C_{50}H_{92}Cl_6Dy_2Li_2N_4O_6S_2Si_4$		μ [mm^{-1}]	2.537
Formula weight [g mol^{-1}]	1573.33		*F*(000)	1592
Temperature [K]	100(2)		Crystal size [mm]	0.256 x 0.118 x 0.086
Wavelength [Å]	0.71073		θ range [°]	1.165 to 26.461
Crystal system	Monoclinic		Reflections collected	7177
Space group	$P2_1/c$		Unique reflections	7177
Unit cell parameters	*a* [Å]	19.244(3)	R_{int}	-
	b [Å]	10.294(3)	Restraints / parameters	485 / 427
	c [Å]	19.311(3)	Goodness-of-fit on F^2	1.040
	α [°]	90	R_1 [$I>2\sigma(I)$]	0.0273
	β [°]	114.72(3)	$R_{2,w}$ (all data)	0.0554
	γ [°]	90	$\Delta\varrho_{\text{max}}/\Delta\varrho_{\text{min}}$ [e Å^{-3}]	0.684 / −0.748
Volume [Å^3]	3474.9(14)		Color and shape	Yellow plates

6.6.4. Crystal structure of DL_MR37

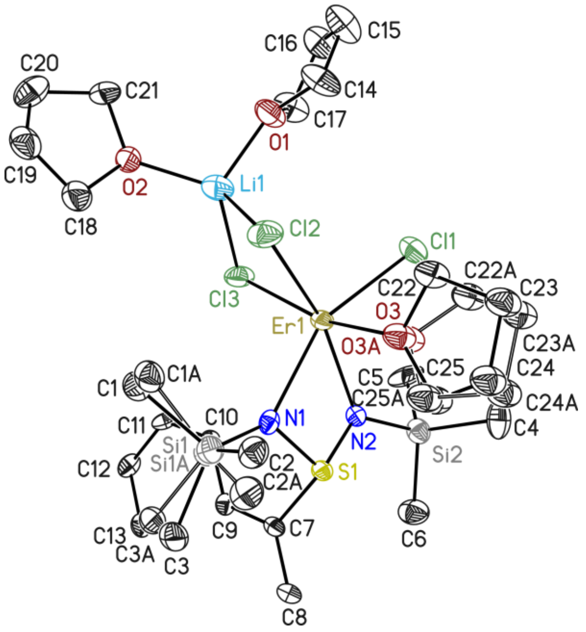

Figure 6.46. The asymmetric unit of **DL_MR37** with thermal ellipsoids at 50% probability level. The hydrogen atoms are omitted for clarity. One thf and trimethylsilyl moiety were disordered about 2 positions and refined with distance restraints and restraints for the anisotropic displacement parameters. The occupancies of the major positions refined to 0.66(2) and 0.871(13). The measured crystal non-merohedrally twinned with the twin law 1 0 0.833   0 −1 0   0 0 −1 was twinned with the fractional contribution refined to 0.3913(8).

Table 6.45. Crystallographic data for **DL_MR37**.

Compound	**DL_MR37**		*Z*	2
CCDC no.	-		ρ_{calc} [Mg m^{-3}]	1.530
Empirical formula	$C_{50}H_{92}Cl_6Er_2Li_2N_4O_6S_2Si_4$		μ [mm^{-1}]	2.834
Formula weight [g mol^{-1}]	1582.85		*F*(000)	1600
Temperature [K]	100(2)		Crystal size [mm]	0.125 x 0.093 x 0.066
Wavelength [Å]	0.71073		θ range [°]	1.172 to 25.435
Crystal system	Monoclinic		Reflections collected	6375
Space group	$P2_1/c$		Unique reflections	6375
Unit cell parameters	*a* [Å]	19.130(3)	R_{int}	-
	b [Å]	10.251(2)	Restraints / parameters	485 / 427
	c [Å]	19.288(3)	Goodness-of-fit on F^2	1.063
	α [°]	90	R_1 [$I>2\sigma(I)$]	0.0492
	β [°]	114.73(2)	$R_{2,w}$ (all data)	0.0896
	γ [°]	90	$\Delta\varrho_{max}/\Delta\varrho_{min}$ [e Å^{-3}]	0.960 / −1.270
Volume [Å^3]	3435.5(11)		Color and shape	Orange plates

6.6.5. Crystal structure of DL_MR16

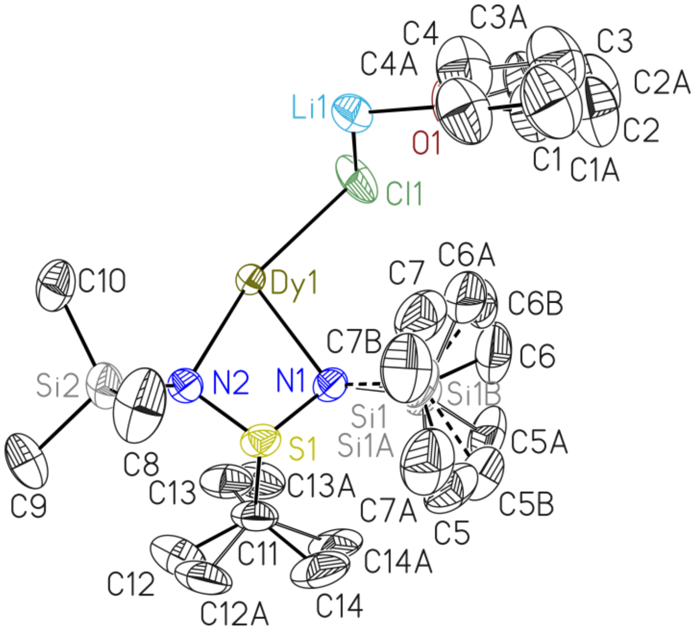

Figure 6.47. The asymmetric unit of **DL_MR16** with thermal ellipsoids at 50% probability level. The hydrogen atoms are omitted for clarity. The *tert*-butyl and thf moieties were disordered about 2 positions, while the trimethylsilyl group was disordered over 3 positions. They were refined with distance restraints and restraints for the anisotropic displacement parameters. The occupancies of the major positions refined to 0.667(3), 0.568(3), 0.765(3), 0.54(2), 0.86(2), 0.768(3), 0.689(3), and 0.920(3)2), respectively.

Table 6.46. Crystallographic data for **DL_MR16**.

Compound	**DL_MR16**		*Z*	4
CCDC no.	-		ρ_{calc} [Mg m^{-3}]	1.078
Empirical formula	$C_{28}H_{70}Cl_2DyLiN_4O_2S_2Si_4$		μ [mm^{-1}]	1.608
Formula weight [g mol^{-1}]	911.70		*F*(000)	1892
Temperature [K]	100(2)		Crystal size [mm]	0.373 x 0.309 x 0.200
Wavelength [Å]	0.71073		θ range [°]	1.366 to 26.823
Crystal system	Monoclinic		Reflections collected	95237
Space group	*C*2/*c*		Unique reflections	6014
Unit cell parameters	*a* [Å]	18.411(3)	R_{int}	0.0368
	b [Å]	25.567(3)	Restraints / parameters	843 / 352
	c [Å]	11.975(2)	Goodness-of-fit on F^2	1.097
	α [°]	90	R_1 [$I>2\sigma(I)$]	0.0206
	β [°]	95.04(2)	$R_{2,w}$ (all data)	0.0533
	γ [°]	90	$\Delta\varrho_{\max}/\Delta\varrho_{\min}$ [e Å^{-3}]	0.706 / −0.383
Volume [Å^3]	5615.0(15)		Color and shape	Yellow plates

6.6.6. Crystal structure of DL_MR17

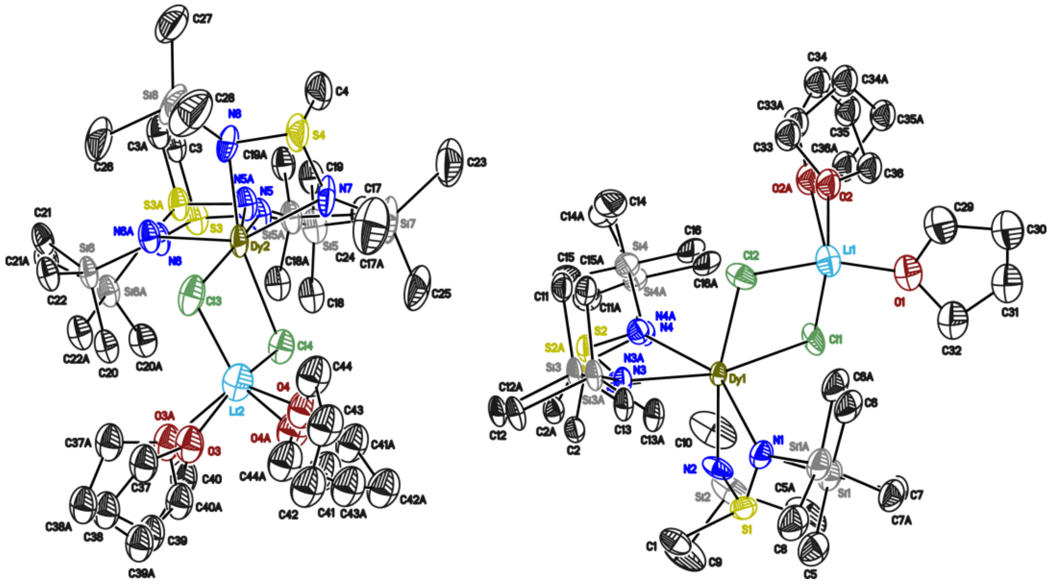

Figure 6.48. The asymmetric unit of **DL_MR17** with thermal ellipsoids at 50% probability level. The hydrogen atoms are omitted for clarity. The thf and trimethylsilyl moieties were disordered about 2 positions. They were refined with distance restraints and restraints for the anisotropic displacement parameters. The occupancies of the major positions refined to 0.523(13), 0.557(10), 0.86(2), 0.582(14), 0.536(7), and 0.518(6), respectively. The measured crystal was pseudo-merohedral twinned with the twin law −1 0 0 0 −1 0 0 0 1 and with the fractional contribution refined to 0.4612(15).

Table 6.47. Crystallographic data for **DL_MR17**.

Compound	**DL_MR17**		*Z*	4
CCDC no.	-		ρ_{calc} [Mg m^{-3}]	1.341
Empirical formula	$C_{22}H_{58}Cl_2DyLiN_4O_2S_2Si_4$		μ [mm^{-1}]	2.195
Formula weight [g mol^{-1}]	827.54		*F*(000)	1700
Temperature [K]	100(2)		Crystal size [mm]	0.285 x 0.149 x 0.134
Wavelength [Å]	0.71073		θ range [°]	1.019 to 27.939
Crystal system	Triclinic		Reflections collected	112018
Space group	$P\bar{1}$		Unique reflections	19092
Unit cell parameters	*a* [Å]	11.657(3)	R_{int}	0.0699
	b [Å]	17.606(4)	Restraints / parameters	5349 / 1078
	c [Å]	19.990(5)	Goodness-of-fit on F^2	1.132
	α [°]	90.09(2)	R_1 [$I>2\sigma(I)$]	0.0753
	β [°]	90.01(2)	$R_{2,w}$ (all data)	0.1486
	γ [°]	92.15(3)	$\Delta\varrho_{\max}/\Delta\varrho_{\min}$ [e Å^{-3}]	2.840 / −4.194
Volume [Å^3]	4100(2)		Color and shape	Colorless blocks

6.6.7. Crystal structure of DL_SK1

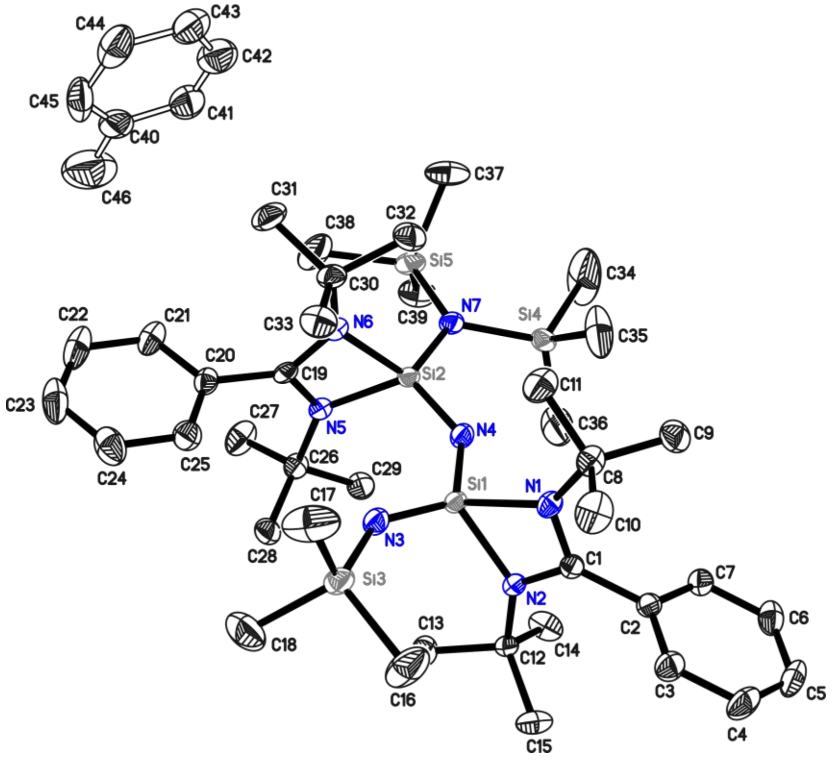

Figure 6.49. The asymmetric unit of **DL_SK1** with thermal ellipsoids at 50% probability level. The hydrogen atoms are omitted for clarity.

Table 6.48. Crystallographic data for **DL_SK1**.

Compound	**DL_SK1**		*Z*	2
CCDC no.	2067321		ρ_{calc} [Mg m^{-3}]	1.097
Empirical formula	$C_{42.5}H_{77}N_7Si_5$		μ [mm^{-1}]	0.178
Formula weight [g mol^{-1}]	826.56		*F*(000)	902
Temperature [K]	100(2)		Crystal size [mm]	0.423 x 0.342 x 0.252
Wavelength [Å]	0.71073		θ range [°]	1.699 to 26.402
Crystal system	Triclinic		Reflections collected	61735
Space group	*P*1		Unique reflections	10267
Unit cell parameters	*a* [Å]	9.957(2)	R_{int}	0.0611
	b [Å]	12.538(2)	Restraints / parameters	122 / 545
	c [Å]	21.328(3)	Goodness-of-fit on F^2	1.050
	α [°]	94.84(2)	R_1 [$I>2\sigma(I)$]	0.0476
	β [°]	100.39(2)	$R_{2,w}$ (all data)	0.1132
	γ [°]	105.63(3)	$\Delta\varrho_{\text{max}}/\Delta\varrho_{\text{min}}$ [eÅ^{-3}]	0.523 / −0.412
Volume [Å^3]	2503.3(8)		Color and shape	Colorless needles

6.6.8. Crystal structure of DL_AHN1

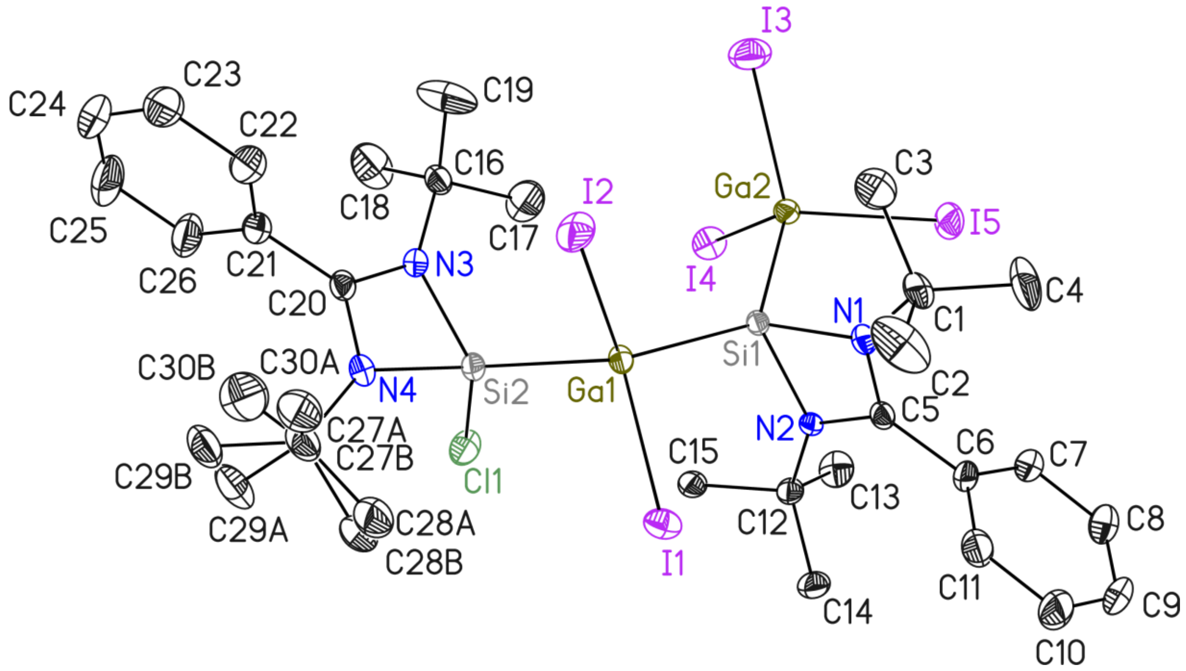

Figure 6.50. The asymmetric unit of **DL_AHN1** with thermal ellipsoids at 50% probability level. The hydrogen atoms are omitted for clarity. The *t*Bu-group at N4 was disordered about 2 positions and refined with distance restraints and restraints for the anisotropic displacement parameters. The occupancy of the major position was refined to 0.788(9), respectively.

Table 6.49. Crystallographic data for **DL_AHN1**.

Compound	**DL_AHN1**		*Z*	2
CCDC no.	-		ρ_{calc} [Mg m^{-3}]	1.942
Empirical formula	$C_{30}H_{46}ClGa_2I_5N_4Si_2$		μ [mm^{-1}]	4.719
Formula weight [g mol−1]	1328.28		*F*(000)	1252
Temperature [K]	100(2)		Crystal size [mm]	0.390 x 0.203 x 0.119
Wavelength [Å]	0.71073		θ range [°]	1.516 to 26.408
Crystal system	Triclinic		Reflections collected	133489
Space group	$P\bar{1}$		Unique reflections	9315
Unit cell parameters	*a* [Å]	12.360(2)	R_{int}	0.0424
	b [Å]	13.842(2)	Restraints / parameters	184 / 440
	c [Å]	14.037(3)	Goodness-of-fit on F^2	1.046
	α [°]	102.57(3)	R_1 [I>2σ(I)]	0.0262
	β [°]	102.84(3)	$R_{2,w}$ (all data)	0.0715
	γ [°]	93.14(2)	$\Delta\varrho_{max}/\Delta\varrho_{min}$ [e Å^{-3}]	1.295 / -2.029
Volume [Å^3]	2271.9(8)		Color and shape	Colorless blocks

6.6.9. Crystal structure of DL_AHN2

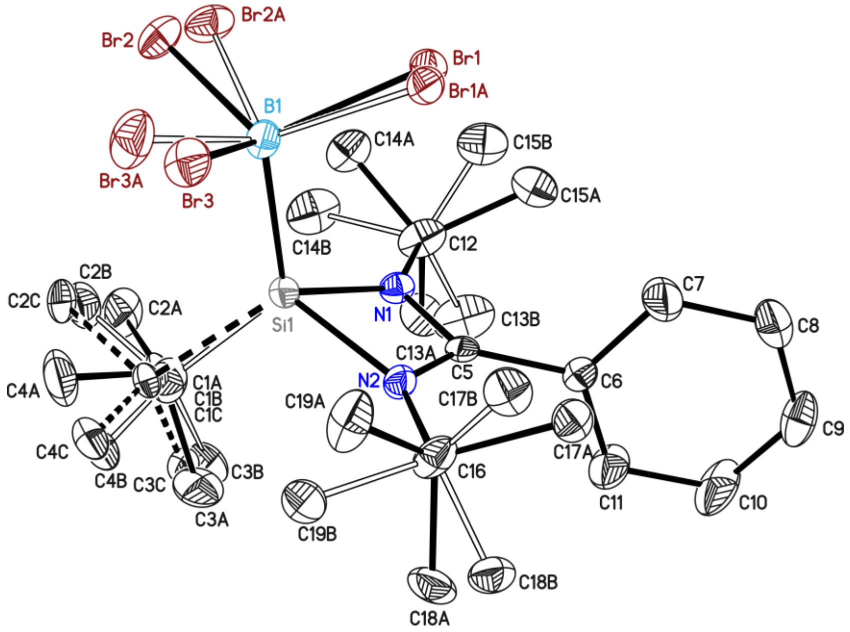

Figure 6.51. The asymmetric unit of **DL_AHN2** with thermal ellipsoids at 50% probability level. The hydrogen atoms are omitted for clarity. The *tert*-butyl groups and the BBr_3 moieties were disordered about 2 positions (Si1-unit over 3 positions) and refined with distance restraints and restraints for the anisotropic displacement parameters. The occupancies of the minor positions were refined to 0.489(3), 0.478(6), 0.489(8), 0.495(3), 0.335(3), and 0.160(3), respectively.

Table 6.50. Crystallographic data for **DL_AHN2**.

Compound	**DL_AHN2**		*Z*	4
CCDC no.	-		ρ_{calc} [Mg m^{-3}]	1.577
Empirical formula	$C_{19}H_{32}BBr_3N_2Si$		μ [mm^{-1}]	5.124
Formula weight [g mol^{-1}]	567.09		*F*(000)	1136
Temperature [K]	100(2)		Crystal size [mm]	0.228 x 0.145 x 0.126
Wavelength [Å]	0.71073		θ range [°]	1.356 to 29.801
Crystal system	Monoclinic		Reflections collected	84358
Space group	$P2_1/n$		Unique reflections	6552
Unit cell parameters	*a* [Å]	8.556(2)	R_{int}	0.0608
	b [Å]	30.023(6)	Restraints / parameters	454 / 409
	c [Å]	10.091(2)	Goodness-of-fit on F^2	1.236
	α [°]	90	R_1 [$I>2\sigma(I)$]	0.0409
	β [°]	112.87(3)	$R_{2,w}$ (all data)	0.0786
	γ [°]	90	$\Delta\varrho_{max}/\Delta\varrho_{min}$ [e Å^{-3}]	0.434 / −0.359
Volume [Å^3]	2388.4(10)		Color and shape	Yellow-brown blocks

6.6.10. Crystal structure of DL_AHN3

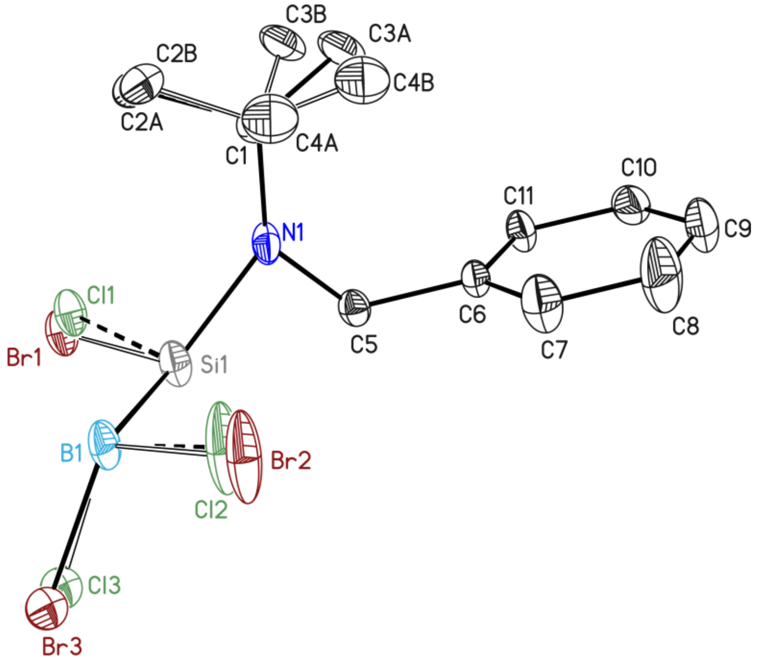

Figure 6.52. The asymmetric unit of **DL_AHN3** with thermal ellipsoids at 50% probability level. The hydrogen atoms are omitted for clarity. The *t*Bu-group was disordered about 2 positions and refined with distance restraints and restraints for the anisotropic displacement parameters. The occupancy of the major position was refined to 0.788(9), respectively.

Table 6.51. Crystallographic data for **DL_AHN3.**

Compound	**DL_AHN3**		*Z*	4
CCDC no.	-		ρ_{calc} [Mgm^{-3}]	1.831
Empirical formula	$C_{15}H_{23}BBr_4N_2Si$		μ [mm^{-1}]	7.578
Formula weight [g mol^{-1}]	589.89		*F*(000)	1144
Temperature [K]	100(2)		Crystal size [mm]	0.143 x 0.123 x 0.110
Wavelength [Å]	0.71073		θ range [°]	2.321 to 25.059
Crystal system	Orthorhombic		Reflections collected	81320
Space group	*Pnma*		Unique reflections	1985
Unit cell parameters	*a* [Å]	13.632(2)	R_{int}	0.0710
	b [Å]	13.826(3)	Restraints / parameters	42 / 137
	c [Å]	11.355(2)	Goodness-of-fit on F^2	1.212
	α [°]	90	R_1 [$I>2\sigma(I)$]	0.0474
	β [°]	90	$R_{2,w}$ (all data)	0.1164
	γ [°]	90	$\Delta\varrho_{\text{max}}/\Delta\varrho_{\text{min}}$ [e Å^{-3}]	0.787 / -1.334
Volume [Å^3]	2140.1(7)		Color and shape	Colorless blocks

6.6.11. Crystal structure of DL_AHN4

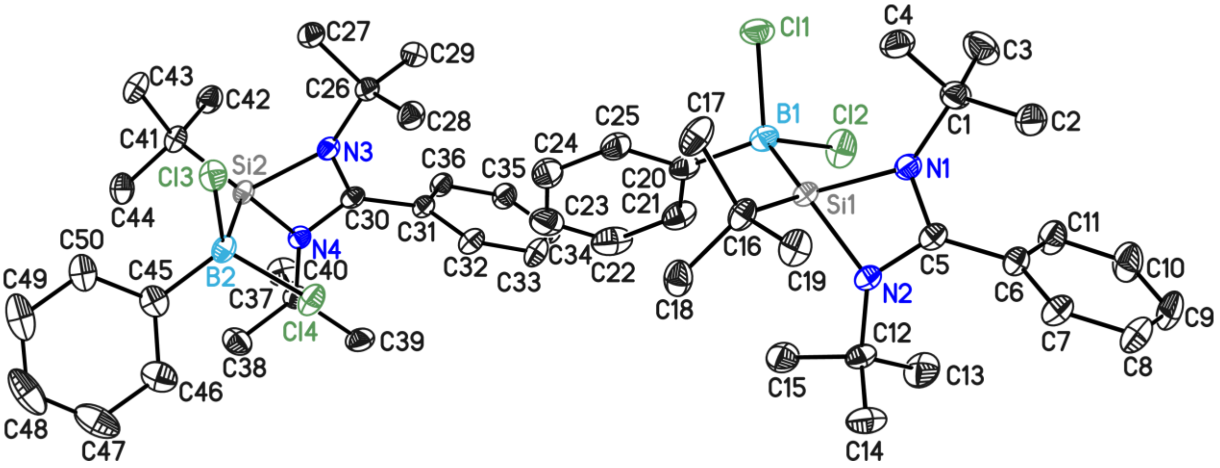

Figure 6.53. The asymmetric unit of **DL_AHN4** with thermal ellipsoids at 50% probability level. The hydrogen atoms are omitted for clarity. Two complex molecules are found in the asymmetric unit and no disorder treatment was required.

Table 6.52. Crystallographic data for **DL_AHN4.**

Compound	**DL_AHN4**		*Z*	8
CCDC no.	-		ρ_{calc} [Mg m^{-3}]	1.183
Empirical formula	$C_{25}H_{37}BCl_2N_2Si$		μ [mm^{-1}]	0.303
Formula weight [g mol^{-1}]	475.36		*F*(000)	2032
Temperature [K]	100(2)		Crystal size [mm]	0.472 x 0.243 x 0.191
Wavelength [Å]	0.71073		θ range [°]	1.365 to 26.490
Crystal system	Monoclinic		Reflections collected	285854
Space group	$P2_1/n$		Unique reflections	10990
Unit cell parameters	*a* [Å]	16.949(2)	R_{int}	0.0803
	b [Å]	16.552(2)	Restraints / parameters	0 / 587
	c [Å]	20.169(3)	Goodness-of-fit on F^2	1.046
	α [°]	90	R_1 [$I>2\sigma(I)$]	0.0370
	β [°]	109.40(2)	$R_{2,w}$ (all data)	0.0869
	γ [°]	90	$\Delta\varrho_{\text{max}}/\Delta\varrho_{\text{min}}$ [e Å^{-3}]	0.289 / -0.238
Volume [Å^3]	5336.9(14)		Color and shape	Colorless blocks

7. References

[1] C. M. Legendre, D. Lüert, R. Herbst-Irmer, D. Stalke, *Dalton Trans.* **2021**, *50*, 16810–16818.

[2] D. Lüert, R. Herbst-Irmer, D. Stalke, *Eur. J. Inorg. Chem.* **2021**, 5085–5090.

[3] D. Lüert, A.-K. Kreyenschmidt, C. M. Legendre, R. Herbst-Irmer, D. Stalke, *Inorg. Chem.* **2022**, *61*, 5234–5244.

[4] D. Lüert, R. Herbst-Irmer, D. Stalke **2022**, *manuscript in preparation*.

[5] D. Lüert, C. M. Legendre, R. Herbst-Irmer, D. Stalke, *Chem. Eur. J.* **2022**, *28*, e202104470.

[6] Y. Ding, S. K. Sarkar, M. Nazish, S. Muhammed, D. Lüert, P. N. Ruth, C. M. Legendre, R. Herbst-Irmer, P. Parameswaran, D. Stalke, Z. Yang, H. W. Roesky, *Angew. Chem. Int. Ed.* **2021**, *60*, 27206–27211.

[7] M. Nazish, A. Harinath, D. Lüert, C. Köhler, R. Herbst-Irmer, D. Stalke, H. W. Roesky **2022**, *manuscript in preparation*.

[8] C. Bazerman, *Handbook of research on writing*: History, society, school, individual, text; L. Erlbaum Associates, New York, **2008**.

[9] P. Ripka, *Magnetic sensors and magnetometers;* Artech House, Boston, Mass, **2001**.

[10] W. Siemens, *Ann. Phys. Chem.* **1867**, *206*, 332–335.

[11] D. B. Richards, M. P. Sharrock, *IEEE Trans. Magn.* **1998**, *34*, 1878–1882.

[12] a) M. M. Waldrop, *Nature* **2016**, *530*, 144–147; b) F. Troiani, M. Affronte, *Chem. Soc. Rev.* **2011**, *40*, 3119–3129; c) E. Pop, *Nano Res.* **2010**, *3*, 147–169;

[13] IDC, & Statista, "Volume of data/information created, captured, copied, and consumed worldwide from 2010 to 2025 (in zettabytes) [Graph]. In Statista", to be found under https://www.statista.com/statistics/871513/worldwide-data-created/, **2021**.

[14] H. L. Feltham, S. Brooker, *Coord. Chem. Rev.* **2014**, *276*, 1–33.

[15] D. Gatteschi, C. Benelli, *Introduction to molecular magnetism*: From transition metals to lanthanides; Wiley-VCH, Weinheim, **2015**.

[16] S. Goswami, A. K. Mondal, S. Konar, *Inorg. Chem. Front.* **2015**, *2*, 687–712.

[17] a) R. Sessoli, D. Gatteschi, A. Caneschi, M. A. Novak, *Nature* **1993**, *365*, 141–143; b) R. Sessoli, H. L. Tsai, A. R. Schake, S. Wang, J. B. Vincent, K. Folting, D. Gatteschi, G. Christou, D. N. Hendrickson, *J. Am. Chem. Soc.* **1993**, *115*, 1804–1816;

[18] J. M. Frost, K. L. M. Harriman, M. Murugesu, *Chem. Sci.* **2016**, *7*, 2470–2491.

[19] a) S. T. Liddle, J. van Slageren, *Chem. Soc. Rev.* **2015**, *44*, 6655–6669; b) O. Kahn, *Molecular magnetism;* VCH, New York, NY, Weinheim, Cambridge, **1993**;

[20] a) D. Gatteschi, R. Sessoli, J. Villain, *Molecular Nanomagnets;* Oxford University Press, Oxford, New York, **2006**; b) M. Hołyńska, Ed, *Single-molecule magnets*: Molecular architectures and building blocks for spintronics; Wiley-VCH, Weinheim, Germany, **2019**;

[21] C. E. Jackson, I. P. Moseley, R. Martinez, S. Sung, J. M. Zadrozny, *Chem. Soc. Rev.* **2021**, *50*, 6684–6699.

[22] R. Marin, G. Brunet, M. Murugesu, *Angew. Chem. Int. Ed.* **2021**, *60*, 1728–1746.

[23] A. Schweiger, G. Jeschke, *Principles of pulse electron paramagnetic resonance;* Oxford Univ. Press, Oxford, **2005**.

[24] K. N. Shrivastava, *phys. stat. sol. (b)* **1983**, *117*, 437–458.

[25] D. Shao, X.-Y. Wang, *Chin. J. Chem.* **2020**, *38*, 1005–1018.

[26] C. J. Milios, A. Vinslava, W. Wernsdorfer, S. Moggach, S. Parsons, S. P. Perlepes, G. Christou, E. K. Brechin, *J. Am. Chem. Soc.* **2007**, *129*, 2754–2755.

[27] A. M. Ako, I. J. Hewitt, V. Mereacre, R. Clérac, W. Wernsdorfer, C. E. Anson, A. K. Powell, *Angew. Chem.* **2006**, *118*, 5048–5051.

[28] M. Murugesu, M. Habrych, W. Wernsdorfer, K. A. Abboud, G. Christou, *J. Am. Chem. Soc.* **2004**, *126*, 4766–4767.

[29] P. Abbasi, K. Quinn, D. I. Alexandropoulos, M. Damjanović, W. Wernsdorfer, A. Escuer, J. Mayans, M. Pilkington, T. C. Stamatatos, *J. Am. Chem. Soc.* **2017**, *139*, 15644–15647.

[30] A. J. Tasiopoulos, A. Vinslava, W. Wernsdorfer, K. A. Abboud, G. Christou, *Angew. Chem.* **2004**, *116*, 2169–2173.

[31] a) O. Waldmann, *Inorg. Chem.* **2007**, *46*, 10035–10037; b) E. Ruiz, J. Cirera, J. Cano, S. Alvarez, C. Loose, J. Kortus, *Chem. Commun.* **2008**, *113*, 52–54; c) F. Neese, D. A. Pantazis, *Faraday Discuss.* **2011**, *148*, 229-238;

[32] a) L. M. C. Beltran, J. R. Long, *Acc. Chem. Res.* **2005**, *38*, 325–334; b) X.-Y. Wang, C. Avendaño, K. R. Dunbar, *Chem. Soc. Rev.* **2011**, *40*, 3213–3238; c) K. S. Pedersen, J. Bendix, R. Clérac, *Chem. Commun.* **2014**, *50*, 4396–4415;

[33] a) R. Sessoli, A. K. Powell, *Coord. Chem. Rev.* **2009**, *253*, 2328–2341; b) A. Dey, J. Acharya, V. Chandrasekhar, *Chem. Asian J.* **2019**, *14*, 4433–4453;

[34] S. G. McAdams, A.-M. Ariciu, A. K. Kostopoulos, J. P. Walsh, F. Tuna, *Coord. Chem. Rev.* **2017**, *346*, 216–239.

[35] a) G. Poneti, K. Bernot, L. Bogani, A. Caneschi, R. Sessoli, W. Wernsdorfer, D. Gatteschi, *Chem. Commun.* **2007**, 1807–1809; b) S. Demir, I.-R. Jeon, J. R. Long, T. D. Harris, *Coord. Chem. Rev.* **2015**, *289-290*, 149–176;

[36] A. E. Thorarinsdottir, T. D. Harris, *Chem. Rev.* **2020**, *120*, 8716–8789.

[37] R. A. Layfield, *Organometallics* **2014**, *33*, 1084–1099.

[38] J. J. Sokol, A. G. Hee, J. R. Long, *J. Am. Chem. Soc.* **2002**, *124*, 7656–7657.

[39] N. Ishikawa, M. Sugita, T. Ishikawa, S.-Y. Koshihara, Y. Kaizu, *J. Am. Chem. Soc.* **2003**, *125*, 8694–8695.

[40] a) S. Stepanow, J. Honolka, P. Gambardella, L. Vitali, N. Abdurakhmanova, T.-C. Tseng, S. Rauschenbach, S. L. Tait, V. Sessi, S. Klyatskaya, M. Ruben, K. Kern, *J. Am. Chem. Soc.* **2010**, *132*, 11900–11901; b) M. Gonidec, R. Biagi, V. Corradini, F. Moro, V. de Renzi, U. Del Pennino, D. Summa, L. Muccioli, C. Zannoni, D. B. Amabilino, J. Veciana, *J. Am. Chem. Soc.* **2011**, *133*, 6603–6612; c) A. Candini, S. Klyatskaya, M. Ruben, W. Wernsdorfer, M. Affronte, *Nano Lett.* **2011**, *11*, 2634–2639;

[41] C. Wei, Y. He, X. Shi, Z. Song, *Coord. Chem. Rev.* **2019**, *385*, 1–19.

[42] S. Osa, T. Kido, N. Matsumoto, N. Re, A. Pochaba, J. Mrozinski, *J. Am. Chem. Soc.* **2004**, *126*, 420–421.

[43] C. A. Gould, K. R. McClain, D. Reta, J. G. C. Kragskow, D. A. Marchiori, E. Lachman, E.-S. Choi, J. G. Analytis, R. D. Britt, N. F. Chilton, B. G. Harvey, J. R. Long, *Science* **2022**, *375*, 198–202.

[44] R. A. Layfield, J. J. W. McDouall, S. A. Sulway, F. Tuna, D. Collison, R. E. P. Winpenny, *Chem. Eur. J.* **2010**, *16*, 4442–4446.

[45] J. D. Rinehart, J. R. Long, *J. Am. Chem. Soc.* **2009**, *131*, 12558–12559.

[46] a) J. D. Rinehart, J. R. Long, *J. Am. Chem. Soc.* **2009**, *131*, 12558–12559; b) D. P. Mills, F. Moro, J. McMaster, J. van Slageren, W. Lewis, A. J. Blake, S. T. Liddle, *Nature Chem.* **2011**, *3*, 454–460; c) N. Magnani, C. Apostolidis, A. Morgenstern, E. Colineau, J.-C. Griveau, H. Bolvin, O. Walter, R. Caciuffo, *Angew. Chem.* **2011**, *123*, 1734–1736; d) V. Mougel, L. Chatelain, J. Pécaut, R. Caciuffo, E. Colineau, J.-C. Griveau, M. Mazzanti, *Nature Chem.* **2012**, *4*, 1011–1017; e) K. R. Meihaus, J. R. Long, *Dalton Trans.* **2015**, *44*, 2517–2528;

[47] a) L. Sun, S. Zhang, C. Qiao, S. Chen, B. Yin, W. Wang, Q. Wei, G. Xie, S. Gao, *Inorg. Chem.* **2016**, *55*, 10587–10596; b) L. Spree, A. A. Popov, *Dalton Trans.* **2019**, *48*, 2861–2871;

[48] R. Westerström, J. Dreiser, C. Piamonteze, M. Muntwiler, S. Weyeneth, H. Brune, S. Rusponi, F. Nolting, A. Popov, S. Yang, L. Dunsch, T. Greber, *J. Am. Chem. Soc.* **2012**, *134*, 9840–9843.

[49] B. M. Day, F.-S. Guo, R. A. Layfield, *Acc. Chem. Res.* **2018**, *51*, 1880–1889.

[50] S.-D. Jiang, B.-W. Wang, H.-L. Sun, Z.-M. Wang, S. Gao, *J. Am. Chem. Soc.* **2011**, *133*, 4730–4733.

[51] a) F.-S. Guo, B. M. Day, Y.-C. Chen, M.-L. Tong, A. Mansikkamäki, R. A. Layfield, *Angew. Chem.* **2017**, *56*, 11445–11449; b) C. A. P. Goodwin, F. Ortu, D. Reta, N. F. Chilton, D. P. Mills, *Nature* **2017**, *548*, 439–442;

[52] F.-S. Guo, B. M. Day, Y.-C. Chen, M.-L. Tong, A. Mansikkamäki, R. A. Layfield, *Science* **2018**, *362*, 1400–1403.

[53] X.-N. Yao, J.-Z. Du, Y.-Q. Zhang, X.-B. Leng, M.-W. Yang, S.-D. Jiang, Z.-X. Wang, Z.-W. Ouyang, L. Deng, B.-W. Wang, S. Gao, *J. Am. Chem. Soc.* **2017**, *139*, 373–380.

[54] P. C. Bunting, M. Atanasov, E. Damgaard-Møller, M. Perfetti, I. Crassee, M. Orlita, J. Overgaard, J. van Slageren, F. Neese, J. R. Long, *Science* **2018**, *362*.

[55] M. Feng, M.-L. Tong, *Chem. Eur. J.* **2018**, *24*, 7574–7594.

[56] J.-L. Liu, Y.-C. Chen, M.-L. Tong, *Chem. Soc. Rev.* **2018**, *47*, 2431–2453.

[57] J. D. Rinehart, J. R. Long, *Chem. Sci.* **2011**, *2*, 2078.

[58] J. Sievers, *Z. Phys. B Cond. Matter.* **1982**, *45*, 289–296.

[59] L. R. Thomas-Hargreaves, M. J. Giansiracusa, M. Gregson, E. Zanda, F. O’Donnell, A. J. Wooles, N. F. Chilton, S. T. Liddle, *Chem. Sci.* **2021**, *12*, 3911–3920.

[60] a) J.-L. Liu, Y.-C. Chen, Y.-Z. Zheng, W.-Q. Lin, L. Ungur, W. Wernsdorfer, L. F. Chibotaru, M.-L. Tong, *Chem. Sci.* **2013**, *4*, 3310–3316; b) J. Liu, Y.-C. Chen, J.-L. Liu, V. Vieru, L. Ungur, J.-H. Jia, L. F. Chibotaru, Y. Lan, W. Wernsdorfer, S. Gao, X.-M. Chen, M.-L. Tong, *J. Am. Chem. Soc.* **2016**, *138*, 5441–5450; c) Y.-C. Chen, J.-L. Liu, L. Ungur, J. Liu, Q.-W. Li, L.-F. Wang, Z.-P. Ni, L. F. Chibotaru, X.-M. Chen, M.-L. Tong, *J. Am. Chem. Soc.* **2016**, *138*, 2829–2837; d) G.-Z. Huang, Z.-Y. Ruan, J.-Y. Zheng, Y.-C. Chen, S.-G. Wu, J.-L. Liu, M.-L. Tong, *Sci. China Chem.* **2020**, *63*, 1066–1074;

[61] C. A. P. Goodwin, D. Reta, F. Ortu, N. F. Chilton, D. P. Mills, *J. Am. Chem. Soc.* **2017**, *139*, 18714–18724.

[62] a) H. A. Kramers, *Proc. R. Acad. Sci. Amsterdam* **1930**, 959–972; b) S. M. Blinder, *Introduction to quantum mechanics;* Academic Press, London, San Diego, CA, **2021**;

[63] a) K. Randall McClain, C. A. Gould, K. Chakarawet, S. J. Teat, T. J. Groshens, J. R. Long, B. G. Harvey, *Chem. Sci.* **2018**, *9*, 8492–8503; b) M. J. Giansiracusa, A. K. Kostopoulos, D. Collison, R. E. P. Winpenny, N. F. Chilton, *Chem. Commun.* **2019**, *55*, 7025–7028; c) M. He, F.-S. Guo, J. Tang, A. Mansikkamäki, R. A. Layfield, *Chem. Sci.* **2020**, *11*, 5745–5752; d) A. Chiesa, F. Cugini, R. Hussain, E. Macaluso, G. Allodi, E. Garlatti, M. Giansiracusa, C. A. P. Goodwin, F. Ortu, D. Reta, J. M. Skelton, T. Guidi, P. Santini, M. Solzi, R. de Renzi, D. P. Mills, N. F. Chilton, S. Carretta, *Phys. Rev. B* **2020**, *101*; e) A. Chakraborty, B. M. Day, J. P. Durrant, M. He, J. Tang, R. A. Layfield, *Organometallics* **2020**, *39*, 8–12;

[64] a) J. Liu, D. Reta, J. A. Cleghorn, Y. X. Yeoh, F. Ortu, C. A. P. Goodwin, N. F. Chilton, D. P. Mills, *Chem. Eur. J.* **2019**, *25*, 7749–7758; b) P.-B. Jin, Y.-Q. Zhai, K.-X. Yu, R. E. P. Winpenny, Y.-Z. Zheng, *Angew. Chem. Int. Ed.* **2020**, *59*, 9350–9354;

[65] R. L. Fagaly, *Rev. Sci. Instrum.* **2006**, *77*, 101101.

[66] Quantum Design, Inc. 10307 Pacific Center Court, San Diego, CA 92121, USA, see www.qdusa.com.

[67] M. Buchner, K. Höfler, B. Henne, V. Ney, A. Ney, *J. Appl. Phys.* **2018**, *124*, 161101.

[68] H. Kammerlingh-Onnes, *Proc. K. Ned. Akad. Wet.* **1911**, *14*.

[69] K.-H. Bennemann, J. B. Ketterson, Eds, *The Physics of Superconductors*: Vol. I. Conventional and High-Tc Superconductors; Springer Berlin Heidelberg; Imprint Springer, Berlin, Heidelberg, **2003**.

[70] J. Bardeen, L. N. Cooper, J. R. Schrieffer, *Phys. Rev.* **1957**, *108*, 1175–1204.

[71] W. Meissner, R. Ochsenfeld, *Naturwissenschaften* **1933**, *21*, 787–788.

[72] B. D. Josephson, *Phys. Lett* **1962**, *1*, 251–253.

[73] C. V. Topping, S. J. Blundell, *J. Phys.: Condens. Matter* **2019**, *31*, 13001.

[74] a) G. Aromí, D. Aguilà, P. Gamez, F. Luis, O. Roubeau, *Chem. Soc. Rev.* **2012**, *41*, 537–546; b) M. J. Graham, J. M. Zadrozny, M. S. Fataftah, D. E. Freedman, *Chem. Mater.* **2017**, *29*, 1885–1897; c) M. S. Fataftah, M. D. Krzyaniak, B. Vlaisavljevich, M. R. Wasielewski, J. M. Zadrozny, D. E. Freedman, *Chem. Sci.* **2019**, *10*, 6707–6714;

[75] a) J. Wahsner, E. M. Gale, A. Rodríguez-Rodríguez, P. Caravan, *Chem. Rev.* **2019**, *119*, 957–1057; b) M. C. Heffern, L. M. Matosziuk, T. J. Meade, *Chem. Rev.* **2014**, *114*, 4496–4539; c) A. E. Merbach, É. Tóth, L. Helm, Eds, *The chemistry of contrast agents in medical magnetic resonance imaging;* John Wiley & Sons Inc, Hoboken, NJ, **2013**;

[76] a) K. V. Raman, A. M. Kamerbeek, A. Mukherjee, N. Atodiresei, T. K. Sen, P. Lazić, V. Caciuc, R. Michel, D. Stalke, S. K. Mandal, S. Blügel, M. Münzenberg, J. S. Moodera, *Nature* **2013**, *493*, 509–513; b) A. L. Buchachenko, V. L. Berdinsky, *Chem. Rev.* **2002**, *102*, 603–612;

[77] C. Godfrin, A. Ferhat, R. Ballou, S. Klyatskaya, M. Ruben, W. Wernsdorfer, F. Balestro, *Phys. Rev. Lett.* **2017**, *119*, 187702.

[78] H. Park, A. K. L. Lim, A. P. Alivisatos, J. Park, P. L. McEuen, *Appl. Phys. Lett.* **1999**, *75*, 301–303.

[79] D. Mitcov, A. H. Pedersen, M. Ceccato, R. M. Gelardi, T. Hassenkam, A. Konstantatos, A. Reinholdt, M. A. Sørensen, P. W. Thulstrup, M. G. Vinum, F. Wilhelm, A. Rogalev, W. Wernsdorfer, E. K. Brechin, S. Piligkos, *Chem. Sci.* **2019**, *10*, 3065–3073.

[80] S. Thiele, F. Balestro, R. Ballou, S. Klyatskaya, M. Ruben, W. Wernsdorfer, *Science* **2014**, *344*, 1135–1138.

[81] a) Y. Dubi, M. Di Ventra, *Rev. Mod. Phys.* **2011**, *83*, 131–155; b) Z. Huang, B. Xu, Y. Chen, M. Di Ventra, N. Tao, *Nano Lett.* **2006**, *6*, 1240–1244;

[82] N. Chilton, *Meet a Chemistry Academic 2020 - Theoretical Chemistry - Dr. Nicholas Chilton - Youtube*, **2020**.

[83] L. Bourget-Merle, M. F. Lappert, J. R. Severn, *Chem. Rev.* **2002**, *102*, 3031–3066.

[84] L. C. Dorman, *Tetrahedron Letters* **1966**, *7*, 459–464.

[85] H. Meerwein, G. Hinz, P. Hofmann, E. Kroning, E. Pfeil, *J. Prakt. Chem.* **1937**, *147*, 257–285.

[86] S. G. McGeachin, *Can. J. Chem.* **1968**, *46*, 1903–1912.

[87] C. Camp, J. Arnold, *Dalton Trans.* **2016**, *45*, 14462–14498.

[88] a) C. L. Honeybourne, G. A. Webb, *Chem. Commun.* **1968**, 739; b) R. H. Holm, A. Chakravorty, L. J. Theriot, *Inorg. Chem.* **1966**, *5*, 625–635; c) R. Bonnett, D. C. Bradley, K. J. Fisher, *Chem. Commun.* **1968**, *0*, 886–887; d) M. Zhong, S. Sinhababu, H. W. Roesky, *Dalton Trans.* **2020**, *49*, 1351–1364;

[89] L. Forlani, C. Boga, E. Del Vecchio, M. Padovani, *Arkivoc* **2004**, *2003*, 75–91.

[90] H. Ben Ammar, J. Le Nôtre, M. Salem, M. T. Kaddachi, P. H. Dixneuf, *J. Organomet. Chem.* **2002**, *662*, 63–69.

[91] D.-R. Dauer, D. Stalke, *Dalton Trans.* **2014**, *43*, 14432–14439.

[92] J. Kretsch, I. Koehne, M. Lõkov, I. Leito, D. Stalke, *Eur. J. Inorg. Chem.* **2019**, *2019*, 3258–3264.

[93] D.-R. Dauer, I. Koehne, R. Herbst-Irmer, D. Stalke, *Eur. J. Inorg. Chem.* **2017**, *2017*, 1966–1978.

[94] D.-R. Dauer, M. Flügge, R. Herbst-Irmer, D. Stalke, *Dalton Trans.* **2016**, *45*, 6149–6158.

[95] I. Koehne, N. Graw, T. Teuteberg, R. Herbst-Irmer, D. Stalke, *Inorg. Chem.* **2017**, *56*, 14968–14978.

[96] I. Koehne, S. Bachmann, T. Niklas, R. Herbst-Irmer, D. Stalke, *Chem. Eur. J.* **2017**, *23*, 13141–13149.

[97] J. Kretsch, A.-K. Kreyenschmidt, T. Schillmöller, M. Lõkov, R. Herbst-Irmer, I. Leito, D. Stalke, *Chem. Eur. J.* **2021**, *27*, 9858–9865.

[98] a) W. Gregory, *J. Pharm.* **1835**, *21*, 315–318; b) E. Soubeiran, *Ann. Chim. Phys.* **1938**, *67, 71, 96*;

[99] R. Schenck, *Liebigs Ann. Chem.* **1896**, *290*, 171.

[100] M. Goehring, *Chem. Ber.* **1947**, *80*, 110–122.

[101] a) D. Clark, *J. Chem. Soc.* **1952**, *1615*; b) B. D. Sharma, J. Donohue, *Acta. Cryst.* **1963**, *16*, 891; c) M. Goehring, D. Voigt, *Naturwissenschaften* **1953**, *40*, 482;

[102] a) R. L. Greene, G. B. Street, L. J. Suter, *Phys. Rev. Lett.* **1975**, *34*, 577–579; b) M. M. Labes, P. Love, L. F. Nichols, *Chem. Rev.* **1979**, *79*, 1–15;

[103] M. Goehring, G. Weis, *Angew. Chem.* **1956**, *68*, 678.

[104] U. Wannagat, H. Kuckertz, *Angew. Chem.* **1962**, *74*, 117–118.

[105] D. H. Clemens, A. J. Bell, J. L. O'Brien, *Tetrahedron Lett.* **1965**, *6*, 1487–1489.

[106] O. Glemser, J. Wegener, *Angew. Chem.* **1970**, *82*, 324.

[107] O. Glemser, S. Pohl, F.-M. Tesky, R. Mews, *Angew. Chem. Int. Ed.* **1977**, *16*, 789–790.

[108] W. Lidy, W. Sundermeyer, W. Verbeek, *Z. Anorg. Allg. Chem.* **1974**, *406*, 228–234.

[109] a) R. Fleischer, S. Freitag, D. Stalke, *J. Chem. Soc, Dalton Trans.* **1998**, 193–198; b) R. Fleischer, S. Freitag, F. Pauer, D. Stalke, *Angew. Chem. Int. Ed.* **1996**, *35*, 204–206;

[110] a) I. Langmuir, *J. Am. Chem. Soc.* **1919**, *41*, 1543–1559; b) I. Langmuir, *J. Am. Chem. Soc.* **1919**, *41*, 868–934;

[111] a) J. Cioslowski, S. T. Mixon, *Inorg. Chem.* **1993**, *32*, 3209–3216; b) J. Cioslowski, P. R. Surján, *J. Mol. Struct. THEOCHEM* **1992**, *255*, 9–33; c) D. Cruickshank, *J. Mol. Struct.* **1985**, *130*, 177–191; d) D. Cruickshank, M. Eisenstein, *J. Mol. Struct.* **1985**, *130*, 143–156; e) W. Kutzelnigg, *Angew. Chem. Int. Ed.* **1984**, *23*, 272–295; f) A. E. Reed, P. v. R. Schleyer, *J. Am. Chem. Soc.* **1990**, *112*, 1434–1445; g) T. Stefan, R. Janoschek, *J. Mol. Model.* **2000**, *6*, 282–288;

[112] a) A. F. Holleman, N. Wiberg, E. Wiberg, *Lehrbuch der anorganischen Chemie;* de Gruyter, Berlin, **2007**; b) C. E. Housecroft, A. G. Sharpe, *Anorganische Chemie;* Pearson Studium, München, **2008**;

[113] D. Stalke, *Chem. Commun.* **2012**, *48*, 9559–9573.

[114] D. Leusser, J. Henn, N. Kocher, B. Engels, D. Stalke, *J. Am. Chem. Soc.* **2004**, *126*, 1781–1793.

[115] a) R. Fleischer, B. Walfort, A. Gbureck, P. Scholz, W. Kiefer, D. Stalke, *Chem. Eur. J.* **1998**, *4*, 2266–2274; b) S. L. Hinchley, P. Trickey, H. E. Robertson, B. A. Smart, D. W. H. Rankin, D. Leusser, B. Walfort, D. Stalke, M. Bühl, S. J. Obrey, *J. Chem. Soc, Dalton Trans.* **2002**, 4607;

[116] J. Henn, D. Ilge, D. Leusser, D. Stalke, B. Engels, *J. Phys. Chem. A* **2004**, *108*, 9442–9452.

[117] E. Carl, S. Demeshko, F. Meyer, D. Stalke, *Chem. Eur. J.* **2015**, *21*, 10109–10115.

[118] J. Jung, F. Benner, R. Herbst-Irmer, S. Demir, D. Stalke, *Chem. Eur. J.* **2021**, *27*, 12310–12319.

[119] J. Jung, C. M. Legendre, S. Demeshko, R. Herbst-Irmer, D. Stalke, *Inorg. Chem.* **2021**, *60*, 9580–9588.

[120] J. Jung, C. M. Legendre, S. Demeshko, R. Herbst-Irmer, D. Stalke, *Dalton Trans.* **2021**, *50*, 17194–17201.

[121] C. M. Legendre, E. Damgaard-Møller, J. Overgaard, D. Stalke, *Eur. J. Inorg. Chem.* **2021**, *30*, 3108–3114.

[122] C. M. Legendre, R. Herbst-Irmer, D. Stalke, *Inorg. Chem.* **2021**, *60*, 13982–13989.

[123] J. Jung, C. M. Legendre, R. Herbst-Irmer, D. Stalke, *Inorg. Chem.* **2021**, *60*, 967–972.

[124] G. M. Sheldrick, *Acta Crystallogr.* **2015**, *C71*, 3–8.

[125] J. Kretsch, A. Kreyenschmidt, R. Herbst-Irmer, D. Stalke, *Dalton Trans.* **2018**, *47*, 12606–12612.

[126] S. Ziegenbalg, D. Hornig, H. Görls, W. Plass, *Inorg. Chem.* **2016**, *55*, 4047–4058.

[127] A. W. Addison, T. N. Rao, J. Reedijk, J. van Rijn, G. C. Verschoor, *J. Chem. Soc, Dalton Trans.* **1984**, 1349–1356.

[128] L. Yang, D. R. Powell, R. P. Houser, *Dalton Trans.* **2007**, 955–964.

[129] Y. Nishida, N. Oishi, S. Kida, *Inorg. Chim. Acta.* **1979**, *32*, 7–10.

[130] V. A. Crawford, *J. Chem. Soc.* **1953**, 2061.

[131] E. Bill, *JulX-2s;* Max-Planck Institute for Chemical Energy Conversion, Mühlheim, Germany, **2013**.

[132] E. A. Suturina, J. Nehrkorn, J. M. Zadrozny, J. Liu, M. Atanasov, T. Weyhermüller, D. Maganas, S. Hill, A. Schnegg, E. Bill, J. R. Long, F. Neese, *Inorg. Chem.* **2017**, *56*, 3102–3118.

[133] A. Sarkar, S. Dey, G. Rajaraman, *Chem. Eur. J.* **2020**, *26*, 14036–14058.

[134] T. Wu, Y.-Q. Zhai, Y.-F. Deng, W.-P. Chen, T. Zhang, Y.-Z. Zheng, *Dalton Trans.* **2019**, *48*, 15419–15426.

[135] a) C. Duboc, *Chem. Soc. Rev.* **2016**, *45*, 5834–5847; b) C. Rajnák, J. Titiš, J. Moncol, R. Mičová, R. Boča, *Inorg. Chem.* **2019**, *58*, 991–994;

[136] D. Reta, N. F. Chilton, *Phys. Chem. Chem. Phys.* **2019**, *21*, 23567–23575.

[137] D. A. Garanin, *Phys. Rev. B* **2007**, *75*, 94409.

[138] N. Lopez, A. V. Prosvirin, H. Zhao, W. Wernsdorfer, K. R. Dunbar, *Chem. Eur. J.* **2009**, *15*, 11390–11400.

[139] a) F. Neese, *Comput. Mol. Sci.* **2012**, *2*, 73–78; b) F. Neese, F. Wennmohs, U. Becker, C. Riplinger, *The Journal of Chemical Physics* **2020**, *152*, 224108;

[140] a) M. Llunell, D. Casanova, J. Cirera, J. Bofill, S. Alemany, *SHAPE 2.1*, Universitat de Barcelona and The Hebrew University of Jerusalem, Barcelona and Jerusalem, **2003**; b) M. Pinsky, D. Avnir, *Inorg. Chem.* **1998**, *37*, 5575–5582; c) S. Alvarez, M. Llunell, *J. Chem. Soc, Dalton Trans.* **2000**, 3288–3303;

[141] X.-N. Yao, J.-Z. Du, Y.-Q. Zhang, X.-B. Leng, M.-W. Yang, S.-D. Jiang, Z.-X. Wang, Z.-W. Ouyang, L. Deng, B.-W. Wang, S. Gao, *J. Am. Chem. Soc.* **2017**, *139*, 373–380.

[142] O. Möller, Bachelor thesis, Georg-August-University Göttingen, **2021**.

[143] a) J.-B. Tan, X.-Y. Chen, J. Fan, S.-R. Zheng, W.-G. Zhang, *Inorg. Chem. Commun.* **2013**, *31*, 49–53; b) O. Iasco, G. Novitchi, E. Jeanneau, J. B. Tommasino, N. Roques, D. Luneau, *Inorg. Chem.* **2012**, *51*, 2588–2596; c) A. Panja, N. Shaikh, S. Gupta, R. J. Butcher, P. Banerjee, *Eur. J. Inorg. Chem.* **2003**, *2003*, 1540–1547; d) B. Mabad, P. Cassoux, J. P. Tuchagues, D. N. Hendrickson, *Inorg. Chem.* **1986**, *25*, 1420–1431;

[144] a) D. Lüert, Masterarbeit, Georg-August-University Göttingen, **2017**; b) D. C. Bradley, J. S. Ghotra, F. A. Hart, *J. Chem. Soc, Dalton Trans.* **1973**, 1021–1023;

[145] W. S. R. Jr, O. Just, D. S. van Derveer, *J. Mater. Chem.* **1999**, *9*, 249–252.

[146] R. A. Andersen, D. H. Templeton, A. Zalkin, *Inorg. Chem.* **1978**, *17*, 2317–2319.

[147] E. D. Brady, D. L. Clark, J. C. Gordon, P. J. Hay, D. W. Keogh, R. Poli, B. L. Scott, J. G. Watkin, *Inorg. Chem.* **2003**, *42*, 6682–6690.

[148] J. S. Ghotra, M. B. Hursthouse, A. J. Welch, *J. Chem. Soc, Chem. Commun.* **1973**, 669–670.

[149] P. B. Hitchcock, A. G. Hulkes, M. F. Lappert, Z. Li, *Dalton Trans.* **2004**, 129–136.

[150] W. A. Herrmann, R. Anwander, F. C. Munck, W. Scherer, V. Dufaud, N. W. Huber, G. R. J. Artus, *Z. Naturforsch. B* **1994**, *49*, 1789–1797.

[151] A. M. Bienfait, B. M. Wolf, K. W. Törnroos, R. Anwander, *Inorg. Chem.* **2018**, *57*, 5204–5212.

[152] M. Niemeyer, *Z. Anorg. Allg. Chem.* **2002**, *628*, 647–657.

[153] G. Scarel, C. Wiemer, M. Fanciulli, I. L. Fedushkin, G. K. Fukin, G. A. Domrachev, Y. Lebedinskii, A. Zenkevich, G. Pavia, *Z. Anorg. Allg. Chem.* **2007**, *633*, 2097–2103.

[154] D. N. Woodruff, R. E. P. Winpenny, R. A. Layfield, *Chem. Rev.* **2013**, *113*, 5110–5148.

[155] D. Casanova, P. Alemany, J. M. Bofill, S. Alvarez, *Chem. Eur. J.* **2003**, *9*, 1281–1295.

[156] P. D'Angelo, A. Zitolo, V. Migliorati, G. Chillemi, M. Duvail, P. Vitorge, S. Abadie, R. Spezia, *Inorg. Chem.* **2011**, *50*, 4572–4579.

[157] a) A. Steiner, D. Stalke, *Inorg. Chem.* **1993**, *32*, 1977–1981; b) H. Gornitzka, D. Stalke, *Angew. Chem.* **1994**, *106*, 695–698; c) A. N. Chekhlov, I. V. Martynov, *Proc. Nat. Acad. Sci. USSR* **1999**, 61; d) T. Kaehler, F. Olbrich, *CSD Communication* **2002**; e) H. Bock, Z. Havlas, K. Gharagozloo-Hubmann, S. Holl, M. Sievert, *Angew. Chem. Int. Ed.* **2003**, *42*, 4385–4389; f) X. Kou, J. Wu, T. R. Cundari, H. V. R. Dias, *Dalton Trans.* **2009**, 915–917; g) M. Podewitz, J. D. van Beek, M. Wörle, T. Ott, D. Stein, H. Rüegger, B. H. Meier, M. Reiher, H. Grützmacher, *Angew. Chem.* **2010**, *122*, 7627–7631; h) J. Bacsa, R. J. Less, H. E. Skelton, Z. Soracevic, A. Steiner, T. C. Wilson, P. T. Wood, D. S. Wright, *Angew. Chem. Int. Ed.* **2011**, *50*, 8279–8282; i) A. I. Ojeda-Amador, A. J. Martínez-Martínez, A. R. Kennedy, C. T. O'Hara, *Inorg. Chem.* **2015**, *54*, 9833–9844;

[158] I. Koehne, R. Herbst-Irmer, D. Stalke, *Eur. J. Inorg. Chem.* **2017**, *2017*, 3322–3326.

[159] a) K. W. Henderson, P. G. Williard, P. R. Bernstein, *Angew. Chem.* **1995**, *34*, 1117–1119; b) P. G. Williard, G. B. Carpenter, *J. Am. Chem. Soc.* **1986**, *108*, 462–468; c) R. A. Woltornist, D. B. Collum, *J. Am. Chem. Soc.* **2020**, *142*, 6852–6855; d) R. A. Woltornist, D. B. Collum, *J. Org. Chem.* **2021**, *86*, 2406–2422; e) R. A. Woltornist, D. B. Collum, *J. Am. Chem. Soc.* **2021**, *143*, 17452–17464; f) D. Moskau, F. Brauers, H. Guenther, A. Maercker, *J. Am. Chem. Soc.* **1987**, *109*, 5532–5534;

[160] a) G. Kleks, D. C. Holland, J. Porter, A. R. Carroll, *Chem. Sci.* **2021**, *12*, 10930–10943; b) M. P. Crockett, H. Zhang, C. M. Thomas, J. A. Byers, *Chem. Commun.* **2019**, *55*, 14426–14429; c) O. Tai, R. Hopson, P. G. Williard, *J. Org. Chem.* **2017**, *82*, 6223–6231; d) D. Li, I. Keresztes, R. Hopson, P. G. Williard, *Acc. Chem. Res.* **2009**, *42*, 270–280; e) G. Kagan, W. Li, R. Hopson, P. G. Williard, *Org. Lett.* **2009**, *11*, 4818–4821; f) D. Li, R. Hopson, W. Li, J. Liu, P. G. Williard, *Org. Lett.* **2008**, *10*, 909–911; g) C. A. Crutchfield, D. J. Harris, *J. Magn. Reson.* **2007**, *185*, 179–182; h) K. F. Morris, C. S. Johnson, *J. Am. Chem. Soc.* **1992**, *114*, 3139–3141;

[161] a) A.-K. Kreyenschmidt, S. Bachmann, T. Niklas, D. Stalke, *ChemistrySelect* **2017**, *2*, 6957–6960; b) S. Bachmann, B. Gernert, D. Stalke, *Chem. Commun.* **2016**, *52*, 12861–12864; c) S. Bachmann, R. Neufeld, M. Dzemski, D. Stalke, *Chem. Eur. J.* **2016**, *22*, 8462–8465; d) R. Neufeld, D. Stalke, *Chem. Sci.* **2015**, *6*, 3354–3364;

[162] S. Alvarez, D. Avnir, M. Llunell, M. Pinsky, *New J. Chem.* **2002**, *26*, 996–1009.

[163] a) M. U. Anwar, A. Al-Harrasi, J. M. Rawson, E. L. Gavey, J. Regier, D. Alexandropoulos, M. Pilkington, L. K. Thompson, *Dalton Trans.* **2019**, *48*, 14269–14278; b) F. Habib, M. Murugesu, *Chem. Soc. Rev.* **2013**, *42*, 3278–3288; c) S. Qiao, J. Zhang, S. Zhang, Q. Yang, Q. Wei, D. Yang, S. Chen, *Inorg. Chim. Acta.* **2018**, *469*, 57–65; d) E. Moreno Pineda, N. F. Chilton, R. Marx, M. Dörfel, D. O. Sells, P. Neugebauer, S.-D. Jiang, D. Collison, J. van Slageren, E. J. L. McInnes, R. E. P. Winpenny, *Nat. Commun.* **2014**, *5*, 5243; e) H. Ke, S. Zhang, X. Li, Q. Wei, G. Xie, W. Wang, S. Chen, *Dalton Trans.* **2015**, *44*, 21025–21031; f) P.-H. Lin, T. J. Burchell, R. Clérac, M. Murugesu, *Angew. Chem. Int. Ed.* **2008**, *47*, 8848–8851;

[164] N. F. Chilton, R. P. Anderson, L. D. Turner, A. Soncini, K. S. Murray, *J. Comput. Chem.* **2013**, *34*, 1164–1175.

[165] a) J. Becquerel, *Z. Phys.* **1929**, *58*, 205–216; b) S. Xue, Y.-N. Guo, L. Zhao, P. Zhang, J. Tang, *Dalton Trans.* **2014**, *43*, 1564–1570;

[166] J. D. Rinehart, T. D. Harris, S. A. Kozimor, B. M. Bartlett, J. R. Long, *Inorg. Chem.* **2009**, *48*, 3382–3395.

[167] a) J.-D. Leng, J.-L. Liu, W.-Q. Lin, S. Gómez-Coca, D. Aravena, E. Ruiz, M.-L. Tong, *Chem. Commun.* **2013**, *49*, 9341–9343; b) P. Panissod, M. Drillon in *Magnetism: Molecules to Materials*; (Eds. J. S. Miller, M. Drillon), Wiley-VCH, Weinheim, New York, **2002**, chapter 7, p. 235;

[168] Y.-N. Guo, G.-F. Xu, Y. Guo, J. Tang, *Dalton Trans.* **2011**, *40*, 9953–9963.

[169] C. Jin, X.-L. Li, Z. Liu, A. Mansikkamäki, J. Tang, *Dalton Trans.* **2020**, *49*, 10477–10485.

[170] a) W. Zhou, D. McKearney, D. B. Leznoff, *Chem. Eur. J.* **2020**, *26*, 1027–1031; b) J. Long, A. O. Tolpygin, A. V. Cherkasov, K. A. Lyssenko, Y. Guari, J. Larionova, A. A. Trifonov, *Dalton Trans.* **2020**, *49*, 11890–11901; c) S. V. Klementyeva, M. Y. Afonin, A. S. Bogomyakov,

M. T. Gamer, P. W. Roesky, S. N. Konchenko, *Eur. J. Inorg. Chem.* **2016**, *2016*, 3666–3672; d) M. T. Gamer, S. Dehnen, P. W. Roesky, *Organometallics* **2001**, *20*, 4230–4236;

[171] H. Tian, B.-L. Wang, J. Lu, H.-T. Liu, J. Su, D. Li, J. Dou, *Chem. Commun.* **2018**, *54*, 12105–12108.

[172] S. A. Sulway, R. A. Layfield, F. Tuna, W. Wernsdorfer, R. E. P. Winpenny, *Chem. Commun.* **2012**, *48*, 1508–1510.

[173] T. Han, M. J. Giansiracusa, Z.-H. Li, Y.-S. Ding, N. F. Chilton, R. E. P. Winpenny, Y.-Z. Zheng, *Chem. Eur. J.* **2020**, *26*, 6773–6777.

[174] a) N. F. Chilton, D. Collison, E. J. L. McInnes, R. E. P. Winpenny, A. Soncini, *Nat. Commun.* **2013**, *4*, 2551; b) Crystal Impact - Dr. H. Putz & Dr. K. Brandenburg GbR, *Diamond - Crystal and Molecular Structure Visualization*, Kreuzherrenstr. 102, 53227 Bonn, Germany;

[175] M. J. Redecker, Masterarbeit, Georg-August-Universität Göttingen, **2021**.

[176] O. J. Scherer, R. Wies, *Z. Naturforsch. B* **1970**, *25*, 1486–1487.

[177] W. Haubold, H. Günter, G. Frey, *Z. Naturforsch. B* **1981**, *36*, 157–160.

[178] T. Schulz, D. Stalke, *Z. Naturforsch. B* **2010**, *65*, 701–710.

[179] F. Pauer, D. Stalke, *J. Organomet. Chem.* **1991**, *418*, 127–145.

[180] a) C. Selinka, Dissertation, Julius-Maximilians Universität Würzburg, **2002**; b) M. Bayram, D. Bläser, C. Wölper, S. Schulz, *Organometallics* **2015**, *34*, 3421–3427;

[181] D. Hänssgen, C. Patermann, R. Plum, *Z. Anorg. Allg. Chem.* **1989**, *571*, 29–36.

[182] J. Jung, A. Münch, R. Herbst-Irmer, D. Stalke, *Angew. Chem. Int. Ed.* **2021**, *60*, 5679–5682.

[183] J. Jung, Dissertation, Georg-August-Universität Göttingen, **2021**.

[184] D. Ilge, Diplomarbeit, Julius-Maximilians Universität Würzburg, **1997**.

[185] a) J. A. Hunter, B. King, W. E. Lindsell, M. A. Neish, *J. Chem. Soc, Dalton Trans.* **1980**, 880; b) C. M. Legendre, A. C. Stückl, C. P. Sindlinger, R. Herbst-Irmer, D. Stalke, *Angew. Chem. Int. Ed.* **2021**, *61*, e202115026;

[186] S. V. Klementyeva, N. P. Gritsan, M. M. Khusniyarov, A. Witt, A. A. Dmitriev, E. A. Suturina, N. D. D. Hill, T. L. Roemmele, M. T. Gamer, R. T. Boeré, P. W. Roesky, A. V. Zibarev, S. N. Konchenko, *Chem. Eur. J.* **2017**, *23*, 1278–1290.

[187] K. Kaleta, M. Kessler, T. Beweries, P. Arndt, A. Spannenberg, U. Rosenthal, *Eur. J. Inorg. Chem.* **2012**, 3388–3393.

[188] D. Ilge, D. S. Wright, D. Stalke, *Chem. Eur. J.* **1998**, *4*, 2275–2279.

[189] F. A. Watt, A. Krishna, G. Golovanov, H. Ott, R. Schoch, C. Wölper, A. G. Neuba, S. Hohloch, *Inorg. Chem.* **2020**, *59*, 2719–2732.

[190] a) M. E. Fieser, C. W. Johnson, J. E. Bates, J. W. Ziller, F. Furche, W. J. Evans, *Organometallics* **2015**, *34*, 4387–4393; b) L. Maria, M. Soares, I. C. Santos, V. R. Sousa, E. Mora,

J. Marçalo, K. V. Luzyanin, *Dalton Trans.* **2016**, *45*, 3778–3790; c) D. Werner, G. B. Deacon, P. C. Junk, *Inorg. Chem.* **2019**, *58*, 1912–1918;

[191] Georg-August-Universität Göttingen, "Virtuelles Labor", to be found under http://www.stalke.chemie.uni-goettingen.de/virtuelles_labor/advanced/13_de.html.

[192] Georg-August-Universität Göttingen, "Virtuelles Labor", to be found under http://www.stalke.chemie.uni-goettingen.de/virtuelles_labor/nmr/de.html.

[193] *Origin(Pro), 8.5;* OriginLab Corporation, Northampton, MA, USA.

[194] P. Rudolph, *Handbook of Crystal Growth*: Bulk Crystal Growth; Elsevier Science, Burlington, **2014**.

[195] T. Kottke, D. Stalke, *J. Appl. Crystallogr.* **1993**, *26*, 615–619.

[196] T. Kottke, R. J. Lagow, D. Stalke, *J. Appl. Crystallogr.* **1996**, *29*, 465–468.

[197] T. Schulz, K. Meindl, D. Leusser, D. Stern, J. Graf, C. Michaelsen, M. Ruf, G. M. Sheldrick, D. Stalke, *J. Appl. Crystallogr.* **2009**, *42*, 885–891.

[198] APEX2 v2012/2. APEX2, Bruker AXS Inc.:, Madison, USA, **2012**.

[199] a) L. Krause, R. Herbst-Irmer, G. M. Sheldrick, D. Stalke, *J. Appl. Crystallogr.* **2015**, *48*, 3–10; b) Bruker AXS Inst. Inc, Ed, *Bruker Apex CCD, SAINT v8.30C*, WI, USA, Madison, **2013**;

[200] L. Krause, R. Herbst-Irmer, D. Stalke, *J. Appl. Crystallogr.* **2015**, *48*, 1907–1913.

[201] G. M. Sheldrick, *XPREP in SHELXTL 2014/2*, USA, Madison, **2014**.

[202] G. M. Sheldrick, *Acta Crystallogr.* **2015**, *A71*, 3–8.

[203] C. B. Hübschle, G. M. Sheldrick, B. Dittrich, *J. Appl. Crystallogr.* **2011**, *44*, 1281–1284.

[204] a) CCDC, *Mercury CSD, Cambridge (UK)*, **2016**; b) G. M. Sheldrick, *XP in SHELXTL v2008/2*, USA, Madison, **2008**;

8. Acknowledgements

Zunächst möchte ich mich herzlich bei PROF. DR. STALKE für die interessante Themenstellung und die gewährte wissenschaftliche Freiheit bedanken. Ihren Forschergeist und Optimismus wusste ich immer sehr zu schätzen. Ich bin dankbar für Ihre Unterstützung während der gesamten Zeit.

Ebenso danke ich PROF. DR. FRANC MEYER für die Übernahme des Korreferates und den bereichernden wissenschaftlichen Diskurs.

PROF. DR. THOMAS WAITZ danke ich für seine Funktion als 3. Gutachter dieser Arbeit und sein wertvolles Feedback.

JUN.-PROF. DR. ANNA KRAWCZUK, PD. DR. MICHAEL JOHN und DR. MATTHIAS OTTE danke ich für ihre Rolle als Mitglieder der Prüfungskommission.

Die Förderung meiner Promotion durch die Fonds der chemischen Industrie (FCI) im Rahmen eines Kekulé Stipendiums haben es mir ermöglicht dieses große Projekt erfolgreich abzuschließen. Dafür bin ich sehr dankbar.

Weiterhin haben folgende Personen einen großen Anteil zum Gelingen dieser Arbeit geleistet:

DR. REGINE HERBST-IRMER danke ich für Ihre zahlreichen Ratschläge und Ideen zu diversen kristallographischen Fragestellungen. Ohne Ihre Expertise wären einige Festkörperstrukturen dieser Arbeit unbekannt geblieben. Auch für die nette Zusammenarbeit bei der Koordination der Lehramtspraktika bin ich dankbar.

HEIKE TAPPE, LAURA HABERSTOCK und TOBIAS ERNEMANN danke ich für die hervorragende Organisation des Arbeitskreises, ihren Einsatz bei der Bereitstellung von Geräten und Chemikalien sowie die Wartung der Röntgendiffraktometer.

Meinem ehemaligen Laborpartner DR. JOCHEN JUNG danke ich für praktische Einführung in die SN Chemie, die interessanten Diskussionen und den täglichen Ausgleich beim Klimmzugcontest.

Meiner aktuellen Laborpartnerin PAULA KALLENBACH danke ich für die produktive Atmosphäre die vielen bereichernden Diskussionen über die Zukunft der SN Chemie.

DR. CHRISTINA LEGENDRE danke ich für die Einführung am SQUID, die ausgezeichnete Zusammenarbeit beim Publizieren sowie die vielen spannenden wissenschaftlichen Diskurse. DR. SERHIY DEMESHKO danke ich für seine große Hilfsbereitschaft bei der Auswertung von magnetischen Daten und der Unterstützung bei diversen SQUID Problemen.

Ferner danke ich den aktuellen und ehemaligen Mitgliedern der Arbeitsgruppe STALKE für das wertvolle Feedback vom Korrekturlesen dieser Arbeit, die schöne gemeinsame Zeit im Pausenraum und die vielen übrigen Aktivitäten, die diese Zeit besonders gemacht haben (#WoDuR).

Die Beschäftigten der Werkstätten sowie den Hausmeistern der Anorganischen Chemie danke ich für die gute Zusammenarbeit und die Unterstützung bei technischen Problemen jeglicher Art. Im besonderen BERND WICHMANN, BENJAMIN BOCK, ANNIKA VON RODEN, NICOLE SCHRICKEL und JOACHIM HILLE.

Besonders danke ich den Personen, welche durch Kooperationen Beiträge zu dieser Arbeit geleistet haben. Genannt seien hier die Bachelor- und Masterstudierenden BENEDIKT MAGULL, MAJ GRIT KRUSE, LASSE BERGMANN, OLIVER MÖNNER, MARVIN JILL REDECKER und MAXIMILIAN PÖHLMANN sowie Mitglieder der ROESKY Gruppe SAMIR KUMAR SARKAR, MOHD NAZISH und ADIMULAN HARINATH.

OLIVER EGGERT vom ZESS-IT Team danke ich für die ausgezeichnete technische Unterstützung zu diversen Microsoft Office Problemen.

Für die vielen lizenzfreien Vektorgrafiken auf *pixabay.com* danke ich OpenClipart-Vectors.

Allen weiteren lieben Menschen, die mich auf diesem Weg begleitet haben bin ich dankbar für Ihre Unterstützung.

Ich danke LENA DRESCHER für ihre liebevolle Art und ihr Verständnis für meine langen Abende im Institut.

Meiner gesamten Familie und speziell meinen Eltern SIMONE und NORBERT LÜERT danke ich dafür, dass sie immer an mich geglaubt haben und mich in jeglicher Situation unterstützt haben. Als ich mit 9 Jahren mein eigenes Mikroskop von euch bekam und wir gemeinsam Schnitte von Insekten- und Pflanzenmaterial angefertigt haben, habt ihr den Grundstein für mein Interesse an naturwissenschaftlichen Fragestellungen gelegt. Dafür bin ich euch sehr dankbar, auch wenn ich jetzt in der anorganischen Chemie gelandet bin.

Zuletzt danke ich meinen Großeltern INGEBORG und ROBERT KRATZ, die mir immer ein großes Vorbild waren und großen Anteil an dem Gelingen meines Studiums und meiner Promotion hatten. Ich bedanke mich auch für die schöne Wohnung, welche sie mir für das gesamte Studium zur Verfügung gestellt haben.